Optimization of the s-SNOM near-field nanoscopy for the investigation of transport phenomena on the nanometer length scale

Dissertation
zur Erlangung des Doktorgrades
der Naturwissenschaften

vorgelegt beim Fachbereich Physik
der Johann Wolfgang Goethe-Universität
in Frankfurt am Main

von
Matthias Marco Wiecha
aus Bad Nauheim

Frankfurt 2021
(D 30)

vom Fachbereich Physik der

Johann Wolfgang Goethe-Universität als Dissertation angenommen.

Dekan: Prof. Dr. Harald Appelshäuser

Gutachter: Prof. Dr. Hartmut G. Roskos
Prof. Dr. Alvydas Lisauskas

Datum der Disputation: 20.06.2022

Contents

Introduction

Classical light microscopy is one of the main tools for science to study small things. Microscopes and their technology and optics have been developed and improved over centuries, however their resolution is ultimately restricted physically by the diffraction of light based on its wave nature described by Maxwell's equations. Hence, the nanoworld – often characterized by sub-100-nm structural sizes – is not accessible with classical far-field optics (apart from special x-ray laser concepts) since its lateral resolution scales with the wavelength.

It was not until the 20th century that various technologies emerged to circumvent the diffraction limit, including so-called near-field microscopy. Although conceptually based on Maxwell's long known equations, it took a long time for the scientific community to recognize its powerful opportunities and the first embodiments of near-field microscopes were developed. One representative of them is the scattering-type Scanning Near-field Optical Microscope (s-SNOM). It is a Scanning Probe Microscope (SPM) that enables imaging and spectroscopy at visible light frequencies down to even radio waves with a sub-100-nm resolution regardless of the wavelength used. This work also reflects this wide spectral range as it contains applications from near-infrared light down to deep THz/GHz radiation[1].

This thesis is subdivided into two parts. First, new experimental capabilities for the s-SNOM are demonstrated and evaluated in a more technical manner. Second, among other things, these capabilities are used to study various transport phenomena in solids, as already indicated in the title.

On the technical side, preliminary studies on the suitability of the qPlus sensor – a novel scanning probe technology – for near-field microscopy are presented. The scanning head incorporating the qPlus sensor –named TRIBUS – is originally intended and built for ultra-high vacuum, low temperature, and high resolution applications. These are desirable environments and properties for sensitive near-field measurements as well. However, since its design was not planned for near-field

---

[1]There is no sharp definition for the transition between the microwave/GHz regime and terahertz (THz) science. Depending on the definition, the frequency used here ($\sim$0.25 THz) can be assigned to both.

measurements, several special technical and optical aspects have to be taken into account, among others the scanning tip design and a spring suspended measurement head.

In addition, in this thesis field-effect transistors are used as THz detectors in an s-SNOM for the first time. Although THz s-SNOM is already an emerging technology, it still suffers from the requirements of sophisticated and specialized infrastructure on both the detector and laser side. Field-effect transistors offer an alternative that is flexible, cost-efficient, room-temperature operating, and easy to handle. Here, their suitability for s-SNOM measurements, which in general require very sensitive and fast detectors, is evaluated.

In the scientific part of this thesis, electromagnetic surface waves on silver nanowires and the conductivity/charge carrier density in silicon are investigated. Both are completely different concepts of transport phenomena, but this already shows the general versatility of the s-SNOM as it can enter both fields.

Silver nanowires are analysed by means of near-infrared radiation. Their plasmonic behaviour in this spectral region is studied complementing other simulations and studies in literature performed on them using for example far-field optics. Furthermore, the surface wave imaging ability of the s-SNOM in the near-infrared regime is thoroughly investigated in this thesis. Mapping surface waves in the mid-infrared regime is widespread in the community, however for much smaller wavelengths there are several important aspects to be considered additionally, such as the smaller focal spot size.

After that, doped and photo-excited silicon substrates are investigated. As the characteristic frequencies of charge carriers in semiconductors – described by the plasma frequency and the Drude model – are within the THz range, the THz s-SNOM is very well suited to probe their behaviour and to reveal contrasts, which has already been shown qualitatively by numerous literature reports. Here, the photo-excitation enables to set and tune the charge carrier density continuously. Furthermore, the analysis of all silicon samples focuses on a quantitative extraction of the charge carrier densities and doping levels.

The chapters of this thesis are structured as follows: Chapter 1 contains a detailed introduction to near-field microscopy in general, then the scattering-type Scanning Near-Field Optical Microscope (s-SNOM) is presented comprehensively including different (interferometric) detection schemes and typical applications. At the end, the state-of-the art of near-field microscopy at different wavelengths is briefly reviewed. Chapter 2 presents the three setups used for this thesis. A new Atomic Force Microscope (AFM) is designed and built in the scope of this thesis. It is used for two purposes, namely first tests in the mid-infrared regime and later for the THz s-SNOM. Afterwards, a brief overview of an already running

s-SNOM is given that is used for the near-infrared measurements. Finally, the TRIBUS measurement head based on the aforementioned qPlus sensor is introduced. Chapter 3 contains tests and analysis of the s-SNOM infrastructure, i.e. some general aspects of the s-SNOM are demonstrated using the mid-infrared spectral region, the preliminary work on the qPlus sensor is presented, and the THz s-SNOM is benchmarked comprehensively. Chapter 4 analyses the near-infrared surface plasmon polariton measurements on silver nanowires and THz measurements on silicon samples in detail.

At the end, the entire thesis is concluded and an outlook on the future of the different topics is given. The appendix treats some supplementary aspects of this work, including an extensive mathematical description of the s-SNOM pseudo-heterodyne detection scheme, the codes of important simulations of this work (MATLAB), some laboratory assistance and hints for s-SNOM alignment, and a performance test of a numerical lock-in amplifier (LabVIEW) written for the purpose of this thesis.

Zusammenfassung

Klassische Lichtmikroskopie ist eines der Hauptwerkzeuge der Wissenschaft um "kleine Dinge" zu untersuchen. Mikroskope und ihre Technik und Optiken wurden jahrhundertelang entwickelt und verbessert. Allerdings ist ihre Auflösung letztendlich durch die Beugungsbegrenzung des Lichtes physikalisch begrenzt, die auf dessen Wellennatur beruht und durch die Maxwell Gleichungen beschrieben wird. Daher ist die Nanowelt (häufig grob eingeordnet als Strukturgrößen unter 100 Nanometer) nicht mit klassischer Fernfeldoptik zugänglich (abgesehen von speziellen Röntgenlasern), da deren laterale Auflösung mit der Wellenlänge skaliert.

Erst im 20. Jahrhundert sind verschiedene Technologien aufgekommen um dieses Limit zu umgehen, u.a. die sogenannte Nahfeld-Mikroskopie. Auch wenn sie konzeptionell auf den lange bekannten Maxwell-Gleichungen basiert, hat es doch eine lange Zeit gebraucht bis die Wissenschaftsgemeinde ihre vielseitigen Möglichkeiten erkannte und es erste Nahfeldmikroskop-Prototypen gab. Ein Repräsentant dieser Kategorie ist das Streutyp optisches Rastersonden-Nahfeld-Mikroskop (*scattering-type Scanning Near-Field Optical Microscope*, s-SNOM). Es basiert auf einem Rastersondenmikroskop (*Scanning Probe Microscope*, SPM) und ermöglicht Bildgebung und Spektroskopie bei sichtbaren Wellenlängen bis hinunter zu Radiowellen jeweils mit einer Auflösung von unter 100 nm unabhängig von der genutzten Wellenlänge. Dieses breite Spektrum möglicher Wellenlängen spiegelt sich auch in dieser Arbeit wider, die Anwendungen vom Nah-Infraroten Spektralbereich bis hinunter in den tiefen Terahertz-/Mikrowellen-Bereich[2] präsentiert.

Diese Doktorarbeit ist unterteilt in zwei Themengebiete. Zuerst werden neue technische Möglichkeiten für das s-SNOM demonstriert und evaluiert. Als Zweites werden u.a. diese neue Technologien genutzt um, wie bereits der Titel andeutet, verschiedene Transport-Phänomene in Festkörpern zu untersuchen.

Auf der technischen Seite werden zum einen vorläufige Ergebnisse zur Eignung des qPlus-Sensors (einer neuen Rastersondenmikroskop-Technologie) als s-

---

[2]Es gibt keine einheitliche Definition für den Übergang zwischen Mikrowellen- und Terahertz-Bereich (THz). Die hier genutzte Frequenz von $\sim$0.25 THz kann je nach Definition beidem zugeordnet werden.

SNOM präsentiert. Der genutzte Messkopf, welcher auf der qPlus-Technologie basiert, wurde ursprünglich für Anwendungen im Ultrahochvakuum (UHV), bei tiefen Temperaturen und mit hohen Auflösungen geplant und gebaut. All das sind auch wünschenswerte Umgebungen und Eigenschaften für empfindliche Nahfeld-Messungen. Allerdings wurde der Messkopf nicht für Nahfeld-Messungen konzipiert, daher müssen viele technische und optische Aspekte beachtet werden.

Die wesentliche technische Neuerung dieser Arbeit ist die Einführung von Terahertz Feldeffekttransistoren (TeraFETs) in die s-SNOM Technologie. Auch wenn das THz s-SNOM zunehmend in der Wissenschaft verbreitet ist, wird es immer noch von seinen hohen Anforderungen an die Emitter und Detektoren limitiert. Feldeffekttransistoren bieten sich als flexible, kostengünstige, bei Raumtemperatur arbeitende und leicht zu handhabende Alternative an. Ihre Eignung für s-SNOM Messungen, die im Allgemeinen sehr sensitive und schnelle Detektoren erfordern, wird hier untersucht.

In dem wissenschaftlichen Abschnitt dieser Arbeit werden elektromagnetische Oberflächenwellen auf Silber Nanodrähten sowie die Leitfähigkeit bzw. Ladungsträger-Dynamik in Silizium untersucht. Beides sind komplett verschiedene Konzepte von "Transport-Phänomenen", was bereits die allgemeine Vielseitigkeit des s-SNOMs andeutet, welches in beiden Feldern neue Erkenntnisse liefern kann.

Die Silber Nanodrähten werden mittels Nah-Infrarot-Strahlung untersucht. Ihr plasmonisches Verhalten in diesem Spektralbereich wird analysiert und ergänzt Simulationen und andere experimentelle Untersuchungen in der Literatur wie Fernfeld-Experimente. Darüber hinaus wird die Fähigkeit des s-SNOMs Oberflächenwellen im Nah-Infraroten darzustellen umfassend untersucht. Das Abbilden von Oberflächenwellen im Mittel-Infraroten ist weit verbreitet in der Wissenschaft, für kleinere Wellenlängen allerdings gibt es einige zusätzliche Aspekte zu beachten wie beispielsweise die kleineren Fokusgrößen.

Anschließend werden dotierte und photo-angeregte Silizium-Proben untersucht. Da die charakteristischen Frequenzen von freien Ladungsträgern in Halbleitern - beschrieben mittels Plasma-Frequenz und dem Drude-Modell - im THz-Bereich liegen, ist das THz s-SNOM gut geeignet um deren Verhalten und Kontraste zu messen, was bereits qualitativ in vielen Studien beschrieben ist. In dieser Arbeit ermöglicht die Photo-Anregung die Ladungsträgerdichte kontinuierlich einzustellen. Der Fokus der Datenanalyse der Silizium-Proben liegt auf der quantitativen Extraktion von Ladungsträgerdichte und Dotierungslevel.

Kapitel 1 beinhaltet eine detaillierte Einführung in die Nahfeldmikroskopie mittels s-SNOM. Nach einer kurzen Beschreibung der mathematischen Grundlagen und wie sub-wellenlängen große Blenden oder Streupartikel und evaneszente Felder dabei helfen die klassische Beugungsbegrenzung zu umgehen, folgt ein tech-

nischer Abschnitt über den Aufbau der Mikroskope (s-SNOM). Sie alle basieren auf dem Prinzip des Rasterkraftmikroskopes (*Atomic Force Microscope*, AFM), das zu den Rastersondenmikroskopen (SPM) gehört. Hierbei rastert eine scharfe Messspitze die Probe ab. Währenddessen sorgt eine Regelungsschleife dafür, dass der Abstand zwischen Messspitze und Probe immer gleich bleibt; die abstandsregelnden Piezo-Elemente folgen also der Oberflächentopographie, sodass bei einer Rastermessung ein zweidimensionales Höhenprofil der Probe entsteht. Zusätzlich wird beim s-SNOM nun die Messspitzen-Proben-Region mit einem Laser bestrahlt. Das vordere Ende der Messspitze wechselwirkt mit der Probe durch eine Nahfeldinteraktion und streut Licht, das optische Informationen über die Probe enthält. Dieses Streulicht wird im s-SNOM aufgesammelt, gemessen und verarbeitet, sodass parallel zur Topographie auch zweidimensionale Messungen der optischen Eigenschaften entstehen. Bereits ein sehr einfaches statisches Punkt-Dipol-Modell reicht aus, um die Nahfeldwechselwirkung qualitativ und phänomenologisch zu erklären und zeigt, dass im s-SNOM im Wesentlichen die lokale dielektrische Funktion der Probe vermessen wird. Ein entscheidender Aspekt ist nun, dass sowohl die AFM als auch die s-SNOM Auflösung von der Geometrie der Messspitze abhängen, genauer gesagt vom Krümmungsradius an deren Ende, sodass in beiden Messsignalen Nanometer-Auflösung erreicht wird. Daher ist die sub-100 nm s-SNOM Auflösung auch, wie bereits oben beschrieben, vollkommen unabhängig von der verwendeten Wellenlänge. Die größte technische Herausforderung im s-SNOM besteht in der Signal-Verarbeitung. Die Messspitze wird mit einem Fernfeld-Fokus beleuchtet, dessen Größe gemäß der klassischen Optik mit der Wellenlänge skaliert. Das zurückgestreute Licht enthält also vorwiegend Anteile von Streulicht und Reflektionen der Probe und von Teilen der Messspitze, die jeweils weit von der Nahfeld-Wechselwirkungszone entfernt liegen. Um den Nahfeld-Anteil zu isolieren, kann man den sogenannten dynamischen Modus des AFM nutzen. Hierbei schwingt die Messspitze nahe ihrer Resonanzfrequenz mit Ω; durch eine starke Nichtlinearität der Nahfeldwechselwirkung entstehen in deren Streusignal höhere Harmonische in 2Ω, 3Ω, 4Ω, ... wohingegen die störenden Streu- und Reflektionsanteile lediglich konstant oder mit 1Ω moduliert sind. Durch Demodulation des gemessenen Signals auf den höheren Harmonischen kann also das Nahfeldsignal isoliert werden. Des Weiteren ergeben sich besondere Anforderungen an die Detektion selbst, da die meisten Detektoren Intensitäten und nicht die elektrischen Felder messen. Da das Hintergrundlicht sehr viel stärker als das eigentliche Nahfeld-Signal ist, wird im s-SNOM also vorwiegend das Produkt aus Nahfeld und Hintergrund gemessen (der sogenannte Intensitäts-Messmodus). Insbesondere der Hintergrundanteil ist aber während einer Messung nicht konstant und schwer kontrollierbar. Des Weiteren ist auch die optische Nahfeld-Phase nicht zugänglich, eine weitere Messgröße, die Absorptionen innerhalb der Probe beschreibt und mathematisch

7

durch eine komplexe Behandlung der entsprechenden Gleichungen erfasst werden kann. All diese Probleme werden mit interferometrischer Detektion gelöst, bei der sowohl das reine Nahfeld wie auch die Phase bestimmt werden können und die eine interferometrische Signalverstärkung ermöglicht. Verschiedene Modi werden detailliert und mathematisch beschrieben. Gemeinsam für alle ist, dass das Streulicht im Detektor mit einer starken Referenz überlagert wird, die entweder konstant (homodyne Detektion), leicht frequenzverschoben (heterodyne Detektion) oder phasenmoduliert (pseudo-heterodyne Detektion) ist. Der nächste Abschnitt dieser Arbeit geht auf typische s-SNOM Anwendungen ein. Zum einen wird das oben genannte Abbilden der dielektrischen Funktion der Probe genauer beschrieben und beispielhaft anhand von Halbleitern simuliert, bei denen die Abhängigkeit der dielektrischen Funktion von der Ladungsträgerdichte oder der Wellenlänge mit dem Drude-Modell modelliert werden kann. Zum anderen wird eine zweite Art von Anwendungen der s-SNOM Technik erläutert. Sie ist in der Lage, propagierende elektromagnetische Oberflächenwellen (z. B. Oberflächenplasmon- und Phonon-Polaritonen) als statisches Interferenzmuster stehender Wellen abzubilden. Diese Fähigkeit hebt das s-SNOM von vielen anderen Mikroskopen der Nanotechnologie ab. Der letzte Abschnitt dieses Kapitels geht nochmal ein auf Besonderheiten und typische Beispiele der s-SNOM Nahfeldmikroskopie in verschiedenen Spektralbereichen wie im Optischen/Nah-Infraroten, im Mittel-Infraroten sowie bei langwelligen Terahertz- und Radiowellen.

Kapitel 2 befasst sich mit der experimentellen Infrastruktur und beschreibt die drei verwendeten Aufbauten und Geräte dieser Arbeit. In deren Rahmen wird ein neues AFM aufgebaut, das zuerst im Mittel-Infraroten getestet und charakterisiert und später zum THz s-SNOM weiterentwickelt wird. Hierfür werden wie bereits erwähnt erstmalig sogenannte Terahertz Feldeffekttransistoren (*terahertz field-effect transistor*, TeraFET) als s-SNOM Detektoren eingesetzt, die am Physikalischen Institut der Goethe-Universität Frankfurt entwickelt wurden. Danach wird ein weiteres bereits vorhandenes s-SNOM kurz dargestellt, an dem die Nah-Infrarot-Messungen durchgeführt werden. Abschließend wird der TRIBUS-Messkopf vorgestellt, der die qPlus-Technik nutzt (einen neuartigen AFM-Sensor basierend auf einer Stimmgabel).

Kapitel 3 befasst sich mit den technologischen Neuerungen dieser Arbeit im Hinblick auf das s-SNOM. Im ersten Abschnitt werden zunächst die Mittel-Infrarot-Komponenten und das entsprechende Interferometer an einem konventionellen s-SNOM Aufbau getestet, wobei einige technische Aspekte genauer betrachtet werden, wie z. B. ein Vergleich verschiedener Detektionsmodi, die Rolle der Fokuslänge im s-SNOM sowie die mechanische Stabilität im Interferometer.

Im darauf folgenden Abschnitt wird dann erfolgreich die s-SNOM Tauglichkeit des qPlus-Sensors im Mittel-Infrarot-Bereich demonstriert. Einige fundamentale Messungen werden gezeigt wie z. B. die sogenannten Annäherungskurven (*approach curves*), bei denen das Nahfeldsignal als Funktion des Messspitzen-Proben-Abstandes aufgenommen wird. Ursprünglich ist der TRIBUS-Messkopf für hochauflösende Messungen im Ultrahochvakuum (UHV) und bei tiefen Temperaturen konstruiert worden, was der Grund für einige besondere Aspekte in der Konstruktion des TRIBUS-Messkopfes ist (Federaufhängung, bewegte Messspitze statt bewegter Probe), deren Konsequenzen für Nahfeldmessungen theoretisch und experimentell diskutiert werden.

Anschließend wird das neu aufgebaute THz s-SNOM, welches auf den TeraFET-Detektoren basiert, behandelt. Nach einer ausführlichen Charakterisierung der entscheidenden Elemente (Strahlungsquelle, Detektor, Strahlenteiler) werden einige Leistungstests gemacht wie z. B. die bereits erwähnten Annäherungskurven oder auch einfache ein- und zweidimensionale Messungen inklusive einer groben Schätzung der Auflösung auf ca. 40 nm.

Kapitel 4 ist der Kern dieser Arbeit und präsentiert die Analyse der beiden Transport-Phänomene Oberflächenwellen und Ladungsträgerdynamik in Halbleitern.

Zuerst werden die Nah-Infrarot-Messungen an Silbernanodrähten (*silver nanowire*, Ag NW) behandelt. Deren Verwendung in Terahertz-Photomixern wird kurz motiviert. Anschließend werden Messungen bei verschiedenen Einfallsrichtungen (parallel und senkrecht zu ihrer Achse) und Polarisationen präsentiert, die Wellenmuster von Oberflächenplasmon-Polaritonen zeigen. Die entstehenden Wellenmuster unterscheiden sich sehr stark für verschiedene Polarisationen und Einfallsrichtungen. Dies kann durch einfache geometrische Überlegungen erklärt werden. Darüber hinaus wird bei einer Messung ein markantes schräges Muster auf dem Nanodraht gemessen. In der Literatur gibt es bereits Hinweise auf solche Muster als Überlagerung verschiedener Moden, die bisher allerdings nur indirekt durch Fernfeldmessungen oder Simulationen zugänglich waren. Zusammenfassend ergänzt diese Arbeit also die Forschung zur Plasmonik an Silbernanodrähten um ein fehlendes Puzzlestück und liefert darüber hinaus allgemeine Erkenntnisse über die Entstehung von Wellenmustern im s-SNOM durch Oberflächenwellen im Optischen/Nah-Infraroten.

Als Letztes wird als konkretes Anwendungsbeispiel das THz s-SNOM genutzt um die Ladungsträgerdichte in Halbleitern zu bestimmen. In der Nähe deren Plasmafrequenz ergeben sich charakteristische Peaks und Gradienten in den THz s-SNOM Signalen (sowohl in der optischen Amplitude als auch Phase) als Funktion der Ladungsträgerdichte oder der genutzten Wellenlänge, was mithilfe des Drude-

Modells erklärt werden kann. Anhand von mehreren Silizium-Proben wird gezeigt, wie man aus den Messdaten die Ladungsträgerdichte extrahieren kann. Zuerst wird ein Substrat optisch angeregt und das entstehende Elektron-Loch Plasma mit dem THz s-SNOM vermessen. Die gemessene Abhängigkeit der Nahfeldsignale von der Anregeleistung (bzw. der hieraus resultierenden Ladungsträgerdichte) kann mit überzeugender Übereinstimmung mit numerischen Modellen reproduziert und erklärt werden. Weitere Effekte der Ladungsträgerdynamik im Silizium (Diffusion, Rekombination) wie auch Effekte der optischen Anregung auf das s-SNOM werden hierbei diskutiert. Als zweites Beispiel wird die Dotierung zweier weiterer Proben durch einzelne THz Messungen gegenüber einer Gold-Referenz bestimmt. Insbesondere die Nahfeld-Phase ist hierfür besser geeignet, da die Phase eine absolute Messgröße ist und nicht wie die s-SNOM Amplitude von vielen weiteren experimentell schwer zu kontrollierenden Faktoren abhängt.

Abschließend werden die Ergebnisse dieser Arbeit zusammengefasst, in den aktuellen Stand der Forschung eingeordnet und Ausblicke auf die Zukunft gegeben. Die Grundlagen für s-SNOM Messungen mittels des qPlus Sensors sind gelegt, im weiteren Verlauf dieses Projektes muss nun das Leistungsvermögen des gesamten Messsystems, insbesondere in Bezug auf Stabilität und erreichbarer Auflösung, charakterisiert werden. Die TeraFET-Detektoren zeigen eine sehr überzeugende Performance und es ist zu erwarten, dass sie sich in den kommenden Jahren zu einer Standardtechnologie nicht nur für THz-Forschung allgemein, aber auch speziell für die THz Nahfeldmikroskopie entwickeln. Sie könnten zusammen mit anderen Raumtemperatur-Detektoren wie Schottky-Dioden schon bald die Tieftemperatur-Bolometer, welche eine aufwendige Kühlung mittels flüssigem Helium benötigen, in vielen Bereichen verdrängen. Die neuen Erkenntnisse zu den Silbernanodrähten fügen sich nahtlos in die bestehende Forschung ein und liefern zusätzliche hochaufgelöste Nahfeldmessungen in einem Bereich, der bisher vorwiegend auf Simulationen oder Fernfeldtechniken basiert. Die Leitfähigkeitsmessungen des THz s-SNOMs öffnen den Weg hin zu einem wichtigen Werkzeug zur zerstörungsfreien und berührungslosen Ladungsträgerprofilierung mit Nanometer-Auflösung in der Halbleitertechnik und zur elektronischen Charakterisierung neuer Materialien.

Im Anhang werden nochmal einige ergänzende Aspekte dieser Arbeit behandelt. Die pseudo-heterodyne Detektion wird detailliert mathematisch hergeleitet, die MATLAB-Programme für einige wichtige Simulationen sind verfügbar, es werden einige praktische Hinweise und Tipps zur s-SNOM Justage gegeben und abschließend wird noch ein numerischer Lock-in Verstärker (LabVIEW) getestet, der im Rahmen dieser Arbeit erstellt und viel genutzt wurde.

Publications, Presentations, & Grants

During the PhD period, the following articles were published (containing already results of this work):

- [1] F. Walla, F. Buerkle, I. Sinev, M. M. Wiecha, N. Mecklenbeck, K. Ladutenko, R. Malureanu, F. Komissarenko, A. Lavrinenko, A. Bogdanov, A. Soltani, and H. G. Roskos: *Near-field observation of guided-mode resonances on a metasurface via dielectric nanosphere excitation*, ACS Photonics, 5(11), 4238-4243, 2018.

- [2] M. M. Wiecha, S. Al-Daffaie, A. Bogdanov, M. D. Thomson, O. Yilmazoglu, F. Kuppers, A. Soltani, and H. G. Roskos: *Direct Near-Field Observation of Surface Plasmon Polaritons on Silver Nanowires*, ACS Omega, 4(26), 21962-21966, 2019.

- [3] A. Soltani, F. Kuschewski, M. Bonmann, A. Generalov, A. Vorobiev, F. Ludwig, M. M. Wiecha, D. Cibiraite, F. Walla, S. Winnerl, S. C. Kehr, L. M. Eng, J. Stake, and H. G. Roskos: *Direct nanoscopic observation of plasma waves in the channel of a graphene field-effect transistor*, Light: Science & Applications, 9(1), 2020.

- [4] M. M. Wiecha, R. Kapoor, A. V. Chernyadiev, K. Ikamas, A. Lisauskas, and H. G. Roskos: *Antenna-coupled field-effect transistors as detectors for terahertz near-field microscopy*, Nanoscale Advances, 3, 1717-1724, 2021.

- [5] M. M. Wiecha, A. Soltani, and H. G. Roskos: *Terahertz nano-imaging with s-SNOM*, book chapter in *Terahertz Technology*, IntechOpen, book edited by Dr. Borwen You, 2021 (accepted).

- [6] M. M. Wiecha, R. Kapoor, and H. G. Roskos: *Terahertz scattering-type near-field microscopy quantitatively determines the conductivity and charge carrier density of optically doped and impurity-doped silicon* (submitted).

Presentations and poster contributions to scientific events and conferences:

- "Surfaces and Interfaces - Summer school 2017", San Sebastián (Spain) (poster *Excitation of surface plasmon polaritons with a scattering-type scanning near-field optical microscope*)

- "7th German-Russian-Travelling Seminar on Nanomaterials and Scattering Methods", 2017, Russia (presentation *Nanophotonics – Confining light at metasurfaces*)

- "9. THz-Frischlingetreffen", 2018, Kaiserslautern (presentation *THz experiments with nanometer resolution by means of near-field microscopy*)

- "15th International Conference on Near-Field Optics, Nanophotonics & Related Techniques - NFO15", 2018, Troyes (France) (poster *Excitation channels for surface plasmon polaritons in scattering-type near-field optical nanoscopy*)

- "10. THz-Frischlingetreffen", 2019, Frankfurt (poster *Near-infrared near-field investigation of silver nanowires for efficient THz photomixers*)

- "French-German Terahertz Conference 2019", Kaiserslautern (presentation *Silver Nanowire Plasmonic Enhancement in Nanoelectrodes THz Photomixer* and poster *Near-infrared near-field investigation of silver nanowires for efficient THz photomixers*)

- "International Conference on Terahertz Emission, Metamaterials and Nanophotonics TERAMETANANO-4", 2019, Lecce (Italy) (poster *Surface Plasmon Polariton Modes on Silver Nanowires*)

- "11. THz-Frischlingetreffen", 2020, Marburg (presentation *Subwavelength resolution by means of near-field microscopy and application examples from THz research*)

- "11th International Conference on Metamaterials, Photonic Crystals and Plasmonics META", 2021 (poster *Terahertz near-field microscopy for quantitative measurements of the conductivity and charge carrier density on the nanoscale*)

- "46th International Conference on Infrared, Millimeter and Terahertz Waves IRMMW", 2021 (presentation *Quantitative determination of the density of photo-excited charge carriers by s-SNOM with field-effect-transistor-based THz detection*)

Successful grant applications:

- Grant extension of the research project *Orts- und zeitaufgelöste Spektroskopie an plasmonischen Strukturen mittels s-SNOM-Nanoskopie* "Dr. Hans Messer Stiftung - Stiftung für Bildung, Wissenschaft und Forschung"

- LOEWE3 project (**L**andes-**O**ffensive zur **E**ntwicklung **W**issenschaftlich-ökonomischer **E**xzellenz - Förderlinie 3; Innovationsförderprogramm des Landes Hessen) *Kryo-sSNOM - Entwicklung eines Tieftemperatur-Nahfeldmikroskopes* together with Sigma Surface Science GmbH (later merged into Scienta Omicron Technology GmbH)

Abbreviations

Short form	Meaning
AC	Alternating Current
ADC	Analog Digital Converter
AFM	Atomic Force Microscope/Microscopy
AM-AFM	Amplitude-Modulated Atomic Force Microscope/Microscopy
AOM	Acousto-Optic Modulator
CAD	Computer-Aided Design
CMOS	Complementary Metal-Oxide Semiconductor
CW	Continuous Wave
DAC	Digital Analog Converter
DC	Direct Current
EELS	Electron Energy-Loss Spectroscopy
FET	Field-Effect Transistor
FM-AFM	Frequency-Modulated Atomic Force Microscope/Microscopy
IR	Infrared
LIA	Lock-In Amplifier
LTG	Low-Temperature Grown

Table 1: Abbreviations used in this work (A-L)

Short form	Meaning
mIR	Mid-Infrared
NA	Numerical Aperture
NEP	Noise-Equivalent Power
nIR	Near-Infrared
NW	Nanowire
PLL	Phase-Locked Loop
PSD	Position Sensitive Diode
SEM	Scanning Electron Microscope/Microscopy
s-SNOM	scattering-type Scanning Near-field Optical Microscope/Microscopy
SNOM	Scanning Near-field Optical Microscope/Microscopy
SNR	Signal-to-Noise Ratio
SPM	Scanning Probe Microscope/Microscopy
SPP	Surface Plasmon Polariton
STED	Stimulated Emission Depletion
STM	Scanning Tunneling Microscope/Microscopy
TeraFET	Terahertz Field-Effect Transistor
TDS	Time-Domain Spectroscopy
UHV	Ultra-High Vacuum

Table 2: Abbreviations used in this work (M-Z)

1. Near-Field Microscopy

This chapter gives a brief introduction into nanophotonics starting from its mathematical and physical basis in section 1.1, followed by a detailed description of the scattering-type Scanning Near-Field Optical Microscopy (s-SNOM) in section 1.2, different (interferometric) detection schemes in section 1.3, its two main applications (probing the dielectric function and mapping of polariton waves) in section 1.4, and a brief review about the state-of-the art of s-SNOM research at different spectral ranges in section 1.5.

1.1 Introduction to nanophotonics

Nanophotonics combines the two key technologies optics and nanotechnology. For instance, optics has been enabling insights into small things by means of optical microscopy and into astronomic objects by means of optical telescopes for several centuries. Nanotechnology started its rise in the 20th century with the development of electron microscopy and new insights of quantum physics.

However, the access of classical optics into the nanoworld is restricted by the wave nature of light (wavelength λ) and the resulting diffraction. Two concepts (with slightly different derivations and meanings) are used to quantify this limit, the Abbe limit and the Rayleigh criterion, which both lead to similar results for the resolution limit Δx of a microscope stated in eq. (1.1) using the numerical aperture $NA = n \cdot sin\Theta$ (with the refractive index of the medium n and half the opening angle of the objective Θ). There are two common ways to derive this limit: Firstly, a grating under a microscope is assumed, and it is calculated when the first diffraction order is just collected by the objective and therefore the grating is still observable. Secondly, the Airy patterns of two neighbouring light sources overlap in such a way that the maximum of the first disc is on top of the minimum of the second disc. [7]

$$\Delta x \approx 0.61 \cdot \frac{\lambda_0}{NA} = 0.61 \cdot \frac{\lambda_0}{n \cdot sin\Theta} \tag{1.1}$$

During the 20th century in parallel with the development of nanotechnology, the question arose if there are ways to overcome the Abbe limit to extend the experimental opportunities to the nanoscale. One concept for this are so-called near-field microscopes; one implementation of them is used in this thesis.

1.1.1   Fundamental ideas

The basic ideas for near-field microscopes are quite old. E. H. Synge discussed them in some letters with A. Einstein [8] and published his ideas and concepts in 1928 [9].

He proposed to scan a sample with a subwavelength aperture (in subwavelength distance above the sample) or with a subwavelength sized scattering-particle (again in subwavelength distance above the sample) and beat the classical Abbe diffraction limit, see fig. 1.1 a) and b)[1].
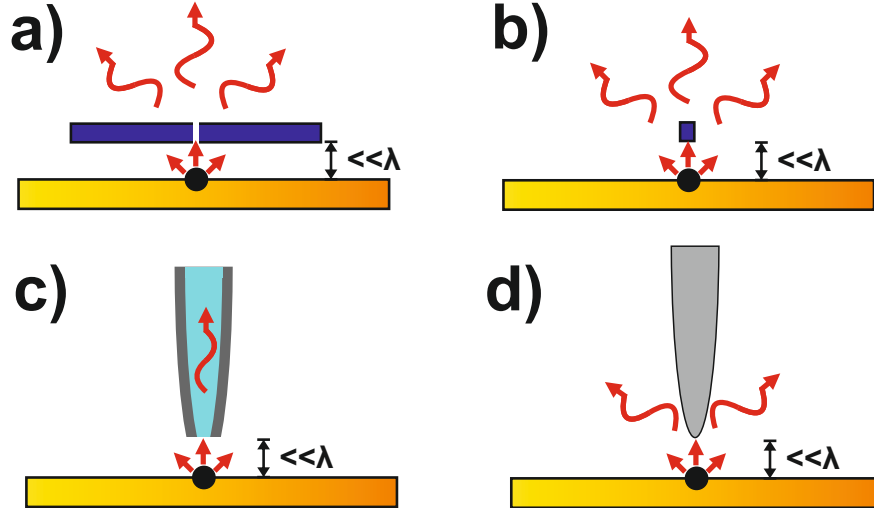

Figure 1.1: Synge's ideas of a) a subwavelength aperture and b) a subwavelength sized scattering particle scanned in subwavelength distance above a sample to convert near-fields (straight arrows) into far-field radiation (waveform arrows). Nowadays, those ideas are realized by means of c) an optical fiber collecting near-fields or d) a metallic tip, both scanned again in subwavelength range above the sample.

The focus of his publication is a discussion about the possible realization and several technical issues that were not easy to solve at that time. Therefore, it is

---

[1]Although Synge described only the first concept in his paper, both of them were discussed in his letters with Einstein.

not surprising that it took some more decades until nowadays his ideas has become technically feasible: A metal coated optical fiber can be used as a subwavelength aperture for optical frequencies (e.g. diameter∼resolution<100 nm [10, 11]) or a small dielectric/metallic tip can act as a scattering particle, see fig. 1.1 c) and d), respectively. The first concept is called Scanning Near-field Optical Microscopy (SNOM); the latter one is the basis for the scattering-type Scanning Near-field Optical Microscopy (s-SNOM).

1.1.2   Mathematical description

The concept of the resolution limit eq. (1.1) can be connected to Heisenberg's uncertainty principle [12] using the uncertainty Δk_x of a lens imaging scheme (k_x is the k-component projected to the surface, factor two for both directions, see fig. 1.2):

$$\Delta k_x = 2k sin\theta = \frac{2 \cdot 2\pi n sin\theta}{\lambda_0} = \frac{4\pi n sin\theta}{\lambda_0} \ . \tag{1.2}$$
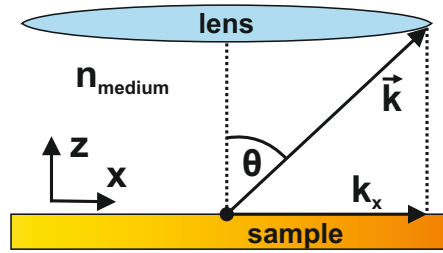

Figure 1.2: The Abbe resolution in classical microscopy is limited by the highest k_x values that can be imaged by the lens.

Inserting this term into the Heisenberg inequality eq. (1.3) leads to eq. (1.4), which corresponds to the Abbe limit eq. (1.1).

$$\Delta x \Delta p_x = \Delta x \frac{h \Delta k_x}{2\pi} \ \geq \ h \ \ \mapsto \ \ \Delta x \geq \frac{2\pi}{\Delta k_x} \tag{1.3}$$

$$\Delta x \geq \frac{2\pi}{\Delta k_x} = \frac{2\pi \lambda_0}{4\pi n \cdot sin\theta} = \frac{\lambda_0}{2n \cdot sin\theta} \tag{1.4}$$

In eq. (1.3) it is already stated that the k-vector is a measure for the achievable resolution (the smaller the features to be observed, the higher the corresponding k-vectors are required). Starting from this, the question arises how near-field microscopes can overcome the Abbe limit. Decomposing the k-vector in its components shows that the highest possible value for any spatial component corresponds to k if only real numbers are considered:

19

$$k = \frac{2\pi}{\lambda} = \sqrt{k_x^2 + k_y^2 + k_z^2}\,. \tag{1.5}$$

However, by using complex k-components (e.g. $k_z = i \cdot |k_z|$) any arbitrary high k_{xy} is possible:

$$k_{xy} = \sqrt{k^2 - k_z^2} = \sqrt{k^2 + |k_z|^2} > k\,. \tag{1.6}$$

Inserting a complex valued k_z into a plane wave equation reveals the physical nature of such fields.

$$
\begin{aligned}
\vec{E}(\vec{x}, t) = E_0 e^{i(\vec{k}\vec{x} - \omega t)} = E_0 e^{i(k_x x + k_y y + k_z z - \omega t)} &= E_0 e^{i(k_x x + k_y y + i|k_z|z - \omega t)} \\
&= E_0 e^{i(k_x x + k_y y - \omega t)} e^{-|k_z|z}
\end{aligned}
\tag{1.7}
$$

Complex k-vectors correspond to exponentially decaying and non-propagating fields, the so-called evanescent fields. They are often utilized at interfaces or surfaces (e.g. they are well known from total internal reflection). Moreover, it is required to be very close to their origin to obtain a measurable value due to their fast exponential decay. [8, 10, 13]. Interestingly, evanescent fields are omnipresent, and even every Gaussian beam is possessing them, although this is usually only relevant for highly focussed beams [10].

1.2 Scattering-type Scanning Near-Field Optical Microscopy (s-SNOM)

The base of every scattering-type Scanning Near-Field Optical Microscope (s-SNOM) is an Atomic Force Microscope (AFM), a standard instrument of nanotechnology. Therefore, first in this section the AFM is briefly introduced and after that the required technical and conceptual modifications and extensions towards an s-SNOM are presented.

1.2.1 Atomic Force Microscopy (AFM)

The main component of an AFM are very sharp probes that are scanned above a sample. During that, a feedback mechanism holds the distance between the probe and the sample surface at a fixed value and a two-dimensional topographical image is built up.

The key element is of course the sharp probe, e.g. fig. 1.3. On the end of a long bar/cantilever (that is bendable with an eigenfrequency Ω) a tip is mounted. Its opposite end possesses a very sharp apex (mostly far beneath <50 nm)
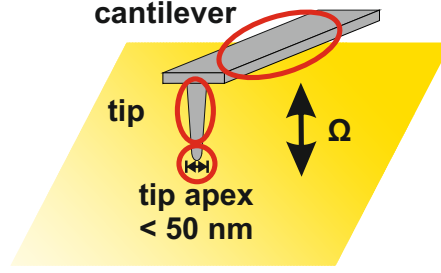
Figure 1.3: Sketch of an AFM cantilever and its components oscillating with the frequency Ω above a sample.

that, among other parameters, defines the resolution of the AFM. For scanning a sample (sample plane xy) and control of the distance to the tip (z-direction), piezo elements are used. In some special crystals the piezo electric effect occurs, i.e. the crystals are extending if an external voltage is applied (or vice versa applying a force induces a voltage). Since this effect is quite small (e.g. ~20 nm/V [14]), it is possible to scan and control very small distances down to the subnanometer range.

Two important modes of AFM operation can be distinguished [15]:

- contact-mode: The tip apex touches the sample and depending on the topography the cantilever is bent. The control parameter for the feedback mechanism is the bending of the cantilever.

- non-contact mode: The cantilever is oscillating. In the vicinity of the sample, the oscillation is affected by the sample. There are several control parameters (see below).

Both modes have their advantages and drawbacks. However, the s-SNOM is based on the non-contact mode, therefore this one will be described in more detail.

As a first approximation the cantilever can be described as a driven harmonic oscillator, therefore its equation of motion (1.8) can be solved [16] (damping α, mass m, amplitude of external force A and its frequency ω, and cantilever resonance ω_0 eq. (1.9) containing the spring constant k).

$$\ddot{z} + 2\frac{\alpha}{m}\dot{z} + \omega_0^2 z = \frac{A}{m}cos(\omega t) + \frac{F_{tip-sample}(z)}{m} \tag{1.8}$$

$$\omega_0 = \sqrt{\frac{k}{m}} \tag{1.9}$$

The effect of the external force from the tip-sample interaction can be interpreted as a changed resonance ω_{eff} assuming $F_{tip-sample}(z) \approx k' \cdot z$ (derived by a

Taylor series of the potential energy close to the equilibrium position in the approximation of a small oscillation in comparison to the length scale of the external force):

$$\omega_{eff} = \sqrt{\frac{k - k'}{m}} \, .$$

(1.10)

From eq. (1.9) it follows that the change in resonance frequency $\Delta\omega$ is proportional to the gradient in the effective spring constant Δk

$$\frac{\Delta\omega}{\omega_0} = \frac{\Delta k}{2k} \, .$$

(1.11)

The most important contributions to $F_{tip-sample}$ are a repulsive force (at the fundamental level due to the Pauli exclusion principle), more long ranging attractive van der Waals forces (due to dipole-dipole interaction), and chemical bonding forces (both attractive and repulsive); the physical details and mathematical models can be found in the corresponding literature [17, 18].

Two feedback modes are common to control the distance between the tip and the sample: Amplitude-modulated AFM (AM-AFM) and frequency-modulated AFM (FM-AFM). In the first one, the cantilever is excited at a fixed frequency (close to the resonance; right/left side depending on the direction of the resonance curve shift), the attractive (repulsive) tip-sample forces in the vicinity of the sample shift the resonance towards lower (higher) values, and the measured amplitude (at a fixed frequency) decreases towards a user chosen setpoint, which is the decisive quantity of the feedback system. During a scan, the controller holds the amplitude at the setpoint level by changing the tip-sample distance; hence, from the movement of the z-piezos the topography is deduced.

In FM-AFM, the tip-sample forces act again on the cantilever and shift its resonance. A phase-locked loop (PLL) follows this shift (by lock-in to the phase) and excites the cantilever continuously in resonance, i.e. the PLL varies the excitation frequency. Now, the change in excitation frequency Δf is the decisive quantity for the feedback system, i.e. during a scan, the controller maintains Δf by changing the tip-sample distance.

The AM-AFM is easier to implement (e.g. no PLL required), on the other side in FM-AFM a second feedback circuit can vary the excitation amplitude (independently of the phase feedback) to maintain a constant oscillation amplitude during the entire measurement to compensate (and analyse) any energy losses. [19]

In summary, in the vicinity of the sample the external forces shift the resonance frequency of the cantilever and both its amplitude and phase could change.

There are two main ways to measure the probe tip dynamics and to create a signal for the distance control feedback loop:
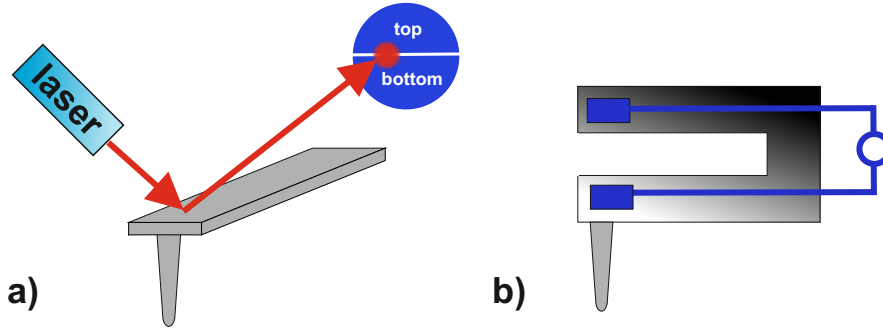
Figure 1.4: Two different concepts for probe measurements a) The light pointer principle where a reflected laser beam transforms the cantilever oscillation into an oscillating "top-bottom" electronic signal of the position sensitive diode and b) a piezo-electric device (e.g. a quartz tuning fork) where the oscillation is directly read out electrically using the piezo-electric effect.

Cantilever based probes

Cantilever based probe tips are nowadays the most widespread solution and a standard consumable article. Their movement can be read out via the light pointer principle sketched in fig. 1.4 a). A laser beam is reflected from the cantilever's backside and measured by a position sensitive diode [15]. The $top - bottom$ signal corresponds to the cantilever bending and can reveal its amplitude and/or its phase.

Tuning fork based probes

Another approach is the usage of a quartz tuning fork fig. 1.4 b). The oscillation can be read out electronically via the piezo-electric effect, avoiding any additional optical components. Due to its size, it can be equipped easily with e.g. user-prepared and etched tungsten or platinum wires [20, 21]. A special embodiment for tuning fork sensors is the qPlus sensor, where one prong is fixed to a solid substrate and the entire design is optimized for SPM applications [18].

The usage of the qPlus sensor is – until now – mainly widespread in the surface science community, which investigates very clean and flat surfaces under ultra-high vacuum UHV (and low-temperature) conditions. The qPlus based AFM offers atomic resolution [22]. For reaching this, the aforementioned FM-AFM is used. Similar to Scanning Tunneling Microscopy (STM), where only the foremost atom of the tip contributes to the tunnel current (due to its high exponential dependence), in the AFM a small amplitude ensures that the short range forces (e.g. chemical bonding forces [18, 23]) of the foremost atom dominates the total resonance frequency shift eq. (1.11) in comparison to the long range forces (e.g. Van

der Waals force) of the entire tip apex. However, stable operation at low amplitudes requires a high stiffness of the lever (to avoid any sticking to the sample), which is provided by the tuning fork based approach (e.g. stiffness 1800 N/m). [18]

In summary, the AFM is widely used in nanoscience, and it is complementary to other techniques. It offers a higher lateral resolution than optical microscopy. In comparison to electron microscopes, it is cheaper and easier to operate (e.g. no vacuum required) and there is no need for conductive samples. The measurement itself is quite slow, on the other hand it is the first choice for analysing the topography and surface of samples on the nanoscale.

1.2.2 Path towards s-SNOM

The AFM is the basis of every s-SNOM and, speaking simplifying, to extend it to an s-SNOM merely a laser beam has to be focused onto the tip-sample-interaction area where a near-field interaction occurs and light scatters away containing information about the sample properties. The resolution of the s-SNOM is not limited by the far-field spot size anymore (which scales with λ, see as well eq. (1.13) in the next paragraph), but by the tip apex geometry independent of the wavelength used as depicted in fig. 1.5. Therefore, nanometer resolution is obtained from optical wavelengths [24], via the infrared regime [24], even down to terahertz frequencies, where the resolution enhancement is the highest (e.g. $< \lambda/8000$ [25]).
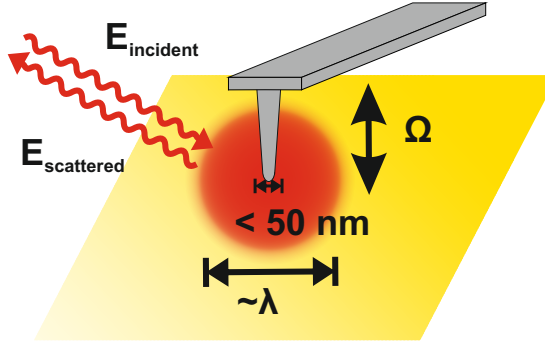

Figure 1.5: A far-field beam focus (which scales with λ) illuminates the tip and a near-field interaction between the nanometer sized tip and the sample occurs scattering light away.

For the s-SNOM, the AFM is operated in the non-contact mode to enable the higher harmonic demodulation (see paragraph "Higher Harmonic Demodulation" later in this subsection). In general, it is useful if the AFM is based on a "scanned sample" instead of a "scanning tip" concept to avoid any dynamic steering of the laser beam or rather any distortion of the s-SNOM images.

Focussing light onto the tip

To focus the light on the tip (and collect the scattered light from the near-field interaction zone), in principle both lenses and parabolic mirrors are possible. However, parabolic mirrors are used widely since they exhibit no dispersion, and thus it is easy to switch quickly between different laser sources at the same microscope (e.g. via flip or magnetic mirror stages or even overlap different laser wavelengths at the same time [26]; in the ideal case of a perfect laser alignment only the difference of collimation between the laser sources has to be compensated). As non-dispersive elements, parabolic mirrors are the first choice for pulsed-laser and spectroscopic applications.

One decisive property of the parabolic mirror for s-SNOM applications is the focal length f, which scales the focal spot size. Starting from the formula describing the radius ω of a Gaussian beam as a function of its propagation distance x eq. (1.12) [27], the beam waist ω_0 is obtained for $f >> x_0$ as eq. (1.13) (confocal parameter $x_0 = \frac{\pi \omega_0^2}{\lambda}$, beam diameter d, focal length f). Of course, also the beam diameter d can be used to enhance the focussing, however this introduces more optics, which hinders the adjustment enormously and is therefore not practical.

$$\omega^2(x) = \omega_0^2 \left(1 + \frac{x^2}{x_0^2} \right) \tag{1.12}$$

$$2 \cdot \omega_0 \approx \frac{4 f \lambda}{\pi d} \tag{1.13}$$

For collecting as much as possible of the scattered light from the tip-sample region, a low focal length is preferable as well since it increases the numerical aperture NA (D diameter of the mirror)

$$NA \propto \frac{D^2}{f^2} \, . \tag{1.14}$$

The majority of the s-SNOM experiments focus and collect the laser light by the same mirror and separate the incident and back scattered light by using a beam splitter (see fig. 1.6 a)). A beam splitter is required for more sophisticated interferometric detection schemes anyway (see subsection 1.3).

However, in some special cases, e.g. terahertz time-domain spectroscopy, the usage of a transmission geometry sketched in fig. 1.6 b) is more advantageous [28, 29]. There is no need neither for interferometric detection nor a beam splitter (which reduces further the already weak signal level) since the electric field is measured directly and not the intensity [30].

Another aspect of the parabolic mirror is its alignment. To obtain a good focal shape, the incident laser beam should be perpendicular to the base plane of
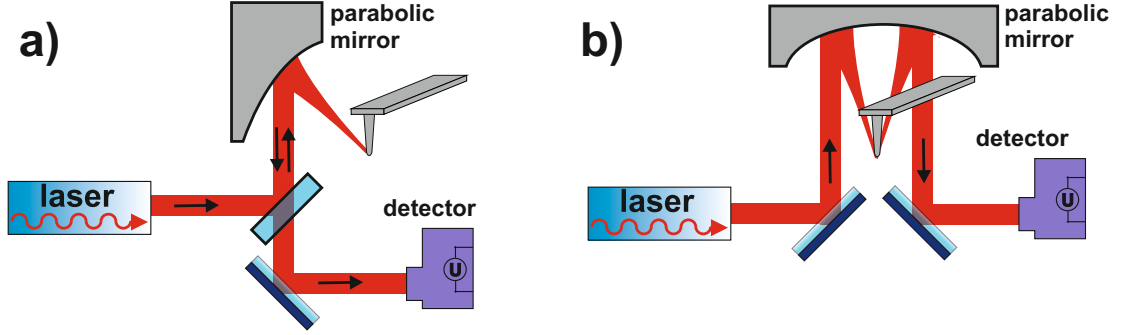
Figure 1.6: Two fundamental optical path designs for s-SNOM experiments: a) The laser beam is steered to the parabolic mirror, which focuses it onto the tip. The scattered light is collected in the backward direction, separated from the incoming light via a beam splitter, and guided to the detector. b) Using the so-called transmission geometry (possible with two small and separate parabolic mirrors or as shown here with a single big one) there is no need for the beam splitter anymore.

the paraboloid. This can be assured during alignment by means of a flat mirror surface parallel to the base plane. To fine adjust the laser beam spot (size $\sim \lambda$), the parabolic mirror should be movable by means of a three-dimensional translation stage (micrometer screws and/or piezo elements, depending on the λ used). The angle of incident to the tip (e.g. around 30° [31] to the horizontal) is determined by the parabolic mirror design and its mounting angle (which part of the entire paraboloid is used) and can be slightly tuned by moving the beam position on the mirror. A well focused beam not only enhances the field strength under the tip, it also provides a well collimated beam to the detector.

Dipole interaction model

To understand many basic features of the s-SNOM signal, already a very simple one-dimensional electrostatical model fig. 1.7 can lead to many insights. The tip itself is considered as a sphere (distance z above the sample) that is polarized by the incident electric field E, which induces a point dipole $p = \alpha E$ with the polarizability α [32] (tip radius a, dielectric function of the tip ϵ_t) expressed by

$$\alpha = 4\pi\epsilon_0 a^3 \frac{\epsilon_t - 1}{\epsilon_t + 2} \,. \tag{1.15}$$

This dipole again induces a mirror dipole in the sample $p' = \beta p$ (dielectric function of the sample ϵ_s) with
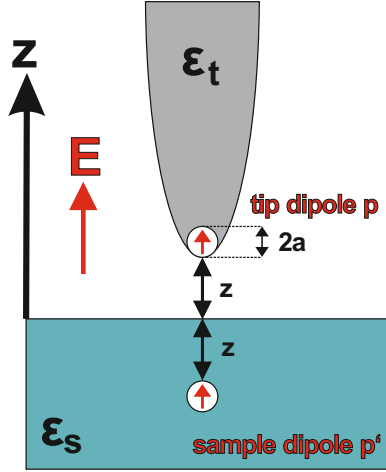
26

Figure 1.7: Sketch of the tip simplified to a point dipole inducing a mirror dipole in the sample.

$$\beta = \frac{\epsilon_s - 1}{\epsilon_s + 1} .$$ (1.16)

Some easy term conversions lead to the effective polarizability α_{eff} of the entire system given by eq. (1.17), which is proportional to the scattered near-field [33]. The comprehensive derivation and more details can be found in the corresponding literature [33, 34].

$$\alpha_{eff} = \frac{\alpha(1 + \beta)}{1 - \frac{\alpha\beta}{16\pi\epsilon_0(z+a)^3}}$$ (1.17)

With this model, it gets clear that the s-SNOM is measuring the dielectric function ϵ_s, since it is the only parameter in this formula that is changing during a measurement (beside the harmonic cantilever oscillation in z). Another important aspect is that all formulas are valid for complex numbers as well. Therefore, not only the optical amplitude is probed, but also the optical phase, which is very useful as well, e.g. for analysing absorption [35, 36].

In some newer publications, the model was adjusted and uses only a factor α as nominator of eq. (1.17) [37–39]:

$$\alpha_{eff} = \frac{\alpha}{1 - \frac{\alpha\beta}{16\pi\epsilon_0(z+a)^3}} .$$ (1.18)

Another extension to this concept is the implementation of the Fresnel reflection coefficient r_p (p-polarized light) in eq. (1.19) that is helpful in fitting some data

since it takes into account the physical reflection of the near-fields from the sample [40].

$$E_{scat} \propto (1 + r_p)^2 \alpha_{eff} E_{incident} \tag{1.19}$$

Besides this so-called point-dipole model, nowadays there is a big variety of different approaches to improve the accuracy of the models, e.g. a finite dipole model [39, 40] and more sophisticated descriptions [41, 42]. It is also useful to take into account the antenna behaviour of the tip [43, 44], and of course numerical electromagnetic simulations are getting more important [45, 46]. However, the first and simplest model eq. (1.17) already includes the fundamental physics.

Higher harmonic demodulation

The key challenge in the s-SNOM is already visible in fig. 1.3 and clarified in fig. 1.8.
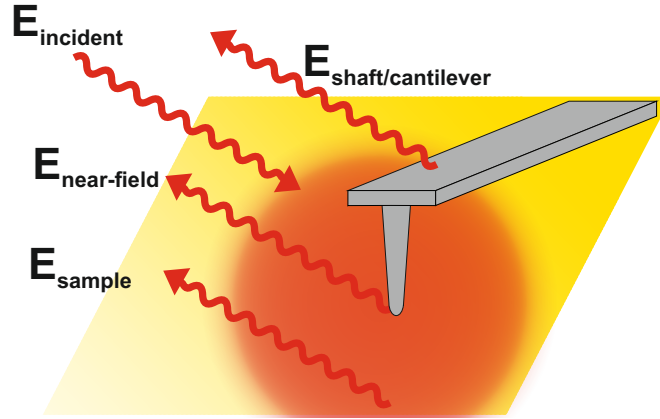

Figure 1.8: The different scattering components from the illuminated tip-sample region. The near-fields are covered by background contributions from the sample, shaft, and cantilever.

There is not only light scattering from the near-field interaction zone, but as $\lambda >> r_{tip}$, there is a lot of additional scattering and reflection from the sample, the shaft, and the cantilever, which dominates the measured signal. A rough estimation illustrates the situation: Assuming an infrared spot size of 10 μm and an effective cross-section around the tip with a size of 100 nm, only a fraction of $\left(\frac{100\,nm}{10\,\mu m}\right)^2 = 0.01\%$ of the electric field will interact for the near-field signal.

To solve this issue, the higher harmonic demodulation was introduced, which takes advantage of the oscillating cantilever of the non-contact AFM mode [47]. The decisive property of the near-field signal is the strong non-linear behaviour

as a function of the distance between tip and sample z (see the $\frac{1}{z^3}$ dependence in the denominator of eq. (1.17)). In fig. 1.9 a) a sinusoidal cantilever movement Ω together with the calculated polarizability eq. (1.17) is plotted. Due to its nonlinear behaviour, only close to the sample surface the signal is enhanced (except of a constant background). Calculating the Fourier transformations of both curves reveals higher harmonics $n\Omega$ in the near-field signal in fig. 1.9 b).
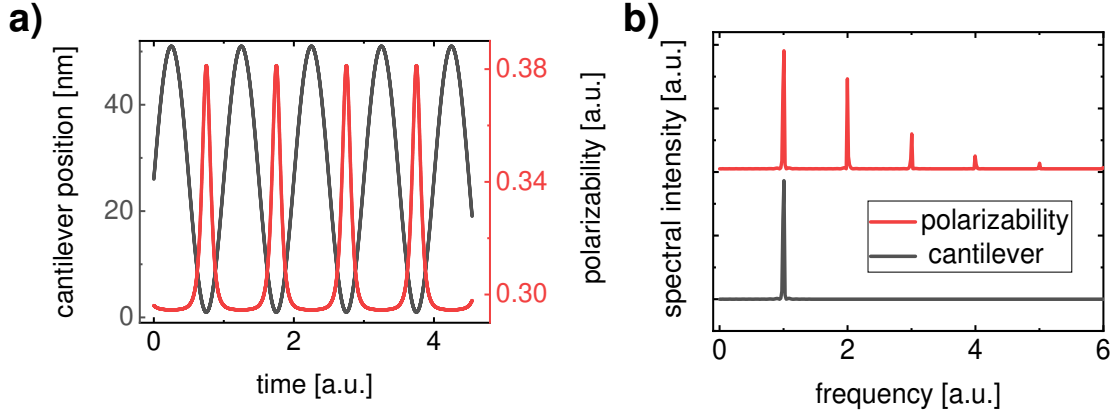

Figure 1.9: a) Oscillation of a cantilever and the corresponding sample-tip polarizability α_{eff} b) The corresponding spectra reveal the higher harmonics in the near-field signal.

All the disturbing background components described in fig. 1.8 are either a constant DC component (e.g. from the sample) or modulated with 1Ω (e.g. from the shaft and cantilever). The near-field interaction is modulated additionally at higher harmonics 2Ω, 3Ω, 4Ω, ... Hence, the detector output signal can be demodulated via a lock-in amplifier (LIA) at those higher harmonics to isolate the near-field interaction contribution.

However, in real experiments there could always be a small amount of background in the low higher harmonics, e.g. at 2Ω. Possible reasons for this are an anharmonic cantilever oscillation due to nonlinearities in the entire voltage-piezo-cantilever chain (especially at strong amplitudes) or due to the tip-sample forces (when the tip touches the sample), which distort the pure sinusoidal shape as well (both effects can be monitored by analysing the control signal from e.g. the position sensitive diode, fig. 1.4). Therefore, there is always a trade-off between high signal strengths (at low higher harmonics) and better background suppression (at high higher harmonics).

Different cantilever types

The tip is the key element for the s-SNOM. Several companies offer hundreds of different models suitable for all kind of Scanning Probe Microscopes (SPM) [48].

One big differentiation is the spring constant of the cantilever. For contact-mode AFM, soft tips are used to reduce the (potentially damaging) force onto the sample (e.g. <1 N/m), whereas for the non-contact mode higher stiffnesses are preferred for a more stable operation (e.g. >10 N/m). The resonance frequency of the cantilever is related to the spring constant (in a first approximation see eq. (1.9)). [15]

Besides the spring constant, a huge variety of different tip materials and shapes is available. A standard version is made of Si with a pyramidal shaft and tip (see fig. 1.10 a)). Often for s-SNOM metallized tips are used [31, 46, 49] (e.g. a 23 nm PtIr5 coating [50]) to support the antenna properties (except of the investigation of antenna/resonant samples themselves; here pure Si tips are preferred [51, 52]). Their spatial resolution is worse due to the coating, however nowadays for many s-SNOM applications a good signal-to-noise ratio is still more important than the highest spatial resolution.
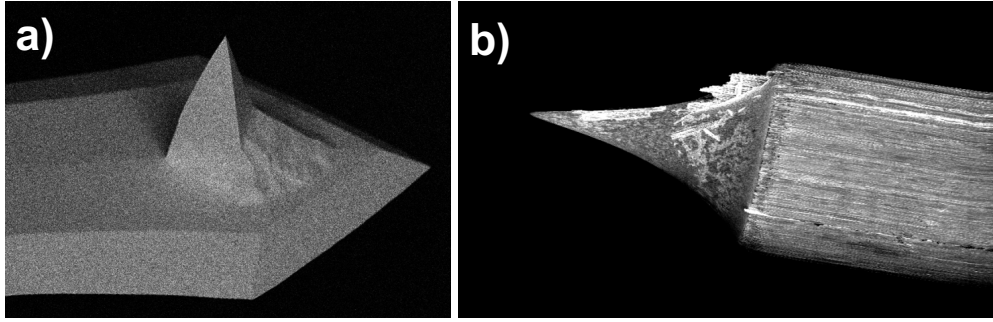

Figure 1.10: Scanning Electron Microscopy (SEM) images of a) a commercial silicon cantilever coated with platinum (MikroMasch, HQ:NSC14/Pt) and b) an etched tip from a tungsten wire (wire diameter ∼75 µm).

In the optical regime, the tip performance can be enhanced by optimization of plasmon resonances [53], whereas in the infrared regime the entire shaft can be used and optimized as an antenna [44, 54].

In the far-infrared and terahertz (THz) regime, the situation is more challenging. There is a technological "THz gap" [30] with a lack of powerful sources and detectors. Therefore, the signal enhancement by using antenna resonances of the tip shape itself is much more important [25]. Typically, the tip shaft is ∼15 µm. However, that is far too short for a suitable antenna resonance. In the near-field literature different approaches are proposed nowadays for THz applications, e.g.

focused ion beam machined tips [43], self-etched tips from tungsten or iridium wires (fig. 1.10 b)) [55, 56] or there is already a first commercial supplier for long tips (∼80 μm [57]), which seems to become the "standard" solution in the community, e.g. in refs. [28, 58, 59].

1.3 Detection modes

Another critical issue of the s-SNOM signal processing, besides higher harmonic demodulation, is the fact that the big majority of detectors are measuring intensities. Hence, cross terms, e.g. $I = E_{near-field} \cdot E_{background}$, are contributing to the signal. The following section describes this issues in more details and how interferometric detection can solve this. [39, 60, 61]

For simplicity, this section uses real representations of electric fields ($E(t) = sin(\omega t + \phi)$) and omits three-dimensional vectors since in s-SNOM the z-direction (parallel to the tip) is the decisive one[2]. Different detection schemes are depicted in fig. 1.11 and further explained in the following paragraphs. The near-field contribution is written as eq. (1.20), where $E_{nf}(\Omega t)$ is the Fourier series of the higher harmonics eq. (1.21) (see fig. 1.9); eq. (1.22) represents all background terms with a global phase ϕ_b.

$$E_{nf}(t) = E_{nf}(\Omega t)sin(\omega t + \phi_{nf}) \tag{1.20}$$

$$E_{nf}(\Omega t) = \sum_{n=0}^{\infty} E_{nf,n}sin(n\Omega t + \phi_c) \tag{1.21}$$

$$E_b(t) = E_b sin(\omega t + \phi_b) \tag{1.22}$$

1.3.1 Self-homodyne detection / intensity mode

The laser light is guided via a beam splitter to a parabolic mirror that focusses the light onto the tip and collects the backscattered light as depicted in fig. 1.11 a). The beam splitter steers it towards the detector. As shown in fig. 1.8, next to the desired $E_{nf}(t)$ there are several background contributions summarized in $E_b(t)$.

The measured intensity in the detector reads as

$$I(t) = E^2(t) = [E_{nf}(t) + E_b(t)]^2 = E_{nf}^2(t) + E_b^2(t) + 2E_{nf}(t)E_b(t). \tag{1.23}$$

---

[2]However, there are sophisticated measurement schemes, which analyse the interplay between different polarizations [62, 63].
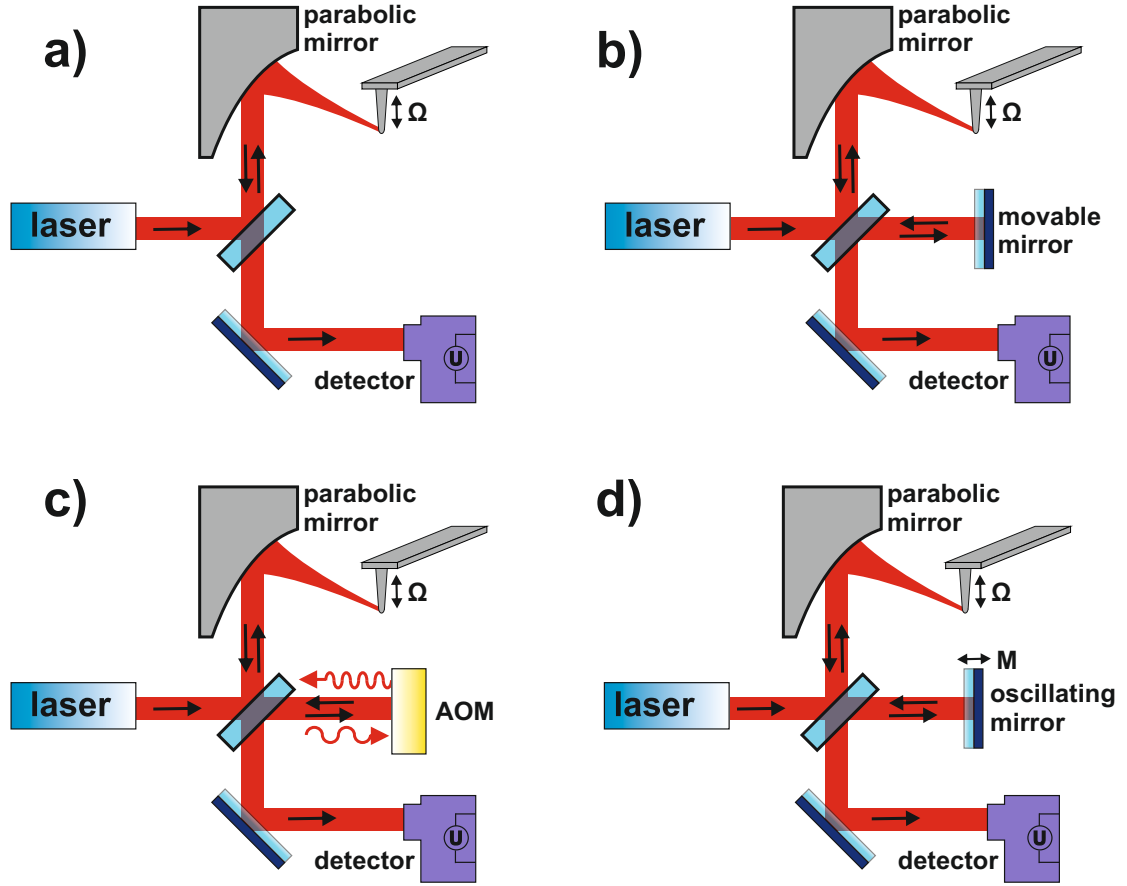
Figure 1.11: Comparison of different s-SNOM detection schemes. The basic components (laser, beam splitter, focussing parabolic mirror, and detector) are identical for all those schemes, the only variation is the role of the fourth open interferometer arm which is a) empty/blocked for self-homodyne/intensity mode, b) equipped with a movable mirror for homodyne detection, c) equipped with an acousto-optic modulator (AOM) for heterodyne detection, or d) the reference arm is phase modulated by means of an oscillating mirror for pseudo-heterodyne detection.

Due to higher harmonic demodulation, the pure background $E_b^2(t)$ is filtered out.[3] Normally, $E_b >> E_{nf,n}$, therefore the term $E_{nf}^2(t)$ is neglected as well. The product of the sine-terms of $E_b(t)$ and $E_{nf}(t)$ can be simplified to eq. (1.24) assuming that the detector bandwidth is far below ω (for details see appendix eq. (6.12) and (6.13)).

In the experimental realization no absolute signal values are measured since many proportionality factors (collecting efficiency of the parabolic mirror, reflection and transmission coefficients from all optics, detector, lock-in amplifier settings, ...) have to be taken into account. However, they can be merged into a single proportionality constant, so that the measured signal demodulated at a single higher harmonic of the series expansion eq. (1.21) S_n is proportional to

$$S_n \propto E_{nf,n} E_b cos(\phi_{nf,n} - \phi_b) \,. \tag{1.24}$$

There are two disturbing dependencies in this formula: The extracted near-field signal depends strongly on both the background E_b and the phase difference between the two fields $\phi_{nf} - \phi_b$. Therefore, it is not possible to assign a change in the measured signal unambiguous to $E_{nf,n}$, E_b or ϕ.

This mode is sometimes called intensity mode since there is no interferometer or self-homodyne mode due to the mixing with the (uncontrolled) background $E_b \cdot E_{nf}$.

1.3.2 Homodyne detection

The idea of homodyne detection is to take advantage of the already available interferometer (only one additional mirror has to be added; fig. 1.11 b)). This reference arm $E_r(t)$ eq. (1.25) is guided to the detector as well, hence three waves are mixed eq. (1.26).

$$E_r(t) = E_r sin(\omega t + \phi_r) \tag{1.25}$$

$$\begin{aligned} I(t) &= [E_{nf}(t) + E_b(t) + E_r(t)]^2 \\ &= E_{nf}^2(t) + E_b^2(t) + E_r^2(t) + 2E_{nf}(t)E_b(t) + 2E_{nf}(t)E_r(t) + 2E_b(t)E_r(t) \end{aligned} \tag{1.26}$$

---

[3]Actually, the 1Ω modulated background in E_b may result in a 2Ω signal, even theoretically: $I = E_b^2(t) = E_b^2 \cdot sin^2(\Omega t) \overset{eq.(6.1)}{=} 0.5 \cdot E_b^2(1 - cos(2\Omega t))$, which emphasizes again the advantage of $3\Omega, 4\Omega, ...$ However, later with sophisticated interferometric detection schemes this effect becomes less relevant.

Applying again the higher harmonic demodulation (cancelling $E_r^2(t)$, $E_b^2(t)$, $2E_b(t)E_r(t)$), assuming eq. (1.27) (cancelling $E_{nf}^2(t)$, $E_{nf}(t)E_b(t)$), and considering the detector (equivalent to eq. (6.13)) yields eq. (1.28).

$$E_r >> E_b >> E_{nf,n} \tag{1.27}$$

$$S_n \propto E_{nf,n} E_r cos(\phi_{nf,n} - \phi_r) \tag{1.28}$$

Although this formula looks quite similar to eq. (1.24), it is a much more powerful measurement mode. The arbitrary background contribution E_b is replaced by an easily controllable reference beam E_r, which is constant during a measurement and which also enhances the signal level.

In addition to this, the homodyne interferometric detection makes the optical phase accessible. By measuring a sample twice ($S_{n,1}$ and $S_{n,2}$) with a shifted reference ϕ_r and $\phi_r + \frac{\pi}{2}$, both the optical near-field amplitude and its phase can be extracted.

$$S_{n,1} = a \cdot E_{nf,n} E_r cos(\phi_{nf,n} - \phi_r) \tag{1.29}$$

$$S_{n,2} = a \cdot E_{nf,n} E_r cos\left(\phi_{nf,n} - \phi_r - \frac{\pi}{2}\right) = a \cdot E_{nf,n} E_r sin(\phi_{nf,n} - \phi_r) \tag{1.30}$$

Based on those two equations (both measurements with the same proportionality constant a), the pure near-field signal eq. (1.31) and the near-field phase eq. (1.32) can be calculated. Eq. (1.32) uses the arctan function for simplicity, however in the later data analysis the atan2 is required to open the entire range $-\pi$ to $+\pi$.

$$\sqrt{S_{n,1}^2 + S_{n,2}^2} = \sqrt{a^2 E_{nf,n}^2 E_r^2 cos^2(\phi_{nf,n} - \phi_r) + a^2 E_{nf,n}^2 E_r^2 sin^2(\phi_{nf,n} - \phi_r)}$$
$$= aE_{nf,n} E_r \sqrt{cos^2(\phi_{nf,n} - \phi_r) + sin^2(\phi_{nf,n} - \phi_r)} \overset{eq.(6.5)}{=} aE_{nf} E_r \tag{1.31}$$

$$arctan\left(\frac{S_{n,2}}{S_{n,1}}\right) = arctan\left(\frac{a \cdot E_{nf,n} E_r sin(\phi_{nf,n} - \phi_r)}{a \cdot E_{nf,n} E_r cos(\phi_{nf,n} - \phi_r)}\right) = \phi_{nf,n} - \phi_r \tag{1.32}$$

It is clear from eq. (1.32) that phase differences (and not absolute phase values) are measured as ϕ_r is normally not known, but it can be assumed as constant during a measurement.

However, the big disadvantage of the homodyne scheme is the requirement of two measurements that takes the double time and that is dangerous due to any alignment or power drifts over time. The entire concept is only as good as the initial approximation eq. (1.27). Based on some estimated values, an error up to 28% is possible [39]. Due to the data post-processing eq. (1.31) and (1.32), the user cannot observe (and optimize) the signals in real time.

1.3.3   Heterodyne detection

The heterodyne detection scheme looks quite similar to the homodyne scheme. However, instead of simply a mirror in the reference arm $E(r)$, the frequency of the light is shifted $\omega \rightarrow \omega_1 = \omega + \Delta\omega$ [4] (e.g. by means of an acousto-optic modulator (AOM) [35]), see fig. 1.11 c)):

$$E_r(t) = E_r sin(\omega_1 t + \phi_r)\,. \tag{1.33}$$

Mixing this term with a higher harmonic of the near-field signal $E_{nf,n}$ results in sidebands at $\Delta\omega \pm n\Omega$ according to

$$
\begin{aligned}
&E_r \cdot sin(\omega_1 t + \phi_r) \cdot E_{nf,n} sin(n\Omega t + \phi_c) \cdot sin(\omega t + \phi_{nf,n}) \\
&\overset{eq.(6.12)}{=} 0.5 \cdot E_r E_{nf,n} sin(n\Omega t + \phi_c) \cdot cos(\Delta\omega t + \phi_r - \phi_{nf,n}) \\
&\overset{eq.(6.4)}{=} 0.25 \cdot E_r E_{nf,n} (\sin((\Delta\omega + n\Omega)t + \phi_c + \phi_r - \phi_{nf,n})... \\
&\quad ... - sin((\Delta\omega - n\Omega)t - \phi_c + \phi_r - \phi_{nf,n}))\,.
\end{aligned}
\tag{1.34}
$$

The detector output is again the mixing of the three electric fields $E_{nf}(t)$, $E_b(t)$, $E_r(t)$; the same as for the homodyne detection in eq. (1.26). However, demodulating the entire signal at one of those sidebands $\Delta\omega \pm n\Omega$ suppresses all other terms without any additional approximation (as in the case of homodyne detection eq. (1.27)) since the other terms are whether constant or depend only on one of $\Delta\omega$ or Ω.

One relevant term for the lock-in amplifier (LIA) is proportional to

$$I_{\Delta\omega+n\Omega} \propto E_{nf} E_r \sin((\Delta\omega + n\Omega)t + \phi_c + \phi_r - \phi_{nf,n})\,. \tag{1.35}$$

This equation shows that demodulating the detector signal at the frequency $\Delta\omega + n\Omega$ directly reveals both near-field quantities, the amplitude and the phase. The magnitude output of the LIA is proportional to the near-field E_{nf} (again

---

[4]Assuming $\Delta\omega >> \Omega$.

enhanced by a factor E_r like for the homodyne detection) and the phase output directly measures $\phi = \phi_c + \phi_r - \phi_{nf,n}$. Thus, a second measurement is no longer required, in contrast to the homodyne detection.

However, the alignment of the AOM is very sophisticated and depends strongly on the wavelength used (one big advantage of the s-SNOM is the ability to switch quickly between wavelengths, which is not possible with an AOM any more), and the requirements for the lock-in amplifier and detector are higher since higher frequencies and sideband detection are used.

Therefore, the heterodyne detection scheme was mainly an intermediate step in the development of the s-SNOM technique; nowadays the pseudo-heterodyne detection is much more common. Indeed, there are some recent developments to revitalize heterodyne detection schemes in near-field microscopy in combination with GHz electronic sources, where a frequency shifted local oscillator is much more common and easier to implement [64].

1.3.4 Pseudo-heterodyne detection

The state-of-the-art technology for s-SNOM is the so-called pseudo-heterodyne detection scheme. Here, the reference beam is phase modulated by means of an oscillating mirror (frequency $M << \Omega$) $E_r(t) = E_r cos(\omega t + \gamma cos(Mt) + \phi_r)$, see fig. 1.11 d). γ is called the modulation depth (the mirror amplitude), ϕ_r is the DC phase offset between the two interferometer arms. The following equations are just a brief sketch, a more solid and comprehensive mathematical derivation of the pseudo-heterodyne detection can be found in the appendix section 6.1.4.

A phase modulated reference wave can be decomposed into a Fourier series containing the Bessel functions of the first kind J_l [65] as follows:

$$E_r(t) \quad \mapsto \quad e^{i(\gamma cos(Mt)+\phi_r)} = \sum_{l=-\infty}^{\infty} J_l(\gamma)e^{i\phi_r+il\pi/2}e^{ilMt} \; . \qquad (1.36)$$

Like in the case of heterodyne detection, again the near-field $E_{nf}(t)$ and the reference field $E_r(t)$ are mixed in the detector. As a consequence, sidebands around the higher harmonics $n\Omega$ occur spaced by multiple of M ($f = n\Omega \pm mM$), see fig. 1.12.

There are two ways to measure those sidebands. The intuitive opportunity is to lock a LIA directly to one of the sideband frequency $f = n\Omega \pm mM$. However, that is technically demanding and not many devices offer such options. The easier way is the so-called tandem-demodulation [66], see the numerical simulation fig. 1.13. A fast LIA demodulates the signal around $n\Omega$ with sufficient low time constant (e.g. $t_c < 0.1 \cdot \frac{1}{mM}$) or sufficient high bandwidth. Hence, the sideband signals around $n\Omega$ are measured as well and the output spectra can be seen as a new
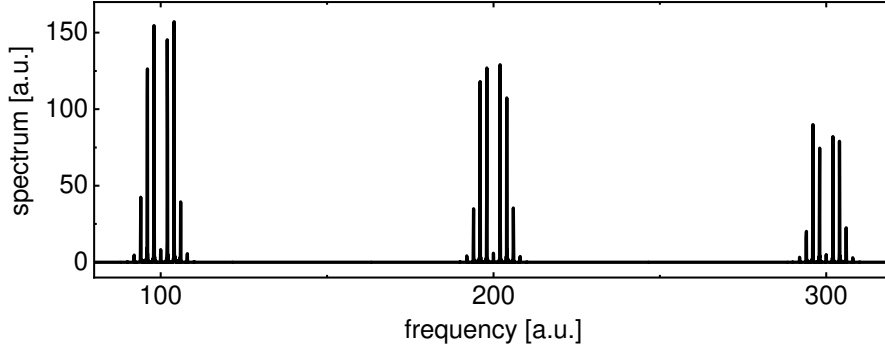
Figure 1.12: Spectrum of the pseudo-heterodyne detection signal simulated by numerical Fourier transformation of eq. (6.27). Next to the main frequencies $n\Omega = n \cdot 100$, sidebands occurred spaced by $mM = m \cdot 2$.

signal centred around $n\Omega$. The X-component is passed to a second LIA, which demodulates this signal at the frequencies $1M$ and $2M$ (with e.g. $t_c > 3 \cdot \frac{1}{mM}$). Of course, the tandem-demodulation is less robust since two devices, more cables and connections are involved. However, it is feasible with standard LIAs.

Two neighbouring sidebands (e.g. $SB_{n,1M}$ and $SB_{n,2M}$) can be used to isolate the optical near-field E_{nf} eq. (1.39) and the optical phase ϕ_{nf} eq. (1.40).

$$SB_{n,1M} \propto E_{nf,n} E_r J_1(\gamma) sin(\phi_r - \phi_{nf,n}) \tag{1.37}$$

$$SB_{n,2M} \propto E_{nf,n} E_r J_2(\gamma) cos(\phi_r - \phi_{nf,n}) \tag{1.38}$$

To enable a simple and more direct measurement, it is helpful to choose the modulation depth to a specific value, so that $J_1(\gamma) = J_2(\gamma) = J_{1/2}(\gamma)$ (see next paragraph).

$$\sqrt{SB_{n,1M}^2 + SB_{n,2M}^2} \propto E_{nf,n} E_r J_{1/2}(\gamma) \sqrt{sin^2(\phi_r - \phi_{nf}) + cos^2(\phi_r - \phi_{nf,n})}$$
$$\stackrel{eq.(6.5)}{=} E_r J_{1/2}(\gamma) E_{nf,n} \propto E_{nf,n} \tag{1.39}$$

$$arctan\left(\frac{SB_{n,1M}}{SB_{n,2M}}\right) = arctan\left(\frac{sin(\phi_r - \phi_{nf,n})}{cos(\phi_r - \phi_{nf,n})}\right) = \phi_r - \phi_{nf,n} \rightarrow \Delta\phi_{nf,n} \tag{1.40}$$

Eq. (1.39) is directly proportional to the optical amplitude, eq. (1.40) is equal to the phase difference between the reference phase ϕ_r and the optical phase ϕ_{nf}[5].

---

[5]Again, in the data analysis the atan2 function is used, see appendix 6.1.4.
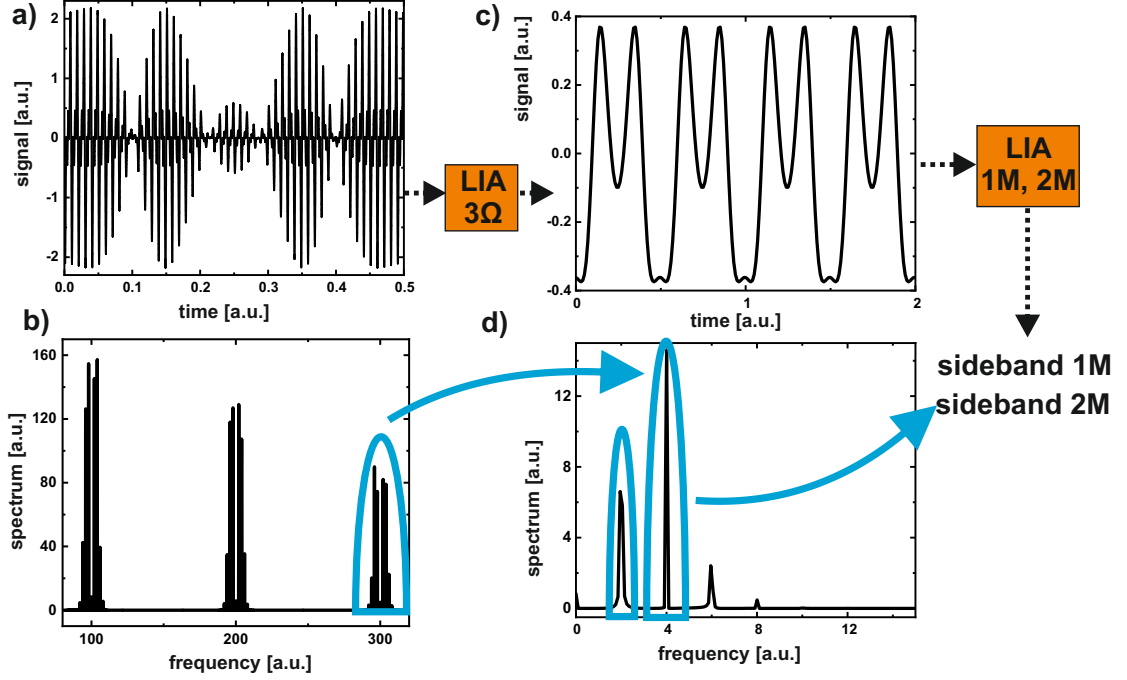
Figure 1.13: Numerical simulation of the pseudo-heterodyne detection scheme: The sidebands can be extracted from the time signal a) and spectrum b) (equal to fig. 1.12) via the so-called "tandem" demodulation using two consecutive lock-in amplifiers (LIA). The first one is set to the higher harmonic of the cantilever (here 3Ω with $\Omega = 100$), its X value (time signal c) and spectrum d)) is passed to a second LIA, which is demodulating $1M$ and $2M$ (here $M = 2$), the two sidebands.
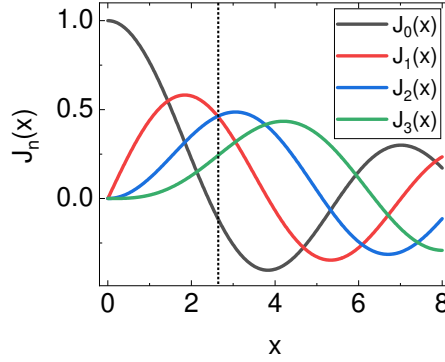
Figure 1.14: The first four Bessel functions of the first kind. The dashed line marks the first intersection of $J_1(x)$ and $J_2(x)$ at $x \approx 2.63$, which is relevant for the pseudo-heterodyne detection.

Both sidebands eq. (1.37) and eq. (1.38) can have negative values. For the near-field amplitude eq. (1.39) those signs are irrelevant since the sideband values are squared. However, the phase eq. (1.40) depends strongly on the signs. Therefore, in both modes (direct $f = n\Omega \pm mM$ and tandem demodulation) the X-components of the demodulated signals have to be used. To avoid cutting away any information in the Y-components, the lock-in amplifier phases have to be set to zero ("auto phase" function).

In this paragraph the emphasis is the demodulation depth γ, which has to be chosen carefully to enable easy calculations eq. (1.39) and eq. (1.40). Without that, both sidebands need to be weighted by their corresponding Bessel function, which causes of course more steps and uncertainties. In fig. 1.14 the Bessel functions are plotted and there are several values where e.g. $J_1(x)$ and $J_2(x)$ are equal. To avoid too large oscillations (which is technical more challenging), the first intersection of the two curves at $\gamma = 2.63$ is used.

To set the modulation depth properly, it has to be translated from a phase information into a length scale for the mirror movement. From eq. (1.36) it is clear that the peak-to-peak oscillation of the optical path Δs should fulfil (assuming $\gamma = 2.63$):

$$\frac{\Delta s}{\lambda} = \cdot \frac{\gamma}{\pi} \quad \to \Delta s = \frac{\gamma \cdot \lambda}{\pi} \approx 0.84\lambda \,. \tag{1.41}$$

Depending on the geometry, the required mirror oscillation d (peak-to-peak) can be reduced up to a factor 2 since the effective path difference Δs depends on the angle α, see fig. 1.15, which yields
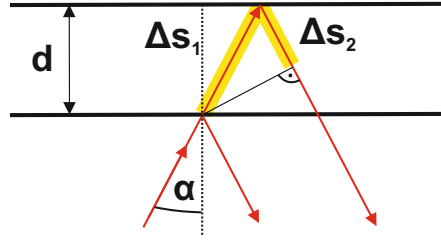
39

Figure 1.15: The displacement d of the pseudo-heterodyne mirror translates into a path difference Δs of the light beam as a function of the incident angle α.

$$\Delta s = \Delta s_1 + \Delta s_2 = \frac{d}{cos\alpha} + \Delta s_1 cos(2\alpha) = d\frac{cos(2\alpha) + 1}{cos\alpha} \; . \qquad (1.42)$$

To ensure a proper mirror oscillation, there are several experimental opportunities (for more details see appendix 6.1.4).

1.3.5 New developments

The near-field extraction in scattering-type Scanning Near-field Optical Microscopy is a highly dynamic research area. There are many new developments in this field, e.g. the already mentioned terahertz time-domain spectroscopy (measuring the electric field directly) that makes the interferometric detection unnecessary [58], the usage of data post-processing in the so-called holographic scheme [26], and the signal measurement within the laser cavity of quantum cascade lasers [59, 67]. It can be expected that new and more sophisticated ideas will emerge in the next years.

1.4 Applications

The majority of s-SNOM applications can be divided into two areas, which will be presented in more details in the following subsections: Probing the dielectric function and imaging of polariton waves.

1.4.1 Probing the dielectric function

As stated in the simple dipole model eq. (1.17), the s-SNOM signal depends on the dielectric function ϵ_s of the sample. For a comprehensive understanding of experimental data, theoretical simulations are necessary. The basic steps for s-SNOM modelling are depicted in scheme fig. 1.16.
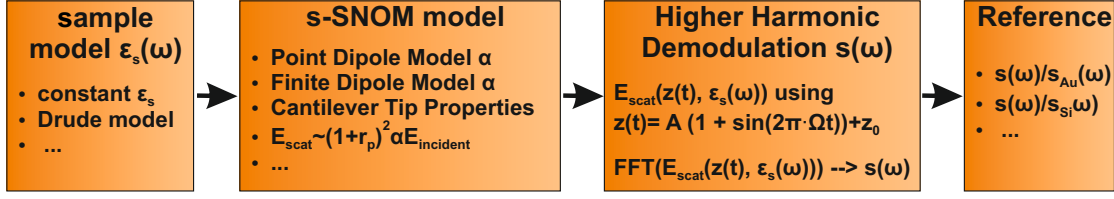
Figure 1.16: Overview about the required steps for simulating near-field contrasts.

- Sample model: Contrasts in the dielectric function can result from different materials, different phases, or different parameters like e.g. the charge carrier density in semiconductors (covered by the Drude model).

- s-SNOM model: The different interaction models and corresponding equations are already described in more details in subsection 1.2.2.

- Higher harmonic demodulation: The next step is the numerical higher harmonic demodulation [47] by feeding the cantilever motion $z(t) = A(1 + sin(2\pi \cdot \Omega t)) + z_0$ into the model equations and performing a subsequent Fourier transformation.

- Reference: Since many proportionality parameters are not known or hard to control experimentally in the s-SNOM[6], it is useful and common to measure contrasts to other materials or to normalize data, e.g. to undoped silicon [68] or simply a Au surface [64] (instead of interpreting absolute values).

A typical application case are semiconducting samples described by the Drude model where ϵ is a function of the charge carrier concentration n and the probing frequency ω, see eq. (1.43) with the conductivity $\sigma(\omega, n)$ eq. (1.44) (lattice contribution ϵ_L, vacuum permittivity ϵ_0, charge carrier density n, elementary charge q, effective mass $m_{eff} = m_0 \cdot m_{e/h}$ [7], and scattering time τ) [69]. Since the s-SNOM models are complex-valued, both the real and the imaginary part of ϵ can be analysed [36].

$$\epsilon(\omega) = \epsilon_L(\omega) + \frac{i\sigma(\omega)}{\omega\epsilon_0} \quad (1.43)$$

$$\sigma(\omega, n) = \frac{nq^2}{m_{eff}} \frac{\tau}{1 - i\omega\tau} \quad (1.44)$$

---

[6]Focal spot size, collecting efficiency of parabolic mirror (numerical aperture), antenna properties of the tip, reflection coefficients of all mirrors/beam splitters, detector and lock-in amplifier properties, general interferometer alignment, ...

[7]Electron mass m_0 and relative effective electron/hole masses $m_{e/h}$.
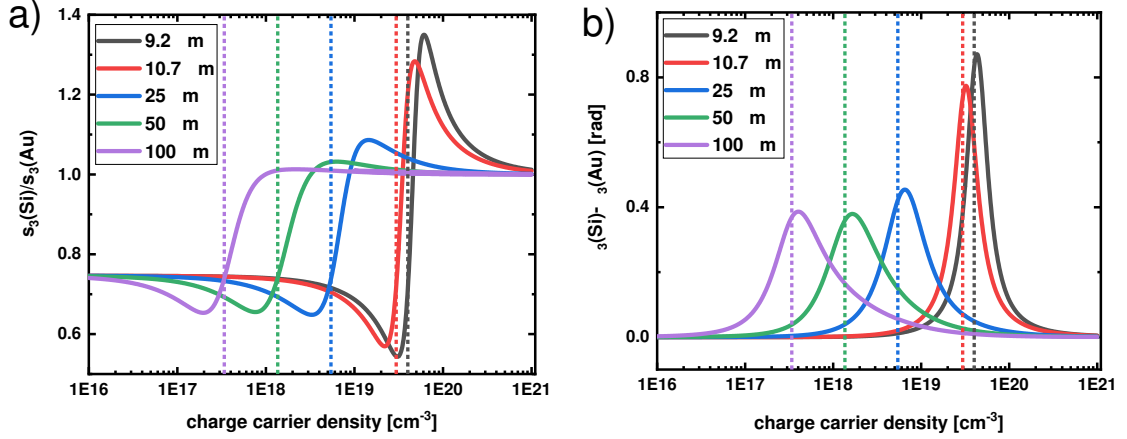
Figure 1.17: Simulation of the 3Ω s-SNOM signal of n-doped silicon at different wavelengths as a function of the charge carrier density n a) near-field amplitude (normalized to Au) and b) near-field phase (referenced to Au as well). The dotted lines indicate the n values corresponding to the plotted plasma frequencies f_P (see colours in the figure legend).

In general, there are many free parameters in those models, e.g. from the Drude model (τ, n, m_{eff}, ϵ_L), from the interaction model itself (see eq. (1.17) and related equations: tip radius a, ϵ_{tip}, Fresnel coefficient r_p), and from the higher harmonic demodulation (amplitude A, minimal distance tip-sample z_0, higher harmonic number). However, there are recent attempts to reduce the requirement of the knowledge of those parameters by sophisticated data processing [70].

Fig. 1.17 and fig. 1.18 are two examples for numerical s-SNOM simulations based on the simple point dipole model eq. (1.17).

The first example fig. 1.17 illustrates the s-SNOM signal (both amplitude and phase) as a function of charge carrier density for different illumination wavelengths, which reveals the Drude behaviour. For low n, there is a fixed contrast between Si and Au in the near-field amplitude fig. 1.17 a), whereas for high doping concentrations the Si is so metallic that its signal converges to Au. In between, there is always a Drude peak around the plasma frequency $\omega_P = 2\pi f_P$ eq. (1.45) [69], e.g. f_P for $n = 3 \cdot 10^{19}$ cm^{-3} corresponds to a wavelength $\lambda = 10.7\,\mu$m [8]. In general, if the s-SNOM probing frequency is below the semiconductor plasma frequency, the s-SNOM signal is similar to Au. If it is above the plasma frequency, there is a clear contrast [71]. In the near-field phase in fig. 1.17 b) the Drude peak is even more distinct. To analyse the doping by means of the s-SNOM, depending on the

---

[8]The tuning range of CO_2 lasers, which are widely used in the near-field community, is between $9.2\,\mu$m to $10.7\,\mu$m.
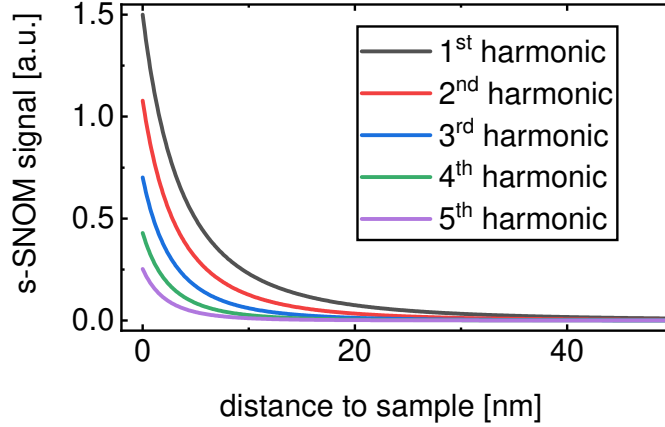
Figure 1.18: Simulated approach-curves of a Pt tip over a Au sample.

charge carrier density n (and the corresponding plasma frequency), a proper laser wavelength has to be chosen to see contrasts, e.g. for low concentrations THz radiation [72] and for high n IR frequencies [68] are suitable. For this simulation the following parameters have been used: s-SNOM parameters (tip radius a=10 nm, oscillating amplitude A=25 nm, minimum distance tip-sample z_0=1 nm, third higher harmonic), Drude model ($m_{eff} = 0.26m_0$, $\epsilon_L = 11.7$) [69, 73, 74], scattering time values τ as a function of n based on a model fitted to experimental data (eq. (6) in [75] for electrons), platinum tips ϵ_{tip} interpolated from [76], and Au reference ϵ_{Au} interpolated from [77].

$$\omega_P = \sqrt{\frac{ne^2}{\epsilon_0 \epsilon_L m_0 m_e}} \tag{1.45}$$

Another important tool to characterize the quality of s-SNOM signals is the measurement of so-called approach curves fig. 1.18, where the tip is retracted from the sample and the corresponding s-SNOM signal is plotted. Such curves can be easily simulated as well (same simulation parameter as above; $\lambda = 10.5\,\mu m$, minimum distance tip-sample z_0 is equal to the x-axis).

Already by using this simple models, the most fundamental properties of the approach curves can be identified: The s-SNOM signal is in general confined to the sample surface (here $\lesssim$20 nm), the signal is more confined to the surface with increasing higher harmonics, and with increasing harmonics the signal strength decreases. So experimentally, the user has always to make a trade-off between high signal (low higher harmonics) and better confinement/background suppression (high higher harmonics).

The MATLAB-codes used for fig. 1.17 and fig. 1.18 can be found in the appendix 6.2.

The mapping of the dielectric function can be used for several applications. Starting from simple material identification [24], observation of material phases [78] and phase transitions [79], pulsed sources can even take entire spectra on the nanoscale [80]. In addition to this surface scanning, in recent developments the subsurface scanning ability of the s-SNOM [81] is used for depth profiling [82, 83], which could open an entire new branch of nanotomography.

1.4.2 Mapping polariton waves

Surface Plasmon Polaritons (SPP)

Polaritons are a general concept of solid state physics, when the states of an intrinsic excitation and a photon are mixed [84]. As an example, in the following the so-called Surface Plasmon Polaritons (SPPs) are presented. Plasmons are collective excitations of electrons in metals. At interfaces (e.g. every surface is an interface between matter and air/vacuum), they can mix up together with photons to the afore mentioned surface plasmon polaritons. Their physics and dispersion can be derived by simply solving Maxwell's equations under the corresponding boundary conditions resulting in the dispersion relation eq. (1.46). In fig. 1.19 it is plotted in the lower green branch assuming an interface between $\epsilon_1 = \epsilon_{air} = 1$ and a free Drude plasma eq. (1.47)[9]. [85]
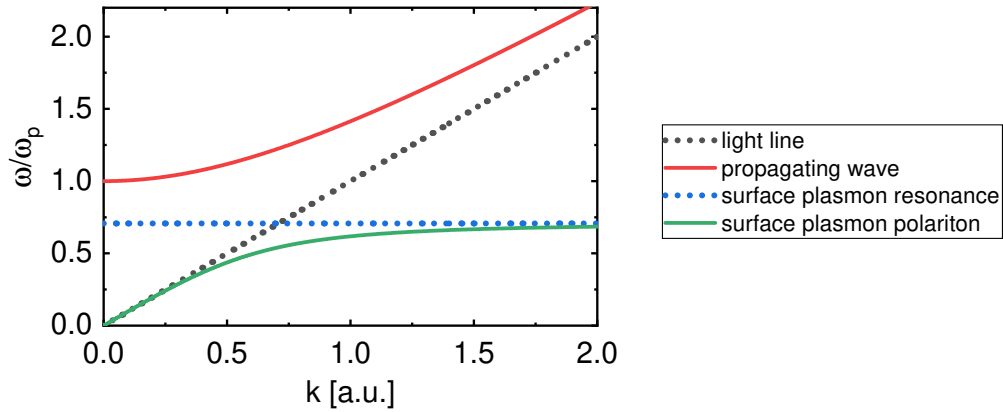

Figure 1.19: Dispersion graph of electromagnetic waves including the light line (dotted black), the surface plasmon resonance (dotted blue), the surface plasmon polariton branch (green line), and the freely propagating wave (red line).

---

[9]Derived from eq. (1.43) and eq. (1.44) in the high-frequency limit $\omega\tau >> 1$ or neglecting the damping $\frac{1}{\tau} \to 0$; $\epsilon_L = 1$.

$$k(\omega) = k_0 \sqrt{\frac{\epsilon_1(\omega)\epsilon_2(\omega)}{\epsilon_1(\omega) + \epsilon_2(\omega)}} \qquad (1.46)$$

$$\epsilon_2(\omega) = 1 - \frac{\omega_p^2}{\omega^2} \qquad (1.47)$$

Additionally, a second upper branch (red) is added representing the freely propagating electromagnetic wave in a solid, which is only possible above the plasma frequency. Solving eq. (1.47) for $\omega(k)$ [85] results in

$$\omega^2(k) = \omega_p^2 + k^2 c^2 \,. \qquad (1.48)$$

Roughly speaking, the SPP-dispersion is the mixture between the light line (dotted black line $\omega = kc$) and the surface plasmon resonance eq. (1.49), here at $\omega_{SPP} = \frac{\omega_p}{\sqrt{2}}$, dotted blue line[10]. Due to the no-crossing rule [86], the dispersion splits into branches. The lower branch starts for low k-value close to the light line and for high k-values it converges to the surface plasmon resonance, whereas the upper branch starts at the bulk plasmon resonance ω_P and approaches the light line. In between those free and bound modes, there is a frequency window where no propagating solution exists. [85]

$$\omega_{SPP} = \frac{\omega_p}{\sqrt{\epsilon_1 + 1}} \qquad (1.49)$$

The dispersion graph fig. 1.19 reveals the energy and momentum of SPPs since the frequency is proportional to the energy $E = \hbar\omega$ and the wave vector corresponds to the momentum $p = \hbar k$: For a fixed frequency (i.e. a horizontal line in the dispersion diagram), there is a mismatch in the momentum since the SPP dispersion is on the right side of the light line, which corresponds to higher momentum values. For this reason, free light photons cannot simply excite SPPs, but on the other side, once an SPP is excited, it is bound to the interface and can only propagate in this plane without radiating into the third dimension. Again recalling the mathematics from the nanophotonic introduction eq. (1.6), the higher k-values in the $k_{||}$ plane correspond to an imaginary evanescent component $k_\perp$.

There are several techniques to overcome the momentum mismatch and excite SPPs, e.g. amongst others prism coupling (using a dielectric prism to "bend" the light line in fig. 1.19 down), grating coupling, and symmetry breaking (by means of edges, defects/particles, and SPM probes). [85, 87, 88]

Since SPPs are propagating on surfaces, they are easily accessible via the s-SNOM and are investigated in various studies [89–92]. Other polariton types like phonon polaritons (both surface phonon polaritons [93–95] and bulk phonon

---

[10]Inserting eq. (1.47) in eq. (1.46) and solving for $k \to \infty$ leads to eq. (1.49).

polaritons [96–98]) and exciton polaritons [99, 100] have been analysed by means of near-field microscopy, too[11]. The next step towards more complicated multilayers and heterostructures with coupled modes has already been initiated [102–104].

However, all those reports are based on the ability of the s-SNOM to map those propagating polaritons as static standing wave patterns, which will be explained in the following subsection.

Interference of electromagnetic waves in the s-SNOM

Propagating waves can be mapped by means of the s-SNOM as static standing wave patterns due to interference. Fig. 1.20 illustrates the corresponding geometry for the sake of simplicity in a one-dimensional case.
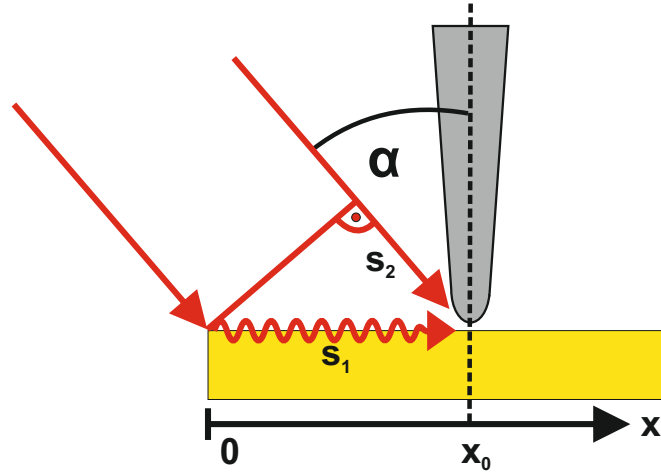

Figure 1.20: Surface waves are launched at the left edge of the substrate, propagate the distance s_1 towards the tip at position x_0, and interfere with the direct illumination path s_2.

At point $x = 0$ (e.g. an edge), a surface wave s_1 is launched by the incident phase front and reaches the tip at position x_0. As explained in the previous section, a sharp feature like the tip can launch surface waves. But therefore, the time reversed process is possible as well: It converts bound surface waves into radiative free space waves. The decisive quantity here is the phase difference $\Delta\phi$ eq. (1.50) between the two light paths s_2 (direct path to the tip apex; due to the normal s-SNOM signal based on the dipole interaction (subsection 1.2.2) light is scattered back) and s_1 (launching a surface wave at the edge that propagates a distance x_0 and is then converted back in free space radiation by the tip). As a function of x, this phase difference changes and causes constructive and destructive interference

---

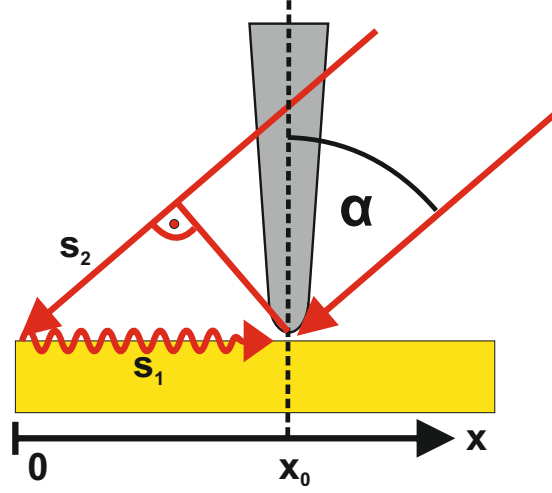[11]For a detailed overview see the corresponding reviews [87, 101].

Figure 1.21: Same principle as fig. 1.20 but with an angle α in the other direction resulting in adding up the two paths s_1 and s_2 to the total path and phase difference.

between the two optical paths. Solving eq. (1.50) equal 2π results in the standing wave pattern wavelength $x_0 = \Lambda$ eq. (1.51) (using the effective polariton refractive index n).

$$\Delta\phi = k_{sw} \cdot s_1 - k_0 \cdot s_2 = k_{sw} \cdot x_0 - k_0 \cdot sin\alpha \cdot x_0 \qquad (1.50)$$

$$\Lambda = \frac{2\pi}{k_{sw} - k_0 sin\alpha} = \frac{\lambda}{n - sin\alpha} \qquad (1.51)$$

To be more accurate, in interferometric detection (e.g. pseudo-heterodyne detection) both beam paths are mixed with the external reference field $E_r \cdot E_{s_1} + E_r \cdot E_{s_2}$.

The angle α in eq. (1.51) is important as well. For values $\alpha > 0$, the incident phase front and the surface wave propagate in the same direction ("co-propagation"), for $\alpha < 0$ they have opposite directions ("counter-propagation") fig. 1.21. This situation is also equivalent with considering in fig. 1.20 a surface wave from the right site propagating into the negative x-direction.

Depending on the mutual orientation of the surface launching feature, the tip position, and the incident light, for a fixed angle α two different wavelengths $\Lambda_\pm$ can be mapped on a sample expressed by

$$\Lambda_\pm = \frac{2\pi}{k_{sw} \pm k_0 sin\alpha} = \frac{\lambda}{n \pm sin\alpha} \; . \qquad (1.52)$$
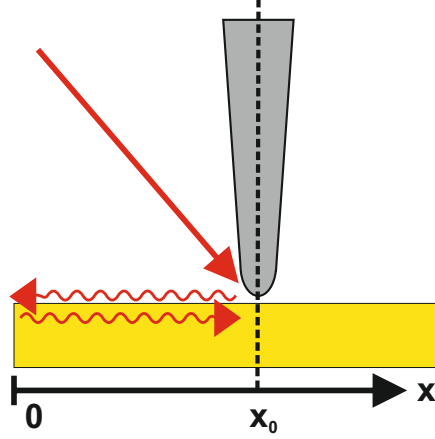
Figure 1.22: Surface waves are launched by the tip, reflected at an edge feature, and propagate back to the tip.

Another interesting case is $\alpha = 0$ (i.e. $\vec{k_0} \perp \vec{k_{sw}}$), where eq. (1.51) or eq. (1.52) simplifies to eq. (1.53) and one is observing directly the wavelength. A possible realization of this geometry is presented later in this thesis.

$$\Lambda = \frac{2\pi}{k_{sw}} = \frac{\lambda}{n} = \lambda_{sw} \tag{1.53}$$

Indeed, there is another approximation where the surface wave wavelength λ_{sw} is mapped directly: For strongly confined modes $k_{sw} >> k_0$, eq. (1.53) is also valid and therefore the effect of distorted measured wavelengths Λ can be neglected in the terahertz range [3], is only weak in the infrared regime [105][12], but very important in the optical regime [89, 90]. Of course, this is not a generalization for those spectral ranges, and it always depends on the specific sample, the measurement design, and the resulting confinement factor.

A special case are tip launched surface waves that are reflected (e.g. by edges) and collected by the tip fig. 1.22. [92]. The total phase difference between the excitation (at the tip) and the collection again at the tip, is given by

$$\Delta\phi = 2 \cdot k_{sw} \cdot x_0 \,. \tag{1.54}$$

The visible wavelength pattern is now half the surface wave wavelength

$$\Lambda = \frac{\lambda_{sw}}{2} \,. \tag{1.55}$$

---

[12]E.g. graphene plasmons with λ_0=11.2 μm and λ_{spp} =200 nm [92] result even for α=90° in Λ_+=196 nm, Λ_-=204 nm according to eq. (1.52).

To obtain more insights into the physics of surface waves, besides their wavelength also their propagation distance can be probed by means of the s-SNOM via fitting the decaying wave with an exponential function according to

$$S(x) \propto e^{-|k_{imag}|x} \,. \tag{1.56}$$

However, there are several aspects which have to taken into account, e.g. the difference between edge (1d) and circularly (2d) launched waves [105] and the spot size[13]. Furthermore, there are many attempts to increase the propagation length, e.g. for graphene plasmons by using suitable h-BN encapsulated graphene layers and/or going to lower temperatures [106].

Based on this framework, further aspects are analysed in the literature. The light paths of near-infrared beams have been analysed in more details [89], and by means of a pulsed laser source the evolution of a polariton wave packet can be revealed directly (and even a negative phase velocity can be verified) [107].

Surface Plasmon Polaritons on Silver Nanowires

The interfaces between the metal and dielectric do not have to be flat. Actually, also the curved surfaces of metallic nanowires support surface plasmon polaritons, which has become an emerging research area over the last years. Their properties can be again derived from Maxwell's equation by solving them under the corresponding boundary conditions in cylindrical coordinates [108–111]. As a result, different spatial plasmon modes on the wires can occur, which can be excited individually or in parallel leading to different interference patterns, e.g. a tilted wave pattern in fig. 1.23 [112, 113].

Of course, many analytical mode calculations assume a homogeneous environment, which is not always possible in reality when nanowires are placed on a substrate in air[14]. Numerical simulations are necessary to analyse the substrate effects. However, the newly forming modes are still related to the homogeneous ones [112, 116–119].

Especially silver nanowires (Ag NWs) are a promising component for future applications due to their chemical and physical properties [119]. A lot of efforts are currently invested to improve their properties (e.g. extending the propagation length of plasmons by using monocrystalline wires [120] or optimizing the substrate

---

[13]If the beam is focussed onto the tip, the distance to the launching points is changing during a measurement; this effect is of course more pronounced with small focal spot sizes at short wavelength, e.g. in the optical range [89, 90].

[14]Depending on the planned experiment, the nanowires can be fully embedded in a material or deposit on a substrate and flooded with an index-matching oil [114, 115]. However, that is not possible for s-SNOM measurements.
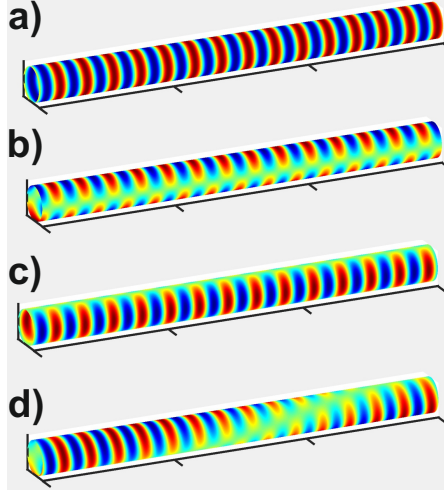
Figure 1.23: a) A fundamental nanowire surface plasmon polariton mode; b) a higher nanowire mode; c) a rotated and $\pi/2$ phase shifted higher mode; d) the sum of all three previous modes results in a tilted wave pattern (concept adapted from [112]).

[121]) and to develop and benchmark designs and concepts for nanophotonic circuits [112, 122].

Several techniques have been utilized to visualize and analyse surface plasmon polaritons on Ag NWs, amongst others classical free-space far-field schemes for excitation/observation [115], quantum dot fluorescence [112], electron energy-loss spectroscopy (EELS) [123], and SNOM [124, 125]. However, most of them are far-field techniques and not capable of resolving single SPPs directly. The near-field reports just show and analyse a single mode as a Fabry-Pérot effect [124]. s-SNOM measurements have been performed so far only at short Ag NWs considering them as antennas [126, 127], or using different material systems, e.g. InAs nanowires [128], both in the mid-infrared.

1.5   s-SNOM in different spectral ranges

As already mentioned, the s-SNOM can be operated over the entire electromagnetic spectrum. However, different spectral ranges have their special features, properties, and applications, which are discussed in the following. After a brief introduction to mid-infrared and optical/near-infrared frequencies, the focus of this subsection is on THz s-SNOM since it is one of the main aspect of this thesis.

1.5.1 Mid-infrared (mIR)

Nowadays, infrared nanoscopy by means of a CO_2 laser (covering typically the spectral range 9.2 μm - 10.7 μm) is the standard and most widespread technology in the near-field community. Historically, in the early days of the s-SNOM in the late nineties [129], CO_2-lasers were already available with high powers, whereas many other spectral ranges were not covered in this quality (sources and/or detectors). Nowadays, CO_2 lasers are a well-established technology, which benefits from its robustness and its comparatively cheap prices. Shorter wavelengths by means of quantum cascade lasers (e.g. 5.3 μm -11 μm [130]) or pulsed laser sources with a broad spectrum (e.g. 4.7 μm -14 μm [80]) have been getting more important mainly over the last years. Typically, for all those sources liquid nitrogen cooled HgCdTe infrared detectors are used, which offer both a high sensitivity and a high bandwidth [131].

In the IR region, the s-SNOM is the superior technology to obtain a high (nanoscale) resolution, its resolution enhancement (e.g. down to $\sim \frac{\lambda}{200}$) is higher than in the optical range (e.g. $\sim \frac{\lambda}{10}$). Indeed, there are fewer competitive other technologies for this purpose[15].

The spot size scales with λ eq. (1.13). Therefore, it is much easier to align and operate a mIR s-SNOM than an optical s-SNOM, for example.

A lot of interesting physics is accessible in the mIR range: Infrared spectroscopy has been implemented to the nanoscale [80], and the entire world of plasmons and phonons in 2d materials like graphene and hexagonal boron nitride [91, 96], which additionally benefits from the polariton mapping ability of the s-SNOM (see subsection 1.4.2), boosted the s-SNOM's breakthrough.

1.5.2 Optical and near-infrared (nIR)

The optical frequencies were accessible in the early days of scattering-type near-field microscopy as well [24]. Although their technology (lasers and detectors operating at room temperature) was even better than the aforementioned mid-infrared technology, optical/near-infrared s-SNOM stayed less important over the entire time: The resolution enhancement in comparison to conventional optics is smaller, the alignment (focussing the spot on the tip, adjusting the interferometric detection) is much more sophisticated, and there are many other technologies available for this spectral range reaching subwavelength resolution [135] (amongst others the Nobel Prize awarded stimulated emission depletion (STED), single-molecule microscopy [136], and aperture SNOM [11, 137, 138]).

---

[15]There are few attempts to use metallic waveguides [132, 133] and sophisticated setup designs [134] for IR SNOM (sharp fibers), however the s-SNOM is much more successful.

Nonetheless, the surface wave mapping ability of the s-SNOM is unique (see subsection 1.4.2), therefore in the research area of plasmonics and waveguides it is an important tool [2, 139].

1.5.3   Far-infrared/terahertz (THz)

The far-infrared/terahertz regime is the newest branch in the s-SNOM community, and it is very promising since it offers the highest resolution enhancement factor due to its long wavelength (e.g. 6000 for f=1 THz and a tip radius of a=50 nm). Although there are some early reports, the development is accelerated enormously only within the last years in parallel with the development of more powerful THz technology (both on the laser and detector side). However, nowadays there is a huge variety of different THz sources, detectors, and experimental designs, and it is likely that this diversity will stay, i.e. in the future depending on the exact application and wavelength a certain setup is the most suitable.

Many kinds of THz sources have been utilized in near-field microscopes: Starting from large-scale research facilities like free electron lasers [140] or big THz gas lasers [25, 72], also smaller table-top systems are used nowadays like quantum cascade lasers [59] and electronic sources [64, 141, 142].

On the detector side, for a long time liquid helium cooled hot-electron bolometers [72] were the first choice, since they are fast enough to resolve higher harmonics $n\Omega$ in the kHz range. However, their cooling makes them impractical. Recently, Schottky diodes have been employed, e.g. in combination with electronic sources [64, 141, 142]. In addition, there are further special designs like self-mixing quantum cascade lasers [59] or graphene-based photodetectors [43].

Especially terahertz time-domain spectroscopy (THz-TDS) seems to be promising [29, 55, 58]. It enables the measurement of entire spectra and there are several techniques (e.g. photoconductive detection, electro-optical sampling [30]) to measure the electric field yielding both amplitude and phase measurements, which makes interferometric detection schemes unnecessary. On the other side, the alignment of the different pulses in a TDS system ensuring temporal and spatial overlap is challenging.

Due to the weak detectors and emitters, the optimization of the tip's antenna resonance seems to be crucial in THz s-SNOM [43, 56], i.e. the required tip lengths are much longer than standard AFM probes. In addition to self-etched wires [55, 56], nowadays commercial tips are available [57], which are becoming the standard solution in the community.

For CW applications, another important issue is the interferometric detection. The pseudo-heterodyne detection as the state-of-the-art has not been used so far for THz s-SNOM due to technical reasons: The required amplitude scales with λ eq. (1.41), i.e. compared to standard mIR frequencies about 100 times higher

oscillations are necessary (assuming a wavelength of 1 mm= 0.3 THz). On the other side, the resonance frequency of piezo stages is decreasing with higher displacement ranges and in addition to this, the heavier optics and mounts (e.g. for THz often 2 inch optics are used) lower it further. Actually, not only the stage, but much more often even the high-voltage supply and control units of the piezo stages are the limiting factor, which have to provide enough power for fast oscillations. Very slow oscillations are possible, but they increase the noise level and the scanning times are getting excessively long. The reduction of the oscillation amplitude leads to unequal sidebands (which has to be compensated in the data-processing), and for small values the signal is decreased since the sidebands scale with the Bessel functions eq. (1.37) and (1.38). Indeed, technological progress and/or special optical designs for phase modulation (e.g. multiple reflections) are possible in future.

Indeed, all other schemes sketched in fig. 1.11 are used nowadays in CW THz s-SNOM: There are still some examples of self-homodyne detection [140], in combination with electronic sources there is a revival of heterodyne detection since a frequency shifted local oscillator is easy to implement electronically [64], and for other cases the homodyne detection scheme is widely used: For samples that are not phase sensitive, the reference mirror is moved into the maximum signal position and the near-field amplitude can be recorded with a single measurement [25]. In addition to this, there are reports which implement the so-called synthetic optical holography detection scheme, which offers phase sensitivity with a single measurement as well, but which is based on sophisticated data post-processing [26, 143].

Besides the aforementioned THz s-SNOM instrumentation and technology developments, more and more scientific THz near-field applications are emerging. One of its powerful properties is the non-contact nano-scaled charge carrier density and conductivity probing ability [55, 64, 72], which is also possible for subsurface structures [81]. In addition, THz s-SNOM has been used amongst other applications for investigating phase transitions [28], graphene [29], biological samples [144], THz resonant structures [67], THz polariton surface waves [145], phase-changed materials [78], and perovskites [146].

2. Experimental Setup

In the scope of this thesis, a new s-SNOM device is designed and built that is mainly used for mid-infrared (mIR) and terahertz (THz) measurements. This chapter describes first the new AFM device in section 2.1 and then its mIR and THz configurations (section 2.2 and section 2.3, respectively). The near-infrared (nIR) measurements of this thesis are performed with another available system that is briefly introduced in section 2.4. The last section 2.5 deals with the TRIBUS head based on the qPlus technology.

2.1 New AFM setup

The aim of the new device was an economical design using already available components and being compatible to the available electronics of a first s-SNOM device used so far mainly in the optical/near-infrared region [89]. The electronics are stored on a movable rack fig. 2.1 b) that can be quickly switched and connected to both setups. Fig. 2.1 a) sketches the functional units of the setup and their connection to the control electronics. The "heart" of the setup is the Anfatec Scanning Probe Microscopy (SPM) controller DS4L, which operates and synchronizes the different processes.

Cantilever oscillation

As already mentioned in subsection 1.2.2, for the s-SNOM the design of a "scanned sample" is advantageous, therefore the cantilever mount is not movable and has only to excite the cantilever oscillation. Fig. 2.2 sketches the design used. A piezo-element PL055.31 from Physik Instrumente (PI) (coloured in red) translates the electrical oscillation signal Ω into a physical movement and induces the cantilever oscillation. It is important that the resonance frequency of the piezo element (here >600 kHz) is much higher than the resonance frequencies of the cantilevers (e.g. Nanoworld Arrow-NCPt cantilever 240-380 kHz) since the piezo load reduces the stated free resonance frequency. A small bridge fig. 2.2 b) (marked yellow) can
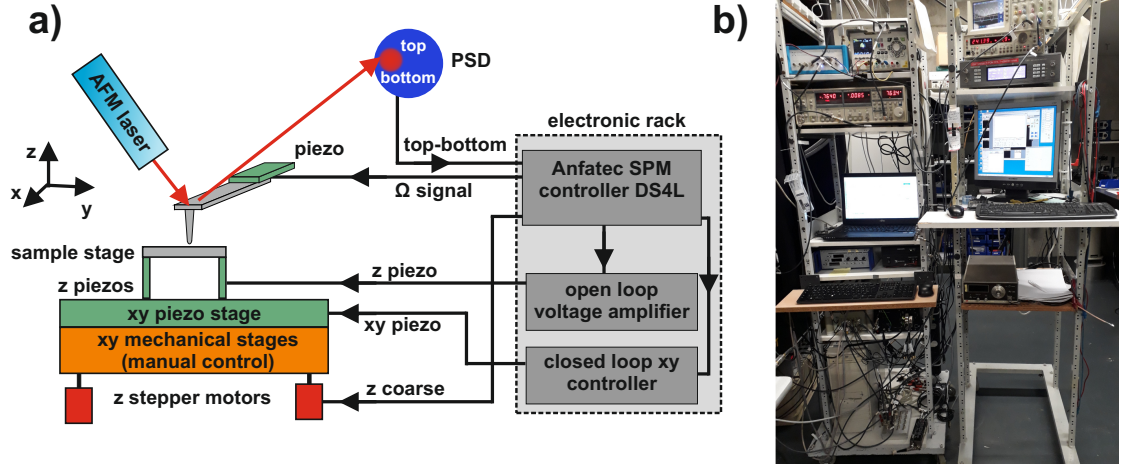
Figure 2.1: a) The basic concept of the AFM used: The sample stage can be moved in all three dimensions finely by means of piezo elements and coarsely by means of manual stages and stepper motors. The cantilever oscillation is read out via light from an AFM laser focussed on the backside of the cantilever pointing towards a position sensitive diode (PSD). An Anfatec SPM controller operates all elements and components. b) All electronic devices used (for AFM and later for the s-SNOM) are compactly placed into a movable rack for quick switching between the different setups.

be removed and put on a heating plate to mount/exchange the cantilever (marked blue), which is fixed by means of a thermal glue (Crystalbond^{TM} 509).

Cantilever read-out

As AFM laser for the light pointer principle (see fig. 1.4), a standard laser diode model CPS635 (λ=635 nm) from Thorlabs GmbH is used. Its laser light is coupled into an optical fiber, focussed by a lens on the backside of the cantilever, and reflected to a position sensitive diode (PSD). The PSD is a four-quadrant diode that is delivered together with the corresponding electronics by Anfatec to ensure easy compatibility with the DS4L controller. To suppress unwanted background light (from the lab or the s-SNOM), a shortpass/bandpass filter can be mounted in front of the detector fig. 2.3.

Three-dimensional sample movement

The sample stage is movable in all three dimensions with both a fine piezo system for the nanometer resolution and a mechanical coarse system for rough sample positioning fig. 2.4 a). The key component is a two-dimensional xy piezo scanning
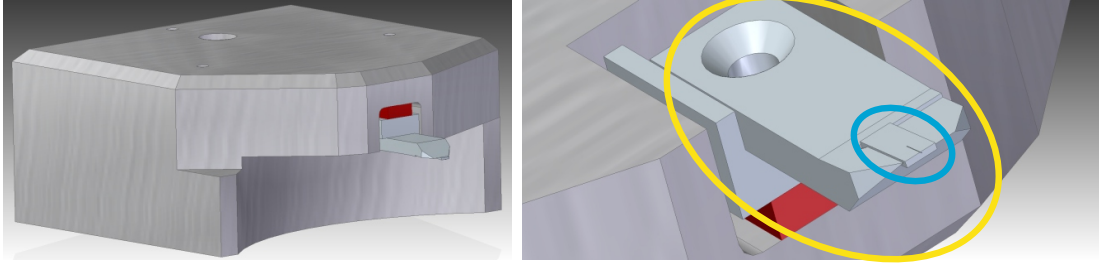
Figure 2.2: The holding block for the cantilever. The piezo element (red) connects the bridge (yellow mark) to the mount. The cantilever chip itself (blue mark) is glued onto the removable bridge.
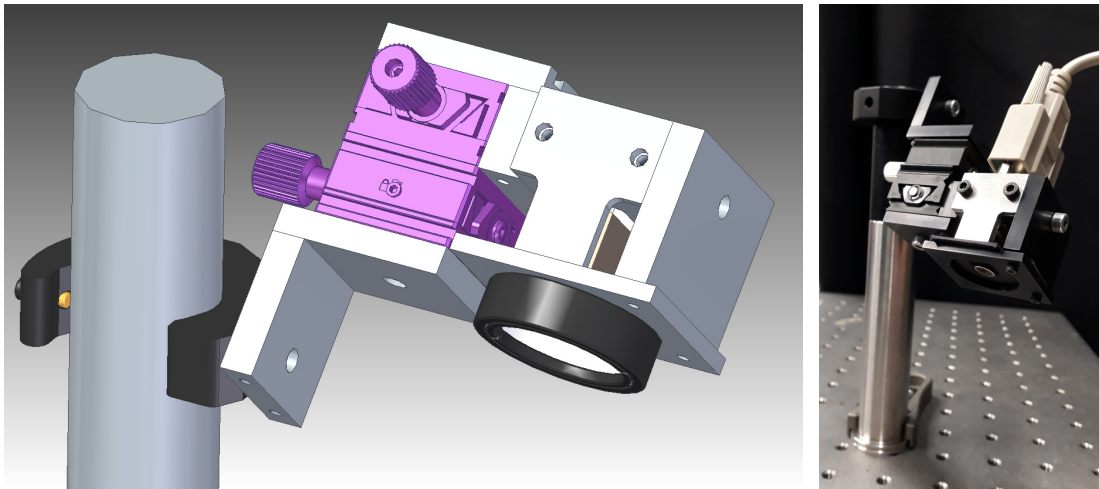

Figure 2.3: CAD and real image of the PSD detector encased in a mount and movable in two directions.
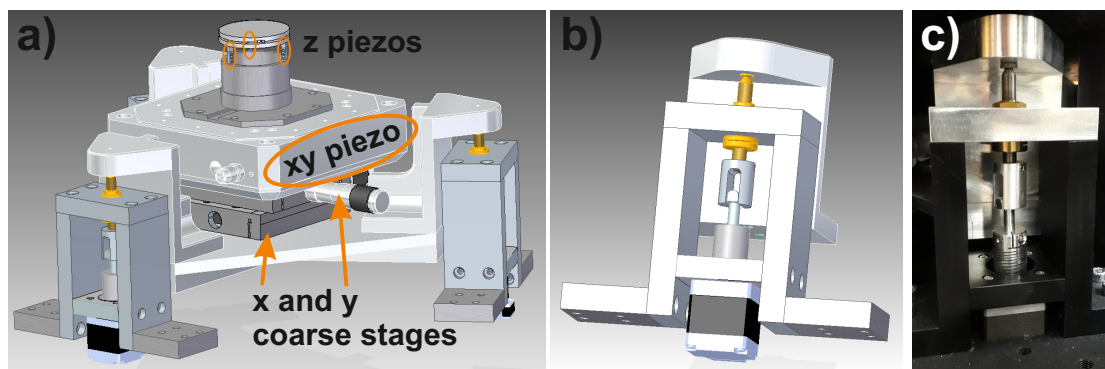
Figure 2.4: a) 3d movement unit for the sample stage: A lowered triangular platform lies on three towers containing the z stepper motors. Two manual x and y stages provide the coarse sample movement, whereas a xy piezo scanner stage is responsible for the fine scanning. On top of it, three z piezos hold the sample stage. Detailed b) CAD and c) real zoom of a single z-tower: The stepper motor (bottom) rotates a fine screw (golden colour) via a suitable coupling.

stage model P-517.2CD from PI, which is operated in closed-loop mode via a suitable digital control unit PI E-727. On top of it, three z-piezos (PI P-883.11) move the sample stage controlled by the high-voltage amplifier model V45BL from Anfatec (open-loop operation). It is important for both, the z-piezos and its amplifier, to have a high bandwidth to enable a fast topography feedback. The coarse z-direction, important for approaching/retracting the sample to the tip, is operated by means of three stepper motors (orientalmotor PKP223U09A2, again compatible with the Anfatec control unit). Their rotation is transferred to a z-movement using a mechanical coupling and a thread, see fig. 2.4 b) and c). The coarse xy movement (e.g. for positioning the sample; the piezo scanner range is limited to 100 μm) is possible with two simple manual mechanical stages mounted beneath the xy piezo stage (to reduce the weight on the piezos for enabling a better dynamical response). To limit the total height of the entire system, the xy coarse and all piezo stages are mounted onto a lowered triangular platform sketched in fig. 2.4 a) that is placed onto the z-motors (three spheres touching a groove, a cone, and a flat carbide pad, respectively; Newport CPP-C-6 and CP-V6).

Housing of all parts

A housing stabilizes and supports the entire three-dimensional sample movement mechanics (see fig. 2.5 a)), and it can be screwed onto an optical table. A big top-plate offers high flexibility in mounting the required components (AFM laser, PSD, cantilever block, and later the s-SNOM optics). The workshop of the
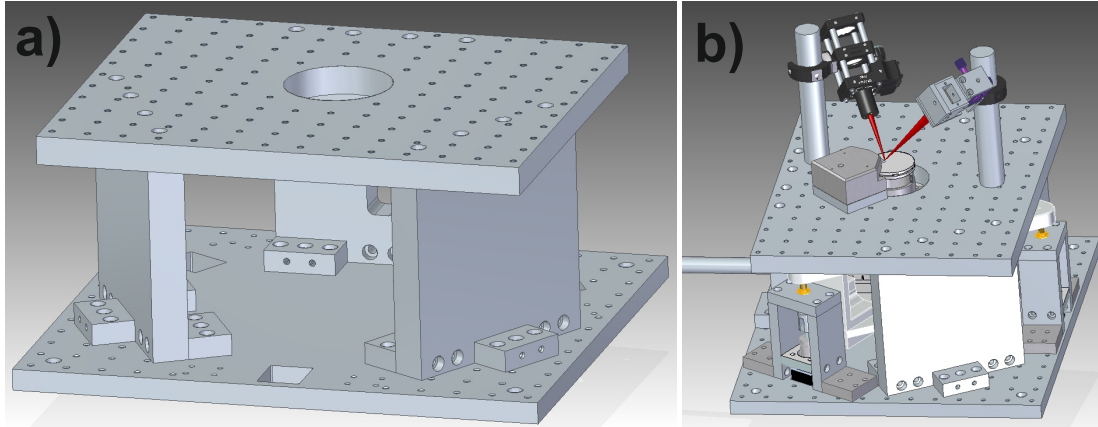
Figure 2.5: a) The housing alone b) The 3d movement unit (fig. 2.4 a)) is integrated and the AFM laser, the PSD, and the cantilever block are placed on the top plate.

"Physikalisches Institut" fabricated the housing and all other plates and adapters of this setup.

Final assembly

Fig. 2.5 b) depicts the assembly of all parts. Since the micrometer screws of the xy coarse movement are not accessible anymore, they are connected via flexible shafts to the exterior, see e.g. the rod on the left side of fig. 2.5 b). To support operation, two cameras are mounted fig. 2.6 a): A top camera controlling the position of the sample fig. 2.6 b) and a side camera that is very useful to monitor the approach of the sample fig. 2.6 c). During the alignment of the s-SNOM both cameras are extremely valuable.

Feedback mechanism

The AFM works due to the capabilities of the Anfatec SPM-controller in the AM-AFM mode (see subsection 1.2.1). During approach to the sample, the (here attractive) tip-sample forces shift the resonance curve to lower values (see eq. (1.10)) until a certain "setpoint" of the free oscillating amplitude is reached, which is illustrated in fig. 2.7[1].

---

[1]Actually, the amplitude drop is the sum of the resonance curve shift and any additional damping. However, those effects cannot be separated in AM-AFM.
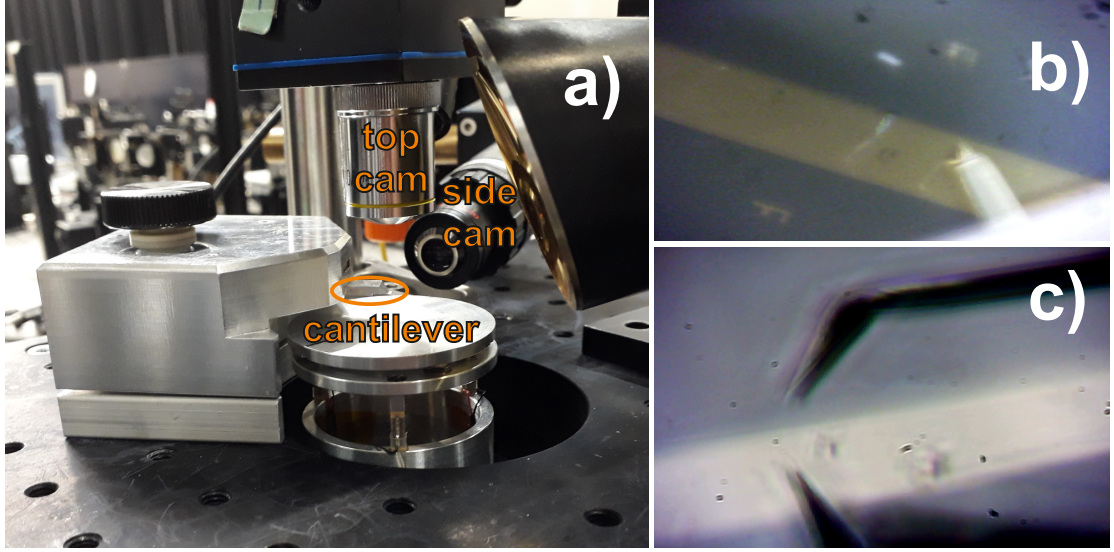
Figure 2.6: a) The top and the side camera are directed towards the cantilever. b) From the top view the sample can be positioned to the desired area. c) The side camera is very helpful to approach the sample close to the tip until the tip reflection on the sample (lower half of image) is close to the real tip (upper half image).
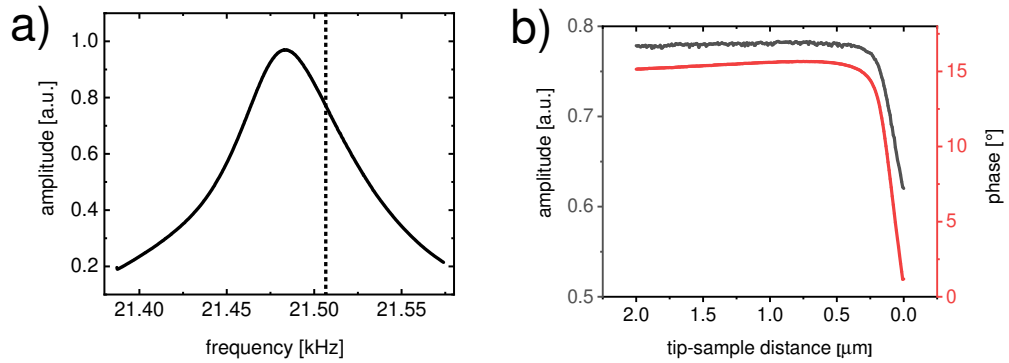

Figure 2.7: a) Resonance curve of a cantilever b) Approach curve at 21.506 kHz (dashed line in a)): The tip-sample forces shift the resonance curve towards lower values (mapped by the changed mechanical cantilever phase); therefore the amplitude decreases until the feedback mechanism reaches its setpoint (here 80% of the free oscillating amplitude).

2.2   Implementation of a mIR laser source

In the scope of this thesis, a new mid-infrared (mIR) s-SNOM interferometer is built that is used together with the TRIBUS head. The mIR optics and elements are initially connected with the aforementioned new AFM to test the performance of all devices and the mIR s-SNOM. A sketch of the infrared s-SNOM optical components is depicted in fig. 2.8.
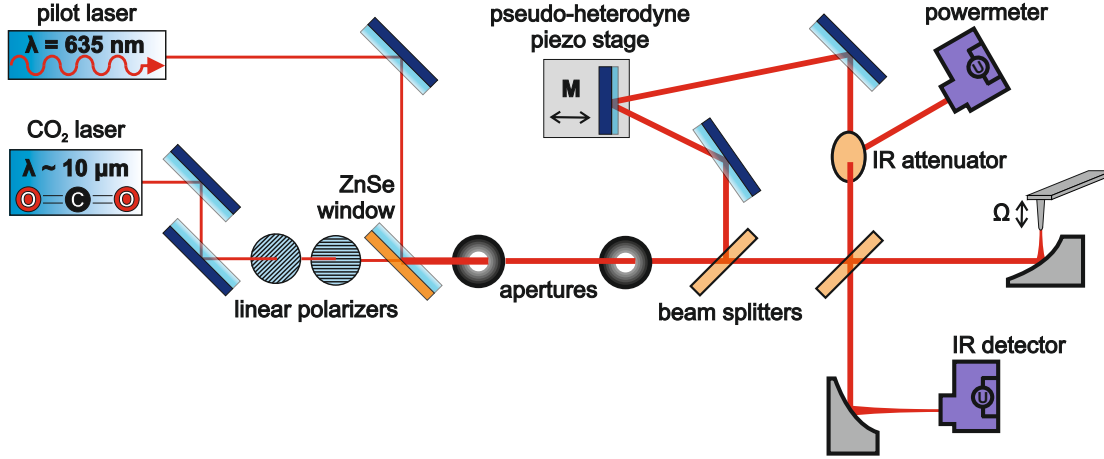

Figure 2.8: The basic components of the infrared system: The optical pilot beam and the CO_2 laser beam are overlapped through a ZnSe window. A Mach-Zehnder type interferometer is used for pseudo-heterodyne detection. The reference beam is phase modulated via a piezo stage and attenuated before it is mixed together with the higher harmonics $n\Omega$ of the cantilever in the detector.

The key components are the following:

- CO_2 laser: A model L4GT from Access Laser is used, which offers up to 910 mW power (on the strongest line) and a tuning range between 9.2 - 10.7 µm. The cooling is provided by an external chiller (TCube edge from Solid State cooling systems). The laser is equipped with the so-called "line-tracker" element: The laser power is measured continuously (internal detector) and processed as a feedback loop for a piezo element that shifts the grating of the laser cavity to increase the power and mode stability of the laser up to ±1%.

- Attenuation: To attenuate the strong CO_2 laser continuously and to set the polarization, two wire grid polarizers Thorlabs WP25H-B are used.

- Pilot beam: For aligning the invisible CO_2 laser, it is overlapped by means of a coated ZnSe window (Thorlabs WG71050-E4; transparent for mIR, reflect-

ive for optical frequencies) with a pilot beam (Thorlabs CPS635R) fig. 2.9 a).
Both can be adjusted and overlapped by using two apertures.

- Beam splitters: For their choice it is important that they work for both
  beams, mIR and optical pilot, e.g. like the model Thorlabs BSW711 used
  here. To deflect internal multi reflections from the beam path, they have
  a wedged shape, which has to be taken into account during alignment. A
  Mach-Zehnder interferometer geometry is used that offers more flexibility in
  steering the reference arm than the classical Michelson interferometer.

- Pseudo-heterodyne stage: The required specifications for the pseudo-hetero-
  dyne piezo stage are quite high. It should be able to oscillate with several
  hundreds of Hz (to reduce noise and enable a faster scanning; this frequency
  is often the lower limit for the s-SNOM scanning speed) even with the load
  of a mirror over a distance of several microns (e.g. 4.2 μm for λ=10 μm
  and $\alpha = 0°$, see eq. (1.41) and eq. (1.42)). A closed-loop operation mode is
  preferred to avoid any non-linearities and assure a proper operation[2]. The
  queensgate piezo stage NPS-X-20 (controller NPC-D-5200) in fig. 2.9 b) fulfils
  those requirements (a HAMEG HM8130 Programmable Function Generator
  provides the signal via an ADC).

- Power measurement: Since the reference beam is much stronger than the
  scattered s-SNOM beam, it has to be attenuated to avoid any detector sat-
  uration. The back reflection of the filter (Thorlabs NDIRxxA series) can be
  used to monitor the current power level (thermal sensor Thorlabs PM16-401),
  which is proportional to the power level reaching the cantilever tip.

- Parabolic mirror: To focus the incident beam onto the tip, two different
  mirrors are used and compared: A big one (both diameter and focal length
  $d = f$=50.8 mm, Thorlabs MPD229-M01) and a small one ($d = f$=12.7 mm,
  Edmund Optics #35-484), fig. 2.10. Their spots can be aligned onto the
  cantilever tip by means of a three-dimensional translation stage based on
  combined piezoelectric micrometer screw elements PI P-854.00 (micrometer
  screw range 18 mm, piezo range ~25 μm) connected to a high voltage am-
  plifier (HVG-300).

- Detector: A liquid nitrogen cooled IR detector from Kolmar technology
  model KLD-0.25-J1/DC/11/PS is used (-3dB bandwidth 2 MHz). It has
  to be quite fast to measure higher harmonics of the cantilever frequency

---

[2]A nonlinear stage response to the frequency M could lead to a movement at the second
harmonic $2M$, which is disturbing for the pseudo-heterodyne detection (see subsection 1.3.4).
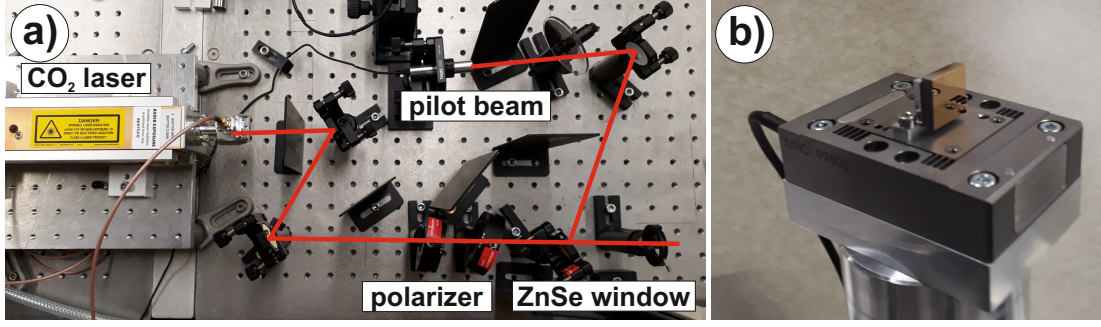
Figure 2.9: a) A ZnSe window overlaps the CO_2 laser light with the pilot beam, as it reflects the optical beam and lets the IR beam pass. In front of the CO_2 laser, two linear polarizers enable to change the polarization and power of the IR beam continuously. b) A small and light mirror is mounted on the queensgate piezo stage to provide the phase modulated reference beam with good dynamical properties.

(e.g. $5\Omega = 1.5$ MHz)[3] and should offer a good signal-to-noise ratio. The detector chip of the model used has a size of 250 µm, therefore the incoming light has to be focussed, e.g. by means of another parabolic mirror.

Fig. 2.11 sketches the s-SNOM setup and how the s-SNOM laser beam (yellow) and AFM laser beam (red) are steered. In the appendix, some practical hints for the mIR s-SNOM alignment are listed in subsection 6.3.

For the pseudo-heterodyne detection scheme, the lock-in amplifier (LIA) technique is decisive. Without sophisticated devices enabling several demodulations and sideband detections in parallel, the so-called "tandem-demodulation" (see fig. 1.13) is used, requiring two LIA devices for each higher harmonics: To demodulate the fast higher harmonic of the cantilever, a Zurich Instruments model MFLI (offering arbitrary higher harmonics up to its limit of 5 MHz) and a Stanford Research Model SR844 (internally only the demodulation at 1Ω, 2Ω is possible; an external self-built 3Ω reference box [147] enables the third harmonic as well) are available. The sidebands can be demodulated by DSP 7265 LIAs, which offer a dual-mode for parallel demodulation at $1M$ and $2M$. However, since the LIA data from the MFLI are already digitized anyway, a LabVIEW LIA is created that calculates the sidebands directly. It is described and tested in the appendix 6.5.

---

[3]Often not the detector chip itself, but the first amplification electronic is the bandwidth limiting factor.
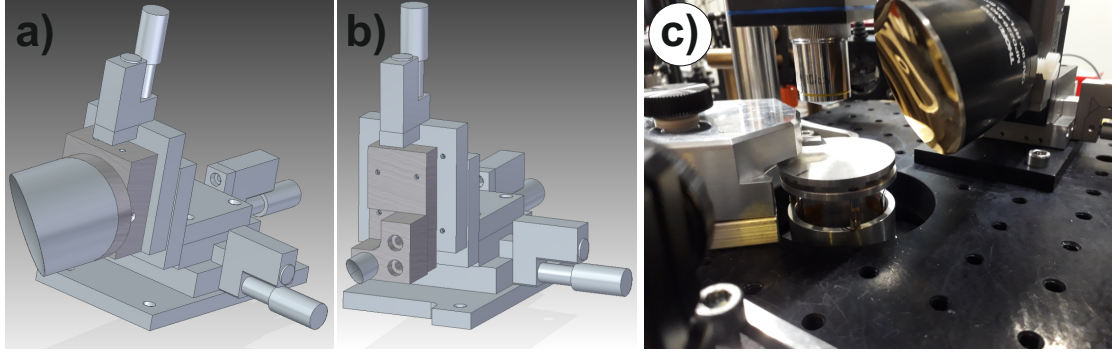
Figure 2.10: CAD view of the a) 2″ parabolic mirror installed on a 3d translation stage and b) the small 0.5″ parabolic mirror c) The big parabolic mirror is mounted on the top-plate of the AFM to focus the s-SNOM laser light onto the cantilever.

Figure 2.11: CAD sketch and picture of the final assembly of the core region of the s-SNOM setup. The AFM laser beam (red) and the s-SNOM beam (yellow) are focussed on the cantilever backside and the tip apex, respectively.

2.3 Terahertz implementation

The new AFM setup described in section 2.1 is used to implement a terahertz s-SNOM based on a homodyne detection scheme (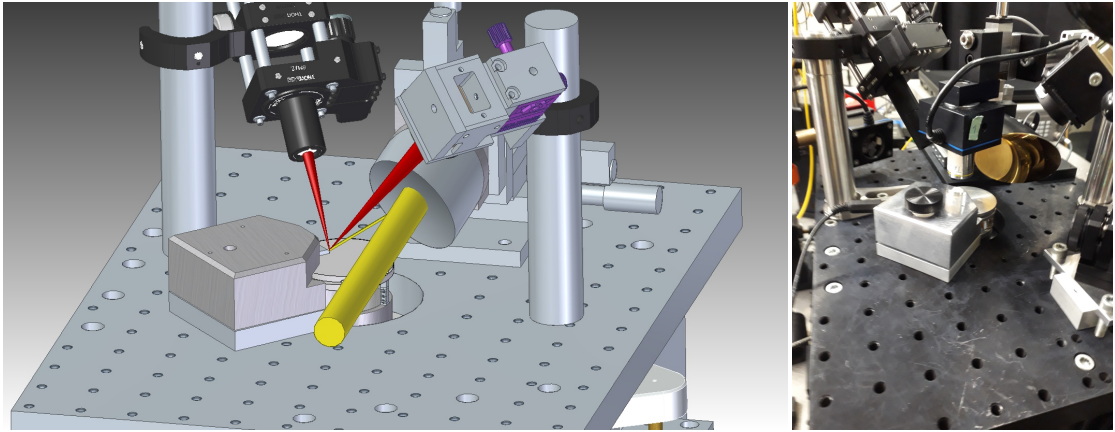for details see subsection 1.3.2). Fig. 2.12 a) sketches the optical components and fig. 2.12 b) shows its real implementation. The entire design is much more compact and simplified, e.g. in comparison to the mIR setup fig. 2.8. For THz radiation, short optical paths are much more important and non-crucial elements should be omitted to preserve as much power as possible since the THz radiation is quite weak. Therefore, interferometric detection is required to enhance the signal to a measurable level (a pure self-homodyne signal is very weak in this setup; the interferometric detection enhances the signal level by a factor of $\sim$50). Pseudo-heterodyne detection is not easy to implement as already explained in subsection 1.5.3. The heterodyne approach has already been successfully demonstrated [64] (at higher frequencies than here: 0.5 to 0.75 THz). However, it is much more complicated to implement than this "standard" homodyne design: For heterodyne detection, a second synchronized source would be required as well as tandem demodulation at higher harmonics of the cantilever frequency $n\Omega$ and the difference frequency of the THz radiation $\Delta\omega$, see eq. (1.35). The corresponding frequencies should be separated distinctly $\Delta\omega >> n\Omega$, but have to be still within the bandwidth of the available lock-in amplifier and detector.
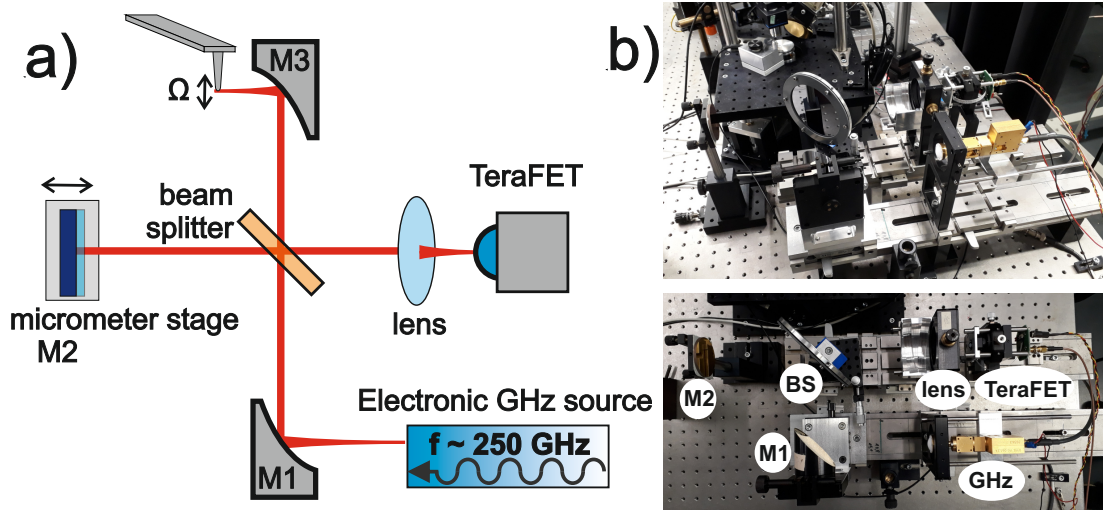

Figure 2.12: a) Sketch of the THz interferometer and b) the corresponding photos of the experiment.

The homodyne setup used comprises the following components:

- Source: Two different electronic sources have been used in the scope of this thesis and the corresponding publications [4, 6]. Both consist of a chain of amplification and multiplying modules resulting at the end in a 18 times multiplied frequency that is coupled out via a horn antenna to free-space radiation. One model is from RPG - Radiometer Physics GmbH (peak power around ∼75 µW measured with a Thomas Keating Absolute Power/Energy Meter System), the other model is from Virginia Diodes, Inc. (peak power around ∼550 µW). Both are fed by synthesizers (model 8761B and model 8673M from Hewlett-Packard), which pass a high-frequency signal (e.g. around 14 GHz) to them.

- Collimating parabolic mirror M1: A f=6″ parabolic mirror (diameter 2″) collects the emission and collimates it towards the s-SNOM.

- Beam splitter: A 2 mm thick silicon wafer acts as a beam splitter.

- The interference arm mirror M2 can be adjusted by a manual micrometer stage.

- Focussing mirror M3: A 2″ (focal length and diameter) Au coated parabolic mirror (Thorlabs MPD 229-M01) is used to focus the light onto the tip. For THz applications, there is no big benefit in using smaller focal lengths due to the common big beam diameter. Smaller focal lengths are mostly available with smaller mirror diameters d. But the spot size scales with the ratio f/d eq. (1.13). Furthermore, it is even easier to align all optics and collimate the THz radiation to a 2″ beam diameter, since slight misalignments are more tolerable than with smaller beam diameters.

- As detector, terahertz Field-Effect Transistors (TeraFET) are used, which are described in more detail in the following subsection 2.3.1. A Teflon lens focusses the GHz radiation onto the detector.

- For alignment a visible pilot beam is available (Thorlabs CPSS635R, $\lambda = 635$ nm). More details about the entire alignment procedure can be found in the appendix 6.4.

2.3.1 Field-Effect Transistors for THz s-SNOM

Many types of detectors are available for THz radiation nowadays. For pulsed THz time-domain spectroscopy, electro-optical sampling or photoconductive antennas are the most widespread and standard technology in the community [30]. However,

66

for CW applications there is a big variety of different technologies, amongst others bolometers, Schottky diodes, Golay cells, liquid helium cooled hot electron bolometers, and Field-Effect Transistors (FET). Due to the weak s-SNOM signals, the detectors should be as sensitive as possible and the higher harmonic demodulation demands a detector bandwidth of at least several tens of kHz, better hundreds of kHz (depending on the higher harmonic used and the cantilever resonance frequency), which excludes for example Golay cells (typical bandwidth <100 Hz). As already reviewed in subsection 1.5.3, the most widespread technologies for CW THz s-SNOM are nowadays hot electron bolometers and Schottky diodes. Especially the requirement of liquid helium cooling makes the bolometers impractical for daily usage, hence Schottky diodes remains the only room-temperature working option for CW THz s-SNOM so far. In this thesis, terahertz Field-Effect Transistors (TeraFETs) are presented as another option and their suitability as THz s-SNOM detectors is demonstrated.

The theory of THz emission and detection in the two-dimensional electron gas of FETs was derived and predicted by Dyakonov and Shur. They described the electrons by using a reduced hydrodynamic model (analogue to shallow water waves) [148, 149]. Under the illumination of THz radiation, plasma waves are launched in the electron gas. An asymmetry in the transistor (e.g. in the antenna design, different (ground) potentials, additional capacitances, ...) is responsible for a rectification effect resulting in a DC signal. Nowadays, there is still an ongoing scientific debate about the exact detection mechanism. Besides the initially stated plasma waves, thermoelectric and bolometric effects can play a crucial role [150], and more sophisticated hydrodynamic models have been developed [151]. Also, the aforementioned plasma waves are a subject of research, e.g. recently their direct observation using s-SNOM was reported (under the involvement of the author of this thesis) [3].

More details about the exact detection mechanisms, their electronic implementation, and equivalent circuits for modelling their performance can be found in the corresponding literature [152–155].

In general, it is not easy to compare the performance of TeraFETs and Schottky diodes directly, since many parameters and benchmark definitions are used [156, 157]. TeraFETs can be easily implemented on chips, e.g. in CMOS technology, and they are designed for free-space applications, whereas Schottky diodes are often embedded in waveguiding setups [64], which makes TeraFETs more flexible and suitable for different applications. Furthermore, Schottky diodes have been established for several years now, whereas TeraFETs are still on an earlier development level. However, their performance is already nowadays comparable, promising a superior performance of TeraFETs in the future [156]. Amongst other groups, the "Physikalisches Institut" of the Goethe-University Frankfurt plays a
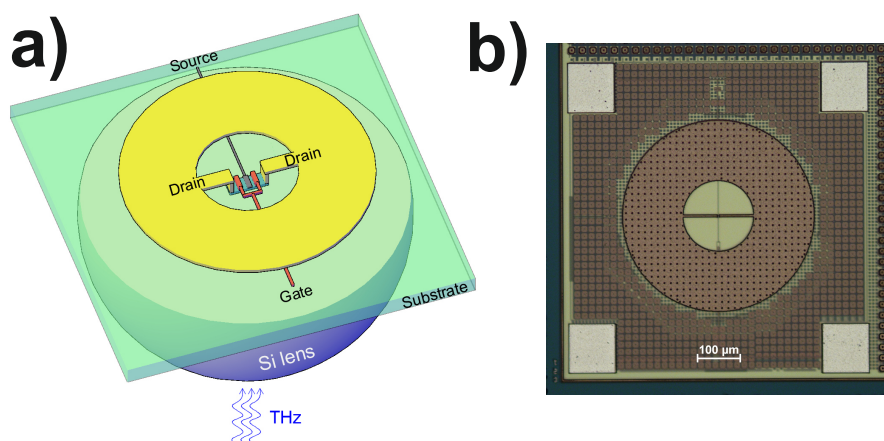
Figure 2.13: a) Schematic sketch of the TeraFET detector: The THz radiation is coupled via its backside and a Si lens b) Real image of the TeraFET chip. Reproduced and adapted from Ref. [4] with permission from the Royal Society of Chemistry.

key role in their development. Some impressive benchmarks are the successful implementation of a heterodyne scheme (which is important for s-SNOM as well) [158] and the measurement of human body radiation [159].

In the scope of this thesis, two different detector generations produced in 90 nm and 180 nm technology are investigated. They are fabricated at the TSMC foundry in Taiwan. A hyperspherical Si lens and a consecutive annular ring antenna couple the THz radiation into the FET from the back side. The design is sketched in fig. 2.13. More technical details and performance tests can be found in refs. [4, 160].

2.4 nIR setup

Some measurements of this thesis are performed with the already mentioned first s-SNOM setup of the "Physikalisches Institut" fig. 2.14 a). In the following, it is briefly described, more details can be found in refs. [89, 147, 161].

Since the new setup shares the electronics with this first setup, both setups are similar and comparable. In the nIR setup the sample is scanned in the xy-direction by means of a piezo stage Physik Instrumente (PI) P-517.3C and three open-loop piezo elements in the z-direction. Stepper motors, equipped with suitable couplers, enable the z coarse movement, the xy coarse movement is possible with a small magnetic stage mounted on top of the z-piezos due to space limitations [161]. A custom-made parabolic mirror (parent focal length $f=10$ mm) can be aligned by
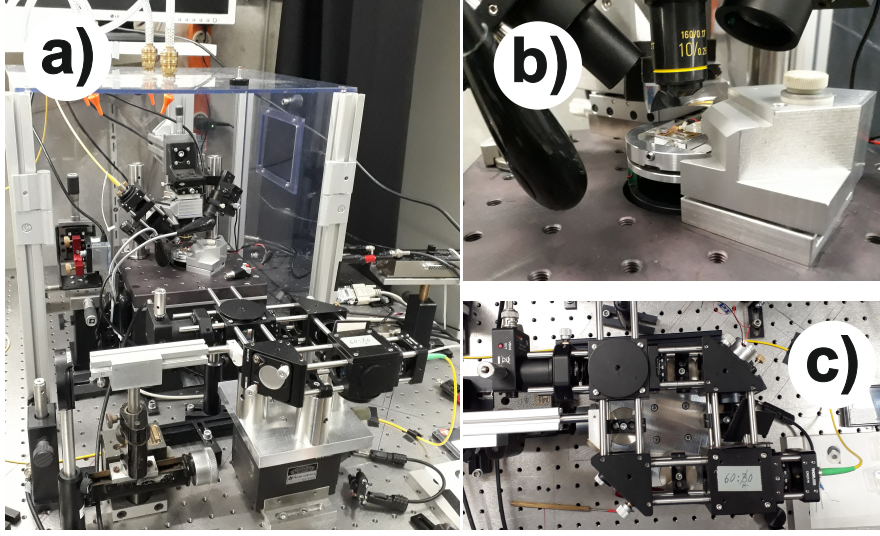
Figure 2.14: a) The entire near-infrared s-SNOM microscope is placed within a plastic housing to protect it from dust. b) The elementary parts including the cantilever holder, parabolic mirror, and sample stage c) Top view of the interferometer that is assembled into a stable cage system and placed in front of the plastic housing.

mechanical translation stages or a 3d piezo stage (PI P611.3S Nanocube).

The main differences are the optical design and components, which are shown in fig. 2.14 c) and sketched in fig. 2.15. The lasers (here Toptica DL100 DFB, tunable around $\lambda \sim 855$ nm; and Sacher Laser Cheetah TEC 50 $\lambda \sim 784$ nm) are fiber coupled (single mode fibers) towards a cage system (from Thorlabs). It contains an interferometer that offers higher rigidity, which is advantageous for shorter wavelengths. Two cubic beam splitters (the Thorlabs BS020 beam splitter guides 70% of the power to the s-SNOM) form a Mach-Zehnder-type interferometer. The reference arm is further attenuated (Thorlabs ND10A) and can be phase modulated using a piezo element PI 802.10 (operating in open-loop mode excited by a function generator HAMEG HM8130). Importantly, the polarization of both arms can be adjusted independently using $\lambda/2$ waveplates Newport 10RP42-3. A standard Si detector Thorlabs DET100A/M measures the signal, which is further processed by the LIAs described in section 2.2 (Stanford SR844 + DSP 7265 LIA for 2Ω; Zhinst MFLI + DSP 7265 LIA for 3Ω). All nIR measurements of this thesis are performed in the pseudo-heterodyne detection mode.
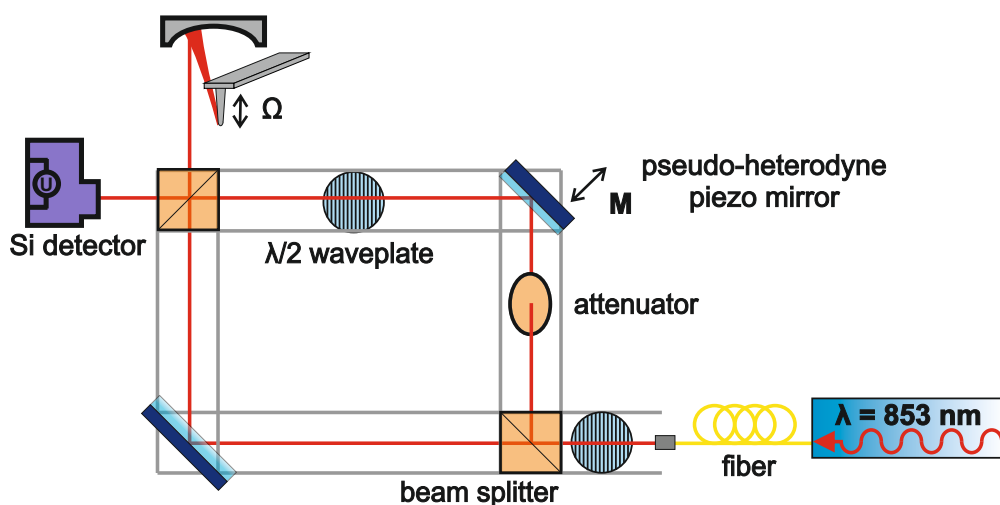
Figure 2.15: Sketch of the nIR optics assembled in a cage system and connected to the s-SNOM setup; the orientation is in accordance to the real image fig. 2.14 c).

2.5   TRIBUS AFM and STM head

The TRIBUS head fig. 2.16 is an established scanning head for a combined Scanning Tunneling Microscope (STM) and qPlus-sensor based AFM device from Scienta Omicron Technology GmbH suitable for ultra-high vacuum (UHV) and low temperatures. Its suitability for near-field measurements should be evaluated in this thesis.

As already introduced in subsection 1.2.1, the qPlus sensor enables sub-nanometer atomic AFM resolution. In addition, the FM-AFM mode is used (and even necessary) since AM-AFM in vacuum with high Q-factor elements – like the qPlus sensor – is very slow due to the low damping, e.g. a rough estimation results in 2 s relaxation time, i.e. this is the time the setup needs at every measurement point to reach an equilibrium [19].

So far, there are only a few reports in the literature using tuning forks for s-SNOM [162, 163], mainly for THz s-SNOM where longer etched tips are preferable [56, 67] (see as well subsection 1.2.2 about suitable THz probes).

The qPlus sensor resonance curve in fig. 2.17 is already in ambient conditions much sharper (here Q factor of 3890; in an UHV environment it is even higher) than for conventional cantilevers (compare as well fig. 2.7 a)).

In fig. 2.18 the approach of the qPlus AFM is plotted as a typical representative of the FM-AFM mode (see as well subsection 1.2.1 and the comparison to

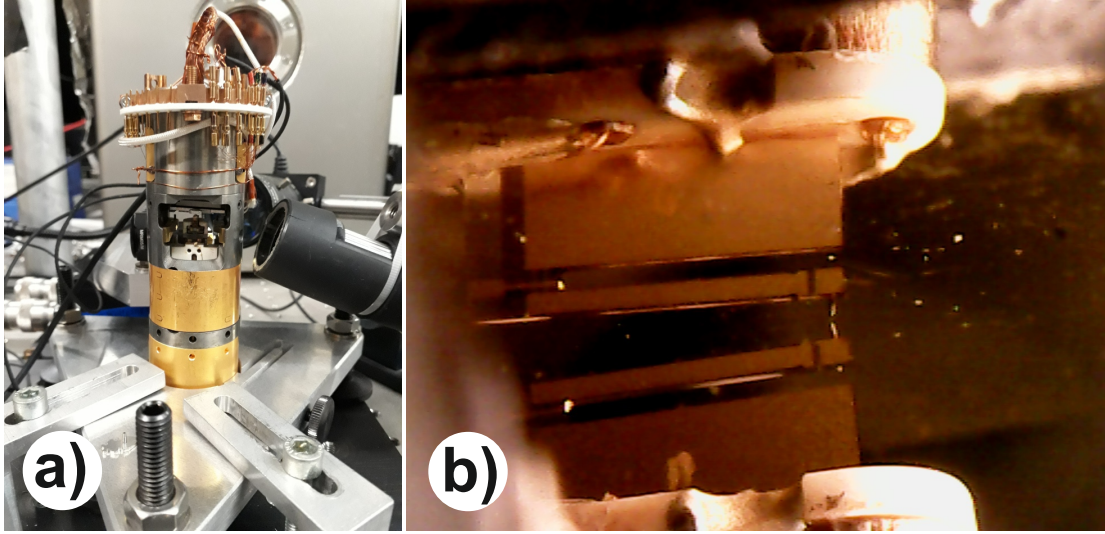Figure 2.16: a) Photo of the TRIBUS head mounted in ambient conditions for the first s-SNOM tests b) The qPlus sensor is nearly approached to a Au sample (only some µm distance); its reflection (upper part) is barely distinguishable from the real device (lower part).
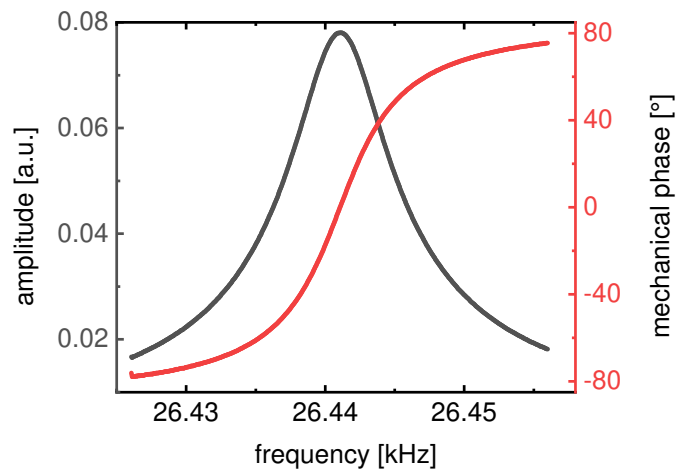

Figure 2.17: The resonance curve (amplitude and phase) of the qPlus sensor possesses already in ambient conditions a very sharp resonance.
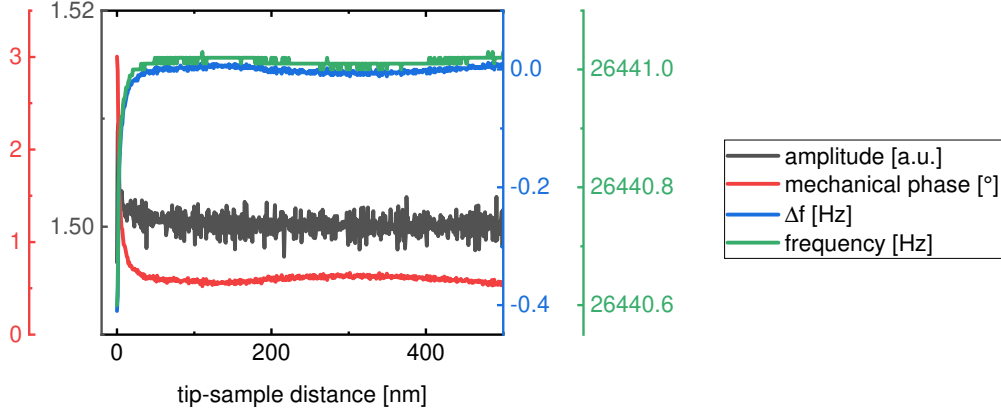
71

Figure 2.18: Approach curve of the qPlus sensor: The amplitude, mechanical phase, excitation frequency f, and frequency shift Δf are measured as a function of the tip-sample distance.

fig. 2.7). Within some noise and background effects, the amplitude stays constant[4], whereas the frequency f and with it Δf (the decisive parameter for the feedback) is shifted until the desired value is reached (here setpoint Δf=-400 mHz).

The TRIBUS was initially designed for atomic STM and qPlus resolution, and not for near-field microscopy. Therefore, there are some special construction dependent issues, which have to be addressed in the scope of this thesis.

As mentioned in the introduction subsection 1.2.2, a "scanned sample" design is advantageous for s-SNOM as the s-SNOM laser beam hits the tip always in the same manner. However, the TRIBUS is based on a scanning tip design for various reasons. Changing it to a "scanned sample" design would require an entire reconstruction of the head. Indeed, its piezo scanning range is limited ($\sim$18 μm at room temperature; further reduced at low temperatures), and the coarse movement motors are positioning the sample (xy plane), which is suitable for s-SNOM. At least for long wavelengths in the infrared, when the tip scan range is far below the corresponding spot size eq. (1.13), this can be accounted for in the data post-processing (see section 3.2).

Another subject of matter is that the TRIBUS head is spring mounted freely in the vacuum chamber to isolate it from environmental vibrations. Hence, all of its movements change as well the optical path distance for the interferometric detection since the main optical components (laser, detector, etc.) are fixed outside the

---

[4]A second feedback loop compensates the drop of the amplitude (induced by the damping) via increasing the amplitude of the electrical excitation signal.
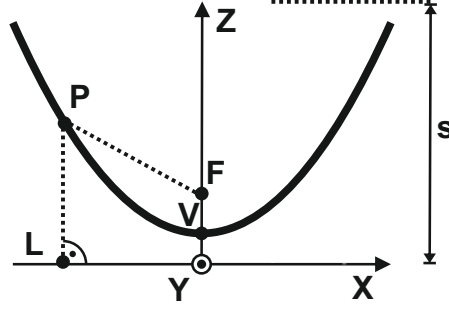
Figure 2.19: Parabolas can be defined as the locus of points with $|PF| = |PL|$.

vacuum chamber in the laboratory system. Nonetheless, the following theoretical considerations show that this effect could be at least partially compensated.

Before dealing with the experimental implementation, some theoretical considerations about parabolic mirrors and a deeper look into the mathematics of parabolas are instructive. For parabolas, besides the well known definition via eq. (2.1), there is another definition as the locus of points P where the distance $|PF|$ (F is the focus of the parabola) is equal to the distance $|PL|$ (the fixed line L is called directrix and lies under the parabola with $|VF| = |VL|$, where V is the vertex of the parabola) fig. 2.19. [164, 165]

$$z = a \cdot x^2 \tag{2.1}$$

Transferred to optics that means that independent of the exact position, where the incident beam (in fig. 2.19 the two red beams parallel to the z-axis) hits the parabola, the optical path length towards the focus stays constant (here the distance s towards the directrix). Parabolic mirrors are three-dimensional paraboloids, the surface of revolution of parabolas: If the incident beam hits the paraboloid at another xy position, this movement can be decomposed into a radial and an azimuthal translation (in cylindrical coordinates); for the radial movement the aforementioned rules hold and for the azimuthal component the optical beam path to the focus stays constant anyway.

Fig. 2.20 is a basic sketch of the IR interferometer (top view) connected with the TRIBUS head (in comparison to fig. 2.8 only the elementary optical components are plotted). The focussing parabolic mirror should be very close to the probe to enable the highest possible numerical aperture eq. (1.14), therefore it is positioned on the spring mounted TRIBUS platform, which is symbolized by the yellow rectangle. The spring suspended platform is free to move with respect to the external laboratory system (grey rectangle).

For any movement of the TRIBUS head in the xy plane, the incident beam hits the parabolic mirror at another position but, as explained before, that will not
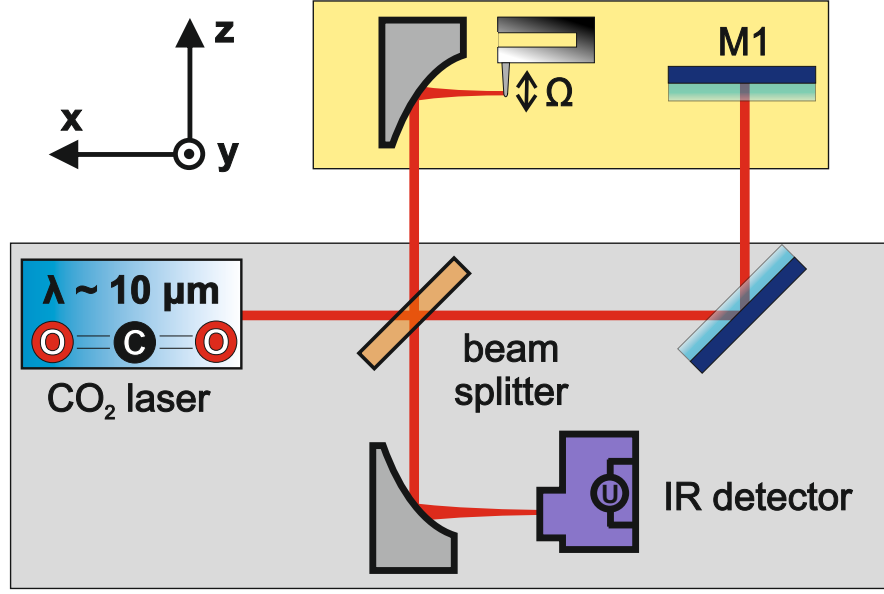
Figure 2.20: The interferometer of the TRIBUS scan head: The vacuum platform (yellow) is spring suspended to isolate it from environmental vibrations, whereas the remaining optical components are fixed on an optical platform (grey).

change the optical path towards the focus, where the probe apex as the origin of the s-SNOM near-field signal is located. To compensate any translation in the z-direction, the reference beam is guided to the TRIBUS platform and reflected from there (mirror M1) as well in parallel to the s-SNOM beam: Now, any translation in the z-direction affects both interferometer arms in the same manner, the resulting phase difference of the two arms stays constant.

In the experimental realization, there is another aspect to be considered. The TRIBUS head and the entire vacuum and cryostat system is constructed in a cylindrical design with the qPlus sensor on its axis, i.e. the beam path towards the qPlus sensor depicted in fig. 2.20 is difficult to implement into the vacuum chamber as an "off-axis" path. Therefore, the design in fig. 2.21 a) is realized (TRIBUS head (in yellow) as a side view, equivalent to fig. 2.16).

The parabolic mirror is mounted onto the TRIBUS platform and illuminated from above via an additional tilted mirror M2, whereas the reference beam is guided further above via M1. As the two beams are so close to each other, they can be guided into the vacuum and cryostat chamber via common windows into the direction of the TRIBUS main axis. Now the compensation of the beam path lengths of s_{ref} and $s_{signal} = s_1 + s_2$ [5] is slightly different. Any movements/vibrations

---

[5]For simplicity, here s_1 is already referred to the directrix as it represents the distance towards the tip.
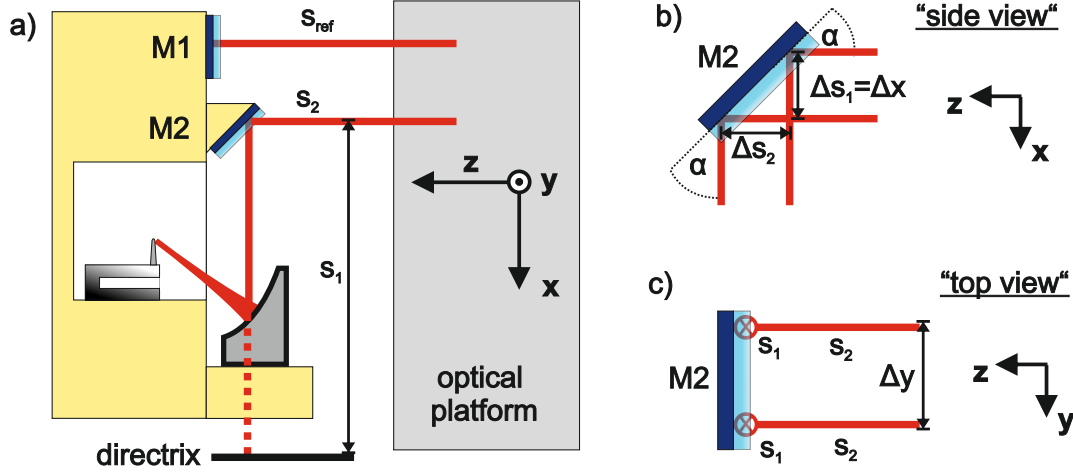
Figure 2.21: a) Side view sketch of the optical elements and beam paths of the TRIBUS platform. b) xz side view and c) yz top view geometry of the mirror M2 and the influence of displacements Δx, Δy on $\Delta s_{1,2}$.

of the TRIBUS platform (yellow) in the xyz-directions affect the optical beam paths as following:

- z-direction: Any Δz equally adds to s_{ref} and s_2, hence the total path difference between the two interferometer arms stays constant.

- x-direction: s_{ref} is not affected. Fig. 2.21 b) is a cross-section of the xz plane of M2. A changed Δx influences both s_1 and s_2. However, as long as $\Delta s_1 = \Delta s_2$, they are compensating each other perfectly (what is even valid for angles others than $\alpha = 45°$).

- y-direction: This direction can be understood equivalently. Again, s_{ref} is not affected. Fig. 2.21 c) is a cross-section of M2 in the yz-plane ("top view"), which reveals that any Δy does not affect s_1 or s_2.

Although those aforementioned mechanisms only neutralize the three translational degrees of freedom, it is expected that they are dominant in comparison to the three rotational degrees of freedom and again the mIR wavelengths are in general not so sensitive against vibrations and rotations like optical frequencies. Indeed, there are more experimental uncertainties like the parallelism of s_{ref} and s_2, the perpendicular incidence of s_{ref} on M1, the proper mounting angles of M2, the focussing of both beams into the detector, ...

Finally, experimental verifications and tests are necessary. Section 3.2 analyses the s-SNOM suitability of the qPlus sensor and the consequences of its "scanning tip" design. Due to the project timetable, the evaluation of the interferometer stability is not included in this thesis.

3. Performance Evaluation of the s-SNOM Setups

This chapter presents tests and evaluations of the newly assembled s-SNOM devices of this thesis. In section 3.1 the mid-infrared equipment is first tested with a conventional setup highlighting insights, which are valid for s-SNOM in general. After that, the mIR components are used to show the s-SNOM suitability of the qPlus sensor in section 3.2, which additionally analyses special aspects of the TRIBUS scanning head. At the end, section 3.3 gives a comprehensive overview about the THz s-SNOM setup based on all-electronic sources and TeraFETs.

3.1 Aspects of the mIR setup

The conventional AFM setup built in this thesis (section 2.1) is used to test and characterize the mIR components and interferometer from section 2.2. The basic interferometer and phase modulation is tested in subsection 3.1.1, exemplary approach curves are presented in subsection 3.1.2, different detection modes are compared in subsection 3.1.3, and the role of the focal length of the parabolic mirror is evaluated in subsection 3.1.4.

3.1.1 Phase modulation

The basic requirement for the pseudo-heterodyne near-field detection is the phase modulated interference, which results in the formation of sidebands (see subsection 1.3.4). As a first test, the coherence length of the CO_2 laser is checked. An interferometer with a difference in the arm lengths of >3.5 m still shows convincing interference (moving the mirror of one arm via a translation stage to pass through the minima/maxima or destructive/constructive interference, respectively). That is in any case sufficient for the s-SNOM and actually not surprising; the manufacturer claims a coherence length up to kilometers [27, 166].
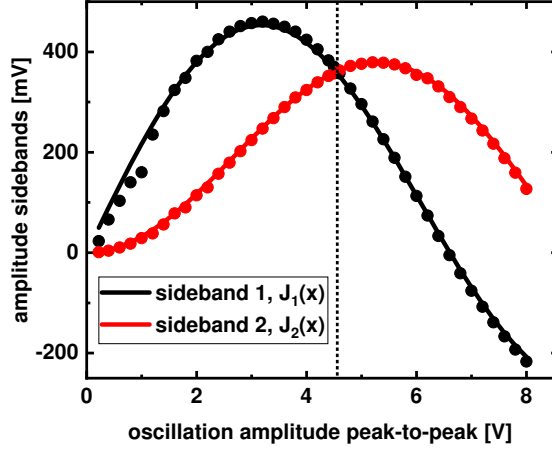
Figure 3.1: The measured first and second sideband (data points) as a function of the peak-to-peak amplitude of the pseudo-heterodyne stage (corresponds to the modulation depth γ) results in the Bessel functions (superimposed curves as data fits). For this measurement, at a fix frequency of 120.32 Hz the amplitude is increased and at each value both sidebands are measured with a DSP 7265 LIA. Since the DC offset tuning range of the function generator HM8130 used is not equal for all amplitudes, different electrical amplifications and attenuators have been used resulting in some jumps in the data sets, e.g. around 1 V.

Subsequently, the dynamic operation of the phase modulated reference is investigated. As stated in the appendix 6.1.4, a constant E-field contribution in the signal arm (here e.g. the flat alignment mirror instead of the s-SNOM parabolic mirror) can be used to measure the sidebands. Fig. 3.1 shows the maximum values for both sidebands as a function of the pseudo-heterodyne mirror amplitude (corresponds to the modulation depth γ of the phase reference) and reveals the Bessel functions $J_{1/2}(\gamma)$ eq. (3.1) and eq. (3.2)[1]: For the measurement, at every single point the reference phase ϕ_r (the DC offset of the piezo stage) is optimized to measure the maximum values ($sin = cos = 1$ in eq. (3.1) and eq. (3.2)); the signs for the negative values have been added manually.

$$SB_{1M} \propto E_0 E_r J_1(\gamma) sin(\phi_r - \phi_0) \tag{3.1}$$

$$SB_{2M} \propto E_0 E_r J_2(\gamma) cos(\phi_r - \phi_0) \tag{3.2}$$

In this specific geometry, the sidebands are equal for a peak-to-peak amplitude of d=4.5 µm (1 V $\Leftrightarrow$ 1 µm). This value can be cross-checked as the piezo stage is equipped with position sensors and works in the closed-loop mode. In the static

---

[1]Those equations correspond to eq. (6.31) and eq. (6.32), respectively.

78

interferometer, the DC position of the stage d is changed. The interference and transitions between minima and maxima are observed and a total stage shift of Δd =13.8 μm corresponds to an optical path difference of $\Delta s = 2.5\lambda$. Out of $\Delta s = \frac{2.5\lambda}{13.8\,\mu m}\Delta d \approx 1.9\Delta d$ the incident angle α of the pseudo-heterodyne mirror fig. 1.15 can be calculated via eq. (1.42) to $\alpha \approx 18°$ and following eq. (1.41) this leads to a necessary amplitude of d=4.64 μm, which is in excellent agreement with the observed value in fig. 3.1 (the amplitude resolution of the function generator is only 0.1 V↦0.1 μm). This test confirms the proper dynamic movement and behaviour of the pseudo-heterodyne piezo stage.

3.1.2 Approach curves

A very powerful test measurement for the s-SNOM are approach curves, which have been already introduced in fig. 1.18 using simulations. Fig. 3.2 shows approach curves of the mIR setup. Up to the 10th harmonic is plotted, and the figure reveals nicely that with increasing demodulation number the signal gets weaker (and more noisy) but on the other hand more confined to the surface (close to 0). Since the s-SNOM quality and therefore the approach curves strongly depend on the alignment (parabolic mirror, interferometer, detector coupling, ...) and the cantilever tip (fresh/damaged tip, antenna resonances, ...), it is difficult to benchmark and/or compare measurements unless they were taken directly one after the other.

The approach curves are recorded consecutively[2]. The lock-in amplifier time constants stay the same (fast demodulation at t_c=100 μs, slow demodulation at t_c=20 ms). Its sensitivity is adjusted to the signal strength during the measurement; the data presented in fig. 3.2 are multiplied by the sensitivity to be able to compare the signal strengths between the different higher harmonics directly.

3.1.3 Comparison of different detection modes

Fig. 3.3 shows an s-SNOM measurement of a ∼80 nm high Au edge on a Si substrate (Si left, Au right). In fig. 3.3 b) the area is scanned at first with homodyne detection (upper half) at 3Ω; after half of the measurement the reference beam is blocked, and it is finished in self-homodyne mode (lower half). Fig. 3.3 c) is the parallelly recorded 4Ω signal. It is only a single homodyne measurement, however the reference offset is chosen to maximize the s-SNOM signal and since it is not a phase changing sample, this simplification is legitimate as a proof-of-principle. The signal enhancement by means of the reference wave (here e.g. 75% for 4Ω)

---

[2]In principle, all higher harmonics can be measured with one scan. But for this measurement, not enough LIAs were available.

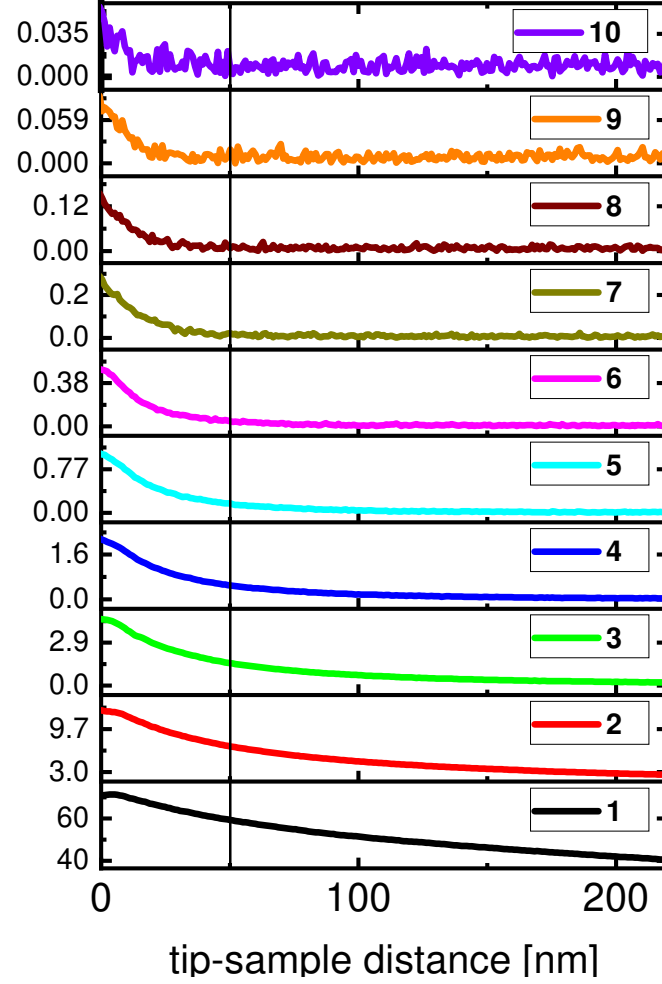Figure 3.2: The first ten pseudo-heterodyne higher harmonics of the mIR s-SNOM setup ($\lambda \approx 10.5$ µm) reveal the increasing confinement of the near-field to the sample surface and the decreasing absolute signal strength with increasing higher harmonics. The y axes are scaled to be comparable to each other (arbitrary unit). The vertical black line at x=50 nm acts as a guide for the eye.
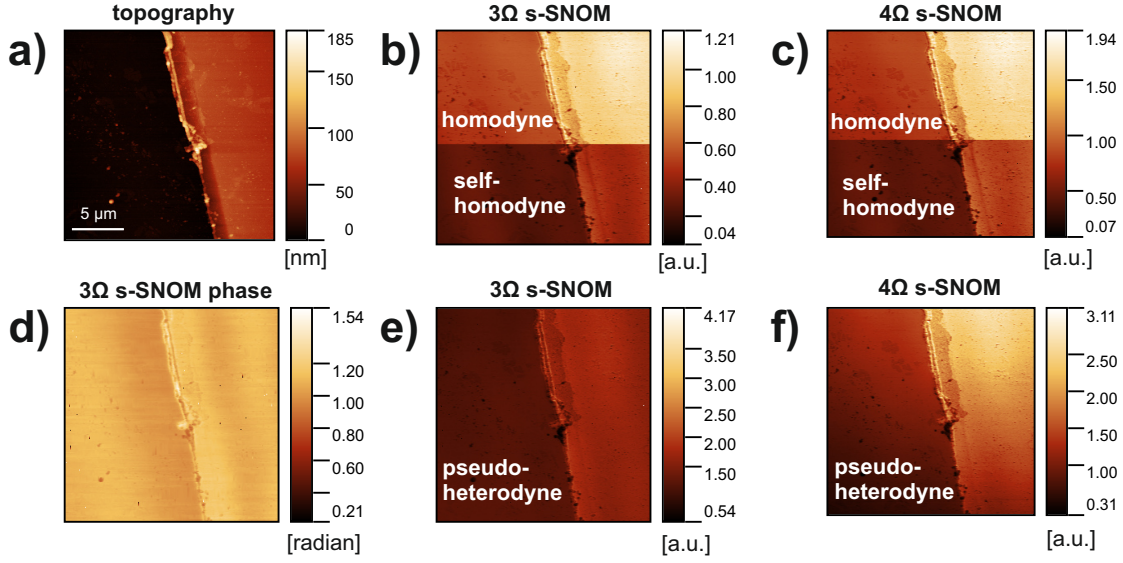
Figure 3.3: a) Topography of a Au edge on a Si substrate b) 3Ω and c) 4Ω s-SNOM signal of the corresponding homodyne and self-homodyne s-SNOM measurement (upper half: homodyne; lower half: self-homodyne) e) 3Ω and f) 4Ω pseudo-heterodyne s-SNOM measurements of the same scan window d) Optical near-field phase from the 3Ω pseudo-heterodyne measurement.

is clearly observable. Also, the pseudo-heterodyne detection scheme is working nicely, the corresponding near-field amplitudes are illustrated in fig. 3.3 e) and f) for 3Ω and 4Ω, respectively. In fig. 3.3 f) a slow decreasing trend (especially on the Au surface from top to bottom) is visible that can be due to any alignment shift during the long measurement (which takes >2.5 h). The corresponding optical near-field phase of 3Ω is shown in fig. 3.3 d), which is flat (except for some spikes). The sample is not clean any more, which is particularly visible in the s-SNOM images ("black points"), and there is some residual material on the edge. All the raw data are processed with the free SPM software Gwyddion: It removes a background/level plane and corrects typical AFM artefacts such as row offsets and scars.

The following parameters and settings are used here:

- CO_2 laser: $\lambda = 10.5$ µm, ~ 7 mW power reaching the parabolic mirror (f=12.7 mm).

- Pt coated cantilever (Arrow-NCPt), oscillating at 319.879 kHz, the feedback is set to 85% of its free amplitude.

- Lock-in amplifier settings: Intensity/homodyne measurement time constant t_c=30 ms (3Ω) and $t_c = 20$ms (4Ω); pseudo-heterodyne measurement both

fast LIAs t_c=100 μs, slow LIAs t_c=50 ms (see subsection 2.2 for details of the LIAs used).

- Pseudo-heterodyne mirror frequency: 241.39 Hz.

- Image: Scanning window 20·20 μm^2, 256 x 256 Pixels, speed 0.1 $\frac{lines}{sec}$ $\left(0.06 \frac{lines}{sec}\right)$ for the intensity/homodyne (pseudo-heterodyne) measurement.

3.1.4 Focal length of parabolic mirror

This subsection analyses the role of the parabolic mirror focussing the s-SNOM laser light onto the tip and collecting the back-scattered light. Unfortunately, it is quite difficult to compare different mirrors experimentally since the entire alignment (interferometer, parabolic mirror, focus, detector coupling) has to be changed in between measurements with different mirrors and all those aspects influence the s-SNOM signal quality probably more than the mirror itself. Therefore, only some basic aspects are discussed and some experimental data analysed here.

The smaller the chosen focal length f, the smaller the focus on the tip (see eq. (1.13)), and therefore the field strength increases (assuming that the incident laser beam diameter d is smaller than the mirror diameter). The back-scattered light is proportional to the incident field strength. The amount of collected light depends on the numerical aperture NA; here the numerical aperture is identical for both tested mirrors (the small one $f = d_{mirror}$=12.7 mm and the big one $f = d_{mirror}$=50.8 mm). Indeed, the diameter of the collimated back-propagating beam is equal to d_{mirror}. Since the entire interferometer optics fig. 2.1 is mainly based on 25.4 mm optics (angles further reduce their effective area), for the big mirror a portion of the s-SNOM signal is cut off by the subsequent optical elements.

The signal S from the detector is proportional to eq. (3.3). E_r stays constant, E_{nf} is reduced with the bigger mirror as explained before (less focussing, cutting by subsequent optics). However, the laser power reaching the big mirror can be increased[3] to compensate the smaller fraction of light from E_{nf} reaching the detector in comparison to the small mirror, so that the same signal strength S is measured. If the SNR of E_{nf} is independent of its power level, both mirror situations are comparable and there is no difference in electronic and detector noise.

$$S \propto E_r \cdot E_{nf} \tag{3.3}$$

Of course, now the total laser power in the s-SNOM region and on the sample is higher, what could be relevant for very sensitive samples (heat dissipation). On

---

[3]That is possible here due to the powerful CO_2 laser. The laser noise is independent of the power level since the latter is adjusted by linear polarizers.

$n\Omega$	f=12.7 mm		f=50.8 mm		f=12.7 mm		f=50.8 mm	
	SB1	SB2	SB1	SB2	amplitude	phase	amplitude	phase
1Ω	0.38%	1.82%	0.51%	4.35%	0.17%	0.007	0.33%	0.015
2Ω	1.60%	0.62%	5.98%	1.27%	0.34%	0.010	0.78%	0.023
3Ω	1.48%	0.75%	1.80%	3.93%	0.57%	0.007	2.02%	0.014
4Ω	1.71%	1.68%	1.60%	1.94%	1.21%	0.012	0.99%	0.014
5Ω	0.92%	0.66%	3.60%	3.48%	0.52%	0.006	1.55%	0.032
6Ω	4.80%	4.66%	2.64%	4.29%	4.63%	0.010	2.57%	0.024
7Ω	5.20%	5.29%	4.00%	3.04%	5.00%	0.016	2.66%	0.022
8Ω	4.97%	3.82%	8.80%	7.34%	3.27%	0.028	6.75%	0.040

Table 3.1: Noise level comparison of the two pseudo-heterodyne sidebands (SB1, SB2) and the resulting near-field amplitude and phase by using the small ($d = f$=12.7 mm) and the big ($d = f$=50.8 mm) mirror (standard deviation normalized to mean value; for the phases absolute values in radian).

the other side, a bigger spot and longer focal length make the alignment process easier and more robust.

In table 3.1 there is an exemplary comparison of the noises (sidebands, near-field signals, and near-field phases) of different higher harmonics for the f=12.7 mm mirror and the same tests performed with the big mirror f=50.8 mm (same t_c and data rates, but higher laser power 21 mW for the big mirror instead of 9 mW for the small one).

As expected, there is no clear trend in the stability of the near-field amplitudes between the two mirrors. Indeed, the phase noise for the 50.8 mm mirror is higher. That can be explained with the interferometer stability: The big mirror is much more massive ($\sim$190 g in comparison to $\sim$4 g for the small mirror; mounts and adapter plates are neglected in those numbers) and hangs on a longer lever fig. 2.10 causing higher torques. Hence, it is quite likely that this increases the phase noise. That is supported by the fact that the noise levels of the single sidebands are always higher than the resulting near-field amplitude noise. Any position instability in the pseudo-heterodyne interferometer corresponds to a changed reference phase ϕ_r eq. (1.37) and eq. (1.38). The measured optical phase eq. (1.40) depends directly on ϕ_r, whereas the optical amplitude eq. (1.39) is independent of it, i.e. for any interferometer noise/instability the two sidebands are compensating each other.

3.2   s-SNOM with qPlus sensor

In the following, the first basic s-SNOM tests with the TRIBUS scan head based on a qPlus sensor are presented. Since the project is ongoing at the end of this thesis, only intermediate results are analysed. For this purpose, the mid-infrared spectral range is used since it is the most common one (and the easiest to handle). All measurements are performed with the TRIBUS scan head mounted simply on an optical table fig. 2.16 a) without any special care of rigidity of the mounting platform (later it will be spring suspended in a vacuum chamber). The s-SNOM laser beam is focused on the qPlus sensor by means of a Thorlabs off-axis parabolic mirror model MPD01M9-M01 (f=33 mm, diameter d=12.7 mm)[4].

3.2.1   Approach curves

In fig. 3.4 exemplary approach curves on a Au surface are presented showing the near-field suitability of the qPlus sensor using a) the homodyne and b) the pseudo-heterodyne detection scheme.

The signal quality is worse in comparison with the conventional s-SNOM setup in fig. 3.2 mainly due to two reasons: First, for STM and qPlus operation the general tip shape is not important since only the foremost atoms are decisive for those operation modes. Hence, it is not common for the user to regularly change the tips (what means to replace the entire tuning fork sensor) or to take special care of their shape and length. Often, as in this case, the tip is already worn-out. The second and more important aspect is the amplitude. The qPlus AFM is working at low oscillation amplitudes, where it is much more stable; the s-SNOM signal however increases with the oscillation amplitude. Whereas in regular cantilever based AFM oscillation amplitudes in the order of ∼50 nm are easy to obtain, in fig. 3.5 even the (already mechanically unstable) high values correspond only to a peak-to-peak oscillation of around ∼8 nm. In an UHV environment, even those mechanical amplitudes could be too high. Due to the missing water film on the sample, the qPlus sensor could easier crash into the surface. The trade-off between high s-SNOM signal (higher mechanical amplitude) and qPlus stability (low mechanical amplitude) has to be further evaluated.

All those measurements are taken with external LIAs (the MFLI alone for homodyne; for the pseudo-heterodyne, a DSP 7265 LIA is used for the sideband demodulation).

---

[4]Later, a custom-made mirror optimized for the space-limited vacuum chamber will be used.
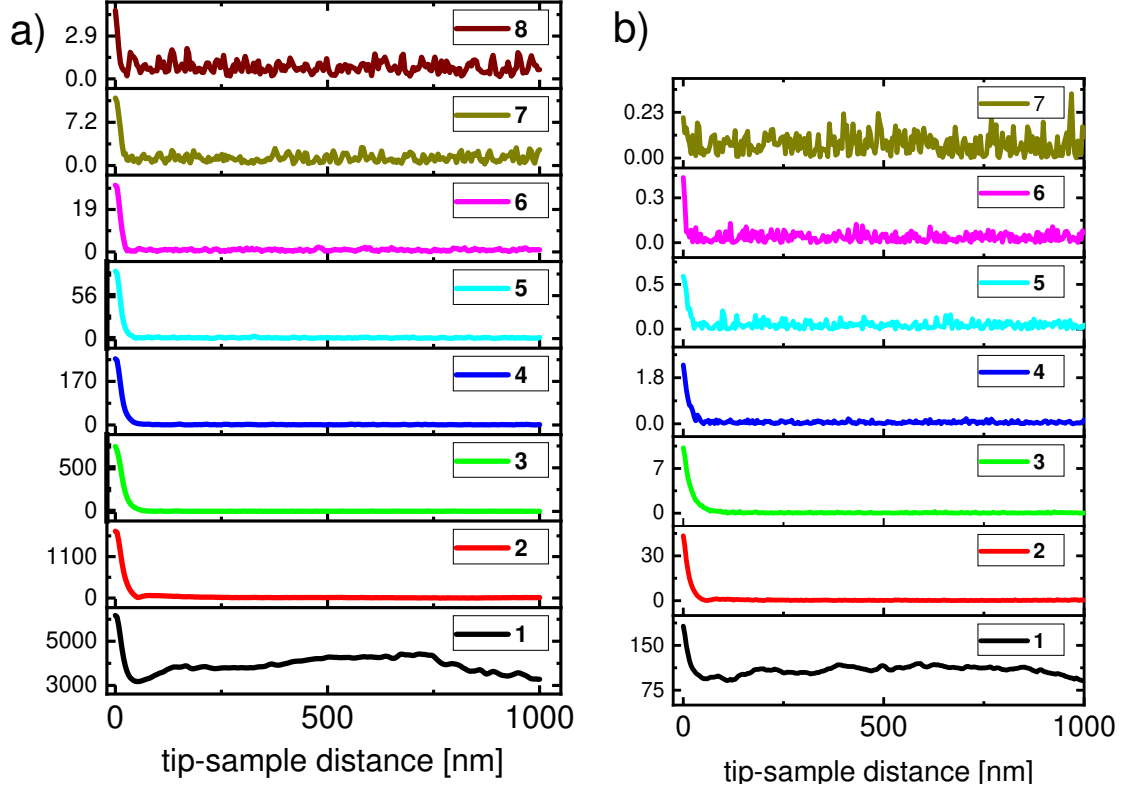
Figure 3.4: a) Homodyne and b) pseudo-heterodyne qPlus sensor s-SNOM approach curves (both [a.u.]) measured at λ=10.5 μm on a Au surface; LIA t_c=50 ms (homodyne), $t_{c,fast}$=100 μs and $t_{c,slow}$=20 ms (pseudo-heterodyne).
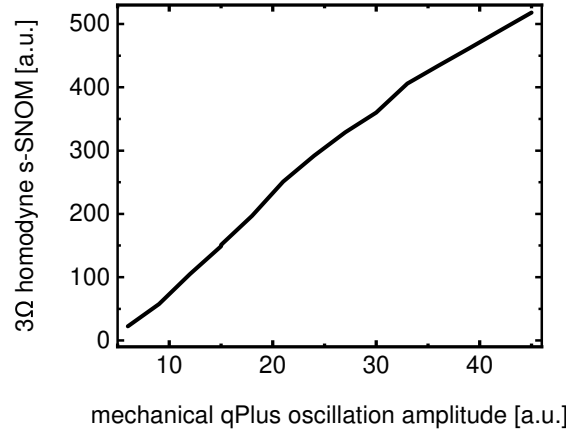

Figure 3.5: The 3Ω homodyne s-SNOM signal depends strongly on the mechanical oscillation amplitude of the qPlus sensor. At high values, the qPlus sensor is already mechanically unstable.

3.2.2 Scanning tip design in s-SNOM

The TRIBUS is based on a "scanning tip" concept, i.e. the qPlus sensor scans the sample that is stationary in the laboratory system. To prevent a complete redesign of the TRIBUS head or a complicated parallel steering of the incident laser light, this subsection analyses the consequences of the moving tip in this setup.

The basic idea is that the spot size of the focus (e.g. 220 μm [5]) is much bigger than the scan area of $\sim$20x20 μm^2 (at room temperature), i.e. the entire s-SNOM scan range is superimposed by a flat Gaussian beam shape. On the other side, the phase effects need more attention. As the tip moves with respect to the incident light, its optical phase is changing. That means that the phase difference between the two interferometer arms (corresponding to ϕ_r, e.g. in eq. (1.37) and eq. (1.38)) is not constant, but a function of the tip coordinates. In fig. 3.6, the tip is scanned closely above the sample (but without contact), the two pseudo-heterodyne sidebands of the first harmonic $1\Omega + 1M$ and $1\Omega + 2M$ (from the tip oscillation without any near-field contribution) are recorded, and the amplitude and phase are calculated (details see appendix 6.1.4).

As expected, the optical amplitude fig. 3.6 c) is nearly constant over the entire range (with a slight curved surface), whereas the phase fig. 3.6 d) strongly depends on the location (the phase jumps are due to the wrapped $\pm\pi$ phase interval). To verify this, a 3Ω s-SNOM line profile is measured in fig. 3.7 [6]. It corresponds to fig. 3.6 e) and reveals an almost constant near-field amplitude and a shifting optical near-field phase. Indeed, those results are independent of the chosen detection mode and valid in general.

In conclusion, the scanning tip design affects the measurements strongly. However, by carefully considering these effects and a suitable data post-processing and/or by scanning only very small areas, it is possible to cope with those issues.

3.2.3 Spring mounted platform

The optical concept to compensate any movements from the spring mounted platform is already depicted and explained in section 2.5. However, here it should be pointed out that even without the compensation near-field measurements could be possible. Equivalent to the discussion in subsection 3.1.4, an instability in the interferometer mainly affects the optical phase and not the near-field amplitude. So, reliable s-SNOM amplitude measurements could be possible even without any compensation (at least for pseudo-heterodyne and heterodyne; the requirement of two measurements in the homodyne scheme is very disadvantageous in this situation). Indeed, in this case the LIA time constant t_c is a crucial parameter.

---

[5]Based on eq. (1.13), f=33 mm, d=2 mm, λ=10.5 μm.

[6]A big area scan like fig. 3.6 is impractical due to the slow scan speed of the qPlus sensor.
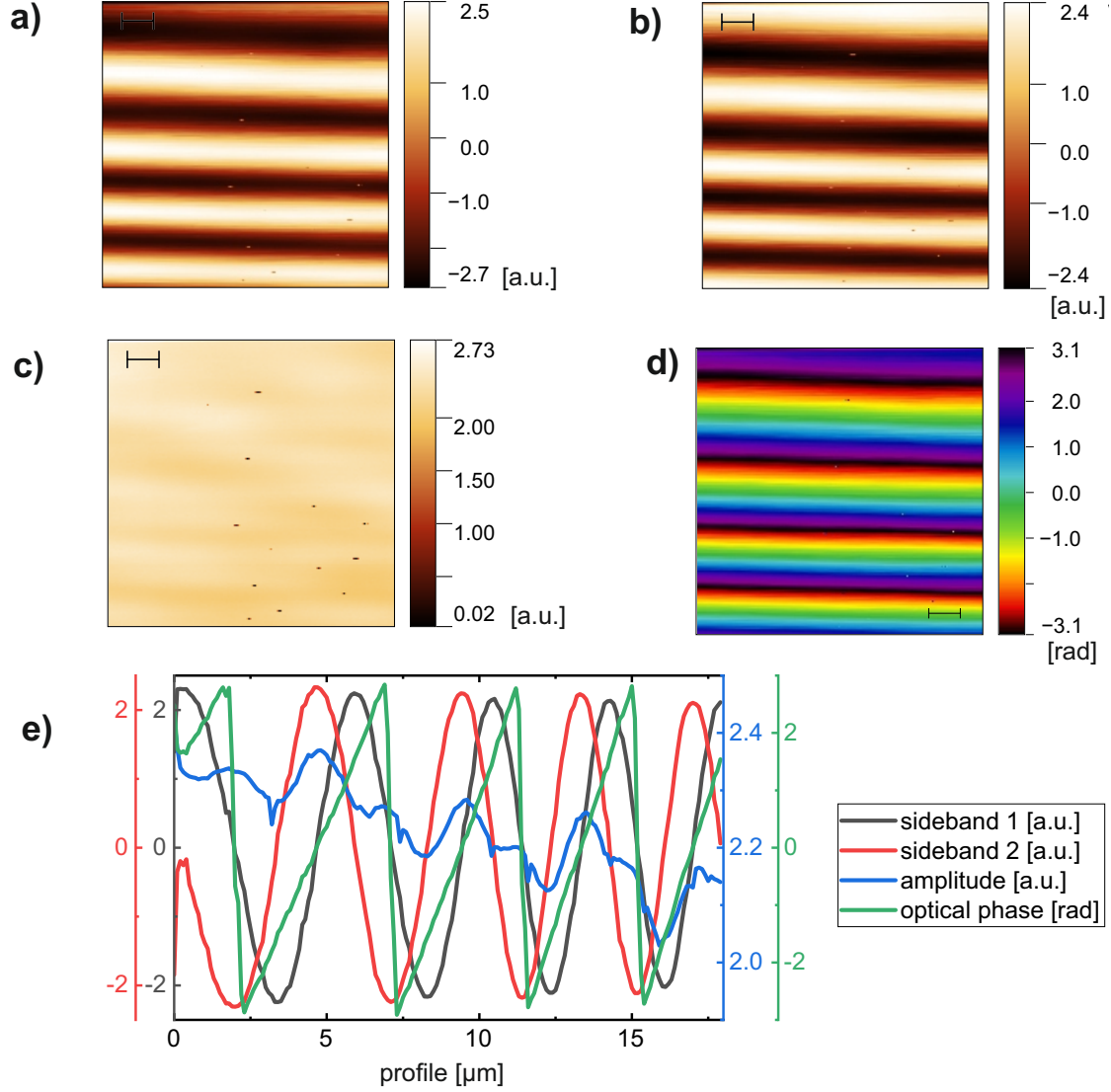
Figure 3.6: a) $1\Omega + 1M$ and b) $1\Omega + 2M$ pseudo-heterodyne sidebands scanned close above the sample surface. The resulting c) amplitude and d) optical phase are calculated. e) Averaged vertical line profiles of the four quantities reveal the phase dependence on the xy coordinates; scale bars 2 μm, entire range: 18x18 μm².
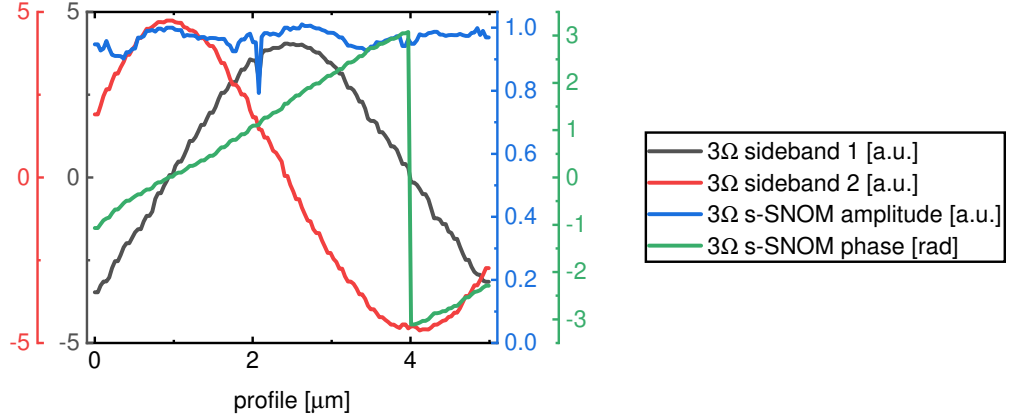
Figure 3.7: A pseudo-heterodyne 3Ω line scan (tip moving parallel to the incident laser light direction) on a Au surface reveals the same behaviour as fig. 3.6 e): The sidebands are oscillating, but the s-SNOM amplitude stays constant and the phase is shifting.

3.2.4 Two-dimensional scan and material contrast

Besides the existence of higher harmonics and the recording of approach curves in fig. 3.4, the third and of course most important test is a material contrast in a two-dimensional sample scan. In fig. 3.8 a surface contamination (probably photo resist) on a Au layer is scanned revealing a clear contrast in the near-field response (and the expected tilted near-field phase that could be aligned numerically). Already with this simple sample the qPlus sensor resolution can be estimated to be ~10 nm.

In the scope of the ongoing project, a suitable sample should be prepared to specify the resolution more reliably. A sharp, but topographically flat, material transition is desirable (e.g. similar to ref. [143], where a flat metal-dielectric transition of a hard disk drive is used): This avoids edge-effects [24, 167] (e.g. interaction from the tip's side surface with the edge feature, shadowing effects, ...) as well as topographically induced artefacts (e.g. if the tip scans small spikes or dips, the near-field interaction volume can change and influence the measured signal).
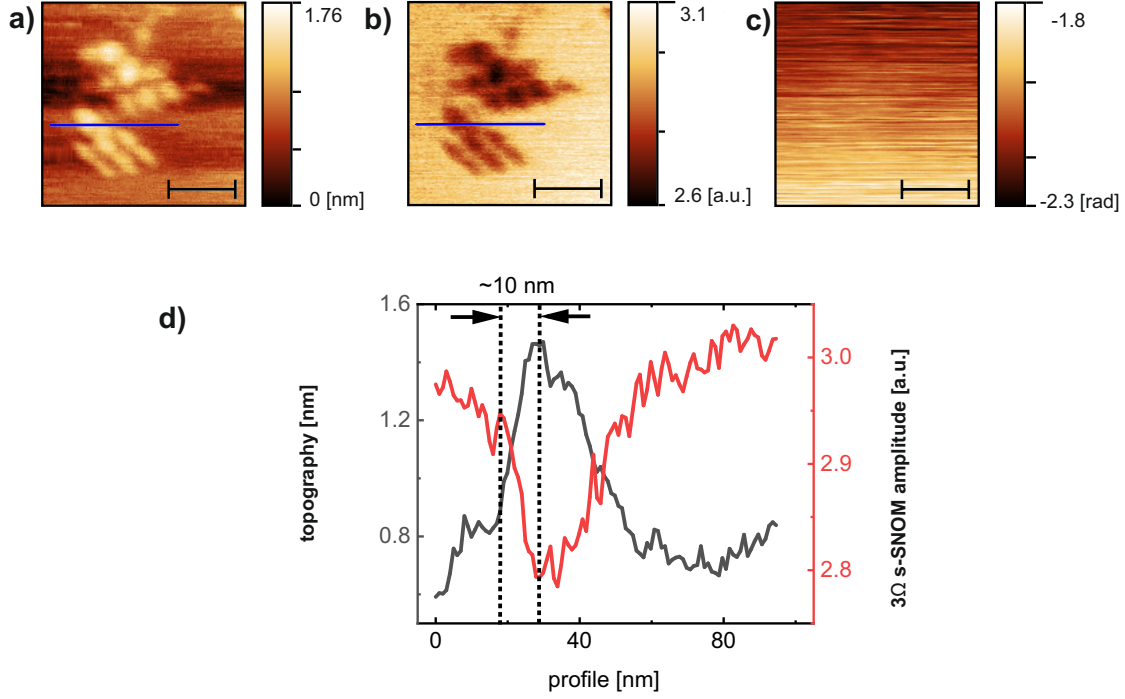
Figure 3.8: a) Topography b) 3Ω s-SNOM amplitude and c) 3Ω s-SNOM phase of a surface contamination on a Au sample (pseudo-heterodyne, $\lambda \sim 9.3$ μm, lock-ins $t_{c,fast}$=100 μs and $t_{c,slow}$=50 ms). The phase image shows clearly the tilted background described in fig. 3.7. Profiles along the fast scan direction (left to right) from the topography and s-SNOM signal (blue lines in a) and b)) are depicted in d) revealing a resolution in the order of $\sim$10 nm; black scale bars 50 nm.

3.3 THz s-SNOM performance and characterization

3.3.1 Frequency choice

One advantage of electronic THz sources is that they are easily tunable over a broad bandwidth. However, for s-SNOM applications the frequency cannot be chosen completely arbitrarily. The resulting s-SNOM signal strength is influenced by the emitter spectrum, the detector spectrum, and the Fabry-Pérot-resonances within the beam splitter used for the homodyne detection scheme.

The emitted spectrum of the two sources is measured by means of the Thomas Keating Absolute Power/Energy Meter System. Its signal-to-noise ratio is very low and depends strongly on the exact alignment and geometry of the optical chopper. However, its output voltage can be calibrated to an absolute power scale, which makes it a powerful tool for THz science. Representative spectra of the two sources are shown in fig 3.9.
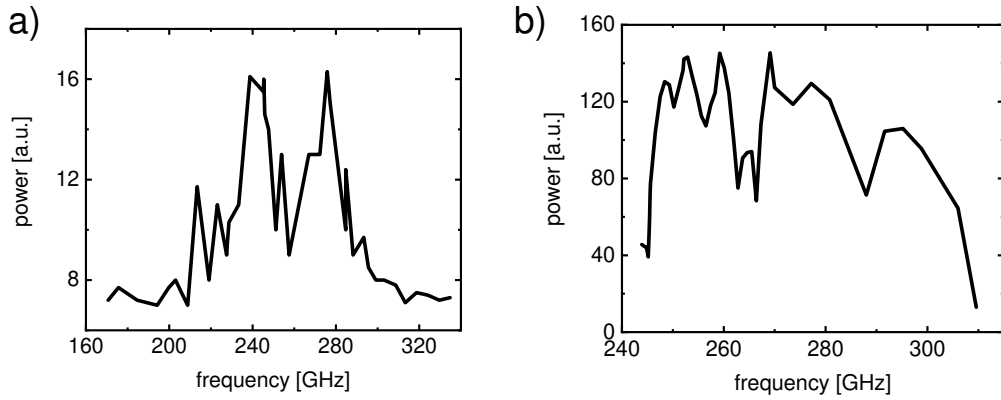
Figure 3.9: Power spectrum of the two electronic THz sources used: a) RPG electronic source and b) Virginia Diodes (uncalibrated detector signals from the Thomas Keating Power/Energy Meter System).

The sensitivity curves and signal-to-noise ratios of the TeraFET detectors used in the scope of this thesis are plotted in fig. 3.10[7]. A responsivity up to 408 V/W (378 V/W) and a noise-equivalent power (NEP) value down to 21 pW/Hz$^{1/2}$ (27 pW/Hz$^{1/2}$) have been measured for the 90 nm (180 nm) device.

The Fabry-Pérot interferences of the beam splitter affect the reflectivity and transmission as a function of the wavelength. Fig. 3.11 shows the interference

---

[7]Those measurements and their analysis were prepared by A. Lisauskas and A. V. Chernyadiev.
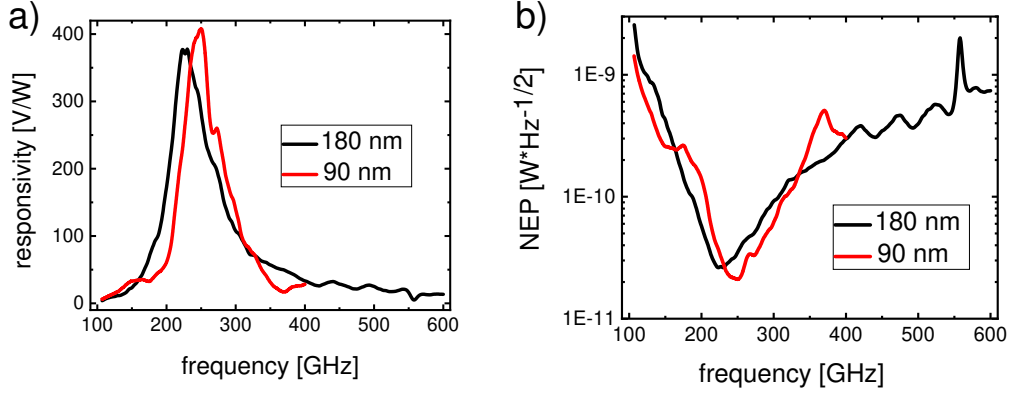
Figure 3.10: a) Voltage responsivity [V/W] and b) noise-equivalent power (NEP) [W·Hz$^{-1/2}$] of the two detectors used. Figure adapted from [4].

pattern of the beam splitter used at incident angles of 0° and 45° measured by means of a photomixer based CW terahertz system from Toptica Photonics AG.
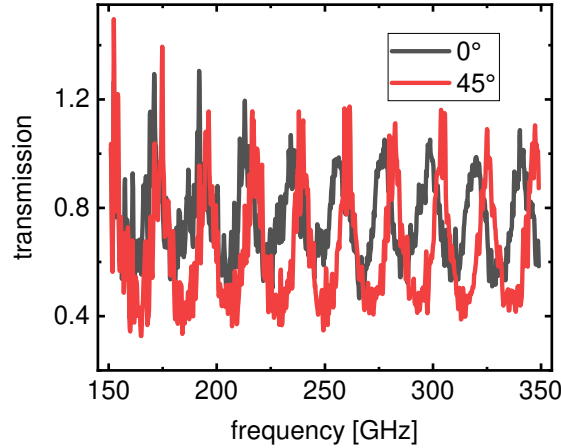
Figure 3.11: The transmission of the beam splitter used is measured at two different angles 0° and 45° over a broad spectrum and reveals Fabry-Pérot resonances.

Using the Fabry-Pérot interferometer formula eq. (3.4) [27] (n=3.41), the thickness of the beam splitter can be extracted L=2069 μm.

$$\Delta f = \frac{c_0}{2nL} \tag{3.4}$$

Apart from those aspects, the interferometer alignment, the beam collimation and shape, the dispersion of lenses and other optical components, the mechanical oscillation amplitude, and the cantilever antenna resonances itself [43] determine the overall performance and signal quality of the THz s-SNOM. Hence, there is

91

no general "optimum" frequency, which can be found with a simple frequency sweep, but rather the setup is iteratively optimized from time to time to reach the best signal-to-noise and signal level. In all the applications presented here, a high signal-to-noise ratio is more important than having a specific frequency.

3.3.2 THz approach curves and signal-to-noise level

As the first performance test in fig. 3.12, approach curves on a Au surface with the two different detectors are recorded (using the RPG source, Rocky Mountain Nanotechnology tip model RMN-25Pt300B, tip length $\sim$80 µm, s-SNOM frequency 246.5 GHz, MFLI LIA t_c =100 ms) in the homodyne setup (single measurements and the reference phase is set to the maximum signal position). The 180 nm (90 nm) device records up to the 7th (10th) harmonic. The signal strengths between the individual harmonics can be compared directly to each other. The 90 nm detector is equipped with an additional amplification step, raising its signal level into the µV regime (instead of nV for the 180 nm device). The dotted lines at 100 nm serve as a guide to the eye.

Again, the fundamental properties of s-SNOM approach curves are visible: With increasing higher harmonics the signal gets weaker and more noisy, but indeed it is more confined to the sample surface. The signal quality is quite impressive. Representative signal-to-noise ratios (SNR) are presented in table 3.2 (same settings and devices as mentioned above for fig. 3.12). "1Ω (free)" corresponds to the reflected/scattered background signal from the tip close, both not approached to the Au sample (distance of few microns by simply retracting the z-piezo elements). This signal is very helpful for the THz beam alignment since it is not superimposed by the near-field noise and from the distance control feedback mechanism. The signal-to-noise ratios are calculated as mean values divided by the standard deviations. Both detectors are compared at a time constant of t_c=1 s. In addition, values for the 90 nm device are taken at t_c=100 ms, which is a proper value for measurements and which can be compared to literature values of other detector technologies.

The comparison between different setups and literature values is in general difficult, as even for the same setup the signal level can vary a lot. Refs. [25, 78] show that a broader tip apex can enhance the signal enormously (due to a higher interaction volume); a controlled "crash" of the tip is nowadays a common option during THz s-SNOM optimization. Nonetheless, the aforementioned values and reviewing the literature give a rough estimate and show that the TeraFETs are at least comparable to other schemes and especially at higher harmonics they show a convincing and better performance.

The SNRs for Schottky diode based THz s-SNOMs have been specified to >10 (2Ω) [141] and to 14 (2Ω), 7 (3Ω) [64] (both on Au/highly doped Si, t_c=100 ms).
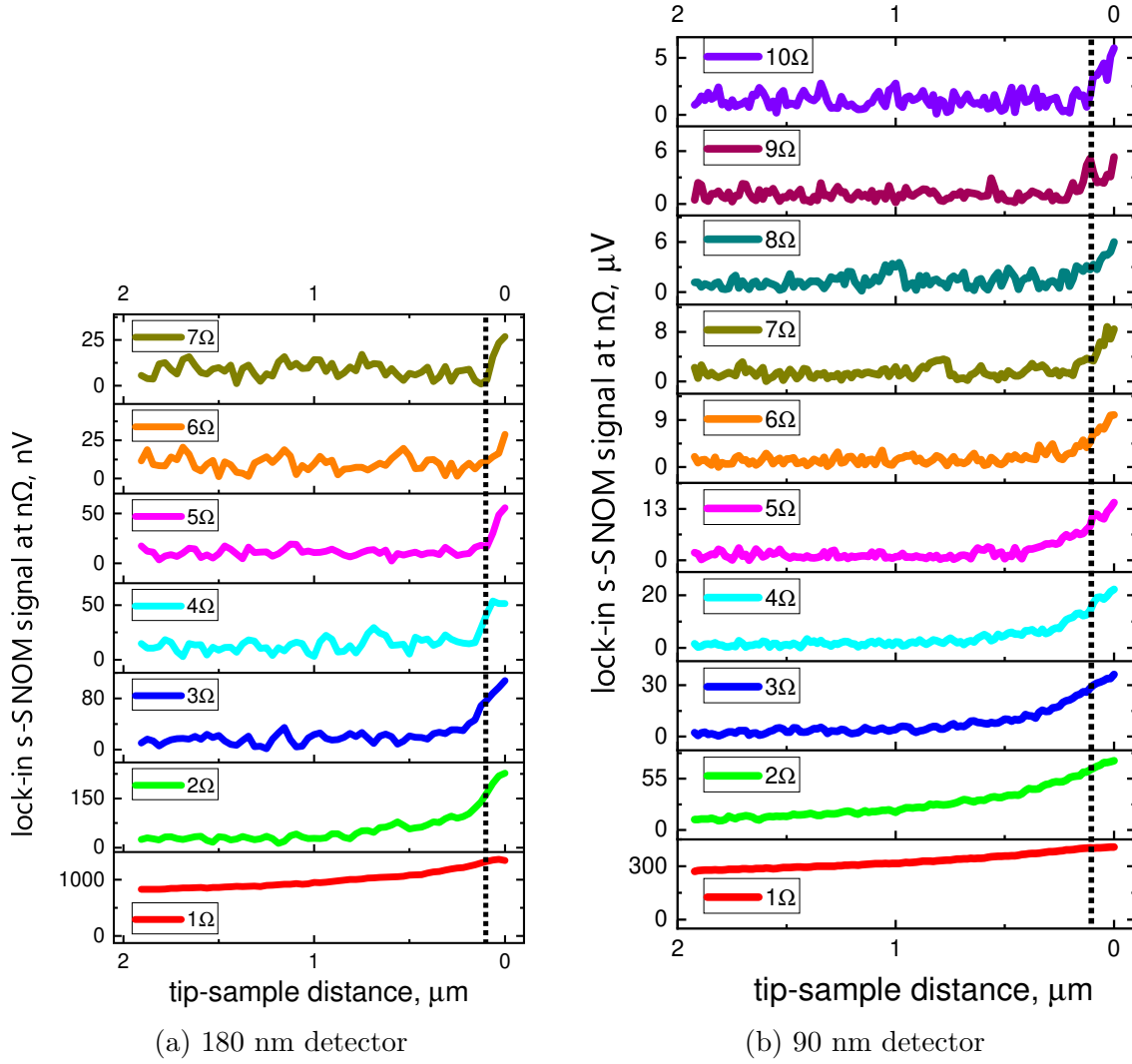
(a) 180 nm detector   (b) 90 nm detector

Figure 3.12: THz (RPG source) approach curves on a Au sample for the two different detector designs. The dotted lines at 100 nm facilitate the comparison of the different harmonics. Reproduced from Ref. [4] with permission from the Royal Society of Chemistry.

SNR	1Ω (free)	1Ω (s-SNOM)	2Ω (s-SNOM)	3Ω (s-SNOM)	4Ω (s-SNOM)
180-nm (1 s)	53	108	39	10	12
90-nm (1 s)	388	387	49	49	39
90-nm (100 ms)	58	78	18	10	8

5Ω (s-SNOM)	6Ω (s-SNOM)	7Ω (s-SNOM)	8Ω (s-SNOM)	9Ω (s-SNOM)	10Ω (s-SNOM)
-	-	-	-	-	-
27	15	12	8	8	5
4.6	4.0	2.9	2.1	1.7	1.4

Table 3.2: Representative SNR THz s-SNOM values reached with the two detectors in 90 nm and 180 nm technology (for t_c=1 s; additional 100 ms values for the 90 nm device) for the s-SNOM higher harmonics $n\Omega$ measured on a Au surface (RPG source). [4]

Also, TDS THz s-SNOM systems report similar benchmarks, i.e. SNR >20 and >14 (on graphene, again t_c=100 ms, both 2Ω) [29, 168].

As already shortly discussed in subsection 2.3.1, it is difficult to compare the performance of TeraFET and other detectors by comparing the published benchmark numbers (SNR and NEP) since different definitions can be used. The s-SNOM SNR numbers presented here contain again a lot of experimental uncertainties. However, they are more independent of definitions than the pure detector benchmarks, and at the end they are the most important parameters for evaluating the s-SNOM performance in experimental applications.

3.3.3 Material contrast and estimated resolution

To assess an s-SNOM device, in addition to the aforementioned higher harmonics and approach curves, a scan containing a signal contrast between different materials is the third essential test and proof of near-field probing. Two representative measurements are depicted in fig. 3.13 and fig. 3.14. Fig. 3.13 is a one-dimensional profile scan across a Si-Au edge (Si left, Au right). The black curve in the lowest graph corresponds to the parallelly recorded topography and reveals the position of the Au step at $x \approx 5$ µm (indicated by the dotted line). This measurement is taken with the 180 nm detector and the RPG source at 246.5 GHz (MFLI LIA, t_c=61.15 ms, 10 scans averaged). Again, the basic properties of the near-fields are clearly revealed, the decreasing signal level and increasing field confinement (steeper edge) with increasing higher harmonics.

Fig. 3.14 displays a two-dimensional scan of the Au-Si edge (Au left, Si right)
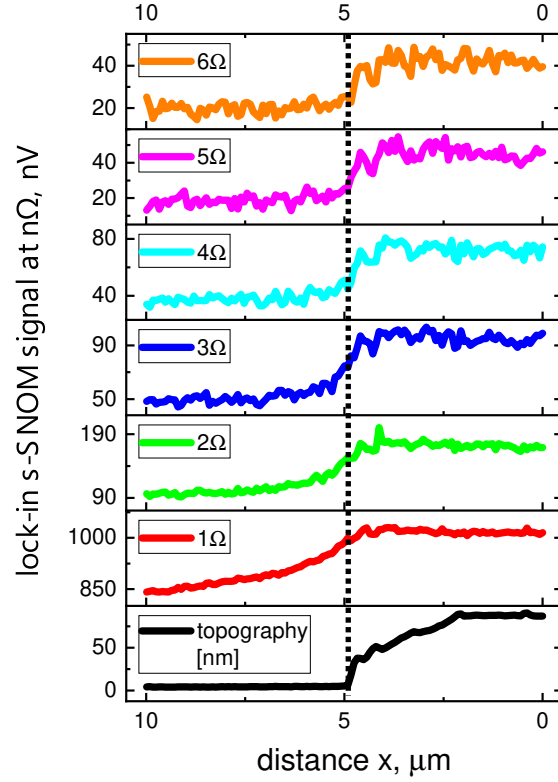
Figure 3.13: One-dimensional homodyne s-SNOM scans (10 measurements averaged) across a Si (left) to Au (right) step at several higher harmonics measured at 246.5 GHz with the 180 nm detector. Reproduced from Ref. [4] with permission from the Royal Society of Chemistry.

95
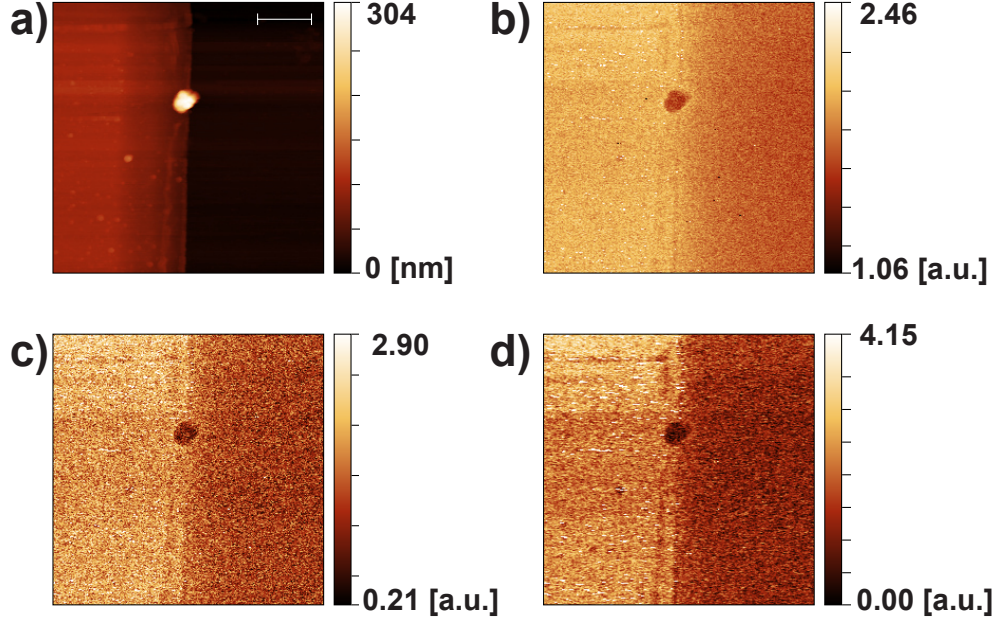
Figure 3.14: Two-dimensional s-SNOM area scan of the already mentioned Au (left) to Si (right) edge, containing a surface contamination sticking to the edge. a) Topography (scale bar 2 μm) b)-d) 1Ω-3Ω homodyne s-SNOM measurements (single scans; interferometer in maximal signal position) at 246.5 GHz using the 180 nm detector. Reproduced from Ref. [4] with permission from the Royal Society of Chemistry.

with an additional dirt particle sticking on the edge.

To limit the overall measurement time, here an integration time of only 20 ms is used (3Ω with the MFLI, 1Ω+2Ω in parallel with a DSP 7265 LIA; again f=246.5 GHz RPG-source, 180 nm detector), which still takes ∼1.5 h. Again, the different materials Au, Si, and the dielectric dirt particle are clearly distinguishable from each other. Surprisingly, even the background contaminated 1Ω measurement shows a convincing imaging quality with relatively sharp edges and contrasts.

A first estimation[8] of the deep subwavelength resolution is given in fig. 3.15, where a dielectric particle (probably remaining from the photoresist) on the Si surface is scanned. A sub 100 nm resolution in the order of the tip apex geometry can be extracted by the red line profiles (f=246.5 GHz, MFLI LIA t_c=61.15 ms, 180 nm detector, RPG-source; profiles in fig. 3.15 c) averaged).

---

[8]For a more accurate determination, see the discussion about suitable samples in subsection 3.2.4.

Figure 3.15: a) Topography and b) 2Ω homodyne s-SNOM signal (again interferometer in maximal signal position) of surface contaminations on a Si surface (scale bars 1 μm) c) Line profiles along the red lines marked in a) and b) reveal a sub 100 nm resolution in both directions along the fast (horizontal) and slow (vertical) scan direction of the AFM. Reproduced from Ref. [4] with permission from the Royal Society of Chemistry.

4. Measurements and Analysis of Transport Phenomena
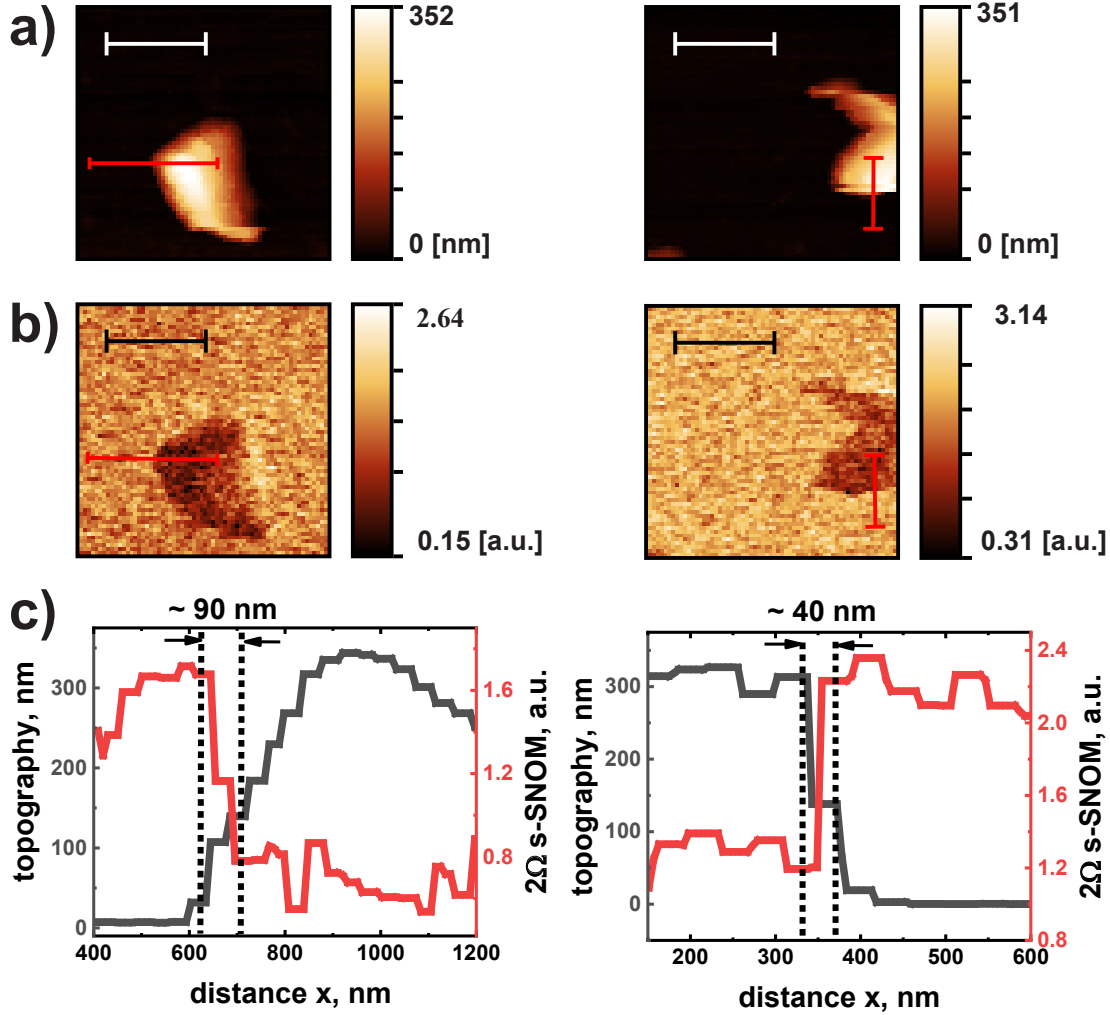
In this chapter, the two main topics of this thesis together with the corresponding analysis are depicted. Silver nanowires and their plasmonics are analysed in the near-infrared in section 4.1, and the THz s-SNOM is applied for charge carrier density investigations on silicon samples in section 4.2.

4.1 Polaritons on Silver Nanowires

4.1.1 Motivation and background

THz photomixing is a promising technology for reaching a continuous wave, tunable, compact, and relatively simple THz source [169, 170]. It is based on two-wave mixing: The output from two close and tunable near-infrared lasers is focused on a photoactive medium. A beating between those laser frequencies occurs eq. (4.1) that can be tuned into the desired THz range. Charge carriers are now generated following the intensity envelope, i.e. the THz frequency $\Delta\omega = \omega_1 - \omega_2$. An applied DC voltage accelerates the free carriers, which emit the THz radiation (the squared terms $sin^2(\omega_1 t)$, $sin^2(\omega_2 t)$ as well as the sum term $(\omega_1 + \omega_2)t$ are far too fast for the photoactive medium).

$$
\begin{aligned}
I(t) &= \left[E_1 sin(\omega_1 t) + E_2 sin(\omega_2 t + \phi) \right]^2 \\
&\overset{eq.(6.2)}{=} E_1^2 sin^2(\omega_1 t) + E_2^2 sin^2(\omega_2 t + \phi) \\
&\quad + E_1 E_2 \left(cos((\omega_1 - \omega_2)t - \phi) - cos((\omega_1 + \omega_2)t + \phi) \right) \\
&\overset{photoactive\ medium}{\approx} E_1 E_2 cos((\omega_1 - \omega_2)t - \phi)
\end{aligned}
\tag{4.1}
$$

There are several things to optimize and design for such devices: First, the substrate as the photoactive medium plays a crucial role. It has to be fast enough

99

to trap the free carriers between two oscillations of the desired frequency; therefore e.g. low-temperature grown (LTG) GaAs is a favourable solution offering a carrier lifetime (due to trapping and/or recombination) down to $\tau_{lt} \approx 150$ fs [170]. The lifetime τ_{lt} is essential and determines the THz output power P_ω at the angular frequency $\omega = 2\pi f$ according to eq. (4.2) (from eq. (4) in [170]).

$$P_\omega \propto \frac{1}{1 + \omega^2 \tau_{lt}^2} \tag{4.2}$$

Another aspect is the design of the substrate and the electronic contacts since on one hand they have to be close to the interaction zone, on the other hand they should not cover or block the exciting light. Furthermore, the excited THz signal has to be coupled into radiation by means of a suitable and optimized antenna.

A recent development uses silver nanowires (Ag NWs) as elementary contacts in THz photomixers resulting in an enhanced THz emission due to a small covered area of the photoactive medium and a reduced capacitance resulting in a better antenna performance [171]. However, the question arises if plasmonic effects occur and what is their role. Therefore, near-field measurements should shine light on those questions.

4.1.2   Measurements

Fig. 4.1 shows some microscope pictures of Ag NWs used for THz photomixers. On LTG GaAs substrates (thickness 1 μm on undoped 350 μm GaAs substrate, Wafer Technology Ltd.), Au antenna structures are fabricated; the Ag NWs (from ACS Materials) are deposited initially in solution randomly on the substrate. Fortunately, due to their high light scattering, they are visible even under a classical light microscope. When they are still in solution, they can be placed and positioned manually under the microscope (indeed, some experience and patience is required). The samples used here are prepared and provided by Prof. Dr.-Ing. Shihab Al-Daffaie (formerly, Institut für Mikrowellentechnnik und Photonik, TU Darmstadt).

For the photomixing operation, the NW has to be in contact with the Au antenna, however for the near-field investigations free NW are selected to avoid disturbing effects (contact point to the antenna, edge effects of the Au layer [167]).

Two different s-SNOM measurement geometries have been performed fig. 4.2 (on the NW marked in fig. 4.1 c)), varying the incident laser beam direction (parallel and perpendicular to the NW) and the incident polarization (s-polarization means electric field vector parallel to the sample plane, p-polarization means perpendicular to this with the main electric field component parallel to the tip, see
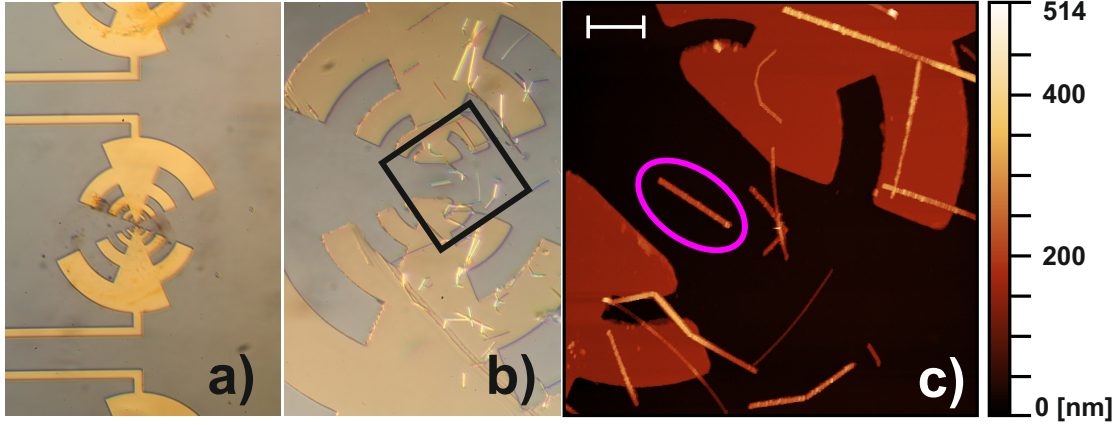
Figure 4.1: a) Microscope view of a log-periodic Au antenna on LTG GaAs substrate connected to electrical pads for applying a voltage b) Several Ag NWs are randomly distributed in the central region of such an antenna c) AFM image of black square of b); the yellow marked NW is used for further measurements; white scale bar 5 µm.

as well fig. 4.4 a) and b))[1]. The measurement setup is already described in section 2.4, as probes platinum coated cantilever from Nanoworld (Arrow, NCPt, $f \approx 285$ kHz) are used. A laser power between ~5.5 mW (p-polarization) and ~7.5 mW (s-polarization) reaches the parabolic mirror (for λ=853 nm). The incident polarization is adjusted with a $\lambda/2$ waveplate (see fig. 2.15), the reference polarization is set for all measurements to "parallel" (electric field parallel to the probe tip). The LIA time constants (tandem-demodulation for pseudo-heterodyne detection) are set to t_c=100 µs for the first fast demodulation and t_c=20/50/100 ms for the sideband detection of fig. 4.2 left column/fig. 4.2 right column/fig. 4.3 right column.

The p-polarization data from 4.2 provides already a satisfying quality (cut-out fig. 4.3 left column), the s-polarization measurement is repeated with a higher resolution and higher time constant in fig. 4.3 right column.

For further analysis, the Ag NWs are considered as mainly one-dimensional objects, and profiles along the NW axis of those data are taken as the main object of interest fig. 4.4: They look completely different and asymmetric indicating a non-trivial image formation in the s-SNOM that should be analysed and investigated in the following subsection 4.1.3. The observed double "ghost" image in the topography in fig. 4.2 and fig. 4.3 (right column) is only an artefact of a damaged AFM-tip (it is the same NW as for the p-polarization measurements in the

---

[1]For different incident directions, the sample on its stage is rotated by hand; hence the angles can be adjusted only roughly.
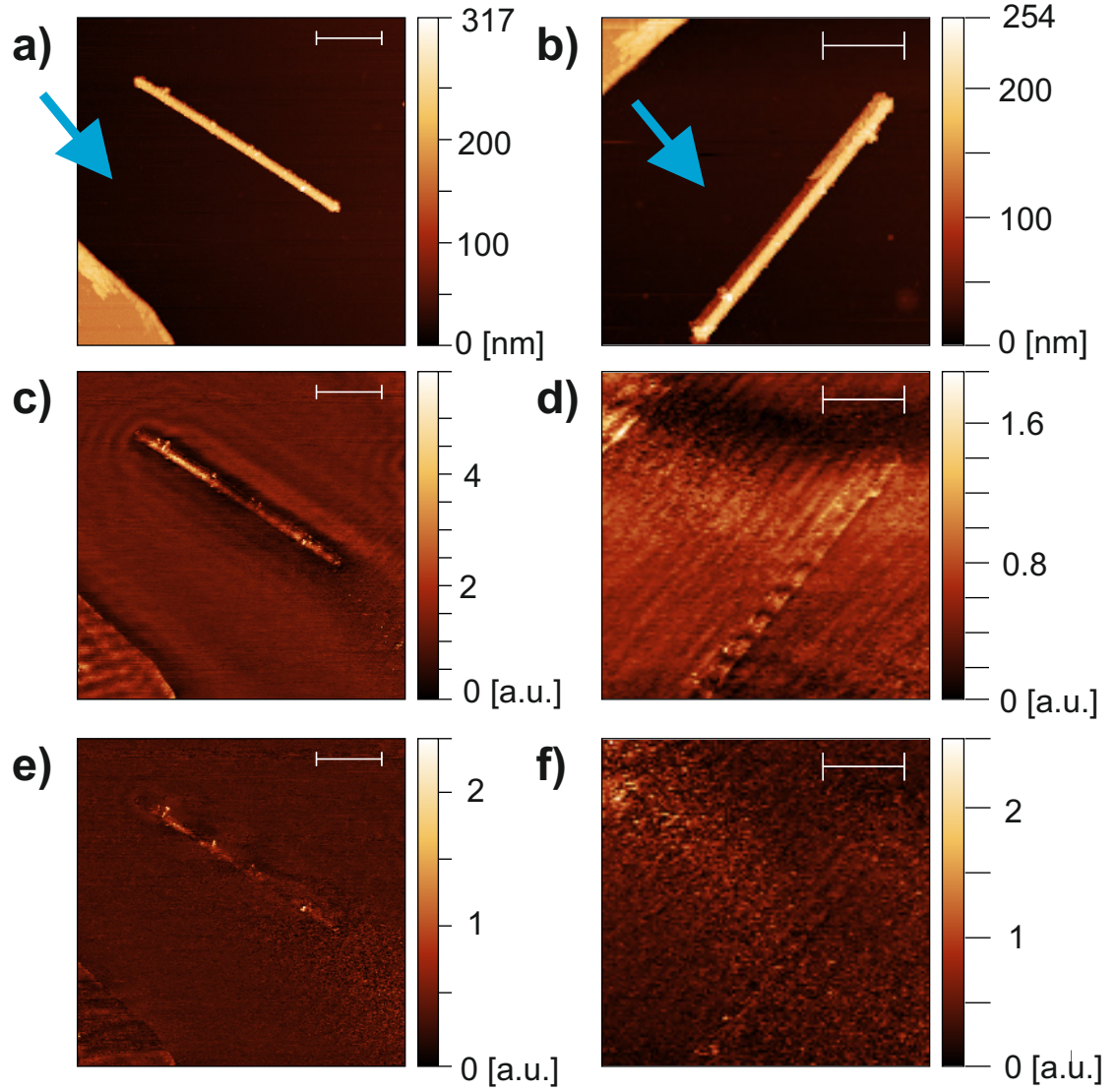
Figure 4.2: p-polarization (left column) and s-polarization (right column) overview data: a)+b) Topography (the blue arrows indicate the incident s-SNOM laser light direction) c)+d) 2Ω s-sSNOM e)+f) 3Ω s-sSNOM; all scale bars 2 μm.
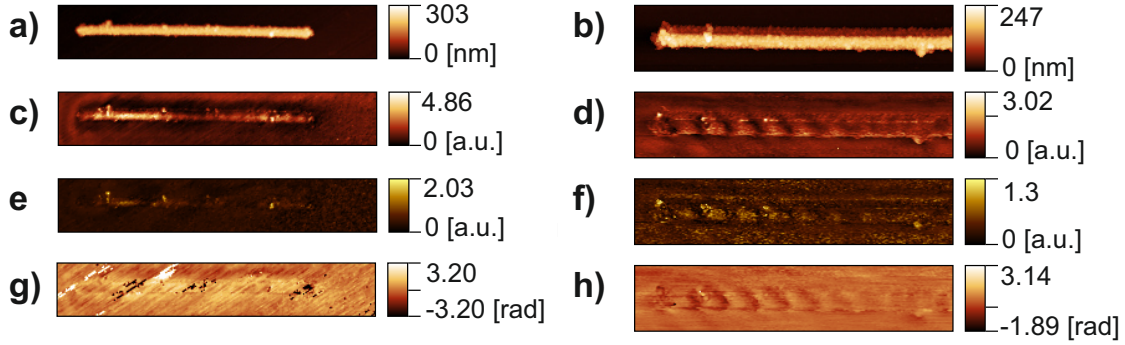
Figure 4.3: Cut-out of fig. 4.2 p-polarization measurements (left column) and new high-resolution s-polarization measurements (right column) a)+b) Topography c)+d) 2Ω s-sSNOM e)+f) 3Ω s-SNOM g)+h) Optical near-field phase from 2Ω measurements.

left columns). However, easy geometrical considerations indicate that the tilted pattern cannot origin from the damaged tip. Since this measurement offers the highest signal-to-noise ratio and only profiles are analysed quantitatively, its usage for further analysis is justified.

4.1.3 Analysis and interference model

The big variation in the visible wavelengths can be explained by an interference model depicted in fig. 4.5 and based on the standing wave formation explained in subsection 1.4.2. For the p-polarization fig. 4.5 a), the wavefront excites SPPs on the left nanowire end at y_1, which are propagating towards the other end. At the cantilever's position, the SPPs are coupled out to far-field radiation interfering with a second electromagnetic wave contribution originating from the dielectric near-field response of the Ag. The decisive quantity is the phase difference between those two contributions as a function of y eq. (4.3) (adapted from eq. (1.50)). According to eq. (1.51), the resulting wavelength fulfils eq. (4.4), and it is clear that the SPP wavelength is shifted towards the revealed long wavelength Λ in the µm range.

$$\Delta\Phi = k_{sw} \cdot y - k_0 \cdot cos\Theta \cdot y \tag{4.3}$$

$$\Lambda = \frac{2\pi}{k_{sw} - k_0 cos\Theta} = \frac{\lambda}{n - cos\Theta} \tag{4.4}$$

The s-polarization is more difficult to understand. The growing wave amplitude on the first microns resembles a beating pattern. Together with the tilted wavefront

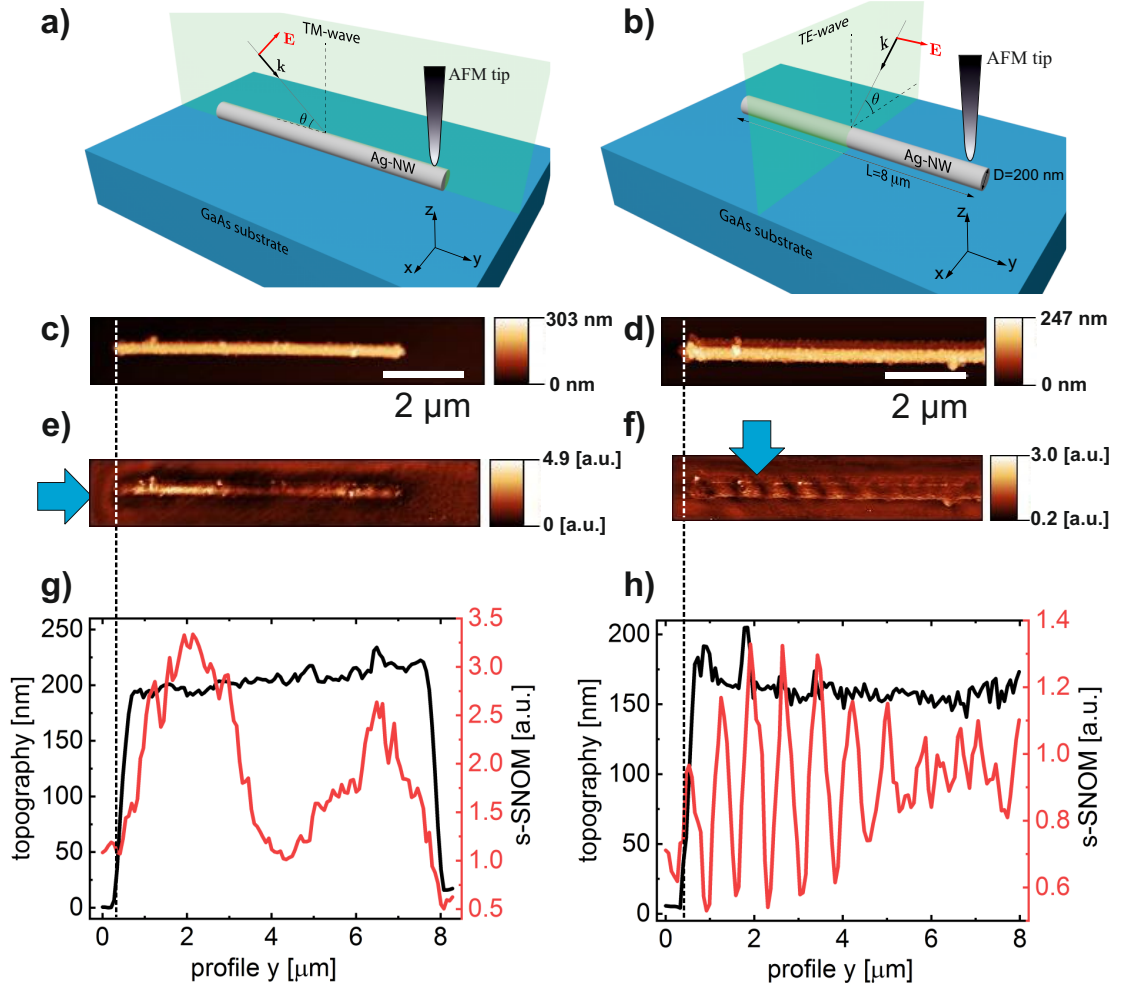Figure 4.4: p-polarization (left column) and s-polarization (right column) data: a)+b) Geometrical orientation of the fields in the different polarizations c)+d) topography of the NW e)+f) parallelly recorded 2Ω s-SNOM images with incident directions indicated by the blue arrows g)+f) Profiles of topography and s-SNOM along the NW axis. Figure taken from [2]. Copyright 2019 American Chemical Society.
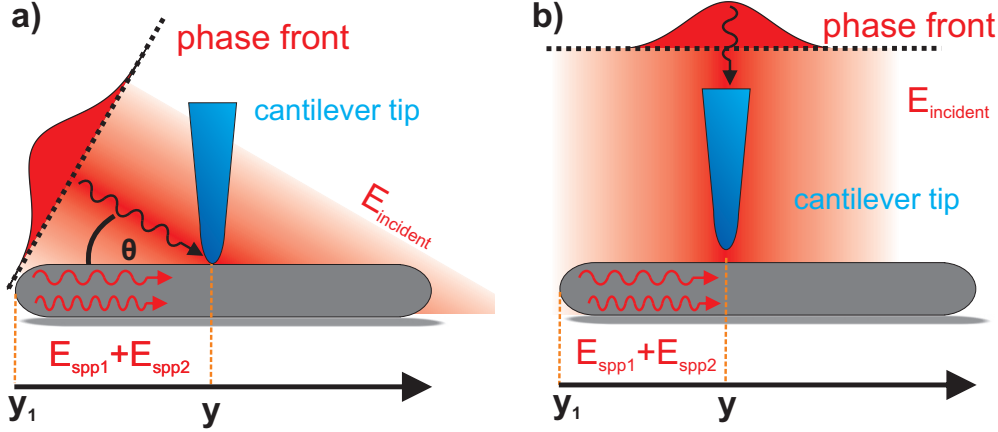
Figure 4.5: Schematic sketch of the interference model for a) p-polarization and b) s-polarization excitation. Figure taken from [2]. Copyright 2019 American Chemical Society.

that is already explained in the literature [112] as the overlap of different modes fig. 1.23, here a model of two parallelly launched modes is applied. Those modes are mapped directly since k_0 and k_{sw} are perpendicular eq. (1.53), i.e. the incident phase is constant on the entire nanowire.

In fig. 4.6 numerical mode calculations using COMSOL Multiphysics support these assumptions. All simulations assume a 200 nm diameter Ag nanowire on GaAs substrate (parameters from [172, 173]). Fig. 4.6 a) is obtained by the frequency domain module and reveals a tilted electric field shape (similar to the measurements) on a 4 µm long wire for s-polarized incident light (λ=853 nm). The mode analysis module simulates an infinitely long NW and can reveal several modes fig. 4.6 b). A portion of them is close to the light line and mainly in the NW-air interface, whereas the others are confined between the Ag NW and the substrate (those modes are converging to the substrate light line). The latter ones are not accessible via the s-SNOM (it probes mainly the surface), therefore only the two dominant and leaky modes close to the light line on the left branch are used for further analysis with λ_1=852 nm and λ_2=859 nm (k_z=1.001k_0 and k_z=0.993k_0, respectively).[2]

However, several aspects of the model fig. 4.5 need further consideration. One main question is, why the excitation is only from one side of the nanowire, e.g. for the p-polarization an excitation from the other side would result in a much shorter

---

[2]Those simulations are planned and performed by Dr. Andrey Bogdanov (Department of Nanophotonics and Metamaterials, ITMO University, St. Petersburg) in the scope of the joint publication [2].
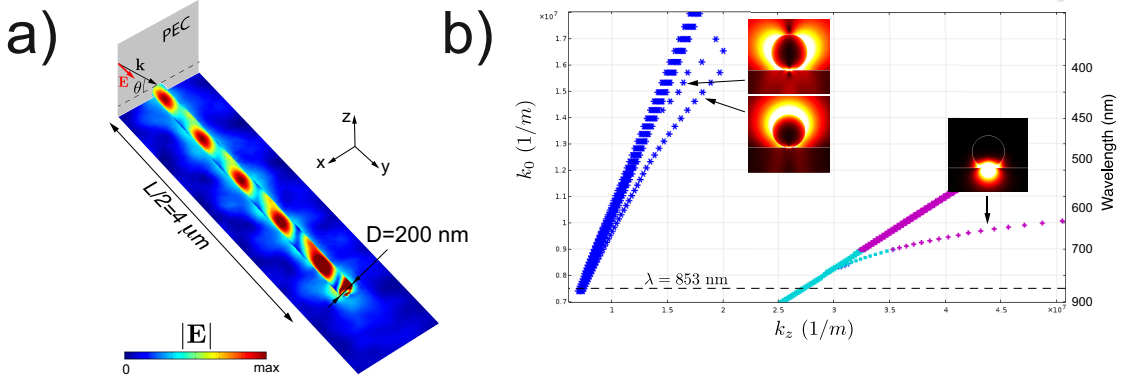
Figure 4.6: Numerical COMSOL simulations reveal a) a tilted wavepattern on the NW-substrate system and b) different modes excitable in this system. Figure taken from [2]. Copyright 2019 American Chemical Society.

Figure 4.7: Depending on the orientation, the excitation geometry on both sides of the NW is different. Figure taken from [2].

wavelength according to eq. (1.52), e.g. 0.67λ=569 nm [3], which is not visible. Indeed, the geometry for the two end facets is not identical, see fig. 4.7. On the left side, the incoming light "sees" the entire surface, whereas on the right side, the lower part is "shadowed" by the nanowire itself.

To exclude any effective launching feature on the NW ends as a reason for this, in fig. 4.8 another NW[4] is measured twice with p-polarization (same geometry as in fig. 4.5 a)) with 180° rotated orientation. The main shape with a bigger first peak is identical, supporting that not a special property of the NW itself, but rather the entire excitation geometry is responsible for the wave pattern shape.

The asymmetrical excitation fig. 4.7 is even valid for the s-polarization if it is considered as a top view in the s-polarization scheme. Fig. 4.9 is another s-polarization measurement with a slightly differently orientated NW resulting in the wave pattern on the other side of the NW confirming this interpretation.

In some literature reports, Ag NW are considered as Fabry-Pérot-etalons [124]. However, here this effect is not observed (reflected waves from the backside would

---

[3]Assuming n=1, α=60°, λ=853 nm and the plus sign in eq. (1.52).

[4]The Ag NWs lose their visible plasmonic response over a time scale of month, which could be attributed to a degenerate sample quality, e.g. by oxidation of the Ag [174]. Therefore, the additional measurements here are performed on other "new" prepared NWs.
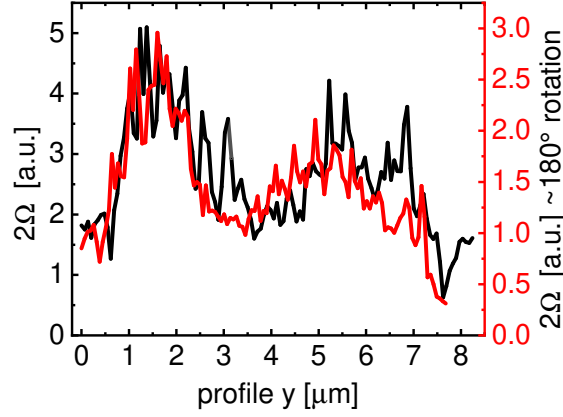
Figure 4.8: Two p-polarization 2Ω s-SNOM measurements of the same NW, but with a 180° rotation, show a nearly identical pattern, which confirms that the excitation geometry determines the pattern. The slight deviations between those two measurements are due to the imperfect sample rotation by hand; λ=853 nm. Figure taken from [2].
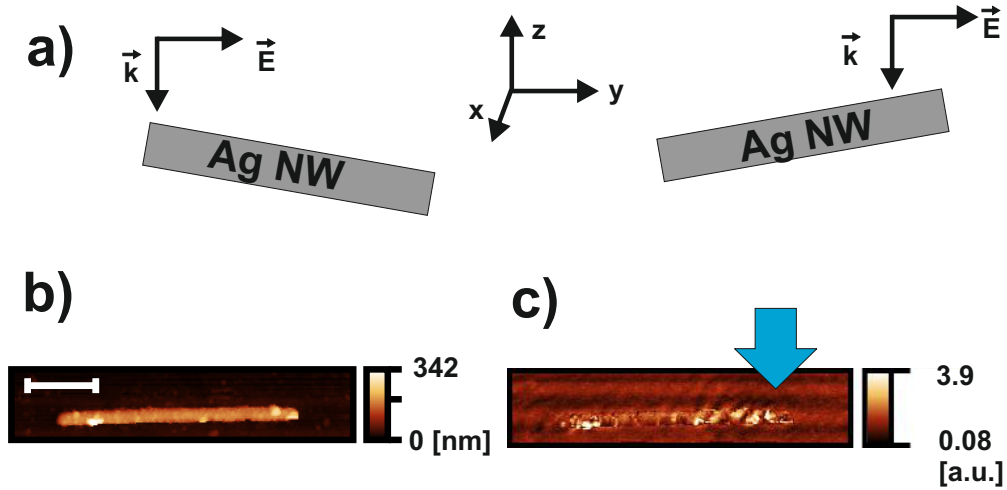
Figure 4.9: a) Similar to fig. 4.7, also for s-polarization the excitation geometry of the two end facets differs. b) Topography and c) corresponding 2Ω s-SNOM signal of another s-polarization measurement, where a slightly different incident angle leads to an SPP excitation from the other side in comparison to fig. 4.4 right column; λ=853 nm. Figure adapted from [2].

have mathematically the same effect as newly launched SPPs from the backside). Two effects have to be considered: First, the length of the NW (e.g. 7.5 μm in fig. 4.2) is relatively long in comparison to typical reported propagation length of SPPs on Ag NWs (e.g. ref. [119] compares the results of several groups; for Ag NW around $\lambda \sim$850 nm propagation lengths between 7.2 - 15 μm have been observed). Another aspect is that the excitation spot is fixed to the tip, see fig. 4.5 (due to the "scanned sample" design). Therefore, the signal drop is a superposition of propagation losses overlaid by a Gaussian beam shape. Hence, the signal is already vanishing before the tip comes close to the opposite end. Another consequence of the Gaussian shaped excitation is that the wave pattern for p-polarization is visible on a longer distance in fig. 4.4 (a wave pattern is visible on the entire $\sim$8 μm length for p-polarization, whereas for s-polarization after $\sim$5 μm it vanishes into the noise level) since the Gaussian beam is projected by a factor of $1/cos\Theta$ onto the sample plane. Additionally, of course the signal-to-noise ratio for the p-polarization is higher, too.
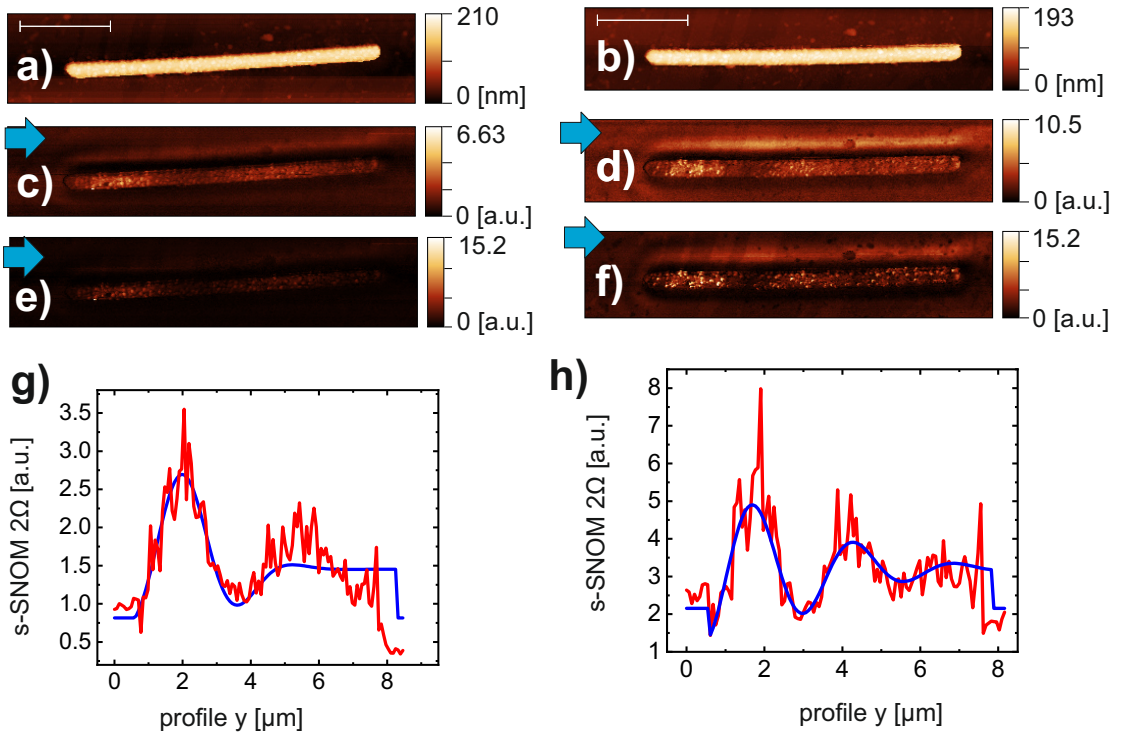
Figure 4.10: Ag NW investigated with λ =853 nm (left column) and λ=780 nm (right column) a)+b) Topography (white scale bar 2 μm) and the parallelly recorded c)+d) 2Ω s-SNOM and e)+f) 3Ω s-SNOM signals (incident laser beam direction from the left side, see blue arrows) g)+h) Profiles (red) of the 2Ω signals together with a fit as guidance for the eye (blue).

So far, the p-polarization measurement fig. 4.4 is explained by only a single mode. Indeed, with this measurement, it is not possible to separate two different modes with similar k-vectors. Calculating their visible wavelengths Λ (due to the phase retardation effect eq. (4.4)) results in observable wavelengths of $\Lambda_1 = 6.3$ μm and $\Lambda_2 = 6.7$ μm [5], which cannot be distinguished on a length scale of $\sim$8 μm for example due to the Gaussian shaping. Nonetheless, the p-polarized data are fitted later with a two mode model.

Fig. 4.10 is another verification for the above introduced analysis. Here, a NW is measured with two wavelengths, the initially used λ=853 nm and λ=790 nm. For this purpose, the Sacher laser (see section 2.4) is used, resulting in a "squeezed" wave pattern indicating again the plasmon nature of the wave pattern. However, the signal-to-noise level of the Sacher laser is worse, therefore it is only presented as a qualitative addition without any quantitative analysis.

4.1.4 Data fit

The model of fig. 4.5 is transferred into mathematical equations. Eq. (4.5) and eq. (4.6) stand for two modes propagating with $k_{1(2)}$ along the y-axis for p- and s-polarization, respectively. All the modes possess their own phase $\phi_{p1,p2,s1,s2}$ and amplitude $E_{p1,p2,s1,s2}$, and are attenuated by the exponential loss coefficients $\alpha_{1,2}$. The two p-polarization modes eq. (4.5) are phase shifted towards the beam path directly pointing on the tip apex (see fig. 4.5 a); phase shift $k_0 cos\Theta(y - y_1))$[6]. For the entire electric fields eq. (4.7) and eq. (4.8), both modes are added, multiplied with a Gaussian shape $\sigma_{p,s}$, and a constant field is added. For p-polarization, E_m represents the material contrast from the light directly illuminating the tip. For s-polarization, an arbitrary background term E_0 comprises all experimental imperfections and polarization couplings. Mathematically, E_m and E_0 are identical, however they represent different physics.

$$mode_{p1(p2)}(y) = E_{p1(p2)} \cdot e^{-i((k_{1(2)} - k_0 cos\Theta)(y-y_1) + \Phi_{p_1(p_2)})} \cdot e^{-\alpha_{1(2)}(y-y_1)} \tag{4.5}$$

$$mode_{s1(s2)}(y) = E_{s1(s2)} \cdot e^{-i(k_{1(2)}(y-y_1) + \Phi_{s_1(s_2)})} \cdot e^{-\alpha_{1(2)}(y-y_1)} \tag{4.6}$$

$$E_{p-pol}(y) = real\left(E_m + (mode_{p1} + mode_{p2}) \cdot e^{-\left(\frac{y-y_1}{\sigma_p}\right)^2}\right) \tag{4.7}$$

$$E_{s-pol}(y) = real\left(E_0 + (mode_{s1} + mode_{s2}) \cdot e^{-\left(\frac{y-y_1}{\sigma_s}\right)^2}\right) \tag{4.8}$$

---

[5]Parameters for eq. (4.4): λ_0 =853 nm, λ_1=852 nm, λ_2=859 nm, $\Theta = 30°$.

[6]Actually, $cos\Theta$ represents the entire projection of the incident light onto the NW, $cos\Theta sin\Phi$.

	E_c [a.u.]	$E_{m/0}$ [a.u.]	E_1 [a.u.]	E_2 [a.u.]	y_1 [μm]	y_2 [μm]
p-polarization	1.01	1.87	1.71	0.09	0.69	7.61
s-polarization	0.76	0.93	6.27	6.72	0.65	8.12
	Φ_1 [rad]	Φ_2 [rad]	α_1 [μm^{-1}]	α_2 [μm^{-1}]	σ [μm]	Θ [rad]
p-polarization	1.81	3.74	0.80	0.93	5.41	0.61
s-polarization	0.35	3.09	0.19	0.68	2.80	-

Table 4.1: Fit-parameters for the p-polarization and s-polarization measurements used with eq. (4.5)-(4.8).

Eq. (4.7) and (4.8) are now fitted to the experimental data fig. 4.4 by using a MATLAB script based on the built-in *fminsearch* function, which optimizes the variables to minimize the mistake-function eq. (4.9), the difference between the measured and a simulated curve (calculated from the parameters and eq. (4.7) and eq. (4.8), respectively). Only values within a certain interval between y_1 and y_2 are taken into account (corresponding to the NW geometry). Outside this range, a constant value E_c is set. The k-values are assumed as constants (values from the COMSOL simulations). To avoid sticking of the algorithm in local minima of its error function, the starting parameters have to be chosen carefully and unphysical values are excluded (e.g. $\alpha < 0$).

$$mis = \sum_i (simulation_i - measurement_i)^2 \qquad (4.9)$$

The resulting data fits are depicted in fig. 4.11 a)+b) and table 4.1 lists the corresponding parameters. The MATLAB code is able to directly plot the modes individually, shown in fig. 4.11 c)+d).

4.1.5 Discussion

The fits in fig. 4.11 can reproduce the measurements quite well, both the long wavelength for the p-polarization and the beating pattern for the s-polarization. Especially the analysis of the single modes is interesting since the p-polarization is mainly fit with a single mode (amplitudes 1.71 vs. 0.09), whereas in the s-polarization both modes are excited with similar amplitudes but with a phase difference of $\sim \pi$ corresponding to the node of the beating pattern.

In general, it is difficult to deduce the direct physical effects of those plasmon modes on the operation of the THz photomixers using the s-SNOM. The probably most important role play the NW-substrate modes fig. 4.6, which are not accessible with the s-SNOM tip. Even scanning "close" to the NW is difficult because all results would be overlapped by the air-NW modes. Additionally, edge
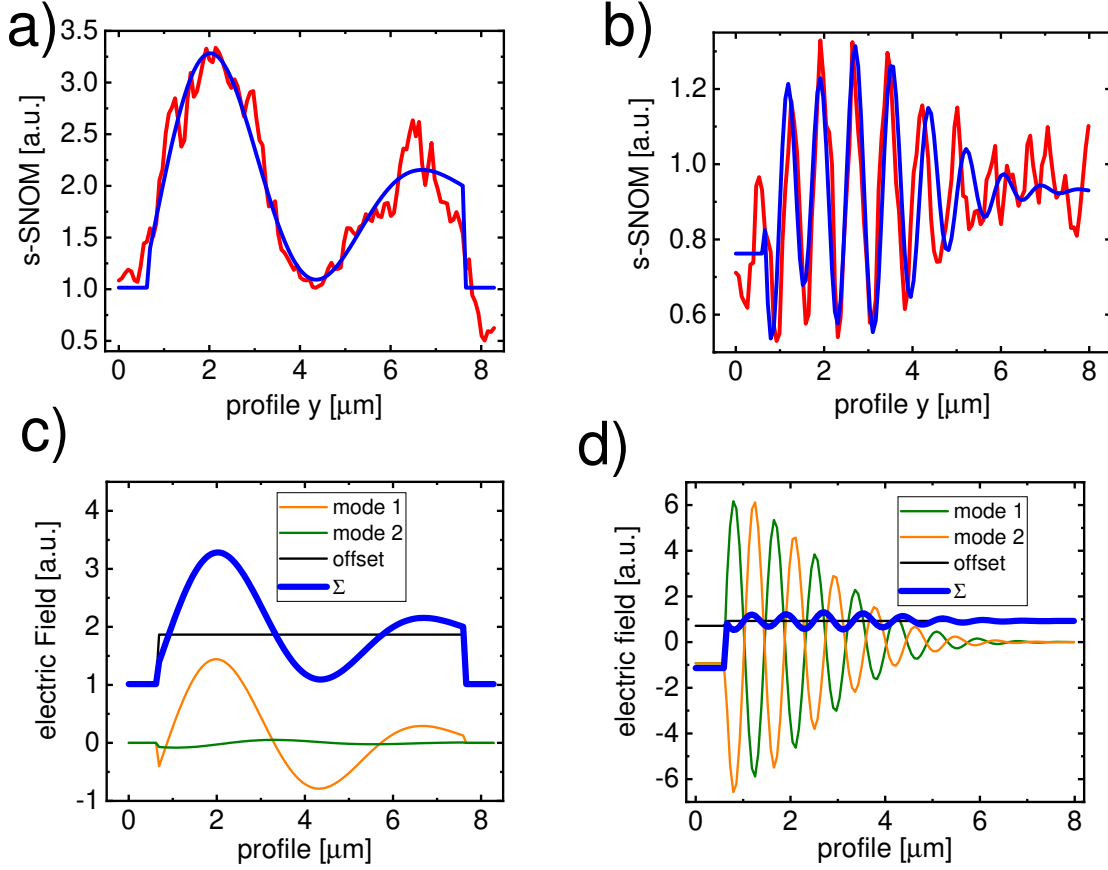
Figure 4.11: The fitted curves of the p-polarization (left column) and s-polarization measurement (right column). a)+b) Direct comparison of the measured data (red) with the model curve (blue). c)+d) Decomposition of the model curve into its three components: Background (black) and two individual modes (yellow, green). Figure taken from [2]. Copyright 2019 American Chemical Society.

effects and s-SNOM artefacts interfere as well. Nonetheless, this analysis enables a comprehensive understanding of the polariton mapping in the near-infrared region. Although many polariton mapping reports in different spectral regions are similar to each other (waves launched and reflected by surface features and the tip itself, background contribution, ...), the exact model and interpretation depend strongly on the specific sample system and geometry. Especially the optical and near-infrared regime is much more difficult. The confinement is weaker than for instance in the mIR range since k_{spp} is close to k_0 and the approximation $k_{spp} >> k_0$ is not valid here.

4.2 Conductivity measurements on Si

In the following, the THz s-SNOM is used to demonstrate the conductivity measurement ability of this spectral range, which is well suited for a broad semiconductor doping level range fig. 4.12.
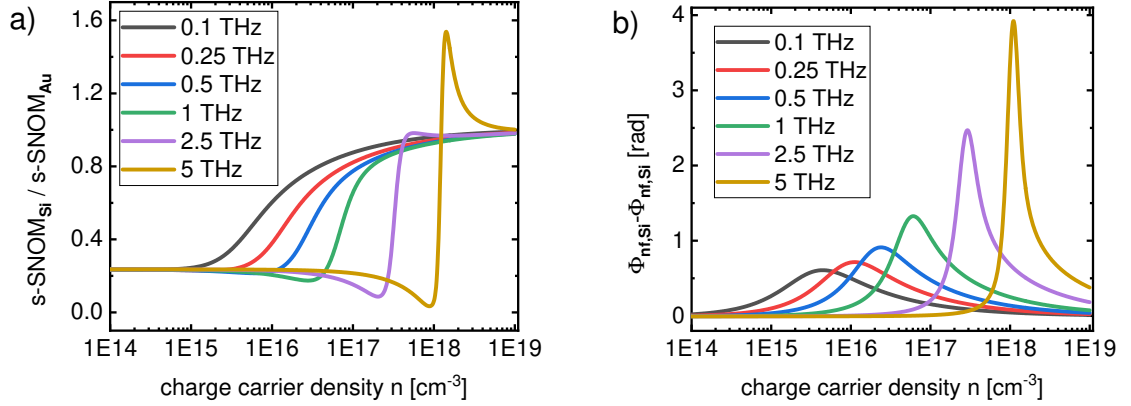
Figure 4.12: Simulation of the a) near-field amplitude and b) near-field phase as a function of the charge carrier density n for various s-SNOM frequencies based on the finite-dipole model eq. (4.35) and referenced to Au; τ_{scatt}=200 fs, $m_{eff} = 0.26m_0$ (n-doped Si).

As briefly reviewed in subsection 1.4.1, there are already some examples in the literature, where the s-SNOM probes the Drude conductivity. CO_2 lasers are best suited for higher charge carrier concentrations in the range of $\sim(10^{18}$-$10^{20})$ cm^{-3}, but they have a limited tuning range, hence mostly up to 3-4 different doping regions are compared to reveal contrasts [68, 175, 176]. The THz regime is more suited for lower charger carrier concentrations, e.g. a sample containing different regions with up to four discrete charge carrier concentration levels between $2 \cdot 10^{16}$ cm^{-3} and $2 \cdot 10^{20}$ cm^{-3} has been probed with a single frequency [64] or with a pulsed TDS system [58], and a sample with a continuously changing charge carrier concentration profile has been investigated qualitatively [72]. Another example probes at a constant CW frequency a semiconducting nanowire with gate-induced charge carriers [150].

Here, two experiments are conducted. First, a CW THz s-SNOM is used to analyse the Drude response by changing the charge carrier density (similar to the last mentioned literature example), but in this case by photo-excitation by means of a near-infrared pump laser at $\lambda \approx 800$ nm, see subsection 4.2.2. By adjusting its pump power, the charge carrier concentration can be set continuously within a broad range. Second, the opportunity to extract the doping density from single

CW THz s-SNOM measurements is evaluated in subsection 4.2.3. Both data analyses focus on quantitative data evaluation. But first, the next subsection 4.2.1 deals with several aspects of the photo-excitation required for the later data analysis and interpretation.

4.2.1 Photo-excited charge carrier density

Excitation and generation

The number of excited electron-hole pairs G (unit $[s^{-1}]$) is calculated according to eq. (4.10) using the laser power $P = p \cdot P_0$ (P_0 is measured in front of a fiber coupling described later in fig. 4.16; the proportionality constant p contains the coupling losses and the splitting ratio of a beam splitter), T_F which comprises the Fresnel reflection losses [7], and the quantum conversion efficiency c_q.

$$G = c_q \cdot T_F \cdot pP_0 \cdot \frac{\lambda}{hc_0} \qquad (4.10)$$

Lifetime and recombination

A closer look at the data (see fig. 4.20) as well as many literature reports motivate to consider the charge carrier lifetime τ_{lt} in the further analysis not as a constant. In general, recombination determines the lifetime of the photo-excited electron-hole pairs. The total lifetime can be calculated using the Matthiessen's rule eq. (4.11) [84, 177], which combines the different recombination channels τ_i.

$$\frac{1}{\tau_{lt}} = \sum_i \frac{1}{\tau_i} \qquad (4.11)$$

Basically, three recombination channels in bulk semiconductors are possible and depicted in fig. 4.13. [178–180]

- Band-to-band recombination: A free electron combines directly with a free hole and radiates a photon. However, due to the indirect band gap and the resulting momentum mismatch, this channel is very unlikely in silicon.

- Shockley-Read-Hall recombination: The Shockley-Read-Hall (SRH) recombination is a trap assisted process: Electronic traps (e.g. impurities, defects, ...) catch a charge carrier, hence the other carrier can simply recombine as the trap can compensate the momentum mismatch easily.

- Auger recombination: This is a three particle process. An electron-hole pair recombines and transfers the energy and momentum to a third charge carrier.

113
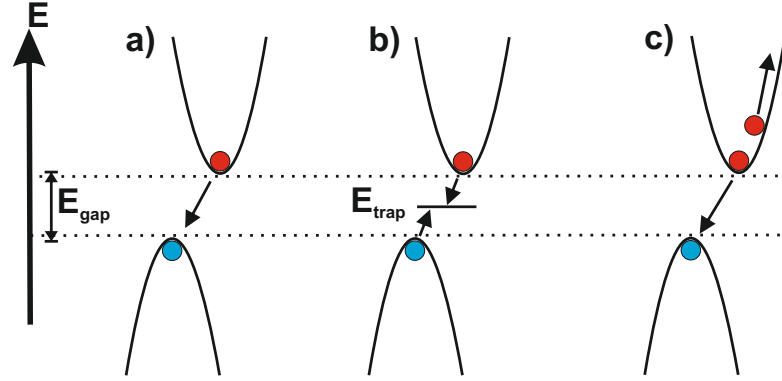
Figure 4.13: The different recombination processes of electrons (red, conduction band) and holes (blue, valence band) for an indirect semiconductor: a) band-to-band recombination; b) Shockley-Read-Hall recombination; c) Auger recombination.

Although there are several models and experimental data fits on both, the SRH recombination [181] and the Auger effect [177, 182], for the sake of simplicity here a constant τ_{SRH} and an inverse quadratic dependence of the Auger recombination $\tau_{Auger} = 1/(c_{Auger}n^2)$ is assumed, which is both justified by the corresponding literature reports.

Therefore, the total lifetime τ_{lt} will be calculated according to eq. (4.11) and the previous discussion by

$$\frac{1}{\tau_{lt}} = \frac{1}{\tau_{SRH}} + c_{Auger}n^2 \,. \tag{4.12}$$

A plot of eq. (4.12) in fig. 4.14 assuming reasonable values shows that the low charge carrier density regime corresponds to the SRH recombination (assumed here as constant), whereas the Auger process dominates the high regime.

Charge carrier density

In the following, the functional dependence of the charge carrier concentration n (in this section n always refers to the pair density) as a function of the exciting laser power should be derived. Besides their average lifetime τ_{lt}, their distribution inside the substrate is decisive as the charge carriers diffuse. The penetration depth of the 800 nm radiation ($\sim$ 10 μm [183]) and the spot size $\sim$50 μm (according to eq. (1.13)) are smaller than the typical diffusion length scale (e.g. $L \sim 400$ μm [184]), therefore the excited carriers have enough time to diffuse and dilute from their generation volume fig. 4.15.

Indeed, the analytical analysis of the diffusion processes of photo-excited charge
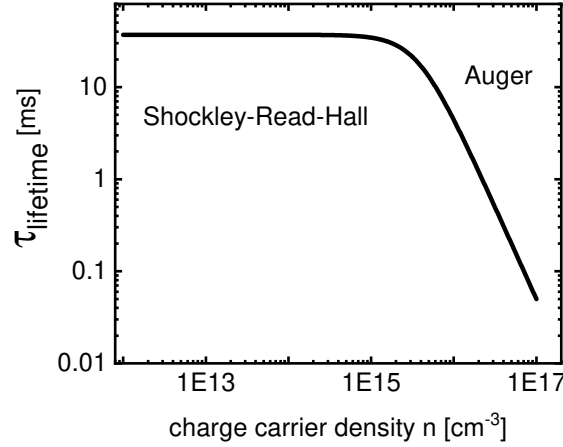
Figure 4.14: The combined charge carrier lifetime τ_{lt} based on $\tau_{SRH} = 37\ ms$ and the ambipolar $c_{Auger} = 2 \cdot 10^{-30}$ cm^{6}s^{-1} [182] according to eq. (4.12). Figure adapted from [6].

carriers is complicated and an own research branch. For a deeper understanding of the charge carrier excitation and diffusion in Si, there are several excellent works dealing with those questions in the scope of solar cells. The photo-excitation in Si has been analysed analytically for the 1d case for CW [185] and pulsed [186] illumination; the latter case is even treated in 3d [184]. Further analytical models can be found in the general literature about (charge carriers) diffusion [187, 188]. However, all those models are based on a constant τ_{lt}. Assuming a dependence $\tau_{lt}(n)$ makes the corresponding differential equations much more complicated, and the available solutions cannot be applied directly any more. Therefore, here an approximation is used to derive at least the functional dependence $n(P_0)$. The dependence of $\tau_{lt}(n)$ is neglected in the derivation of $n(\vec{r})$, as well as the surface recombination and the finite thickness of the Si substrate.[7] At the end, not the absolute n value is important, but its dependences because later a fit parameter scales the entire data set.

The decisive differential diffusion equation (diffusion constant D) [184–186] is given by

$$\frac{\partial n}{\partial t} = D\Delta n - \frac{n}{\tau_{lt}}\ . \tag{4.13}$$

There are two possibilities to model the charge carrier diffusion. It can be assumed as spherical diffusion fig. 4.15 a), or as the s-SNOM tip probes only a small nanometer sized volume within the much bigger excitation spot (on the scale of microns), in the tip's vicinity the incident laser light is very homogeneous and

---

[7]A comprehensive mathematical treatment of those simplifications is presented in [6].
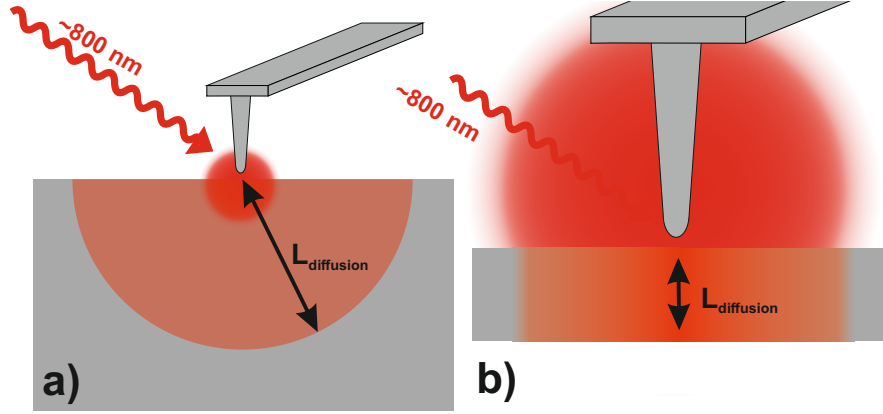
Figure 4.15: The electron-hole plasma is created beneath the tip by the 800 nm near-infrared laser. The excited charge carriers diffuse into the bulk material. a) Spherical diffusion and b) zoomed-in view reveals a one-dimensional diffusion in the vicinity of the tip apex.

a one-dimensional diffusion into the sample can be taken into account depicted in fig. 4.15 b). Both cases are treated mathematical in the next paragraphs to estimate the dependence $n(\tau_{lt})$.

1d diffusion   The differential equation (4.13) simplifies in the steady-state case ($\partial n/\partial t = 0$) for 1d to eq. (4.14) and is solved by the ansatz eq. (4.15); the quantity $L = \sqrt{D\tau_{lt}}$ corresponds to the diffusion length.

$$D\frac{\partial^2 n}{\partial x^2} = \frac{n}{\tau_{lt}} \tag{4.14}$$

$$n(x) = Ae^{-\frac{x}{\sqrt{D\tau_{lt}}}} = Ae^{-\frac{x}{L}} \tag{4.15}$$

The constant A can be solved by inserting eq. (4.15) into Fick's first law of diffusion eq. (4.16) as the corresponding boundary conditions at $x = 0$ resulting in the solution eq. (4.17). J is the diffusion flux from the photo excitation (unit $[m^{-2}s^{-1}]$), i.e. the generated charge carriers eq. (4.10) divided by the spot size (therefore J is proportional to the excitation power P_0).

$$J = -D\frac{\partial n}{\partial x} \tag{4.16}$$

$$n(x) = \frac{JL}{D}e^{-\frac{x}{L}} = J\sqrt{\frac{\tau_{lt}}{D}}e^{-\frac{x}{L}} \tag{4.17}$$

Hence, close to the surface ($x = 0$, the probing region of the tip) the functional dependence $n(x) \propto \sqrt{\tau_{lt}}$ is valid and for this case the overall functional dependence is expressed by

$$n(P_0) = a \cdot \sqrt{\tau_{lt}} P_0 \,. \tag{4.18}$$

The global constant a takes into account all the proportional parameters, e.g. like those in eq. (4.10) and eq. (4.17).

3d diffusion For the 3d solution, spherical coordinates are used. Replacing the Laplace operator [164] in eq. (4.13) and considering again the steady-state case leads to

$$D \left(\frac{2}{r} \frac{\partial n}{\partial r} + \frac{\partial^2 n}{\partial r^2} \right) - \frac{n}{\tau_{lt}} = 0 \,. \tag{4.19}$$

This differential equation can be simplified by the substitution $u = n \cdot r$ [188] to eq. (4.20) and subsequently solved equivalently to eq. (4.15) leading to the solution eq. (4.21).

$$D \frac{\partial^2 u}{\partial r^2} - \frac{u}{\tau_{lt}} = 0 \tag{4.20}$$

$$n(r) = B \frac{1}{r} e^{-\frac{r}{L}} \tag{4.21}$$

The formula eq. (4.21) diverges at $r = 0$, the position of the s-SNOM tip. However, its volume integral is finite due to the r^2 term in the spherical volume element $dV = r^2 \sin\Theta \, d\Theta \, d\Phi \, dr$. In the subsequent analysis, the integral eq. (4.22) (for integration of eq. (4.21)) is essential and used two times (eq. (4.23) and eq. (4.27)).

$$\int r \cdot e^{-\frac{r}{L}} dr = -L^2 \left(1 + \frac{r}{L} \right) e^{-\frac{r}{L}} + const. \tag{4.22}$$

To determine the constant B, the diffusion flux J is integrated over the penetration volume r_p eq. (4.23) (as hemisphere only factor 2π) resulting in a generation velocity G_v (unit $[m \cdot s^{-1}]$) corresponding to the incident laser power (using again Fick's first law and eq. (4.21)).

117

$$G_v = \int_0^{r_p} J dV = 2\pi \int_0^{r_p} J r^2 dr = 2\pi \int_0^{r_p} \left(-D \frac{\partial n}{\partial r} \right) r^2 dr$$

$$= -2\pi D \int_0^{r_p} \left(-\frac{B}{r^2} e^{-\frac{r}{L}} - \frac{B}{rL} e^{-\frac{r}{L}} \right) r^2 dr = 2\pi DB \int_0^{r_p} \left(e^{-\frac{r}{L}} + \frac{1}{L} \cdot r \cdot e^{-\frac{r}{L}} \right) dr$$

$$= 2\pi DB \left(\left[-L e^{-\frac{r}{L}} \right]_0^{r_p} + \frac{1}{L} \left[-L^2 e^{-\frac{r}{L}} \left(1 + \frac{r}{L} \right) \right]_0^{r_p} \right)$$

$$= 2\pi DB \left[-L e^{-\frac{r_p}{L}} + L - L e^{-\frac{r_p}{L}} \left(1 + \frac{r_p}{L} \right) + L \right] = 2\pi DB \left[2L - 2L e^{-\frac{r_p}{L}} - r_p e^{-\frac{r_p}{L}} \right]$$

$$(4.23)$$

Solving eq. (4.23) for the constant B leads to the final formula

$$n(r) = \frac{G_v}{2\pi D \left[2L - 2L e^{-\frac{r_p}{L}} - r_p e^{-\frac{r_p}{L}} \right]} \frac{1}{r} e^{-\frac{r}{L}} . \tag{4.24}$$

The denominator in the prefactor can be further simplified eq. (4.25) using the Taylor expansion of the exponential function ($e^x \approx 1 + x + x^2/2$) as the penetration depth r_p is much smaller than the diffusion length L.

$$2L - 2L e^{-\frac{r_p}{L}} - r_p e^{-\frac{r_p}{L}} \overset{Taylor}{\approx} 2L - 2L \left(1 - \frac{r_p}{L} + \frac{r_p^2}{2L^2} \right) - r_p \left(1 - \frac{r_p}{L} + \frac{r_p^2}{2L^2} \right)$$

$$= 2L - 2L + 2r_p - \frac{r_p^2}{L} - r_p + \frac{r_p^2}{L} - \frac{r_p^3}{2L^2} = r_p - \frac{r_p^3}{2L^2} = r_p \left(1 - \frac{r_p^2}{2L^2} \right) \approx r_p$$

$$(4.25)$$

Inserting eq. (4.25) in eq. (4.24) results in

$$n(r) \approx \frac{G_v}{2\pi D r_p} \frac{1}{r} e^{-\frac{r}{L}} . \tag{4.26}$$

For approximating the charge carrier density directly beneath the tip $r = 0$, again the diverging $1/r$ dependence in eq. (4.26) is avoided by integrating a small hemisphere r_0 around the zero point (again the Taylor expansion and $r_0 << L$ are used as approximations):

$$N(r_0) = \int_0^{r_0} n(r)dV = 2\pi \int_0^{r_0} \frac{G_v}{2\pi Dr_p}\frac{1}{r}e^{-\frac{r}{L}}r^2 dr = \frac{G_v}{Dr_p}\int_0^{r_0} re^{-\frac{r}{L}}dr$$

$$= \frac{G_vL^2}{Dr_p}\left[-e^{-\frac{r}{L}}\left(1+\frac{r}{L}\right)\right]_0^{r_0} = \frac{G_vL^2}{Dr_p}\left[-e^{-\frac{r_0}{L}}\left(1+\frac{r_0}{L}\right)+1\right]$$

$$\overset{Taylor}{\approx} \frac{G_vL^2}{Dr_p}\left[-\left(1-\frac{r_0}{L}+\frac{r_0^2}{2L^2}\right)\left(1+\frac{r_0}{L}\right)+1\right] \tag{4.27}$$

$$= \frac{G_vL^2}{Dr_p}\left[-1-\frac{r_0}{L}+\frac{r_0}{L}+\frac{r_0^2}{L^2}-\frac{r_0^2}{2L^2}-\frac{r_0^3}{2L^3}+1\right]$$

$$= \frac{G_vL^2}{Dr_p}\left(\frac{r_0^2}{2L^2}-\frac{r_0^3}{2L^3}\right) = \frac{G_vr_0^2}{2Dr_p}\left(1-\frac{r_0}{L}\right) \approx \frac{G_vr_0^2}{2Dr_p}.$$

The charge carrier density n is independent of the lifetime τ_{lt}. Hence, for this case the overall functional dependence (the constant a is equivalent to eq. (4.18)) is determined by

$$n(P_0) \approx a \cdot P_0. \tag{4.28}$$

Experimental setup extension

The base of the photo-excitation experiments is again the setup introduced in fig. 2.12. Since the Drude behaviour shows a prominent peak in the optical phase, now the interferometric phase sensitivity of the homodyne scheme is used. To reach the required phase difference of $\pi/2$ at the frequency of e.g. 257.6 GHz (λ=1164 μm; Virginia Diodes source), the interferometer mirror has to be shifted between the two homodyne measurements eq. (1.29) and eq. (1.30) by a distance of $\lambda/8$=145.5 μm (additional factor of 0.5 as the reference propagates this distance twice) using a micrometer stage. Here, working in the THz regime is quite advantageous because, for example, mechanical drifts and instabilities are not as severe as for shorter wavelengths.

To excite the Si sample, $\sim$800 nm near-infrared light from a Tsunami Ti:sapphire laser (operated in CW; pumped via a Millennia diode-pumped laser; both from Spectra-Physics Laser Inc.) is used, fiber coupled (for alignment the fiber output port is mounted on a 3d translation stage), and focussed with a f=100 mm lens (Thorlabs LA1207-B) onto the tip-sample region, see fig. 4.16.

The power P reaching the sample can be adjusted by means of a round variable filter wheel and monitored by measuring a portion of the incident beam with a powermeter P_0, see fig. 4.17, which is proportional to the transmitted power $P = p \cdot P_0$ (p contains e.g. the beam splitter ratio and the fiber coupling losses).
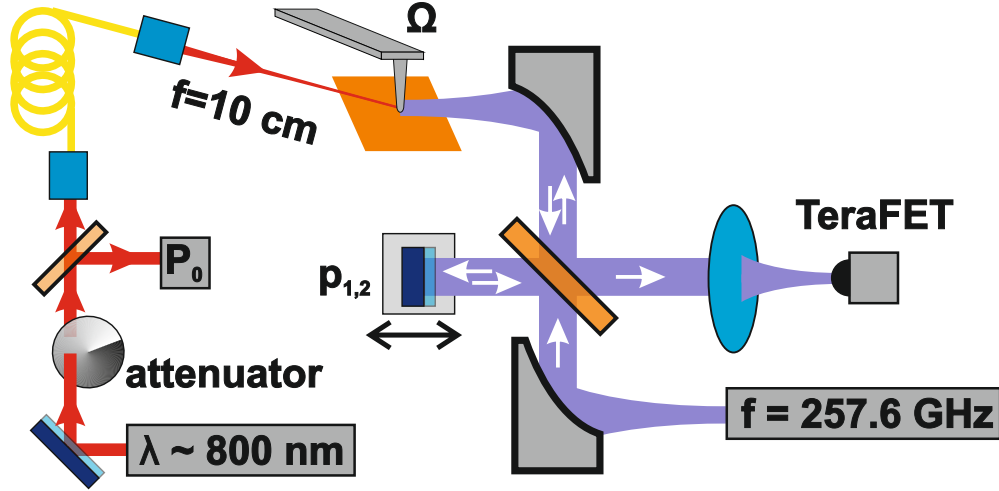
Figure 4.16: Sketch of the photo-exciting THz s-SNOM: The cantilever (Ω) and sample (orange) are placed in the centre in the top. From the right side, the THz interferometer (THz beam in purple) is connected incorporating the all-electronic source, the homodyne delay stage $p_{1,2}$, and the TeraFET detector. From the left side, the $\sim$800 nm laser light (in red) is attenuated, split (for power measurement P_0), fiber coupled, and focussed beneath the tip. Figure taken from [6].

As the data are later fitted numerically, p is merged into the a constant eq. (4.18) and eq. (4.28).

Effects of the laser pump power

One special issue with the photo-excited charge carrier experiment is the relatively high power (up to the order of 80 mW) impinging on and around the cantilever that can influence the tip behaviour. Fig. 4.18 shows the resonance curve of a freely oscillating tip (RMN-25Pt300B), once with blocked photo-excitation and once with the 800 nm on. The sample is driven far away to exclude any electrostatical effects between the tip and sample.

The observed shift in resonance can be explained thereby that the laser is heating up the cantilever, affecting the Young's modulus $E(T)$ of the material, which again shifts the resonance. The following calculations support this explanation. By assuming a simplified cantilever geometry, the dependence of the resonance frequency ω_0 on the Young's modulus E can be calculated by [189, 190]

$$\omega_0 \propto \sqrt{E}\,. \tag{4.29}$$

A change in E induces a change in ω_0 given by
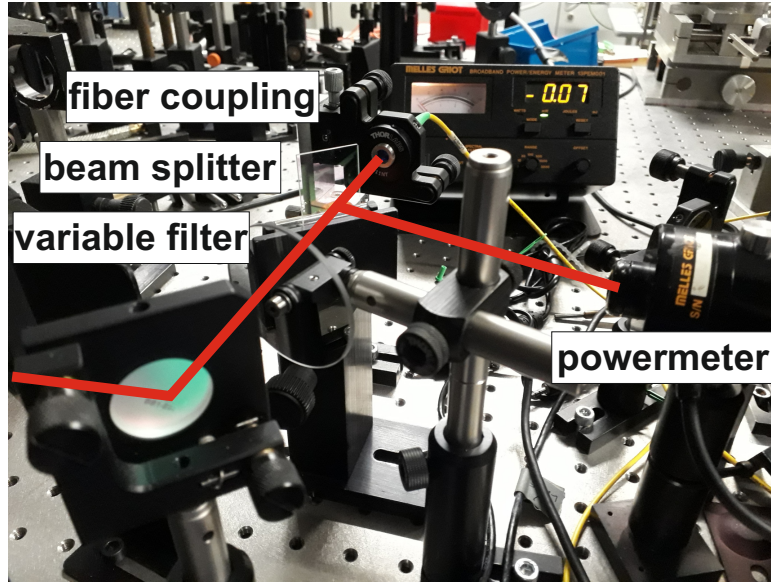
Figure 4.17: The variable filter can be used to adjust the power level reaching the fiber coupling. A beam splitter (manufacturer specified splitting ratio T:R=90:10; Thorlabs BSN11R) guides a portion of this light towards a powermeter (Melles Griot 13PEM001), enabling a fast real-time power measurement.

Figure 4.18: Exemplary resonance curve of the freely oscillating cantilever recorded twice with the 800 nm photo-excitation laser on and off.

$$\frac{\Delta\omega_0}{\omega_0} = \frac{1}{2}\frac{\Delta E}{E} \; . \tag{4.30}$$

The corresponding material parameters for Pt eq. (4.31) are taken from [191] resulting in dE/dT=-3.38·10^7 N/(m^{2}K) and E(T=20 °C)=1.67·10^{11}N/m^2.
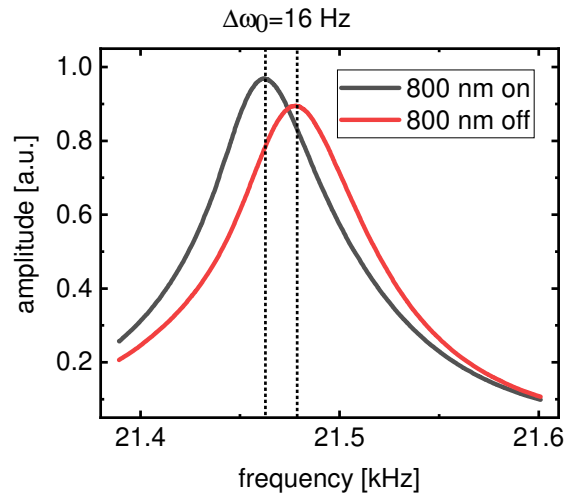
$$E = (1.68 - 3.38 \cdot 10^{-4} \cdot T[°C] \pm 0.046) \cdot 10^{11} \frac{N}{m^2} \tag{4.31}$$

Now, the observed change in resonance frequency in fig. 4.18 of $\Delta\omega_0$=16 Hz can be calculated back into a heating of $\Delta T \approx$7 K, which sounds quite reasonable for the situation of a strongly focussed laser beam. There are several literature reports of optical excited and heated silicon cantilevers (less reflective, more absorption, worse thermal conductivity) reaching hundreds of K [189, 192, 193].

The setup used is working in the AM-AFM mode, i.e., as explained in section 2.1, the cantilever is constantly excited with a fixed frequency and its amplitude acts as the feedback parameter for the z-distance control loop. However, as already visible in fig. 4.18 a shifted resonance curve corresponds to a drop/rise of the free amplitude (when working on the right side of the resonance, the amplitude is dropping). This is illustrated in fig. 4.19 a), where the tip is oscillating close to the sample (distance of some microns, only the z-piezos are retracted). In the middle, the photo-excitation laser is opened affecting all properties, the free mechanical oscillating amplitude, the mechanical cantilever phase (supporting the interpretation of the shifted resonance curve), and the backreflected 1Ω signal (following the amplitude). In general, the oscillation amplitude affects strongly the s-SNOM signal strength ([25, 47], or as well fig. 3.5). On the other side, the z-feedback mechanism is set to a certain amplitude value, i.e. during the approach, the tip is moved towards the sample until a user chosen amplitude is reached. That guarantees an equal oscillation amplitude during the approached state in both cases, photo-excitation laser on/off. Indeed, the situation between those cases is not completely identical as the following example illustrates: Assuming a free oscillation of 100 ([a.u.]) (without photo-excitation) and a setpoint of 90 % means, that during approach the tip is moved towards the sample until the amplitude drops to 90. Now the 800 nm laser is turned on, the free oscillation amplitude is dropping to 95 (operating frequency on the right side of the resonance curve), whereas the setpoint still remains at 90. If the tip is approached now, it moves less close to the sample, namely until the amplitude drops from 95 to 90.

This effect is illustrated as well in fig. 4.19 b): The cantilever is approached to a Au sample and the 3Ω THz s-SNOM signal is plotted. In the Au, no charge carrier generation and with this no s-SNOM signal change is expected due to the optical excitation. After opening the excitation laser, the feedback mechanism
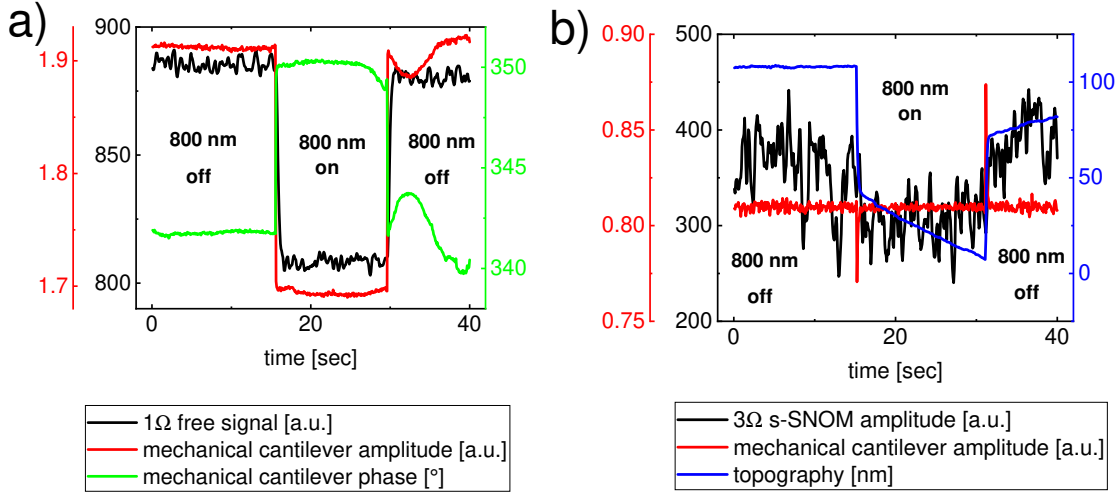
Figure 4.19: AFM and THz s-SNOM response to the photo-excitation laser (800 nm on/off) a) When the cantilever is oscillating freely above the sample, the 800 nm laser shifts the mechanical resonance affecting both the amplitude and phase. The 1Ω reflection from the s-SNOM laser follows the mechanical amplitude. b) If the cantilever is approached to a Au sample, the feedback mechanism holds the oscillation amplitude at a constant level and compensates the effect of the 800 nm illumination by a topography jump. However, the effect on the s-SNOM signal in this example is close to the noise level.

holds the mechanical amplitude at a constant level via changing the tip-sample distance (jump in topography), which is compensating the shifted resonance curve effect[8].

Some numerical simulations indicate that the minimum distance between the tip and sample weakly affects the s-SNOM signal strength (parameter z_0 in fig. 1.16). Also in the experimental data fig. 4.19 b) it is visible. However, further test measurements show that there is no constant value or a clear functional link, but it depends on various parameters (e.g. the setpoint, the pump power and focussing, the cantilever material and shape, ...). Therefore, this effect is difficult to quantify, and it is not considered in the further analysis for the sake of simplicity.

4.2.2 Si measurement scheme 1: Photo-excitation

As sample, a boron doped p-type silicon wafer, 10-20 Ω·cm, $< 100 >$, thickness 500 μm, from University Wafer Inc. is used. It is photo-excited and the resulting homodyne THz s-SNOM signal (257.6 GHz, Virginia Diodes Inc. all-electronic

---

[8]Additionally, this topography jump comprises any thermal expansion of the tip/sample, too.
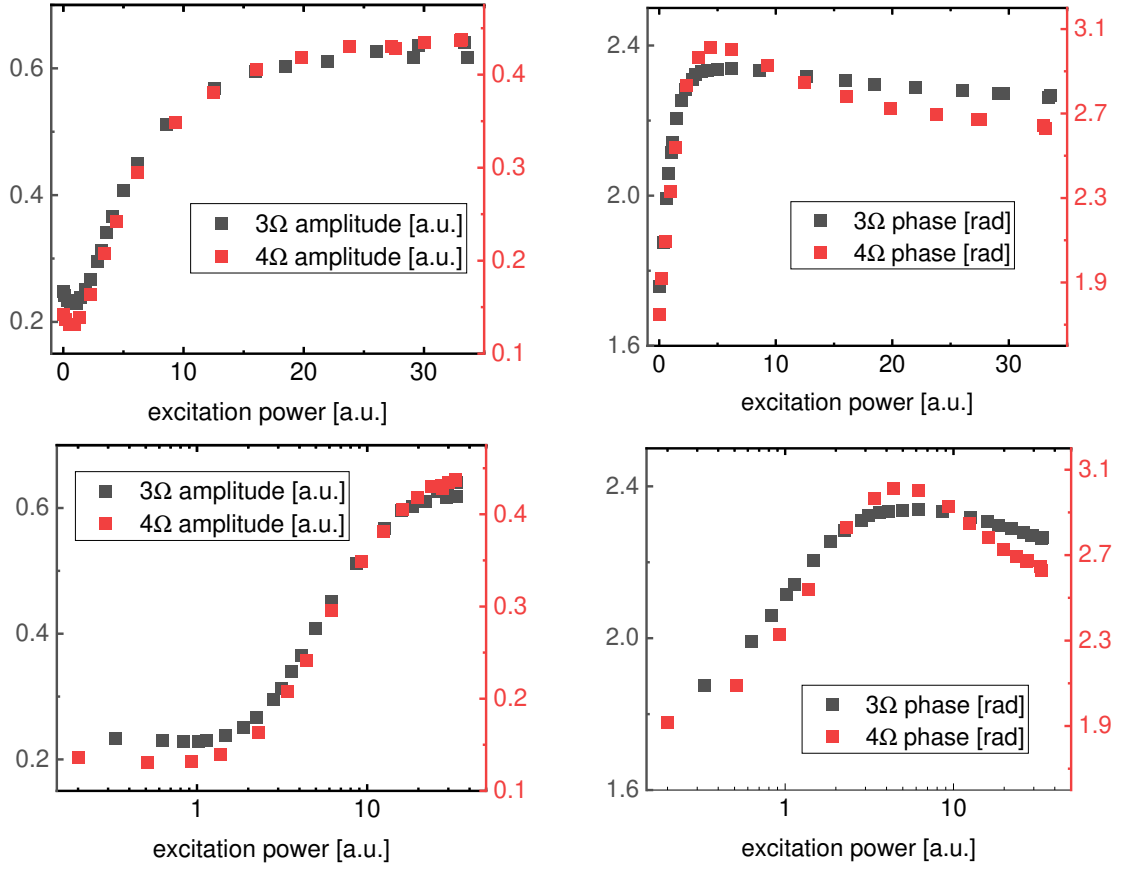
Figure 4.20: The THz s-SNOM amplitude (left column) and s-SNOM phase (right column) of the photo-excited silicon sample plotted with the x-axis in a linear scale (upper row) and in a logarithmic scale (lower row).

source, 90 nm TeraFET detector) is measured. To minimize drift effects, at each power level the two homodyne measurements are taken consecutively. Using a lock-in time-constant of τ_c=100 ms (MFLI LIA), for each measurement 20 s of data are averaged. Fig. 4.20 shows the recorded 3Ω and 4Ω near-field amplitudes and phases.

The measurement series are started with the high laser power, then the incident power level is decreased stepwise. At the end, some single measurements are taken again at high power to exclude any drifts (see the double measurements around 29 a.u. and 33 a.u. excitation power). The slow decrease of the phase data at high power levels is one indication that the excited charge carrier density is not proportional to the incident power, which leads to the aforementioned consideration of the Auger recombination.

Data analysis and fit

The 4Ω data in fig. 4.20 are now fitted to a numerical model following the scheme introduced in subsection 1.4.1. For the charge carrier pair density both the one-dimensional eq. (4.18) and the radial diffusion eq. (4.28) are tested. However, the one-dimensional dependence leads to a better agreement in the data fit. This indicates that the photo-excitation in the vicinity of the s-SNOM tip is so uniform that the one-dimensional diffusion is dominant.

Based on eq. (4.18) and eq. (4.12) one obtains the final dependence

$$n^4 + \frac{1}{\tau_{SRH} \cdot c_{Auger}} n^2 - \frac{a^2 P_0^2}{c_{Auger}} = 0 \,. \tag{4.32}$$

It can be solved for n by first a quadratic equation for n^2 and subsequently taking the square root (the signs are already determined by the requirement for a positive and real n):

$$n(P_0) = \sqrt{-\frac{1}{2 \cdot c_{Auger}\tau_{SRH}} + \sqrt{\left(\frac{1}{2 \cdot c_{Auger}\tau_{SRH}}\right)^2 + \frac{a^2}{c_{Auger}}P_0^2}} \,. \tag{4.33}$$

Moreover, the charge carrier density calculates the dielectric function of the sample ϵ_s according to the Drude model eq. (1.43) and eq. (1.44). The s-SNOM response corresponds to eq. (1.19) depicted here again:[9]

$$E_{scat} \propto (1 + r_p)^2 \alpha_{eff} E_{incident} \,. \tag{4.34}$$

Differing from subsection 1.4.1, here α_{eff} is not calculated with the simple point-dipole model, but with the more advanced finite-dipole model eq. (4.35) [39, 40], which depends again on the β parameter eq. (1.16) ($\beta(\epsilon_s)$), the tip radius a, the effective spheroid length L (in the finite-dipole model, the tip is modelled as a spheroid), and a numerical parameter g.

$$\alpha_{eff}(z) = \epsilon_0 a^2 L \frac{\frac{2L}{a} + ln\frac{a}{4eL}}{ln\frac{4L}{ae^2}} \left(2 + \frac{\beta(g - \frac{a+z}{L})ln\frac{4L}{4z+3a}}{ln\frac{4L}{a} - \beta(g - \frac{3a+4z}{4L})ln\frac{2L}{2z+a}}\right) \tag{4.35}$$

Both models are compared qualitatively in the simulations fig. 4.21 (Si sample with reasonable parameters: 5Ω, 250 GHz, τ_{scatt}=200 fs, $m_{eff} = 0.26m_0$). The finite-dipole model exhibits a stronger contrast in both the s-SNOM amplitude and phase. During the fit optimization, it shows a better agreement to the data, which is already reported in the literature for other samples [40].

---

[9]Here, r_p refers again to the Fresnel reflection coefficient for p-polarized light and not the penetration depth anymore.

a)

b)
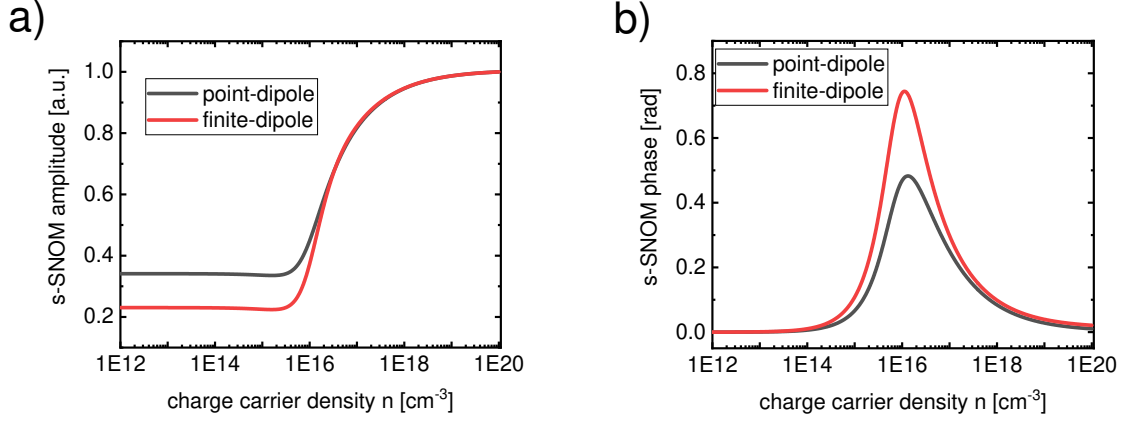
Figure 4.21: Comparison of the s-SNOM a) amplitude and b) phase between the point-dipole and the finite-dipole interaction model.

The fitting procedure is executed by a MATLAB code again based on the *fminsearch* algorithm [194]: It minimizes the deviation *dev* eq. (4.36) between the experimental data $s_{nf,l}^{exp.}$, $\phi_{nf,l}^{exp.}$ and simulated curves $s_{nf,l}^{sim.}$, $\phi_{nf,l}^{sim.}$ by optimizing several parameters. The index l subscripts the single data points, and both curves (near-field amplitude and phase) are fitted with a common parameter set. The scale constant m brings both quantities (near-field amplitude and phase) to a similar numerical level, therefore the algorithm is considering them equally. As there are more data points at high excitation power (amongst others due to the logarithmic plot fig. 4.20), the low-energy data are weighted by an additional factor w_l.

$$dev = \sum_l w_l \left[(s_{nf,l}^{exp.} - s_{nf,l}^{sim.})^2 + m \cdot (\phi_{nf,l}^{exp.} - \phi_{nf,l}^{sim.})^2 \right] \qquad (4.36)$$

The code excludes several unphysical values by constraining some variables. All together it uses ten fitting parameters:

- Drude model eq. (1.44) (going into the β parameter eq. (1.16) and the Fresnel coefficient r_p eq. (4.34)): τ_{scatt}. The effective mass of the photo-excited electron-hole plasma ($m_{eff} = (1/m_e + 1/m_h)^{-1} m_0 = 0.15 m_0$ combining electron and hole effective masses $m_e = 0.26$ and $m_h = 0.386$) and $\epsilon_L = 11.7$ are considered as constants [73, 74].

- Finite-dipole model eq. (4.35): Tip geometry parameters radius a and length L, and numerical parameter g.

- Fresnel coefficient eq. (4.34): Incident angle Θ (with respect to the tip axis), which is required to calculate r_p.

126
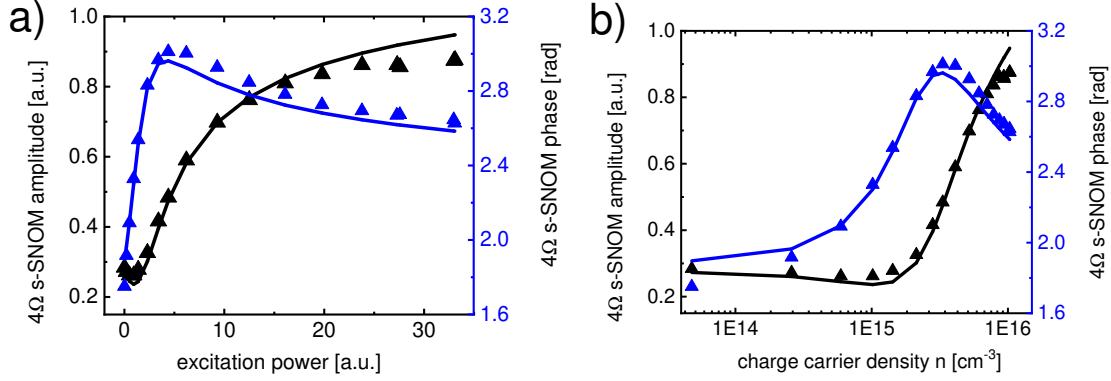
Figure 4.22: Experimental data (triangles; correspond to fig. 4.20) and their fit as a function of a) the experimental controlled parameter P_0 and b) the numerical extracted electron-hole pair density n. Figure taken from [6].

- Unexcited charge carrier density: $n_{initial}$ (this value is simply added to the calculated n eq. (4.33)).

- Photo-excitation + diffusion fit parameters eq. (4.33): $c_1 = a^2/c_{Auger}$, $c_2 = c_{Auger} \cdot \tau_{SRH}$.

- An arbitrary y-scaling factor for the near-field amplitude and an arbitrary phase offset for the near-field phase.

It is possible to fit the experimental data properly with a convincing accordance fig. 4.22. Indeed, at higher excitation values there is a slight deviation, which can have various reasons, e.g. the inaccuracy of the simple Auger recombination model, the simplified diffusion processes, thermal effects, ...

The fitting parameters τ_{scatt}=504 fs, tip radius a=12 nm, tip length L=51 µm, g=0.648, Θ=69.8°, $n_{initial}$=3.7·10^{13}cm^{-3}, $c_{Auger} \cdot \tau_{SRH} = 1.12 \cdot 10^{-43}$m^6 sound reasonable, only the scattering time is higher than expected. In literature scattering times around ∼250 fs are reported for photo-excited charge carriers [195]. The fitting code shifts the scattering time to higher values to follow the slope of the phase curve, even if shorter values are taken initially as start parameters. The maximal phase change in the experimental data fig 4.22 (difference between maximum and minimum value) is quite high (∼1.2 rad), which can be reached within this framework mainly by higher scattering times (see as well later fig. 4.23). Hence, τ_{scatt}=504 fs can be the real physical value, or there are other effects in the experiment that can affect strongly the phase contrast and which are not covered by the model and its equations so far.

In general, the code is numerically unstable and reacts sensitive towards small changes in the start parameters, which have to be optimized as well and have been

chosen carefully here. That undermines the reliability of the single parameters as all the ten parameters are affecting and influencing each other.

In the following, a second measurement scheme is used to demonstrate the quantitative capabilities of the THz s-SNOM to determine single parameters, namely the conductivity and the charge carrier density of doped Si samples.

4.2.3   Si measurement scheme 2: Single data point

In this subsection, the reliable parameter extraction from THz s-SNOM measurements is demonstrated. Two other Si sample with well-known doping densities are used: A Si wafer with a manufacturer specified charge carrier density of $n=2.4(\pm0.5)\cdot10^{15}$cm^{-3}, 2.4 Ωcm, n-doped (phosphorus; fabricated by the Leibniz-Institut für Kristallzüchtung IKZ, Berlin) and a second p-doped (boron) sample with $n=5\cdot10^{16}$cm^{-3} (from MTI Corp., thickness 275 μm, $< 100 >$). Furthermore, to simplify the entire procedure and modelling, instead of photo-excitation just a single THz s-SNOM measurement is taken against a Au reference surface.

The Au is evaporated on another Si substrate positioned on the sample stage next to the Si samples of interest. For the measurements, first the Au reference is taken, then the sample stage is retracted, the other silicon samples are driven consecutively beneath the tip and finally measured. As the tip is stationary ("scanned sample" design), this procedure will not affect the optical interferometer path length. Of course, in this easy example a Au reference surface fabricated directly on the Si samples of interest would mean "shorter" translation ways, however this scheme with different samples is more general and feasible with arbitrary samples. In addition, unstructured homogeneous samples are easier to interpret and avoid disturbing effects from edges [167] and metal structures [141].

The measurement set is performed using the Virginia Diodes source at 260.7 GHz, again in the standard homodyne setup (reference position shift 142.5 μm) with the 90 nm TeraFET detector and a LIA time constant τ_c=100 ms (MFLI device).

First, three different positions on the Au sample are measured (several hundreds of μm away from each other). At each position the two homodyne reference positions are read from the lock-in amplifier for 2Ω, 3Ω, 4Ω. Then three arbitrary positions on each Si substrate are approached and measured. At the end, three Au references are taken again to exclude any interferometer drifts. The near-field amplitudes and phases are calculated (36 data sets; 12 positions times 3 higher harmonics) according to eq. (1.29) and eq. (1.30) and listed in table 4.2.

For further analysis, only the near-field phase is taken into account. The phase is an absolute measure, whereas the near-field amplitude is relative and depends on various proportionality constants, amongst others the THz signal strength, all reflectivity and transmission coefficients of optical instruments, the alignment of the THz beam on the tip, the tip amplitude, the tip shape [25], the detector sensit-

	Au	Au	Au	n-Si	n-Si	n-Si
2Ω r [a.u.]	1926	2002	2036	219	195	206
2Ω Φ [rad]	-0.48	-0.55	-0.55	-0.21	-0.35	-0.39
3Ω r [a.u.]	1138	1213	1229	105	90	97
3Ω Φ [rad]	-0.48	-0.55	-0.54	-0.19	-0.35	-0.38
4Ω r [a.u.]	837	887	902	66	53	58
4Ω Φ [rad]	-0.46	-0.54	-0.54	-0.15	-0.36	-0.37
	p-Si	p-Si	p-Si	Au	Au	Au
2Ω r [a.u.]	556	754	710	2169	2062	839
2Ω Φ [rad]	0.01	0.14	0.00	-0.59	-0.60	-0.52
3Ω r [a.u.]	237	416	365	1342	1247	287
3Ω Φ [rad]	0.06	0.26	0.06	-0.58	-0.61	-0.51
4Ω r [a.u.]	127	286	237	1005	904	122
4Ω Φ [rad]	0.10	0.35	0.10	-0.56	-0.60	-0.49

Table 4.2: s-SNOM amplitude (r) and phase (Φ) measurements on different positions on the Au and both Si substrates.

ivity fig. 3.10, the LIA settings, the overall interferometer alignment... Therefore, the near-field amplitude is less reliable and robust. This is already apparent in table 4.2 for the last reference measurement on the Au surface. The amplitude values are much weaker in comparison to the other positions (e.g. caused by a surface contamination on the sample or a tip degeneration), however the corresponding phase values still fit to the other ones. The effect of dust shadowing the near-field amplitude but barely visible in the phase image has already been reported in the literature [64]. Another example for a surface contamination decreasing the s-SNOM amplitude, but not affecting the phase image, is the measurement in fig. 3.8.

As the near-field phase does not depend strongly on the higher harmonic used, for further analysis all 18 Au and 2 times 9 Si near-field phases are averaged to mean values resulting in phase differences between the Au and the Si samples of $\Delta\phi$=0.235 rad (n-doped) and $\Delta\phi$=0.662 rad (p-doped). The mean deviations of this averaging are 0.03 rad, 0.08 rad, 0.09 rad for Au, n-type Si, and p-type Si, respectively.

In the last step, those phase values have to be translated into charge carrier densities. Here, again the challenge of several available model parameters emerges (see previous section). However, many of them do not influence the near-field phase signal significantly. Exemplary, fig. 4.23 shows the near-field phase for swept parameters in a) the tip radius a (within a range from 1 nm to 1000 nm, which
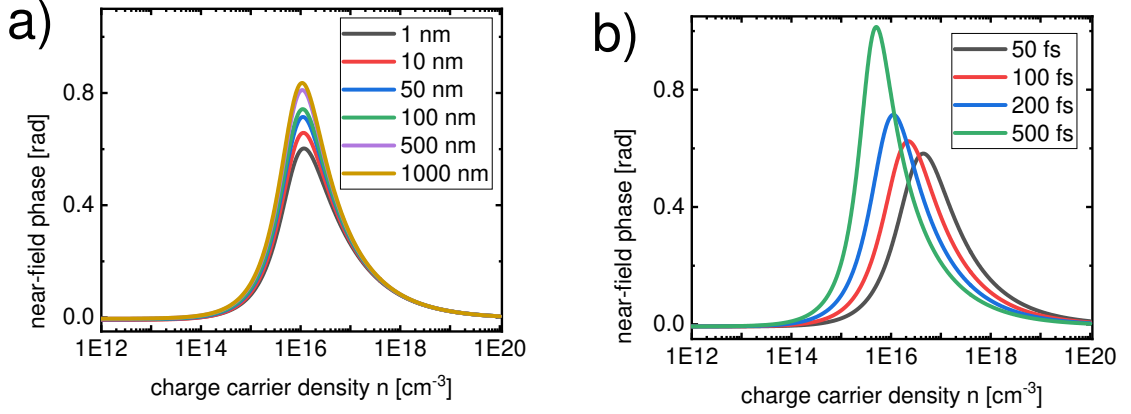
Figure 4.23: s-SNOM phase for n-type Si with swept parameters a) tip radius a and b) Drude scattering time τ_{scatt}. Figure taken from [6].

also covers unrealistic values) and in b) the Drude scattering time τ_{scatt}. The other parameters are taken here as constant with reasonable values: 250 GHz, 3Ω, a=50 nm (if not swept), L=50 μm, τ_{scatt}=200 fs (if not swept), $m_e = 0.26$, g=0.7, $\Theta = 60°$. The majority of these parameters behaves like the tip radius and slightly scales the phase curve around its resonance. The only critical parameter is indeed the scattering time.

In fig. 4.24 the phase responses of the two samples are simulated again with reasonable parameters: The s-SNOM frequency 260.7 GHz, reasonable finite dipole model parameters (a=50 nm, L=50 μm, g=0.7) and geometries ($\Theta = 60°$, mechanical cantilever amplitude 200 nm, minimal tip-sample distance 10 nm), 3Ω, and literature values for the effective masses ($m_e = 0.26$, $m_h = 0.386$ [73]) and $\epsilon_L = 11.7$ [74]. The scattering times τ_{scatt} as a function of the n- and p-doping density for both samples are deduced from a DC mobility $\mu(n)$ model fitted to experimental data in [196]; the model is used here for T=300 K and plotted in fig. 4.25 ($\tau_{scatt}(n) = \frac{\mu(n) \cdot m_0 \cdot m_{e/h}}{q}$); e.g. the two Si substrates used correspond to scattering times of 197 fs (81 fs) for the n-type (p-type) sample (see dashed lines in fig. 4.25).

Now, the corresponding doping densities can be read off (see dashed lines in fig. 4.24) and compared to the manufacturer specifications table 4.3. The last column translates the mean phase deviations of 0.08 rad (0.09 rad) for the n-type (p-type) Si into the corresponding n-intervals based on fig. 4.24.

The accordance to the manufacturer values is convincing. For the p-doped Si the measured near-field phase is even a little higher than the simulated peak value, which can be explained by the uncertainties in the other parameters stretching the phase curve in the y-direction, e.g. fig. 4.23 b).
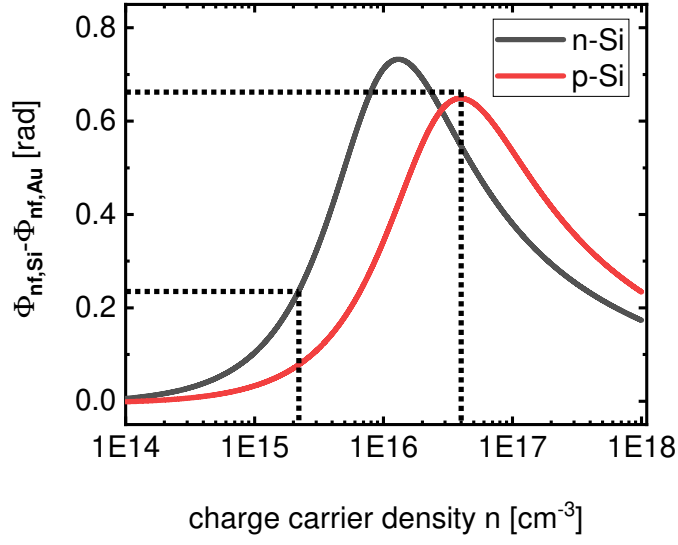
Figure 4.24: Simulated near-field phase response for n-type and p-type Si samples at 260.7 GHz. The dashed lines marked the measured values of the two specimen. Figure taken from [6].
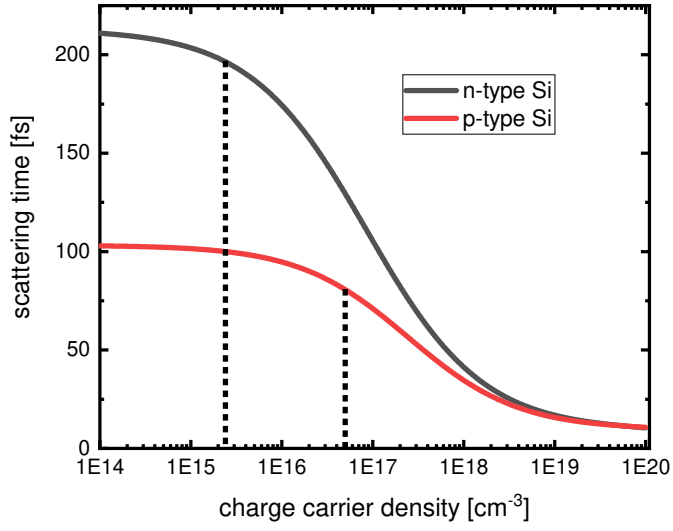

Figure 4.25: The Drude scattering time τ_{scatt} as a function of n calculated with the model introduced by Reggiani et al. [196].

131

	n specification [cm^{-3}]	n measured [cm^{-3}]	uncertainty [cm^{-3}]
n-type Si	$2.4 \cdot 10^{15}$	$2.2 \cdot 10^{15}$	$(1.5\text{-}2.9) \cdot 10^{15}$
p-type Si	$5 \cdot 10^{16}$	$4.0 \cdot 10^{16}$	$(2.2\text{-}8.1) \cdot 10^{16}$

Table 4.3: Comparison between the manufacturer specifications and the s-SNOM based measurements of n for the two samples.

4.2.4 Discussion

The photo-excited sample reveals nearly the entire Drude peak in an impressive quality not reached by means of THz s-SNOM microscopy so far. The essential change to the existing reports is the ability to tune the charge carrier density continuously by the tunable photo-excitation. Although the numerical fit is convincing, the extraction of single Si parameters is difficult due to the complexity of the charge carrier dynamics in Si (excitation, diffusion, recombination) and the near-field modelling itself. Nonetheless, those experiments are a step towards optical-pump THz-probe nanoscopy.

The second scheme, which uses only the phase measurement, is more powerful. The charge carrier density of the Si samples can be extracted with a convincing agreement. In comparison to already reported literature reports, here pure Si samples with well-known parameters are used without any additional structures, and they are referenced to a separate pure Au surface. The focus on only the phase information seems to be promising as well. However, further investigations about the robustness and accuracy of this method are required to develop this technique as a tool for metrological purposes. Another disadvantage is that every THz frequency covers only a certain range of accessible n values (see e.g. fig. 4.12): The steeper the phase curve, the more accurate measurements are possible in principle. Therefore, here the accuracy of the n-type Si table 4.3 is much better. However, there seems to be some uncertainties around the resonance itself fig. 4.23 a) and of course there is always the ambiguity of two n values for each $\Delta\Phi$. On the other side, technical progress in widely tunable THz sources and broad-band detectors can overcome those limitations by measuring multiple discrete frequencies.

5. Conclusion and Outlook

The combination of "Scanning Probe Microscopy" and "electromagnetic radiation" is getting more and more important in the scientific community and leads to a big variety of different techniques partially related to each other, but all with their own strengths and drawbacks, apart from the s-SNOM for example Scanning Near-field Optical Microscopy (SNOM) [11], Tip Enhanced Raman Spectroscopy (TERS) [197], THz Scanning Tunneling Microscopy (THz STM) [198], AFM-IR [199]... The s-SNOM is only one of them. However, it is still emerging, versatile, and powerful for a broad range of possible applications. The THz s-SNOM in particular is right now on the edge from being the subject of research to become an established technique for research. That is reflected in this thesis as well. It contributes to both, the development of the technique itself (by introducing TeraFETs as a new detector type) and specific research topics (conductivity measurements on semiconductors).

In summary, this work contributes to the scientific progress in different fields of s-SNOM research.

The proof of the suitability of the qPlus sensor for near-field measurements has been given. The higher harmonics and first 2d scans show a promising signal quality. However, for a comprehensive evaluation of the entire measurement system and especially the question of any advantages against the state-of-the-art, its spatial s-SNOM resolution has to be tested with suitable samples and the s-SNOM stability of the spring suspended TRIBUS platform in a vacuum chamber has to be evaluated in the ongoing project.

The establishment of a THz s-SNOM is successful as well. The TeraFET detectors show an impressive performance. It is expected, that they will develop to a standard technology in THz science and replace together with other room-temperature working solutions (e.g. Schottky diodes) the liquid helium cooled hot-electron bolometers not only in near-field microscopy, but also in several other THz applications. The next step towards new experimental THz s-SNOM capabilities is already initiated in the "Physikalisches Institut". THz oscillators will be tested

as radiation sources in the s-SNOM; together with the TeraFET detectors, they could become a powerful and versatile on-chip platform and infrastructure for THz near-field microscopy.

The investigation of the plasmonic behaviour of Ag NWs in the nIR and especially the visualization of the tilted pattern based on different modes seamlessly complete other complementary studies that have observed them in far-field configurations. All those studies are in convincing accordance to theoretical simulations. Furthermore, some special aspects of s-SNOM in the nIR are addressed in this thesis, e.g. the effect of the moving Gaussian beam excitation spot and the consequences of plasmon and free-space k-vectors, which are close to each other. For a deeper understanding of the Ag NW equipped THz photomixers, this analysis is only a first step. Unfortunately, the probably most important modes between the NW and the substrate are barely accessible via s-SNOM. Nonetheless, these results are a good foundation for further studies and experiments.

The conductivity and charge carrier measurements of this thesis further develop this application aspect of the THz s-SNOM. In comparison to other literature reports, by using lower THz frequencies, the corresponding Drude response can be reached and especially tuned continuously via photo-excitation of a silicon substrate and the Drude peak is revealed nearly entirely. Therefore, the quantitative fit of the data is possible with a convincing quality. In addition to this performance demonstration, in another experiment the doping densities of silicon substrates are extracted based on a single THz s-SNOM measurement referenced to a Au surface. Especially the near-field phase is a better quantity for this purpose since it is more robust as an absolute quantity in comparison to the near-field amplitude. This latter example is already close to future applications of the THz s-SNOM as a tool for non-contact non-destructive charge carrier density and conductivity imaging on the nanoscale on electronic and semiconducting devices as well as on new materials.

Bibliography

1. Walla, F. *et al.* Near-Field Observation of Guided-Mode Resonances on a Metasurface via Dielectric Nanosphere Excitation. *ACS Photonics* **5,** 4238–4243 (2018).

2. Wiecha, M. M. *et al.* Direct Near-Field Observation of Surface Plasmon Polaritons on Silver Nanowires. *ACS Omega* **4,** 21962–21966 (2019).

3. Soltani, A. *et al.* Direct nanoscopic observation of plasma waves in the channel of a graphene field-effect transistor. *Light: Science & Applications* **9,** 1–7 (2020).

4. Wiecha, M. M. *et al.* Antenna-coupled field-effect transistors as detectors for terahertz near-field microscopy. *Nanoscale Advances* **3,** 1717–1724 (2021).

5. Wiecha, M. M., Soltani, A. & Roskos, H. G. in *Terahertz Technology* (ed You, B.) (IntechOpen, 2021).

6. Wiecha, M. M., Kapoor, R. & Roskos, H. G. Terahertz scattering-type near-field microscopy quantitatively determines the conductivity and charge carrier density of optically doped and impurity-doped silicon. *submitted.*

7. Hecht, E. *Optik* 5., verb. Aufl. (München, 2009).

8. Novotny, L. in *Progress in Optics, Volume 50* 137–184 (2007).

9. Synge, E. H. A suggested method for extending microscopic resolution into the ultra-microscopic region. *Philosophical Magazine* **6,** 356–362 (1928).

10. Zayats, A. V. & Richards, D. in *Nano-optics and near-field optical microscopy* (Boston [u.a.], 2009).

11. Pohl, D. W., Denk, W. & Lanz, M. Optical stethoscopy: Image recording with resolution $\lambda/20$. *Applied Physics Letters* **44,** 651–653 (1984).

12. Courjon, D., Bainier, C., Girard, C. & Vigoureux, J. Near field optics and light confinement. *Annalen der Physik* **505,** 149–158 (1993).

13. Novotny, L. & Hecht, B. *Principles of Nano-Optics* second edition (Cambridge, 2012).

14. *Physik Instrumente (PI) GmbH* visited on 2020-05-14. `https : / / www . physikinstrumente . de / de / produkte / piezoelektrische – wandler – transducer-piezoaktoren/pl0xx-picma-chip-aktoren-100800/`.

15. Eaton, P. & West, P. *Atomic Force Microscopy* (Oxford, 2010).

16. Nolting, W. *Grundkurs: Theoretische Physik : 1. Klassische Mechanik* 8., Auflage (Berlin, 2006).

17. Haugstad, G. *Atomic Force Microscopy - Understanding Basic Modes and Advanced Applications* (Hoboken, 2012).

18. Giessibl, F. J. The qPlus sensor, a powerful core for the atomic force microscope. *Review of Scientific Instruments* **90,** 011101 (2019).

19. García, R. & Pérez, R. Dynamic atomic force microscopy methods. *Surface Science Reports* **47,** 197–301 (2002).

20. Sorensen, A. H., Hvid, U., Mortensen, M. W. & Morch, K. A. Preparation of platinum/iridium scanning probe microscopy tips. *Review of Scientific Instruments* **70,** 3059–3067 (1999).

21. Chang, W.-T. *et al.* Method of electrochemical etching of tungsten tips with controllable profiles. *Review of Scientific Instruments* **83,** 083704 (2012).

22. Giessibl, F. J. Atomic resolution on Si(111)-(7×7) by noncontact atomic force microscopy with a force sensor based on a quartz tuning fork. *Applied Physics Letters* **76,** 1470–1472 (2000).

23. Lantz, M. A. *et al.* Quantitative Measurement of Short-Range Chemical Bonding Forces. *Science* **291,** 2580–2583 (2001).

24. Taubner, T., Hillenbrand, R. & Keilmann, F. Performance of visible and mid-infrared scattering-type near-field optical microscopes. *Journal of Microscopy* **210,** 311–314 (2003).

25. Maissen, C., Chen, S., Nikulina, E., Govyadinov, A. & Hillenbrand, R. Probes for Ultrasensitive THz Nanoscopy. *ACS Photonics* **6,** 1279–1288 (2019).

26. Schnell, M., Carney, P. & Hillenbrand, R. Synthetic optical holography for rapid nanoimaging. *Nature Communications* **5,** 3499 (2014).

27. Yariv, A. & Yeh, P. *Photonics : optical electronics in modern communications* 6. ed. (Oxford [u.a.], 2007).

28. Stinson, H. T. *et al.* Imaging the nanoscale phase separation in vanadium dioxide thin films at terahertz frequencies. *Nature Communications* **9,** 3604 (2018).

29. Zhang, J. *et al.* Terahertz nanoimaging of graphene. *ACS Photonics* **5,** 2645–2651 (2018).

30. Zouaghi, W. *et al.* Broadband terahertz spectroscopy: principles, fundamental research and potential for industrial applications. *European Journal of Physics* **34,** S179–S199 (2013).

31. Haefliger, D., Plitzko, J. M. & Hillenbrand, R. Contrast and scattering efficiency of scattering-type near-field optical probes. *Applied Physics Letters* **85,** 4466–4468 (2004).

32. Jackson, J. D. *Klassische Elektrodynamik* 5. Auflage (Berlin, 2007).

33. Keilmann, F. & Hillenbrand, R. Near-field microscopy by elastic light scattering from a tip. *Philosophical Transactions of the Royal Society of London. Series A: Mathematical, Physical and Engineering Sciences* **362,** 787–805 (2004).

34. Hillenbrand, R., Knoll, B. & Keilmann, F. Pure optical contrast in scattering-type scanning near-field microscopy. *Journal of Microscopy* **202,** 77–83 (2001).

35. Hillenbrand, R. & Keilmann, F. Complex optical constants on a subwavelength scale. *Physical Review Letters* **85,** 3029–3032 (2000).

36. Schmidt, P. *et al.* Nano-imaging of intersubband transitions in van der Waals quantum wells. *Nature Nanotechnology* **13,** 1035–1041 (2018).

37. Amarie, S. & Keilmann, F. Broadband-infrared assessment of phonon resonance in scattering-type near-field microscopy. *Physical Review B* **83,** 045404 (2011).

38. Raschke, M. B. & Lienau, C. Apertureless near-field optical microscopy: Tip–sample coupling in elastic light scattering. *Applied Physics Letters* **83,** 5089–5091 (2003).

39. Ocelic, N. *Quantitative Near-field Phonon-polariton Spectroscopy* PhD thesis (Technische Universität München, 2007).

40. Cvitkovic, A., Ocelic, N. & Hillenbrand, R. Analytical model for quantitative prediction of material contrasts in scattering-type near-field optical microscopy. *Optics Express* **15,** 8550–8565 (2007).

41. Esslinger, M. & Vogelgesang, R. Reciprocity theory of apertureless scanning near-field optical microscopy with point-dipole probes. *ACS Nano* **6,** 8173–8182 (2012).

42. McLeod, A. S. *et al.* Model for quantitative tip-enhanced spectroscopy and the extraction of nanoscale-resolved optical constants. *Physical Review B* **90,** 085136 (2014).

43. Mastel, S. *et al.* Terahertz nanofocusing with cantilevered terahertz-resonant antenna tips. *Nano Letters* **17,** 6526–6533 (2017).

44. Huth, F. *et al.* Resonant antenna probes for tip-enhanced infrared near-field microscopy. *Nano Letters* **13,** 1065–1072 (2013).

45. Esteban, R., Vogelgesang, R. & Kern, K. Tip-substrate interaction in optical near-field microscopy. *Physical Review B* **75,** 195410 (2007).

46. Muller, J., Parent, G. & Lacroix, D. Tip optimization for improvement of detection in scanning near-field optical microscopy. *Journal of Optics* **14,** 075703 (2012).

47. Knoll, B. & Keilmann, F. Enhanced dielectric contrast in scattering-type scanning near-field optical microscopy. *Optics Communications* **182,** 321–328 (2000).

48. *Bruker AFM Probes Nanofabrication Center* visited on 2020-04-01. `https://www.brukerafmprobes.com/`.

49. Bek, A., Vogelgesang, R. & Kern, K. Apertureless scanning near field optical microscope with sub-10 nm resolution. *Review of Scientific Instruments* **77,** 043703 (2006).

50. *Nanoworld AG* visited on 2020-04-01. `https://www.nanoworld.com/tapping-mode-platinum-coated-afm-tip-arrow-ncpt`.

51. Rang, M. *et al.* Optical near-field mapping of plasmonic nanoprisms. *Nano Letters* **8,** 3357–3363 (2008).

52. Schnell, M. *et al.* Amplitude- and phase-resolved near-field mapping of infrared antenna modes by transmission-mode scattering-type near-field microscopy. *The Journal of Physical Chemistry C* **114,** 7341–7345 (2010).

53. Vasconcelos, T. L. *et al.* Tuning localized surface plasmon resonance in scanning near-field optical microscopy probes. *ACS Nano* **9,** 6297–6304 (2015).

54. Brehm, M., Schliesser, A., Čajko, F., Tsukerman, I. & Keilmann, F. Antenna-mediated back-scattering efficiency in infrared near-field microscopy. *Optics Express* **16,** 11203–11215 (2008).

55. Von Ribbeck, H.-G. *et al.* Spectroscopic THz near-field microscope. *Optics Express* **16,** 3430–3438 (2008).

56. Siday, T., Hale, L. L., Hermans, R. I. & Mitrofanov, O. Resonance-Enhanced Terahertz Nanoscopy Probes. *ACS Photonics* **7,** 596–601 (2020).

57. *Rocky Mountain Nanotechnology LLC* visited on 2020-04-01. `https://rmnano.com/tech-data`.

58. Aghamiri, N. A. *et al.* Hyperspectral time-domain terahertz nano-imaging. *Optics Express* **27,** 24231–24242 (2019).

59. Giordano, M. C. *et al.* Phase-resolved terahertz self-detection near-field microscopy. *Optics Express* **26,** 18423–18435 (2018).

60. Ocelic, N., Huber, A. & Hillenbrand, R. Pseudoheterodyne detection for background-free near-field spectroscopy. *Applied Physics Letters* **89,** 101124 (2006).

61. Gomez, L. *et al.* Apertureless scanning near-field optical microscopy: a comparison between homodyne and heterodyne approaches. *JOSA B* **23,** 823–833 (2006).

62. Schnell, M., Garcia-Etxarri, A., Alkorta, J., Aizpurua, J. & Hillenbrand, R. Phase-resolved mapping of the near-field vector and polarization state in nanoscale antenna gaps. *Nano Letters* **10,** 3524–3528 (2010).

63. Esslinger, M., Dorfmüller, J., Khunsin, W., Vogelgesang, R. & Kern, K. Background-free imaging of plasmonic structures with cross-polarized apertureless scanning near-field optical microscopy. *Review of Scientific Instruments* **83,** 033704 (2012).

64. Liewald, C. *et al.* All-electronic terahertz nanoscopy. *Optica* **5,** 159–163 (2018).

65. Abramowitz, M. & Stegun, I. A. *Handbook of Mathematical Functions with Formulas, Graphs, and Mathematical Tables* (1972).

66. *Alem, M., Zurich Instruments AG* visited on 2020-04-06. `https://blogs.zhinst.com/mehdia/2018/03/20/how-to-demodulate-multi-frequency-signals-such-as-am-fm-and-pm/`.

67. Degl'Innocenti, R. *et al.* Terahertz Nanoscopy of Plasmonic Resonances with a Quantum Cascade Laser. *ACS Photonics* **4,** 2150–2157 (2017).

68. Huber, A. J., Kazantsev, D., Keilmann, F., Wittborn, J. & Hillenbrand, R. Simultaneous IR Material Recognition and Conductivity Mapping by Nanoscale Near-Field Microscopy. *Advanced Materials* **19,** 2209–2212 (2007).

69. Lloyd-Hughes, J. & Jeon, T.-I. A review of the terahertz conductivity of bulk and nano-materials. *Journal of Infrared, Millimeter, and Terahertz Waves* **33,** 871–925 (2012).

70. Guo, X., Bertling, K. & Rakic, A. D. Optical constants from scattering-type scanning near-field optical microscope. *Applied Physics Letters* **118** (2021).

71. Keilmann, F., Huber, A. J. & Hillenbrand, R. Nanoscale Conductivity Contrast by Scattering-Type Near-Field Optical Microscopy in the Visible, Infrared and THz Domains. *Journal of Infrared Milimeter and Terahertz Waves* **30.** 33rd International Conference on Infrared, Millimeter, and Terahertz Waves, Pasadena, CA, SEP, 2008, 1255–1268 (2009).

72. Huber, A. J., Keilmann, F., Wittborn, J., Aizpurua, J. & Hillenbrand, R. Terahertz near-field nanoscopy of mobile carriers in single semiconductor nanodevices. *Nano Letters* **8,** 3766–3770 (2008).

73. *Principles of Semiconductor Devices, Bart Van Zeghbroeck* visited on 2021-05-18. `https://ecee.colorado.edu/~bart/book/effmass.htm`.

74. *NSM Archive* visited on 2021-05-18. `http://www.ioffe.ru/SVA/NSM/Semicond/Si/optic.html`.

75. Jacoboni, C., Canali, C., Ottaviani, G. & Alberigi Quaranta, A. A review of some charge transport properties of silicon. *Solid-State Electronics* **20,** 77–89 (1977).

76. Ordal, M. A., Bell, R. J., Alexander, R. W., Long, L. L. & Querry, M. R. Optical properties of fourteen metals in the infrared and far infrared: Al, Co, Cu, Au, Fe, Pb, Mo, Ni, Pd, Pt, Ag, Ti, V, and W. *Applied Optics* **24,** 4493–4499 (1985).

77. Ordal, M. A. *et al.* Optical properties of the metals Al, Co, Cu, Au, Fe, Pb, Ni, Pd, Pt, Ag, Ti, and W in the infrared and far infrared. *Applied Optics* **22,** 1099–1119 (1983).

78. Chen, C. *et al.* Terahertz Nanoimaging and Nanospectroscopy of Chalcogenide Phase-Change Materials. *ACS Photonics* **7,** 3499–3506 (2020).

79. Qazilbash, M. M. *et al.* Infrared spectroscopy and nano-imaging of the insulator-to-metal transition in vanadium dioxide. *Physical Review B* **79** (2009).

80. Huth, F. *et al.* Nano-FTIR absorption spectroscopy of molecular fingerprints at 20 nm spatial resolution. *Nano Letters* **12,** 3973–3978 (2012).

81. Moon, K. *et al.* Subsurface nanoimaging by broadband terahertz pulse near-field microscopy. *Nano Letters* **15,** 549–552 (2015).

82. Govyadinov, A. A. *et al.* Recovery of permittivity and depth from near-field data as a step toward infrared nanotomography. *ACS Nano* **8,** 6911–6921 (2014).

83. Mester, L., Govyadinov, A. A., Chen, S., Goikoetxea, M. & Hillenbrand, R. Subsurface chemical nanoidentification by nano-FTIR spectroscopy. *Nature Communications* **11** (2020).

84. Czycholl, G. *Theoretische Festkörperphysik* 3. Auflage (Berlin, 2008).

85. Maier, S. A. *Plasmonics: Fundamentals and Applications* (Boston, 2007).

86. Klingshirn, C. F. *Semiconductor Optics* Third edition (Berlin, 2007).

87. Basov, D. N., Fogler, M. M. & De Abajo, F. J. G. Polaritons in van der Waals materials. *Science* **354,** aag1992 (2016).

88. Zayats, A. V. & Smolyaninov, I. I. Near-field photonics: surface plasmon polaritons and localized surface plasmons. *Journal of Optics A: Pure and Applied Optics* **5,** 16–50 (2003).

89. Walla, F. *et al.* Anisotropic excitation of surface plasmon polaritons on a metal film by a scattering-type scanning near-field microscope with a non-rotationally-symmetric probe tip. *Nanophotonics* **7,** 269–276 (2018).

90. Li, Y., Zhou, N., Kinzel, E. C., Ren, X. & Xu, X. The origin of interferometric effect involving surface plasmon polariton in scattering near-field scanning optical microscopy. *Optics Express* **22,** 2965–2972 (2014).

91. Chen, J. *et al.* Optical nano-imaging of gate-tunable graphene plasmons. *Nature* **487,** 77–81 (2012).

92. Fei, Z. *et al.* Gate-tuning of graphene plasmons revealed by infrared nano-imaging. *Nature* **487,** 82–85 (2012).

93. Huber, A., Ocelic, N., Kazantsev, D. & Hillenbrand, R. Near-field imaging of mid-infrared surface phonon polariton propagation. *Applied Physics Letters* **87,** 081103 (2005).

94. Li, P. *et al.* Optical nanoimaging of hyperbolic surface polaritons at the edges of van der Waals materials. *Nano Letters* **17,** 228–235 (2017).

95. Huber, A. J., Ocelic, N. & Hillenbrand, R. Local excitation and interference of surface phonon polaritons studied by near-field infrared microscopy. *Journal of Microscopy* **229,** 389–395 (2008).

96. Dai, S. *et al.* Tunable phonon polaritons in atomically thin van der Waals crystals of boron nitride. *Science* **343,** 1125–1129 (2014).

97. Chaudhary, K. *et al.* Polariton nanophotonics using phase-change materials. *Nature Communications* **10,** 1–6 (2019).

98. Dai, S. *et al.* Subdiffractional focusing and guiding of polaritonic rays in a natural hyperbolic material. *Nature Communications* **6,** 1–7 (2015).

99. Babicheva, V. E. *et al.* Near-field surface waves in few-layer MoS_2. *ACS Photonics* **5,** 2106–2112 (2018).

100. Hu, F. *et al.* Imaging exciton–polariton transport in $MoSe_2$ waveguides. *Nature Photonics* **11,** 356–360 (2017).

101. Low, T. *et al.* Polaritons in layered two-dimensional materials. *Nature Materials* **16,** 182–194 (2017).

102. Dai, S. *et al.* Graphene on hexagonal boron nitride as a tunable hyperbolic metamaterial. *Nature Nanotechnology* **10,** 682–686 (2015).

103. Huber, M. A. *et al.* Femtosecond photo-switching of interface polaritons in black phosphorus heterostructures. *Nature Nanotechnology* **12,** 207–211 (2017).

104. Barcelos, I. D. *et al.* Graphene/h-BN plasmon–phonon coupling and plasmon delocalization observed by infrared nano-spectroscopy. *Nanoscale* **7,** 11620–11625 (2015).

105. Dai, S. *et al.* Efficiency of launching highly confined polaritons by infrared light incident on a hyperbolic material. *Nano Letters* **17,** 5285–5290 (2017).

106. Ni, G. X. *et al.* Fundamental limits to graphene plasmonics. *Nature* **557,** 530–533 (2018).

107. Yoxall, E. *et al.* Direct observation of ultraslow hyperbolic polariton propagation with negative phase velocity. *Nature Photonics* **9,** 674–678 (2015).

108. Schmidt, M. A. & Russell, P. J. Long-range spiralling surface plasmon modes on metallic nanowires. *Optics Express* **16,** 13617–13623 (2008).

109. Chang, D. E., Sørensen, A. S., Hemmer, P. R. & Lukin, M. D. Strong coupling of single emitters to surface plasmons. *Physical Review B* **76,** 035420 (2007).

110. Pfeiffer, C. A., Economou, E. N. & Ngai, K. L. Surface polaritons in a circularly cylindrical interface: surface plasmons. *Physical Review B* **10,** 3038–3051 (1974).

111. Weeber, J.-C., Dereux, A., Girard, C., Krenn, J. R. & Goudonnet, J.-P. Plasmon polaritons of metallic nanowires for controlling submicron propagation of light. *Physical Review B* **60,** 9061–9068 (1999).

112. Wei, H., Pan, D. & Xu, H. Routing of surface plasmons in silver nanowire networks controlled by polarization and coating. *Nanoscale* **7,** 19053–19059 (2015).

113. Zhang, S. *et al.* Chiral surface plasmon polaritons on metallic nanowires. *Physical Review Letters* **107,** 096801 (2011).

114. Jia, Z., Wei, H., Pan, D. & Xu, H. Direction-resolved radiation from polarization-controlled surface plasmon modes on silver nanowire antennas. *Nanoscale* **8,** 20118–20124 (2016).

115. Sanders, A. W. *et al.* Observation of plasmon propagation, redirection, and fan-out in silver nanowires. *Nano Letters* **6,** 1822–1826 (2006).

116. Song, M. *et al.* Imaging symmetry-selected corner plasmon modes in penta-twinned crystalline Ag nanowires. *ACS Nano* **5,** 5874–5880 (2011).

117. Shegai, T. *et al.* Unidirectional broadband light emission from supported plasmonic nanowires. *Nano letters* **11,** 706–711 (2011).

118. Zhang, S. & Xu, H. Optimizing substrate-mediated plasmon coupling toward high-performance plasmonic nanowire waveguides. *ACS Nano* **6,** 8128–8135 (2012).

119. Wei, H. *et al.* Plasmon waveguiding in nanowires. *Chemical Reviews* **118,** 2882–2926 (2018).

120. Kusar, P., Gruber, C., Hohenau, A. & Krenn, J. R. Measurement and reduction of damping in plasmonic nanowires. *Nano Letters* **12,** 661–665 (2012).

121. Zhang, D. *et al.* Extending the propagation distance of a silver nanowire plasmonic waveguide with a dielectric multilayer substrate. *Nano Letters* **18,** 1152–1158 (2018).

122. Fang, Y. & Sun, M. Nanoplasmonic waveguides: towards applications in integrated nanophotonic circuits. *Light: Science & Applications* **4,** e294 (2015).

123. Rossouw, D., Couillard, M., Vickery, J., Kumacheva, E. & Botton, G. A. Multipolar plasmonic resonances in silver nanowire antennas imaged with a subnanometer electron probe. *Nano Letters* **11,** 1499–1504 (2011).

124. Ditlbacher, H. *et al.* Silver nanowires as surface plasmon resonators. *Physical Review Letters* **95,** 257403 (2005).

125. Fang, Z. *et al.* Plasmonic coupling of bow tie antennas with Ag nanowire. *Nano Letters* **11,** 1676–1680 (2011).

126. Jones, A. C. *et al.* Mid-IR plasmonics: near-field imaging of coherent plasmon modes of silver nanowires. *Nano Letters* **9,** 2553–2558 (2009).

127. Dorfmueller, J. *et al.* Fabry-Perot resonances in one-dimensional plasmonic nanostructures. *Nano Letters* **9,** 2372–2377 (2009).

128. Zhou, Y. *et al.* Tunable Low Loss 1D Surface Plasmons in InAs Nanowires. *Advanced Materials* **30,** 1802551 (2018).

129. Knoll, B. & Keilmann, F. Scanning microscopy by mid-infrared near-field scattering. *Applied Physics A: Materials Science & Processing* **66,** 477–481 (1998).

143

130. Meyns, M., Primpke, S. & Gerdts, G. Library based identification and characterisation of polymers with nano-FTIR and IR-sSNOM imaging. *Analytical Methods* **11,** 5195–5202 (2019).

131. *Kolmar Technologies Inc.* visited on 2020-08-21. `http://www.kolmartech.com/kld_ser.htm`.

132. Keilmann, F. FIR microscopy. *Infrared Physics & Technology* **36,** 217–224 (1995).

133. Knoll, B. & Keilmann, F. Electromagnetic fields in the cutoff regime of tapered metallic waveguides. *Optics Communications* **162,** 177–181 (1999).

134. Piednoir, A., Licoppe, C. & Creuzet, F. Imaging and local infrared spectroscopy with a near field optical microscope. *Optics Communications* **129,** 414–422 (1996).

135. Vangindertael, J. *et al.* An introduction to optical super-resolution microscopy for the adventurous biologist. *Methods and Applications in Fluorescence* **6,** 022003 (2018).

136. *The Nobel Foundation* visited on 2021-02-26. `https://www.nobelprize.org/prizes/chemistry/2014/press-release/`.

137. Lereu, A. L., Passian, A. & Dumas, P. Near field optical microscopy: a brief review. *International Journal of Nanotechnology* **9,** 488–501 (2012).

138. Hecht, B. *et al.* Scanning near-field optical microscopy with aperture probes: Fundamentals and applications. *The Journal of Chemical Physics* **112,** 7761–7774 (2000).

139. Prämassing, M., Liebtrau, M., Schill, H. J., Irsen, S. & Linden, S. Interferometric near-field characterization of plasmonic slot waveguides in single-and poly-crystalline gold films. *Optics Express* **28,** 12998–13007 (2020).

140. Kuschewski, F. *et al.* Narrow-band near-field nanoscopy in the spectral range from 1.3 to 8.5 THz. *Applied Physics Letters* **108,** 113102 (2016).

141. Chen, X. *et al.* THz Near-Field Imaging of Extreme Subwavelength Metal Structures. *ACS Photonics* **7,** 687–694 (2020).

142. Dai, G. *et al.* W-band near-field microscope. *IEEE Access* **7,** 48060–48067 (2019).

143. Mastel, S. *et al.* Understanding the Image Contrast of Material Boundaries in IR Nanoscopy Reaching 5 nm Spatial Resolution. *ACS Photonics* **5,** 3372–3378 (2018).

144. Yang, Z. *et al.* Near-Field Nanoscopic Terahertz Imaging of Single Proteins. *Small,* 2005814 (2020).

145. De Oliveira, T. V. A. G. *et al.* Nanoscale-Confined Terahertz Polaritons in a van der Waals Crystal. *Advanced Materials,* 2005777 (2020).

146. Wehmeier, L. *et al.* Phonon-induced near-field resonances in multiferroic BiFeO$_3$ thin films at infrared and THz wavelengths. *Applied Physics Letters* **116,** 071103 (2020).

147. Walla, F. W. *Implementation of a Scattering-type Near-Field Optical Microscope for the Characterisation of Electromagnetic Surface Modes in Metallic Nanostructures* Master thesis (Johann Wolfgang Goethe-Universität Frankfurt am Main, 2016).

148. Dyakonov, M. & Shur, M. Shallow water analogy for a ballistic field effect transistor: New mechanism of plasma wave generation by dc current. *Phys. Rev. Lett.* **71,** 2465–2468 (1993).

149. Dyakonov, M. & Shur, M. Detection, mixing, and frequency multiplication of terahertz radiation by two-dimensional electronic fluid. *IEEE Transactions on Electron Devices* **43,** 380–387 (1996).

150. Pogna, E. A. A. *et al.* Unveiling the detection dynamics of semiconductor nanowire photodetectors by terahertz near-field nanoscopy. *Light: Science & Applications* **9,** 189 (2020).

151. Bauer, M. *Hydrodynamic modeling and experimental characterization of the plasmonic and thermoelectric terahertz response of field-effect transistors with integrated broadband antennas in AlGaN/GaN HEMTs and CVD-grown graphene* PhD thesis (Johann Wolfgang Goethe-Universität Frankfurt am Main, 2017).

152. Knap, W. *et al.* Nanometer size field effect transistors for terahertz detectors. *Nanotechnology* **24,** 214002 (2013).

153. Preu, S. *et al.* Ultra-fast transistor-based detectors for precise timing of near infrared and THz signals. *Optics Express* **21,** 17941–17950 (2013).

154. Knap, W. *et al.* Field Effect Transistors for Terahertz Detection: Physics and First Imaging Applications. *Journal of Infrared Millimeter and Terahertz Waves* **30,** 1319–1337 (2009).

155. Knap, W. & Dyakonov, M. in *Handbook of Terahertz Technology for Imaging, Sensing and Communications* (ed Saeedkia, D.) 1st Edition, 121–155 (Woodhead Publishing, 2013).

156. Sakhno, M., Golenkov, A. & Sizov, F. Uncooled detector challenges: Millimeter-wave and terahertz long channel field effect transistor and Schottky barrier diode detectors. *Journal of Applied Physics* **114,** 164503 (2013).

157. Bauer, M. *et al.* A High-Sensitivity AlGaN/GaN HEMT Terahertz Detector With Integrated Broadband Bow-Tie Antenna. *IEEE Transactions on Terahertz Science and Technology* **9,** 430–444 (2019).

158. Yuan, H., Voss, D., Lisauskas, A., Mundy, D. & Roskos, H. G. 3D Fourier imaging based on 2D heterodyne detection at THz frequencies. *APL Photonics* **4,** 106108 (2019).

159. Čibiraitė-Lukenskienė, D. *et al.* Passive Detection and Imaging of Human Body Radiation Using an Uncooled Field-Effect Transistor-Based THz Detector. *Sensors* **20,** 4087 (2020).

160. Čibiraitė-Lukenskienė, D. *et al. Field-effect transistor-based detector for hyperspectral THz imaging* in *Proc. of the 23rd International Microwave and Radar Conference (MIKON)* (IEEE, 2020), 1–5.

161. Wiecha, M. M. *Further Development and Characterization of a scattering-type Scanning Near-field Optical Microscope (s-SNOM) and Infrared Measurements on Boron Nitride* Master thesis (Johann Wolfgang Goethe-Universität Frankfurt am Main, 2016).

162. De Wilde, Y., Formanek, F. & Aigouy, L. Apertureless near-field scanning optical microscope based on a quartz tuning fork. *Review of Scientific Instruments* **74,** 3889–3891 (2003).

163. Raschke, M. B. & Lienau, C. Apertureless near-field optical microscopy: Tip–sample coupling in elastic light scattering. *Applied Physics Letters* **83,** 5089–5091 (2003).

164. Merziger, G., Mühlbach, G., Wille, D. & T, W. *Formeln + Hilfen - Höhere Mathematik* 6. Auflage (Barsinghausen, 2010).

165. Bronstein, I. N. & Semendjajew, K. A. *Taschenbuch der Mathematik* 18. Auflage (Frankfurt/Main, 1979).

166. *Access Laser Company* visited on 2020-06-03. `https://www.accesslaser.com/low-power-co2-lasers-emphasize-stability-and-tunability/`.

167. Babicheva, V. E., Gamage, S., Stockman, M. I. & Abate, Y. Near-field edge fringes at sharp material boundaries. *Optics Express* **25,** 23935–23944 (2017).

168. Yao, Z. *et al.* Photo-induced terahertz near-field dynamics of graphene/InAs heterostructures. *Optics Express* **27,** 13611–13623 (2019).

169. Preu, S., Döhler, G. H., Malzer, S., Wang, L. J. & Gossard, A. C. Tunable, continuous-wave terahertz photomixer sources and applications. *Journal of Applied Physics* **109,** 061301 (2011).

170. Duffy, S. M., Verghese, S. & McIntosh, K. A. in *Sensing with Terahertz Radiation* (ed Mittleman, D.) 193–236 (Berlin, Heidelberg, 2003).

171. Al-Daffaie, S., Yilmazoglu, O., Küppers, F. & Hartnagel, H. L. 1-D and 2-D nanocontacts for reliable and efficient terahertz photomixers. *IEEE Transactions on Terahertz Science and Technology* **5,** 398–405 (2015).

172. Johnson, P. B. & Christy, R.-W. Optical constants of the noble metals. *Physical Review B* **6,** 4370–4379 (1972).

173. Adachi, S. Optical dispersion relations for GaP, GaAs, GaSb, InP, InAs, InSb, $Al_xGa_{1-x}As$, and $In_{1-x}Ga_xAs_yP_{1-y}$. *Journal of Applied Physics* **66,** 6030–6040 (1989).

174. Tsai, Y.-J., Chang, C.-Y., Yu, P. & Ahn, H. *Oxidation of Ag nanowires studied by terahertz spectroscopy* in *Conference on Lasers and Electro-Optics (CLEO)* (2013).

175. Knoll, B. & Keilmann, F. Infrared conductivity mapping for nanoelectronics. *Applied Physics Letters* **77,** 3980–3982 (2000).

176. Stiegler, J. M. *et al.* Nanoscale Free-Carrier Profiling of Individual Semiconductor Nanowires by Infrared Near-Field Nanoscopy. *Nano Letters* **10,** 1387–1392 (2010).

177. Altermatt, P., Schmidt, J., Heiser, G. & Aberle, A. Assessment and parameterisation of Coulomb-enhanced Auger recombination coefficients in lowly injected crystalline silicon. *Journal of Applied Physics* **82,** 4938–4944 (1997).

178. Li, S. S. in *Semiconductor Physical Electronics* (ed Li, S. S.) 134–170 (New York, NY, 2006).

179. Sinton, R. & Swanson, R. Recombination in highly injected silicon. *IEEE Transactions on Electron Devices* **34,** 1380–1389 (1987).

180. Tyagi, M. & Van Overstraeten, R. Minority-carrier recombination in heavily-doped silicon. *Solid-state Electronics* **26,** 577–597 (1983).

181. Rein, S., Rehrl, T., Warta, W. & Glunz, S. Lifetime spectroscopy for defect characterization: Systematic analysis of the possibilities and restrictions. *Journal of Applied Physics* **91,** 2059–2070 (2002).

182. Kerr, M. & Cuevas, A. General parameterization of Auger recombination in crystalline silicon. *Journal of Applied Physics* **91,** 2473–2480 (2002).

183. Jonak-Auer, I., Synooka, O., Kraxner, A. & Roger, F. *Characterization of various Si-photodiode junction combinations and layout specialities in 0.18 mu m CMOS and HV-CMOS technologies* in *6th International Conference on Materials and Applications for Sensors and Transducers, (IC-MAST 2016)* **939** (2017).

184. Boyd, K. M. W. & Kleiman, R. N. Diffusion and recombination of optically-injected carriers in a semiconductor wafer in 3-dimensions. *Journal of Applied Physics* **126** (2019).

185. Giesecke, J. A., Schindler, F., Buehler, M., Schubert, M. C. & Warta, W. Accurate determination of minority carrier mobility in silicon from quasi-steady-state photoluminescence. *Journal of Applied Physics* **113** (2013).

186. Luke, K. & Cheng, L. Analysis of the interaction of a laser-pulse with a silicon-wafer - Determination of bulk lifetime and surface recombination veolcity. *Journal of Applied Physics* **61,** 2282–2293 (1987).

187. Nilsson, N. Determination of carrier lifetime, diffusion length, and surface recombination velocity in semiconductors from photo-excited infrared absorption. *Solid-State Electronics* **7,** 455–463 (1964).

188. Crank, J. *The Mathematics of Diffusion* Second Edition (Clarendon Press, Oxford, 1975).

189. Milner, A. A., Zhang, K., Garmider, V. & Prior, Y. Heating of an Atomic Force Microscope tip by femtosecond laser pulses. *Applied Physics A - Material Science & Processing* **99,** 1–8 (2010).

190. Han, J., Zhu, C., Liu, J. & He, Y. Dependence of the resonance frequency of thermally excited microcantilever resonators on temperature. *Sensors and Actuators A - Physical* **101,** 37–41 (2002).

191. Farraro, R. & McLellan, R. B. Temperature dependence of the Young's modulus and shear modulus of pure nickel, platinum, and molybdenum. *Metallurgical Transactions A* **8,** 1563–1565 (1977).

192. Aguilar Sandoval, F., Geitner, M., Bertin, E. & Bellon, L. Resonance frequency shift of strongly heated micro-cantilevers. *Journal of Applied Physics* **117** (2015).

193. McCarthy, B., Zhao, Y., Grover, R. & Sarid, D. Enhanced Raman scattering for temperature measurement of a laser-heated atomic force microscope tip. *Applied Physics Letters* **86** (2005).

194. *MathWorks Help Center* visited on 2021-04-30. `https://de.mathworks.com/help/matlab/ref/fminsearch.html`.

195. Meng, F., Thomson, M. D., Sernelius, B. E., Jörger, M. & Roskos, H. G. Ultrafast dynamic conductivity and scattering rate saturation of photoexcited charge carriers in silicon investigated with a midinfrared continuum probe. *Physical Review B* **91,** 075201 (2015).

196. Reggiani, S. *et al.* Electron and hole mobility in silicon at large operating temperatures - Part I: Bulk mobility. *IEEE Transactions on Electron Devices* **49,** 490–499 (2002).

197. Deckert-Gaudig, T., Taguchi, A., Kawata, S. & Deckert, V. Tip-enhanced Raman spectroscopy - from early developments to recent advances. *Chemical Society Reviews* **46,** 4077–4110 (2017).

198. Cocker, T. L., Peller, D., Yu, P., Repp, J. & Huber, R. Tracking the ultrafast motion of a single molecule by femtosecond orbital imaging. *NATURE* **539,** 263+ (2016).

199. Dazzi, A. & Prater, C. B. AFM-IR: Technology and Applications in Nanoscale Infrared Spectroscopy and Chemical Imaging. *Chemical Reviews* **117,** 5146–5173 (2017).

200. Weisstein, E. W. *Jacobi-Anger Expansion* visited on 2020-04-15. `https://mathworld.wolfram.com/Jacobi-AngerExpansion.html`.

201. *MATLAB R2018b - Technical documentation and help center - page about "atan2" function*

202. *Zurich Instruments AG* visited on 2021-02-26. `https://www.zhinst.com/americas/products/mf-md-multi-demodulator?from=MFLI`.

6 Appendix

6.1 Detailed mathematical descriptions

6.1.1 Useful trigonometric identities [164]

$$sin^2x = 0.5 \cdot (1 - cos(2x)) \tag{6.1}$$

$$sinx \cdot siny = \frac{1}{2}\left[cos(x - y) - cos(x + y)\right] \tag{6.2}$$

$$cos(x + y) = cosx \cdot cosy + sinx \cdot siny \tag{6.3}$$

$$sinx \cdot cosy = \frac{1}{2}\left[sin(x - y) + sin(x + y)\right] \tag{6.4}$$

$$sin^2x + cos^2x = 1 \tag{6.5}$$

Jacobi-Anger expansion eq. (6.6) and its real-valued variations eq. (6.7) and eq. (6.8) containing the Bessel functions of the first kind $J_n(\gamma)$. [65, 200].

$$e^{izcos\theta} = \sum_{n=-\infty}^{\infty} i^n J_n(z)e^{in\theta} \tag{6.6}$$

$$cos(zcos\theta) = J_0(z) + 2\sum_{n=1}^{\infty}(-1)^n J_{2n}(z)cos(2n\theta) \tag{6.7}$$

$$sin(zcos\theta) = -2\sum_{n=1}^{\infty}(-1)^n J_{2n-1}(z)cos(2(n - 1)\theta) \tag{6.8}$$

6.1.2 Multiplying two electromagnetic waves

$$E_1(t) = E_1 \cdot sin(\omega_1 t + \phi_1) \tag{6.9}$$

$$E_2(t) = E_2 \cdot sin(\omega_2 t + \phi_2) \tag{6.10}$$

Multiplying[1] two arbitrary electromagnetic waves eq. (6.9) and eq. (6.10) results in

$$E_1(t) \cdot E_2(t) = E_1 E_2 sin(\omega_1 t + \phi_1) \cdot sin(\omega_2 t + \phi_2)$$
$$\stackrel{eq.(6.2)}{=} 0.5 \cdot E_1 E_2 \left[cos((\omega_1 - \omega_2)t + \phi_1 - \phi_2) - cos((\omega_1 + \omega_2)t + \phi_1 + \phi_2) \right] . \tag{6.11}$$

If intensities $I = E^2$ are measured, the bandwidth of the detector for the majority of applications is much slower than the light frequency ω, therefore the second cosine term in eq. (6.11) oscillating at $\omega_1 + \omega_2$ is vanishing[2], which yields

$$E_1(t) \cdot E_2(t) \stackrel{detector}{=} 0.5 \cdot E_1 E_2 cos((\omega_1 - \omega_2)t + \phi_1 - \phi_2) . \tag{6.12}$$

If mixing of two fields with the same $\omega = \omega_1 = \omega_2$ is considered, eq. (6.12) simplifies further to a static term without any time dependence:

$$E_1(t) \cdot E_2(t) \mapsto 0.5 \cdot E_1 E_2 cos(\phi_1 - \phi_2) = 0.5 \cdot E_1 E_2 cos\Delta\phi . \tag{6.13}$$

Multiplying a sine and a cosine wave instead of eq. (6.9) and eq. (6.10) results in similar identities, only eq. (6.4) has to be used. Now, the fast oscillating vanishing term is a sine as well as the remaining one; eq. (6.12) and eq. (6.13) translate into eq. (6.14) and eq. (6.15).

$$E_1(t) \cdot E_2(t) \stackrel{detector}{=} 0.5 \cdot E_1 E_2 sin((\omega_1 - \omega_2)t + \phi_1 - \phi_2) \tag{6.14}$$

$$E_1(t) \cdot E_2(t) \mapsto 0.5 \cdot E_1 E_2 sin(\phi_1 - \phi_2) = 0.5 \cdot E_1 E_2 sin\Delta\phi \tag{6.15}$$

---

[1]For example, if two electromagnetic waves are mixed in an intensity sensitive detector $|E_1 + E_2|^2$, next to the squared terms $|E_1|^2$ and $|E_2|^2$, the cross-term $E_1 \cdot E_2$ occurs, which is treated in this subsection.

[2]An alternative way to get rid of those fast oscillating terms is using real values of a complex representation of the electric fields [27]. However, using real values directly is the more rigorous derivation.

6.1.3 Mathematical description of a lock-in amplifier

A lock-in amplifier (LIA) isolates a small bandwidth around a single frequency within a signal. Mathematically, it multiplies the signal (e.g. eq. (6.16); here already the isolated component of ω) with two ($\frac{\pi}{2}$ phase shifted) references of the desired frequency eq. (6.17), eq. (6.18), and the resulting signals are guided through a low-pass filter leading to the X and Y component of the LIA eq. (6.19) and eq. (6.20). All other contributions expect the desired frequency are cancelled since the multiplication of two sine or cosine waves with different frequencies integrated over a sufficient long time constant goes to 0 (their product oscillates around 0). The longer the time constant, the smaller the bandwidth around the desired frequency that still contributes to the LIA signal.

$$E(t) = E \cdot sin(\omega t + \phi) \tag{6.16}$$

$$R_1(t) = R \cdot sin(\omega t + \phi_1) \tag{6.17}$$

$$R_2(t) = R \cdot sin(\omega t + \phi_1 + \frac{\pi}{2}) = R \cdot cos(\omega t + \phi_1) \tag{6.18}$$

$$
\begin{aligned}
E(t) \cdot R_1(t) &= E \cdot R \cdot sin(\omega t + \phi) \cdot sin(\omega t + \phi_1) \\
&\overset{eq.(6.2)}{=} 0.5 \cdot E \cdot R \left[cos(\phi - \phi_1) - cos(2\omega t + \phi + \phi_1) \right] \\
&\overset{low-pass}{=} 0.5 \cdot E \cdot R \cdot cos(\phi - \phi_1) = X
\end{aligned}
\tag{6.19}
$$

$$
\begin{aligned}
E(t) \cdot R_2(t) &= E \cdot R \cdot sin(\omega t + \phi) \cdot cos(\omega t + \phi_1) \\
&\overset{eq.(6.4)}{=} 0.5 \cdot E \cdot R \left[sin(\phi - \phi_1) + sin(2\omega t + \phi + \phi_1) \right] \\
&\overset{low-pass}{=} 0.5 \cdot E \cdot R \cdot sin(\phi - \phi_1) = Y
\end{aligned}
\tag{6.20}
$$

From the X and Y component, it is easy to obtain the signal amplitude (with a proportionality constant) eq. (6.21) and its phase eq. (6.22)[3].

$$\sqrt{X^2 + Y^2} = 0.5 \cdot E \cdot R \cdot \sqrt{cos^2(\phi - \phi_1) + sin^2(\phi - \phi_1)} \overset{eq.(6.5)}{=} 0.5 \cdot E \cdot R \propto E \tag{6.21}$$

$$arctan\left(\frac{Y}{X}\right) = arctan\left(\frac{0.5 \cdot E \cdot R \cdot sin(\phi - \phi_1)}{0.5 \cdot E \cdot R \cdot cos(\phi - \phi_1)}\right) = \phi - \phi_1 \tag{6.22}$$

[3]To span the entire 2π range, in the data analysis the atan2 function is used, see as well next section 6.1.4.

6.1.4 Detailed mathematics of pseudo-heterodyne detection

In the pseudo-heterodyne detection scheme, three electric fields are involved containing the laser frequency ω, the cantilever frequency Ω, and the mirror frequency M with $\omega >> \Omega >> M$: The near-field signal itself eq. (6.23), the background contribution eq. (6.24), and the phase modulated reference field eq. (6.25).

$$E_{nf}(t) = E_{nf}(\Omega t)sin(\omega t + \phi_{nf}) = \sum_{n=0}^{\infty} E_{nf,n}sin(n\Omega t + \phi_c)sin(\omega t + \phi_{nf,n}) \quad (6.23)$$

$$E_b(t) = E_b sin(\omega t + \phi_b) \quad (6.24)$$

$$E_r(t) = E_r sin(\omega t + \gamma cos(Mt) + \phi_r) \quad (6.25)$$

In the detector, all three contributions are mixed, resulting in six terms (as for homodyne and heterodyne detection eq. (1.26)) given by

$$
\begin{aligned}
I &= [E_r(t) + E_b(t) + E_{nf}(t)]^2 \\
&= E_r^2(t) + E_b^2(t) + E_{nf}^2(t) + 2E_r(t)E_b(t) + 2E_{nf}(t)E_b(t) + 2E_{nf}(t)E_r(t)\,.
\end{aligned}
\quad (6.26)
$$

Due to the higher harmonic demodulation at $n\Omega$ and demodulation at the mirror frequency M, only the product between the reference field and the near-field term $2E_{nf}(t)E_r(t)$ remains after the LIAs (sideband or tandem demodulation) since it contains both contributions (again equivalent to the heterodyne detection, see subsection 1.3.3).

$$
\begin{aligned}
I_{n\Omega,M} &\propto E_{nf}(t)E_r(t) \\
&= \sum_{n=0}^{\infty} E_{nf,n}E_r sin(n\Omega t + \phi_c)sin(\omega t + \phi_{nf,n})sin(\omega t + \gamma cos(Mt) + \phi_r) \\
&\overset{eq.(6.12)}{\propto} \sum_{n=0}^{\infty} E_{nf,n}E_r sin(n\Omega t + \phi_c) \cdot cos(\gamma cos(Mt) + \phi_r - \phi_{nf,n})
\end{aligned}
$$
$$(6.27)$$

The phase modulated term from the reference beam can be rewritten in its harmonics using the Jacobi-Anger identities eq. (6.7) and eq. (6.8) as well as $\Phi = \phi_r - \phi_{nf,n}$.

$$cos(\gamma cos(Mt) + \phi_r - \phi_{nf,n})$$

$$\stackrel{eq.(6.3)}{=} cos(\gamma cos(Mt))cos\Phi + sin(\gamma cos(Mt))sin\Phi$$

$$\stackrel{eq.(6.7),(6.8)}{=} J_0(\gamma) + 2 \cdot \sum_{l=1}^{\infty} \left[(-1)^l J_{2l}(\gamma)cos(2lMt)cos\Phi - (-1)^l J_{2l-1}(\gamma)cos((2l-1)Mt)sin\Phi \right]$$

$$(6.28)$$

Combining both equations (6.27) and (6.28) leads to

$$I_{n\Omega,mM} \propto \sum_{n=0}^{\infty} E_{nf,n}E_r sin(n\Omega t + \phi_c) \cdot ...$$

$$... \left[J_0(\gamma) + 2 \cdot \sum_{l=1}^{\infty} \left[(-1)^l J_{2l}(\gamma)cos(2lMt)cos\Phi - (-1)^l J_{2l-1}(\gamma)cos((2l-1)Mt)sin\Phi \right] \right] .$$

$$(6.29)$$

Eq. (6.29) helps to understand the tandem demodulation better (see fig. 1.13): The first fast LIA at $n\Omega$ (in phase with the cantilever movement ϕ_c) passes the signal in the big brackets (which is equal to eq. (6.28)) to the slow LIA. Autophasing the slow LIA means to set it in phase with the mirror oscillation M. If the two phases (cantilever phase ϕ_c and reference phase ϕ_r) are constant during a measurement, the tandem demodulation is working (the role of the cantilever phase is analysed more deeply in the last paragraph of this subsection).

From calculating the products in equation (6.29) it is clear that (next to the higher harmonics at frequencies $n\Omega$) sidebands spaced by M occur $f = n\Omega \pm mM$ according to

$$SB_{n,l=1} \propto E_{nf,n}E_r sin(n\Omega t + \phi_c)...$$
$$... \cdot [J_0(\gamma) - 2(J_2(\gamma)cos(2Mt)cos\Phi + J_1(\gamma)cos(Mt)sin\Phi)]$$
$$\stackrel{eq.(6.4)}{=} E_{nf,n}E_r J_0(\gamma)sin(n\Omega t + \phi_c)...$$
$$... - E_{nf,n}E_r J_2(\gamma) \cdot sin((n\Omega + 2M)t + \phi_c)cos\Phi...$$
$$... - E_{nf,n}E_r J_2(\gamma) \cdot sin((n\Omega - 2M)t + \phi_c)cos\Phi...$$
$$... + E_{nf,n}E_r J_1(\gamma) \cdot sin((n\Omega + 1M)t + \phi_c)sin\Phi...$$
$$... + E_{nf,n}E_r J_1(\gamma) \cdot sin((n\Omega - 1M)t + \phi_c)sin\Phi .$$

$$(6.30)$$

Taking two arbitrary neighbouring sidebands (one odd $m = 1$, one even $m = 2$) enables to further isolate the near-field signal and its phase, e.g. the sidebands at $n\Omega + 1M$ and $n\Omega + 2M$ expressed by

$$SB_{n,1M} \propto E_{nf,n}E_r J_1(\gamma)sin(\phi_r - \phi_{nf,n}) \tag{6.31}$$

$$SB_{n,2M} \propto E_{nf,n}E_r J_2(\gamma)cos(\phi_r - \phi_{nf,n})\,. \tag{6.32}$$

As mentioned in subsection 1.3.4, it is required to choose the modulation depth γ properly to simplify these equations $J_1(\gamma) = J_2(\gamma) = J_{1/2}(\gamma)$. Now the optical amplitude $E_{nf,n}$ eq. (6.33) and the optical phase $\phi_{nf,n}$ eq. (6.34) can be isolated by processing the two sidebands.

$$\sqrt{SB_{n,1M}^2 + SB_{n,2M}^2} \propto E_{nf,n}E_r J_{1/2}(\gamma)\sqrt{sin^2(\phi_r - \phi_{nf,n}) + cos^2(\phi_r - \phi_{nf,n})}$$
$$\stackrel{eq.(6.5)}{=} E_r J_{1/2}(\gamma)E_{nf,n} \propto E_{nf,n} \tag{6.33}$$

$$arctan\left(\frac{SB_{n,1M}}{SB_{n,2M}}\right) = arctan\left(\frac{sin(\phi_r - \phi_{nf,n})}{cos(\phi_r - \phi_{nf,n})}\right) = \phi_r - \phi_{nf,n} \rightarrow \Delta\phi_{nf,n} \tag{6.34}$$

As already mentioned in the main text, the arctan function limits the phase range to the interval $-\frac{\pi}{2}$ to $+\frac{\pi}{2}$. The $atan2(x,y)$ function is related to the arctan function, but depending on the signs of the arguments different signs and ϕ shifts are used to span the entire $-\pi$ to $+\pi$ range [201].

$$atan2(SB_{n,1M}, SB_{n,2M}) = \phi_r - \phi_{nf,n} \rightarrow \Delta\phi_{nf,n} \tag{6.35}$$

Setting the proper reference mirror oscillation

For ensuring the proper reference oscillation γ=2.63 (see subsection 1.3.4), three methods are possible:

- For mirrors moved by a closed-loop piezo system, it can be easily set directly to the proper amplitude value d. The angle α in eq. (1.42) can be measured by sweeping the mirror in a static interferometer and observing the interference pattern (as described in subsection 3.1.1).

- If γ is not set properly, the calculated near-field signal depends on ϕ_r, see fig. 6.1 (ϕ_r corresponds to the DC offset of the piezo stage). If the sidebands are processed in real-time to the s-SNOM amplitude $\sqrt{SB_{1M}^2 + SB_{2M}^2}$, the user can vary the AC stage amplitude d until the s-SNOM signal stays constant independent of the DC offset ϕ_r (which is swept automatically or manually).
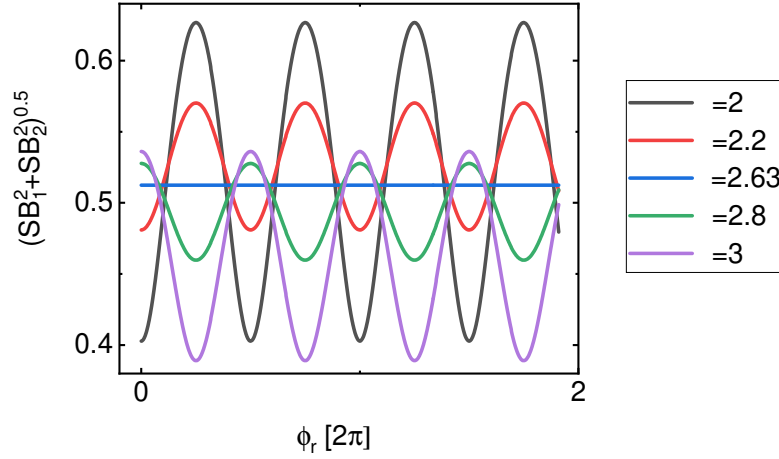
Figure 6.1: Calculated near-field signal eq. (6.33) as a function of the reference offset ϕ_r for different modulation depths γ; the sidebands are calculated using eq. (6.31) and eq. (6.32), respectively.

- An experienced user can observe the (in)equality of the sidebands directly at the detector/fast LIA ($n\Omega$) output on an oscilloscope triggered to the mirror frequency M fig. 6.2: Again, the AC amplitude is optimized; at each value the DC offset is swept and depending on the pattern the amplitude is proper or has to be increased/lowered.

All those three schemes can be conducted by using the higher harmonics of the s-SNOM near-field signal itself (n=2, 3, 4, ... in eq. (6.27)), or the $1\Omega \pm mM$ signal from a freely oscillating tip (no sample required and noise from the s-SNOM is avoided; mathematical equivalent to n=1 in eq. (6.27)), or with a half-static interferometer (phase modulated E_r and static second term from the cantilever arm, whether E_b or the reflection from an alignment mirror; both correspond to n=0 in eq. (6.27)).

Effect of cantilever phase

This subsection should highlight the role of the cantilever phase ϕ_c in the s-SNOM signal and pseudo-heterodyne detection scheme experimentally. The fast LIA at $n\Omega$ is demodulating X (with its phase set to 0 to be in parallel with the cantilever movement), picking out the corresponding cosine term in eq. (6.36) (from eq. (6.27)) belonging to the corresponding higher harmonic. However, the autophase function is only performed once before a measurement (otherwise π jumps can occur).
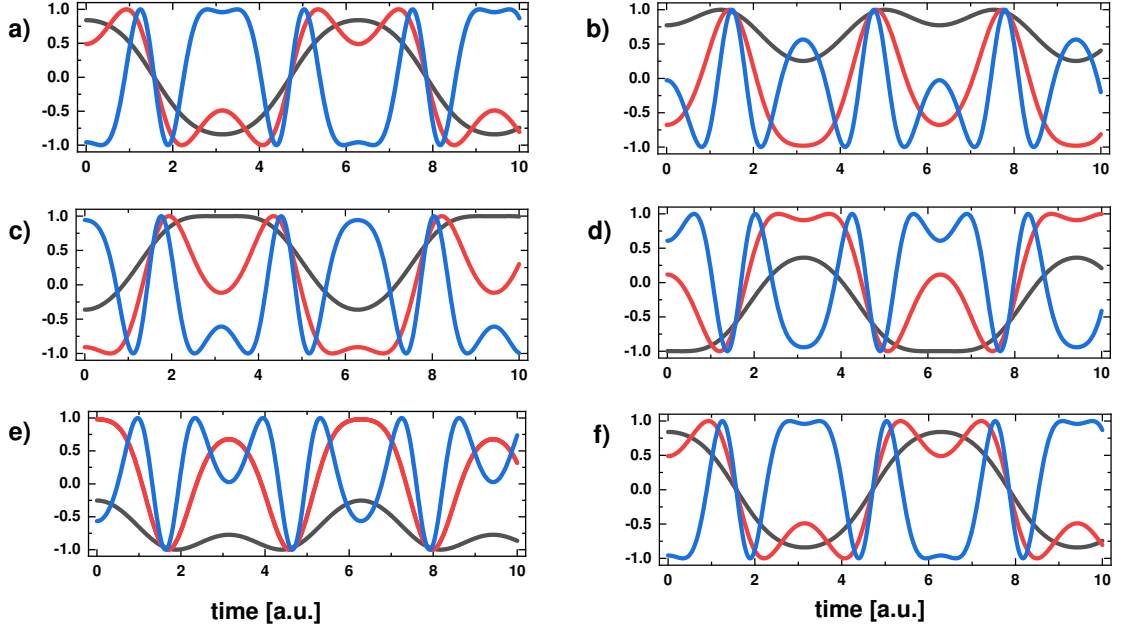
Figure 6.2: Simulated oscilloscope signals (based on the phase-modulated cosine term on the left side of eq. (6.28) triggered to the mirror frequency M at different phase positions ϕ_r a)-f) ($0 - \pi$ in 0.2π steps). For $\gamma = 1 < 2.63$ (black), the minimum and maximum values oscillate (here between -1 and +1). For $\gamma = 2.63$ (red; optimum value), the minimum and maximum of the curve are always constant (again -1 and +1). For $\gamma = 5 > 2.63$ (blue), additional extrema occur in the curve.
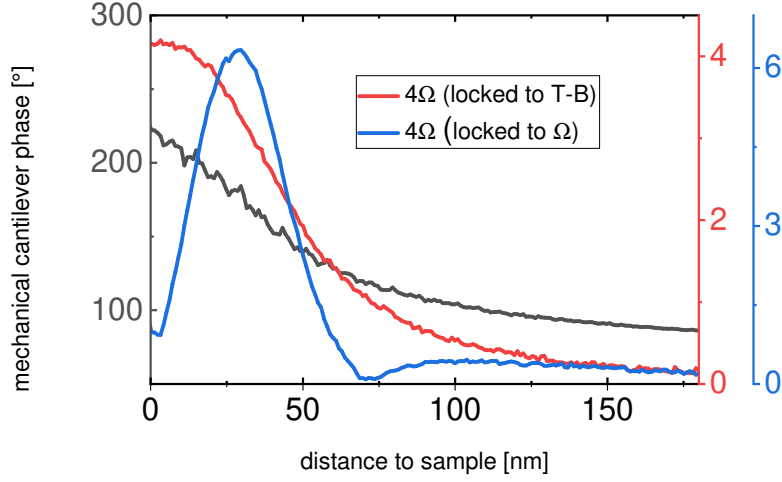
Figure 6.3: During an approach to the sample surface, the mechanical cantilever phase is changing. If the fast LIA is locked on the cantilever excitation signal Ω, this phase change induces a change of the near-field signal and a dip. If it is locked on the T-B signal from the PSD (which corresponds to the real cantilever movement), smooth approach curves are measured as expected (mIR pseudo-heterodyne s-SNOM approach curves on Au).

$$I_{n\Omega,M} \propto \sum_{n=0}^{\infty} E_{nf,n}E_r sin(n\Omega t + \phi_c) \cdot cos(\gamma cos(Mt) + \phi_r - \phi_{nf,n}) \qquad (6.36)$$

Thus, if the cantilever phase is changing during a measurement (e.g. the mechanical cantilever phase is an indication of the sample's mechanical properties, see phase imaging [15]), the s-SNOM signal is changing as well. Another example of changing ϕ_C are approach curves: During the approach, the resonance is shifted (see eq. (1.10)) and therefore the current phase as well. A simple solution to overcome this disturbing effect is to lock the LIAs $n\Omega$ directly on the real cantilever movement (the control signal for the AFM, e.g. the top-bottom (T-B) signal from the position sensitive diode fig. 2.1)) instead of the excitation signal Ω. Of course, the signal quality is worse; but the LIAs are still able to lock on this signal. The approach curve fig. 6.3 illustrates this effect and how the T-B lock-in makes a difference.

6.2 Numerical s-SNOM simulations

Fig. 6.4 shows the MATLAB-code used for creating fig. 1.17 and fig. 1.18. Both codes are using additional functions depicted in fig. 6.5.

```matlab
%%%%%%%%%%%%%%%%%%%%%%%%%%%%%%%%%%%%%%%%%%%%%%%%%%%%%%%%%%
%%%%%%%%%%%%%%%%%% MAIN FILE s-SNOM-CONTRAST %%%%%%%%%%%%%%%%%%%%%%%
%%%%%%%%%%%%%%%%%%%%%%%%%%%%%%%%%%%%%%%%%%%%%%%%%%%%%%%%%%
% PARAMETERS
c0=299792458;                % speed of light
lambdaSI=9.2*1e-6;           % wavelength        (changed for every curve)
epsTip=-1110+563*i;          % Pt tip            (changed for every curve)
eps2=-4746+1009*i;           % Au sample         (changed for every curve)
a=10e-9;                     % tip radius
hh=3;                        % higher harmonic
n=10.^(linspace(16,21, 1000)); % x-axis [cm^-3]
m_eff=0.26;
epsL=11.7;
tau_model                    % calculate "tau" (function of n) (external file)

% CALCULATIONS
eps1=Drude(n*1e6, tau, m_eff, lambdaSI, epsL);
alpha=alphaFunc(a, epsTip);
[t z fz]=t_z_vectors(1.5, 20, 5, 1e-9, 25e-9);

scat1=polarizability2(alpha, eps1, a, z);
scat0=polarizability2(alpha, eps2, a, z);
[s1 phase1]=higher_harmonics(scat1,t,fz, hh);
[s0 phase0]=higher_harmonics(scat0,t,fz, hh);
normal=s1./s0;

% PLOTS
plot(n,normal);
ylabel('s_3(Si)/s_3(Au)')
xlabel('charge carrier density [cm^{-3}]')
set(gca, 'XScale', 'log')
figure
plot(n, (phase1-phase0))
ylabel('\Phi_3(Si)-\Phi_3(Au) [rad]')
xlabel('charge carrier density [cm^{-3}]')
set(gca, 'XScale', 'log')
%%%%%%%%%%%%%%%%%%%%%%%%%%%%%%%%%%%%%%%%%%%%%%%%%%%%%%%%%%
%%%%%%%%%%%%%%%%%% MAIN FILE APPROACH CURVES %%%%%%%%%%%%%%%%%%%%%%%
%%%%%%%%%%%%%%%%%%%%%%%%%%%%%%%%%%%%%%%%%%%%%%%%%%%%%%%%%%
% PARAMETERS
epsTip=-1320+797*i;          % 10.5 microns Pt
eps=-5736+1475*i;            % 10.5 microns Au
a=10e-9;                     % tip radius
hh=1;                        % higher harmonic    (changed for every curve)

% CALCULATIONS
alpha=alphaFunc(a, epsTip);
z0=linspace(1,101,1000)*1e-9;
[t z fz]=t_z_vectors(1.5, 100, 10, z0, 25e-9);
scat=polarizability2(alpha, eps, a, z);
[s phase]=higher_harmonics(scat,t,fz, hh);

% PLOT
plot(z0*1e9,s*1e35); % 1e35 arbitrary scale constant
ylabel('s-SNOM signal [a.u.]')
xlabel('distance to sample [nm]')
```

Figure 6.4: MATLAB code used for fig. 1.17 and fig. 1.18.

```
%%%%%%%%%%%%%%%%%%%%%%%%%%%%%%%%%%%%%%%%%%%%%%%%%%%%%%%%%%%%
%%%%%%%%%%%%%%%%% ADDITIONAL FUNCTIONS %%%%%%%%%%%%%%%%%%%%%%%%%%%%%
%%%%%%%%%%%%%%%%%%%%%%%%%%%%%%%%%%%%%%%%%%%%%%%%%%%%%%%%%%%%
function eps=Drude(n, tau, m_eff, lambda, epsL)
% Drude model
eps0=8.8554*1e-12;
e=1.6021766208*1e-19;
me=9.10938356*1e-31;
c0=299792458;
omega=2*pi*c0./lambda;
eps=epsL-n.*e^2/(me*m_eff*eps0)*1./(omega.^2+i*omega./tau);
end


function alpha=alphaFunc(a, epsTip);
% polarizability of a sphere
eps0=8.8554*1e-12;
alpha=4*pi*eps0*a^3*(epsTip-1)/(epsTip+2);
end


function [t z fz]=t_z_vectors(fz, points_per_sin, oscillations, z0, amplitude)
% harmonic oscillation z(t) at frequency fz
L=points_per_sin*oscillations;        % number of data points
T=1/points_per_sin/fz;                % distance between points
t = (0:L-1)*T;
z=(sin(2*pi*t*fz)+1)*amplitude+z0';
end


function alphaEff=polarizability2(alpha, eps, a, z)
% provides complex scattering coefficients alpha as matrix (depending on
% z-position and epsilon-value)
eps0=8.8554*1e-12;
beta=(eps-1)./(eps+1);
alphaEff=(alpha.*(1+beta)./(1-alpha.*beta./(16*pi*eps0.*(z'+a).^3)));
end


function  [sx phase]=higher_harmonics(scat,t,f_z, hh)
% performing numerical higher harmonic demodulation
T=(max(t)-min(t))/(length(t)-1);
L=length(t);
Fs=1/T;
% FFT (adapted from https://de.mathworks.com/help/matlab/ref/fft.html,
% 26.08.2020)
% FFT from each column
%(1 column corresponds to alpha(z) for a specific eps-value)
Y=fft(scat);
abs2 = abs(Y/L);
abs1 = abs2(1:L/2+1,:);
abs1(2:end-1,:) = 2*abs1(2:end-1,:);
f = Fs*(0:(L/2))/L;
phase2=angle(Y/L);
phase1=phase2(1:L/2+1,:);
% extract desired higher harmonics out of spectrum (amplitude and phase)
signal=abs1.*(f>(hh-0.5)*f_z&f<(hh+0.5)*f_z)';
sx=max(signal);
[val, coordinate]=min(abs(f-hh*f_z));
phase=phase1(coordinate,:);
end
```

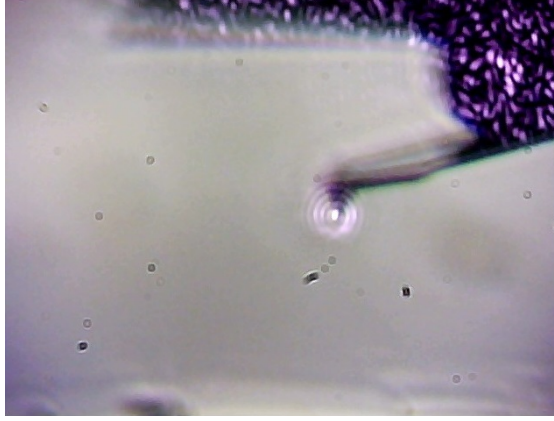Figure 6.5: Additional functions used in fig. 6.4.

Figure 6.6: By using a visible s-SNOM beam or a visible pilot laser beam, the parabolic mirror focus can be aligned onto the cantilever tip apex.

6.3 Alignment of mIR s-SNOM

In the following, some hints for the mIR s-SNOM alignment are listed:

- The interferometer (i.e. the overlap of both arms) can be optimized by using a reflecting surface (parallel to the base of the parabolic mirror) for a static interferometer.

- The pilot beam can be aligned onto the tip apex by using the side camera (see fig. 6.6).

- To find the focus of the CO_2 laser, first the 1Ω signal of a freely oscillating tip can be optimized. This optimum is mostly already close to the tip apex (depending on the tip geometry and the focal spot size). Subsequently, from this position, the final s-SNOM focus can be found quickly. However, one has to take care of disturbing interferences that can occur.

- The pseudo-heterodyne detection scheme can be optimized by using the sidebands of a freely oscillating tip at $1\Omega \pm mM$ (avoiding any uncertainties and noise from the near-field interaction). This signal can be used as well to optimize the focus of the parabolic mirror in a first step.

- The alignment and coupling of the s-SNOM beam to the detector by the parabolic mirror is very sensitive. An aperture in front of it and monitoring the detector power level to avoid saturation is advantageous.
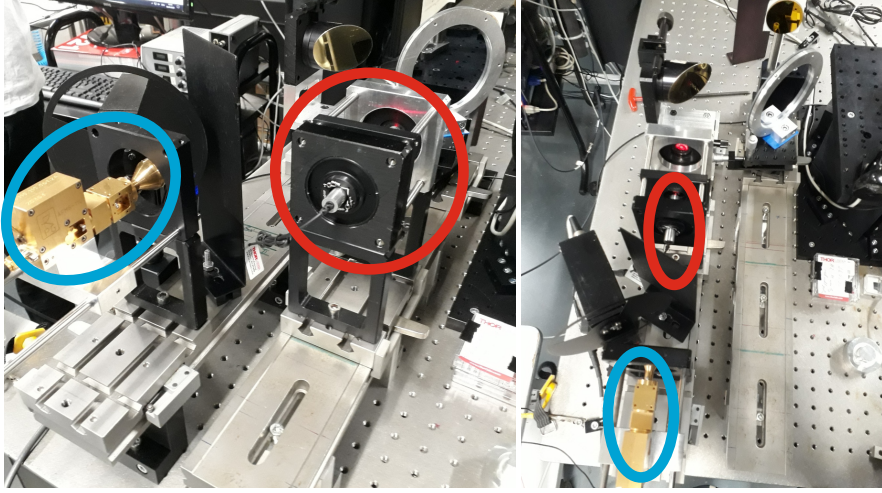
Figure 6.7: Both the GHz electronic source (blue circle) and the pilot laser (red circle) are mounted on a rail system. Both arms of the interferometer can be adjusted consecutively by placing the pilot laser in each arm.

6.4 Alignment of THz s-SNOM

In the following, a possible procedure for the THz s-SNOM alignment is suggested. Since the THz silicon beam splitter is not transparent (only reflective) for the optical pilot beam, both sides of the interferometer have to be adjusted separately.

Here, nearly all components (especially source, detector, and pilot beam) are mounted on a rail system adjusted to the same beam directions and heights, see fig. 6.7. So, the pilot beam can be easily placed on the detector and emitter positions covering both sides of the interferometer.

The mirror labelling refers to fig. 6.8 (adapted from fig. 2.12).

1. First, the parabolic mirror M3 is replaced by a flat mirror M4 sharing its parent orientation plane. The pilot beam is placed on the emitter position (beam splitter removed), a lens in front of the pilot beam can mimic the divergence of the electronic source (to have a collimated beam after M1), and an aperture in front of the pilot beam enables the alignment of the back reflection from M4 (to ensure a perpendicular incidence on M4) by moving M1 and the rail itself.

2. The beam splitter is placed into the setup.

3. The pilot beam is placed on the detector position (without the detector lens and pilot beam lens; indeed, the aperture for the back reflection is
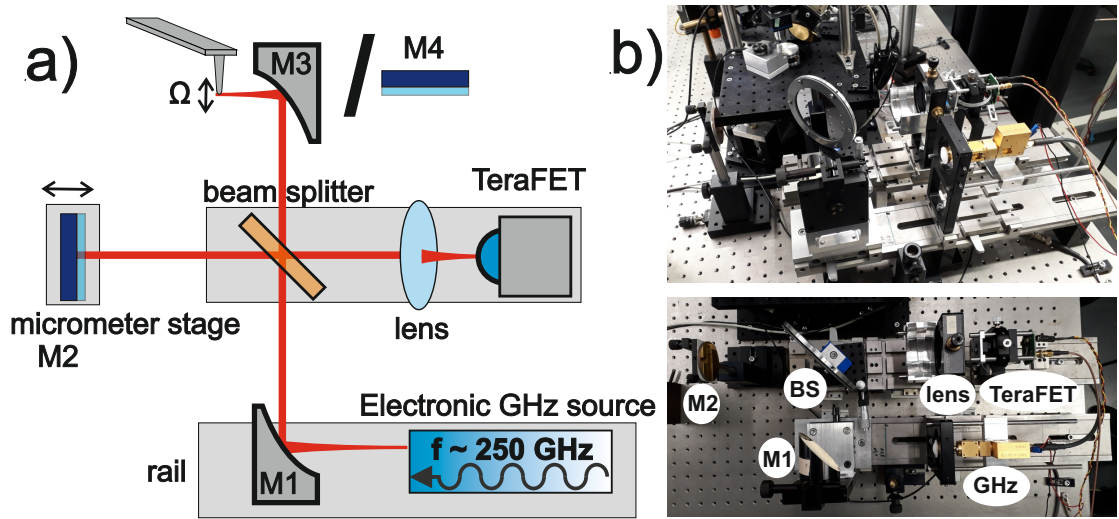
Figure 6.8: a) Sketch of the THz interferometer and b) the corresponding photos of the experiment.

required) to adjust the beam splitter: The beam should be again centred and perpendicular to the M3/M4 plane.

4. The pilot beam is positioned back on the emitter position. Now the reference arm is adjusted perpendicularly only by M2 (back reflection to the pilot beam). Due to the finite thickness of the beam splitter, there can be a small parallel position offset of the beams in the interferometer.

5. All components are switched to the GHz radiation (GHz emitter, TeraFET, and focussing lens in front of the detector). For measuring a signal, a modulation is required (electronic modulation or mechanical chopping). The effective focal point of the emitter should be known in advance (for the proper distance to M1) as well as the focal point of the lens.

6. The signal arm of the interferometer (source - M1 - beam splitter - M4 - beam splitter - lens - detector) can be optimized.

7. At the end, the reference arm is optimized solely by using M2 (to avoid misalignment of the signal arm).

8. The interference of both arms can be checked (changing the position of M2) and optimized.

9. At the end, M4 is again replaced by the parabolic mirror M3 focussing the light onto the oscillating cantilever. The electronic/mechanical chopping can

be removed. Now the 1Ω signal of the cantilever should be measurable and can be used to further optimize the setup. A higher cantilever amplitude is helpful, especially for weak signals at the beginning. Furthermore, placing a Au sample beneath the tip (distance of some microns; for better reflection of the 1Ω signal) is beneficial and can enhance the signal as well. Due to the wavelength, the focus of M3 can be adjusted solely by micrometer screws, a piezo alignment is not necessary.

10. Due to the spot size of the GHz radiation (several mm) that is much bigger than the cantilever size ($\sim$100 µm for long probes), the optimum of the 1Ω signal is very close to the optimum of the s-SNOM signal.

6.5   Numerical LabVIEW lock-in amplifier

As mentioned in the main part, the Zurich Instruments MFL lock-in amplifier provides the demodulated signals $n\Omega$ in digital form anyway. Therefore, instead of transferring the signal for the slow demodulation to the DSP 7265 devices (including a DAC and an ADC step), it is tried to extend the MFL with a numerical LIA using LabVIEW (version 2019, conceptual sketched in fig. 6.9). It makes the entire detection scheme and instrumentation more compact and flexible. Especially in combination with possible software upgrades (the MF MD package, which offers four demodulators in parallel [202]; it could be purchased only at the end of this project), it is an interesting option.

The MFLI saves the data of the demodulated signal $n\Omega$ and the data from the reference wave M, which is fed into an auxiliary input port, at a user chosen data rate Δt. The corresponding time stamps of both signals are attached as well. The LabVIEW-vi collects data packages of duration τ (a user chosen time; labelled as "recording time" in the MFLI *ziPollDataExDemodTime.vi* from Zurich Instruments) and continues their processing. The LabVIEW integrated sub-vi "Extract Single Tone Information.vi" (labelled with "ESTI.vi" in fig. 6.9) analyses the reference wave and extracts its frequency M and phase Φ. Out of this information, four reference signals are calculated for demodulating the signal at $1M$ and $2M$ (two reference waves X and Y for both harmonics, respectively). Φ_1 and Φ_2 are two user chosen phase offsets to set the sideband phases to zero (equal to the "auto phase" function). The numerical LIA processing follows the mathematics presented in the appendix 6.1.3. The resulting values for the sidebands can be sent via the auxiliary output channels of the MFLI to the Anfatec SPM controller. Of course, it is not only possible to send the sidebands to the SPM controller, but the s-SNOM amplitude and its phase can be calculated in real time directly in LabVIEW following eq. (1.39) and eq. (1.40), too. It is quite important to
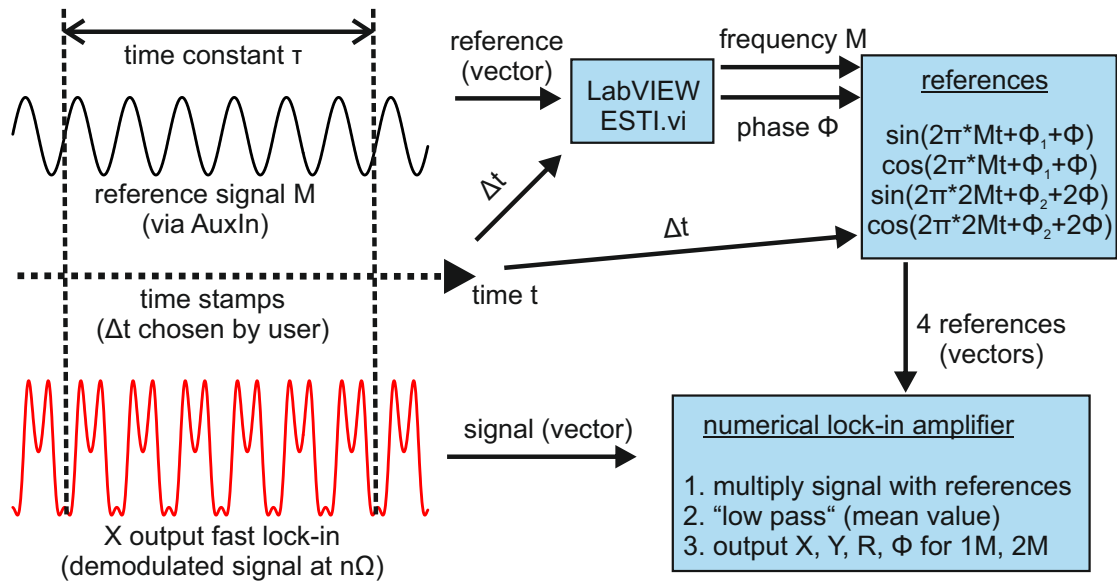
165

Figure 6.9: The concept of the LabVIEW LIA used: The reference as well as the demodulated X signal are provided by the MFLI together with the corresponding time stamps. The four required reference waves are formed and used for the numerical lock-in amplification.

take the right phase of the reference wave Φ into account and to feed it into the numerical LIA[4] to enable the extraction of proper X values of the sidebands.

The performance of this LabVIEW LIA is tested and analysed with the scheme sketched in fig. 6.10. The MFLI LIA demodulates the signal at a higher harmonic and passes its X signal in parallel to a DSP 7265 LIA (analogue via BNC cable) and to the lock-in.vi (digital).

Table 6.1 lists the noise values of the sidebands, the calculated near-field amplitudes (standard deviation divided by mean value), and phases (standard devi-

---

[4]For the second sideband 2M, the phase of the M-reference has to be multiplied by a factor of 2.
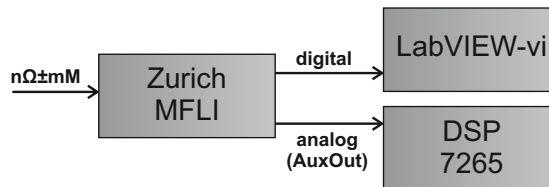

Figure 6.10: To test the LabVIEW lock-in.vi, the Zurich MFLI LIA sends the demodulated signal in parallel to the DSP 7265 LIA and the LabVIEW program.

| $n\Omega$ | DSP 7265 | | lock-in.vi | | DSP 7265 | | lock-in.vi | |
	SB1	SB2	SB1	SB2	amplitude	phase	amplitude	phase
1Ω	0.38%	1.82%	3.38%	0.57%	0.17%	0.007	0.44%	0.012
2Ω	1.60%	0.62%	1.28%	5.77%	0.34%	0.010	2.17%	0.026
3Ω	1.48%	0.75%	1.17%	2.82%	0.57%	0.007	1.13%	0.011
4Ω	1.71%	1.68%	2.09%	3.51%	1.21%	0.012	1.87%	0.018
5Ω	0.92%	0.66%	1.64%	2.07%	0.52%	0.006	1.24%	0.014
6Ω	4.80%	4.66%	5.49%	5.30%	4.63%	0.010	5.03%	0.019
7Ω	5.20%	5.29%	6.48%	6.46%	5.00%	0.016	5.89%	0.027
8Ω	4.97%	3.82%	6.22%	9.09%	3.27%	0.028	5.47%	0.050

Table 6.1: Noise level comparison of the DSP 7265 LIA and the LabVIEW digital LIA for the two sidebands and the resulting near-field amplitudes and phases (standard deviation normalized to mean value; for the phases, absolute values in radian are given).

ation in radian) of eight measurements of higher harmonics. They are performed sequentially, with the two slow mM LIA demodulations in parallel. For each measurement, 1000 data points (waiting time between those points 20 ms) of the demodulated sidebands are recorded (LIA time constant t_c= 50 ms for both LIA; digital data rate to LabVIEW 20k points/s). The near-field amplitude and phases are calculated according to eq. (1.39) and eq. (1.40), respectively[5].

The DSP performance is superior in all measurements, the near-field noise and the phase noise is in average half of the LabVIEW LIA. A complementary measurement covering a longer time (5Ω; 1000 points with 1 s waiting time, other parameters as above) confirms the trend, but the deviation is smaller (DSP near-field 2.15%, phase 0.020; LabVIEW near-field 2.37%, phase 0.024). Also, the direct comparison of approach curves supports this outcome fig. 6.11.

Amongst others, a limiting factor is the computational speed of the LabVIEW-vi. In its current form, it is too slow to record and process all the data, e.g. only a bunch of 50 ms data is processed every 200 ms. Of course, in future a faster performance with, for example, better hardware or a speed optimized LabVIEW code is possible.

However, often in s-SNOM the noise level is not a critical limiting factor. Fig. 6.12 directly compares the two LIAs and their imaging quality is quite comparable (5Ω, $\lambda = 10.5$ µm, $t_{c,MFLI}$=100 µs, $t_{c,slow}$=20 ms).

Hence, the LabVIEW LIA is a useful tool and extension that was frequently used during this thesis.

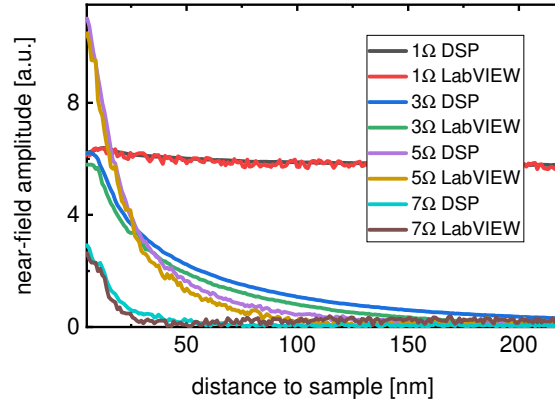[5]The data for the DSP 7265 are those from the mirror comparison in table 3.1.

Figure 6.11: s-SNOM approach curves at different harmonics as a direct comparison between the DSP 7265 LIA and the LabVIEW LIA.
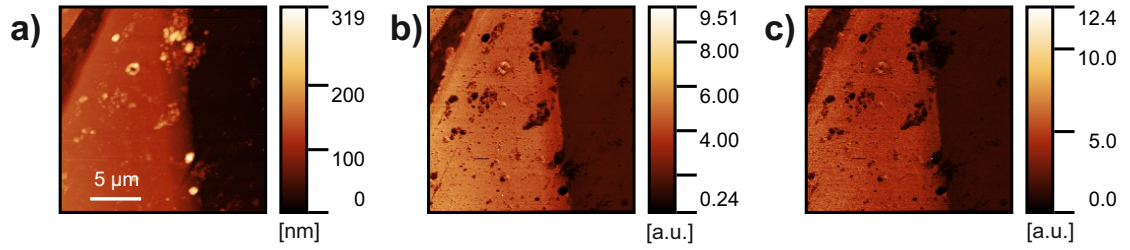

Figure 6.12: a) AFM topography image of a (dirty) Au structure on Si substrate and the corresponding 5Ω s-SNOM signals (amplitude) recorded using the b) DSP LIA and c) the LabVIEW-vi.